# Weak or Strong On Coupled Problems In Continuum Mechanics

Bernd Markert
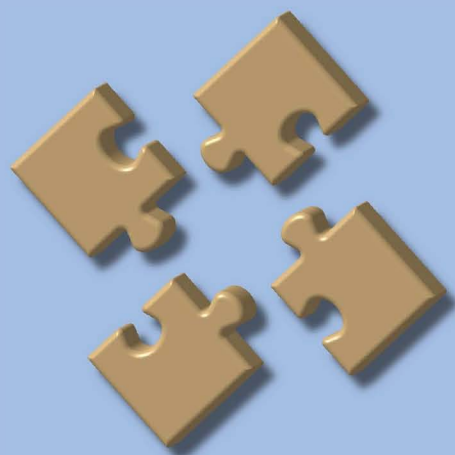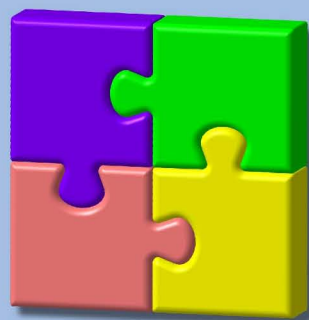
# Weak or Strong
# On Coupled Problems in Continuum Mechanics

Vom „Stuttgart Research Centre for Simulation Technology"
und der Fakultät Bau- und Umweltingenieurwissenschaften
der Universität Stuttgart genehmigte Habilitationsschrift

vorgelegt von

## Dr.-Ing. Bernd Markert

aus

Mayen/Eifel

Hauptberichter:  Prof. Dr.-Ing. Wolfgang Ehlers
1. Mitberichter:  Prof. Dr.-Ing. Rainer Helmig
2. Mitberichter:  Prof. dr. ir. René de Borst

Tag der mündlichen Prüfung:  9. Juni 2010

Institut für Mechanik (Bauwesen) der Universität Stuttgart
Lehrstuhl für Kontinuumsmechanik
Prof. Dr.-Ing. W. Ehlers
2010

**Editor:**

Prof. Dr.-Ing. W. Ehlers

# PREFACE

The work described in this habilitation thesis was carried out between the years 2005 and 2010 at the Institute of Applied Mechanics (Civil Engineering), Chair of Continuum Mechanics, University of Stuttgart. During this period of my further academic and scientific development as postdoc and senior lecturer, it was my intention to elucidate the notion *coupled problem* from a more general perspective. This idea was also inspired by the observation that the '*multi*' words, such as multi-field, multi-physics, multi-scale, etc., which naturally imply some sort of coupling or interaction, find more and more their way into the computational mechanics community, not least because of the increased computer power. The profound expertise at the institute, particularly in the field of coupled multi-phase and porous media mechanics, was the self-evident starting point to set up a fundamental theoretical framework which comprises most of the coupled formulations conceivable in continuum physics without loosing the link to real application problems.

It is worth mentioning that during the years numerous people contributed in many ways to the realization of this work – all their support is most gratefully acknowledged. First of all, I particularly want to thank my academic mentor, Professor Wolfgang Ehlers, for giving me the opportunity to prepare the thesis in the institute and for granting me all the scientific freedom to make this work possible. He supported me in an open-minded and unreserved fashion, which led to many valuable and fruitful discussions. Besides the scientific support, I also thank him for the friendly and familiar atmosphere at the institute as well as the companionable relationship that grew over the past 15 years. I am also very grateful to Professor Rainer Helmig from the Institute of Hydraulic Engineering, Chair of Hydromechanics and Modeling of Hydrosystems, University of Stuttgart and to Professor René de Borst, Dean of the Department of Mechanical Engineering, Eindhoven University of Technology for taking the co-chairs in my habilitation procedure. Moreover, I want to thank all of my current and former colleagues, who always shared their experience and knowledge with me. In this regard, also the effort of my countless student assistants, diploma, and master students is hereby acknowledged with thanks, as they allowed me to follow new ideas, test unconventional methods, and carry out time-consuming numerical simulations besides the daily university business. Finally, I like to deeply thank my family, who really had a hard time during the writing process of my habilitation thesis and often had to share me with the computer at evenings and weekends. Actually, they provided me with the strength to bring this work to a successful end.

Stuttgart, June 18, 2010 <span style="float:right">Bernd Markert</span>

*Science is facts; just as houses are made of stones, so is science made of facts;*
*but a pile of stones is not a house and a collection of facts is not necessarily science.*
*Jules Henri Poincaré* (1854 – 1912)

# Contents

## II   A Selection of Coupled Problems          71

## 3  Introductory Notes to Part II         73

## 4  Monolithic vs. Splitting Solutions in Porous Media Dynamics   77

# Deutsche Zusammenfassung

KURZFASSUNG

Es ist das Ziel der vorliegenden Arbeit, einen umfassenden Einblick in das weite Feld der gekoppelten Probleme zu geben, wobei vor allem diejenigen Fragestellungen im Vordergrund stehen, die von besonderer Bedeutung in den computerorientierten Ingenieur- und Naturwissenschaften sowie der Physik sind. Hierzu werden zunächst einige grundlegende Begriffe eingeführt und damit die Basis für eine einheitliche Terminologie geschaffen, um im Anschluss eine sinnvolle Klassifizierung gekoppelter Probleme und der sie beschreibenden Gleichungssysteme durchführen zu können. Aufbauend auf diesen Grundlagen werden die Möglichkeiten der theoretischen und numerischen Behandlung gekoppelter Probleme dargestellt und erörtert. Die Aufmerksamkeit richtet sich hierbei vor allem auf volumetrisch gekoppelte Mehr-Feld-Formulierungen, die sich aus der kontinuumsmechanischen Beschreibung von Mehr-Physiken-Problemen auf natürliche Weise ergeben. Darüber hinaus werden auch geometrisch gekoppelte Probleme angesprochen. Anhand aktueller Fragestellungen aus den Bereichen der Poroelastodynamik, der Kontinuumsbiomechanik und der fluidgesättigten porösen Medien im allgemeinen werden sowohl die theoretische Modellbildung mittels gekoppelter Kontinuumsgleichungen als auch effiziente numerische Lösungsstrategien im Rahmen der Finite-Elemente-Methode (FEM) ausführlich vorgestellt und problemorientiert diskutiert.

## Motivation

Gemäß dem umfassenden Online-Wörterbuch `www.dictionary.com` bedeutet *gekoppelt* (engl. *coupled*) mit einem Link verbunden, zusammenhängend oder -gehörend, und ein *Problem* ist eine Fragestellung, die eine Lösung, in der Regel unter Zuhilfenahme mathematischer Operationen, erfordert.

Durchsucht man das Internet mit einer der populären Suchmaschinen nach *coupled problem* (gekoppeltes Problem) findet man derzeit (Juni 2010) ca. 35.000 Treffer, von denen fast alle einen mathematischen, physikalischen oder computerorientierten Hintergrund aufweisen.

Im täglichen Leben sind wir ständig mit gekoppelten Phänomenen konfrontiert, oftmals ohne uns dessen bewusst zu sein. Betrachten wir zum Beispiel das schnelle zyklische Biegen einer metallischen Büroklammer bis zum Bruch. Was wir beobachten, ist, dass sich die Büroklammer im Bereich der Bruchstelle aufgrund der dissipierten plastischen Arbeit im Material erwärmt. Es handelt sich hierbei offensichtlich um ein gekoppeltes thermomechanisches Problem, bei dem das Deformationsfeld mit dem Temperaturfeld interagiert und umgekehrt. Ein weiteres Beispiel eines gekoppelten Problems ist immer bei uns, nämlich die kontinuierlich stattfindenden Wachstums-, Degradations- und Umbauprozesse in unserem Körper. Nehmen wir Knochengewebe als Beispiel, welches, getrieben durch äußere Reize, chemische Faktoren sowie die vorhandenen Stoffwechselbedingungen, ständig abgebaut und neu gebildet wird. So verlieren Astronauten im Weltraum innerhalb von

6 Monaten bis zu 30 % ihrer Knochenmasse, da die Belastung infolge Schwerkraft fehlt und das Knochengewebe versucht, seine innere Struktur an die neue Belastungssituation anzupassen. Aus Sicht der theoretischen Modellierung ist die Knochenadaption ein sehr komplexes Beispiel eines gekoppelten Mehr-Physiken-Problems (engl. *coupled multiphysics problem*) unter Einbeziehung mechanischer, chemischer und biologischer Phänomene, deren Interaktionsmechanismen noch nicht vollständig verstanden sind, wie etwa die Mechanosensorik der Knochenzellen, die biochemische Wachstumsprozesse steuert.

In Wissenschaft und Technik haben wir es immer mit einer bestimmten Art von System (mechanisch, chemisch, biologisch usw.) zu tun, für das wir aufgrund einer Erregung oder Veränderung der äußeren Bedingungen eine Systemantwort suchen. Die diversen physikalischen Prozesse, die ein System hierbei regieren, können unterschiedlichen Systemkomponenten zugeordnet sein, stehen möglicherweise miteinander in Wechselwirkung, sind nichtlinear und finden auf unterschiedlichen Zeitskalen und räumlichen Gebieten statt. Diese Eigenschaften zeichnen ein allgemeines gekoppeltes System aus, bei dem aufgrund der dynamischen und multidirektionalen Interaktion der Systemkomponenten die gesuchte Systemantwort nur unter Berücksichtigung aller simultan ablaufenden Prozesse gefunden werden kann. Um derartig gekoppelte Probleme erfolgreich lösen zu können, müssen die einzelnen Komponenten des Systems durch geeignete theoretische und numerische Modelle beschrieben werden, die zusätzlich in der Lage sein müssen, die inhärenten Kopplungsmechanismen zwischen den abhängigen Feldgrößen situationsgerecht zu erfassen. Hierbei sind neben den üblichen Effizienz- und Genauigkeitsanforderungen insbesondere die Stabilitätseigenschaften der verfolgten Lösungsstrategie bzw. deren algorithmischer Umsetzung von Bedeutung.

Genau hier setzt die vorliegende Arbeit an, indem basierend auf einer sinnvollen Klassifizierung gekoppelter Probleme und der zugrundeliegenden Gleichungssysteme geeignete Lösungsmethoden in Abhängigkeit der auftretenden Kopplungsmechanismen behandelt werden. Zudem wird ein universeller theoretischer Rahmen zur Modellierung volumengekoppelter Mehr-Physiken-Probleme auf Basis der Kontinuumsmechanik bereitgestellt, wobei neben interagierenden multiplen Phasen (Festkörper und Fluide) zusätzlich sowohl thermomechanisch als auch elektromagnetisch gekoppelte Felder berücksichtigt werden. Die Anwendbarkeit der vorgestellten Methoden sowie der universellen Mehr-Feld-Formulierung wird im Anschluss anhand ausgewählter Problemstellungen verdeutlicht.

## Themenkomplex und Problemstellung

Die zunehmende Notwendigkeit, komplexe Probleme in der Numerischen Mechanik und Physik unter Beachtung aller auftretenden Kopplungsphänomene auf den unterschiedlichen Skalen eines Problems zu behandeln, erfordert die kontinuierliche Entwicklung neuer Strategien und Methoden, die genaue numerische Lösungen in überschaubaren Rechenzeiten ermöglichen. Hierbei liegen die Herausforderungen vor allem bei gekoppelten Systemen, für die die Berechnung der Interaktionsmechanismen nur schwer zu bewältigen ist oder die auf sehr unterschiedlichen Zeitkonstanten basieren (z. B. steife Probleme) bzw. auf weit zurückliegenden transienten Antworten aufbauen. Aus theoretischer Sicht sind

die meisten der auftretenden physikalischen Prozesse recht gut verstanden und es existieren in der Regel etablierte Modelle zu deren mathematischer Beschreibung. Zum Beispiel werden multifunktionale und intelligente Materialien (engl. *smart materials*), wie etwa Piezokeramiken oder elektroaktive Polymere (EAP), seit Jahrzehnten mittels mechanischer Theorien behandelt. Allerdings erlaubt erst die gestiegene Rechenleistung moderner EDV-Anlagen in Kombination mit ausgeklügelten numerischen Algorithmen unter Ausnutzung der neuen Hardware-Funktionalitäten eine effiziente Lösung realitätsnaher und praxisrelevanter Fragestellungen.

Die theoretischen Modelle hinter den gekoppelten Problemen basieren meist auf Erhaltungsgesetzen und führen in der Regel auf gekoppelte partielle Differentialgleichungen (PDE) in Raum und Zeit. Partielle Differentialgleichungen sind ihrem Wesen nach stetige Funktionen, die für eine rechnerische Behandlung zuerst in Raum und Zeit diskretisiert werden müssen. Im Zusammenhang mit Computer-Simulationen kann die räumliche Semidiskretisierung z. B. mit Hilfe der Finite-Elemente-Methode (FEM), der Finite-Differenzen-Methode (FDM) oder auch der Rand-Elemente-Methode (BEM) durchgeführt werden. Im Fall von gekoppelten Mehr-Physiken-Problemen können hierbei verschiedene räumliche Diskretisierungstechniken für die unterschiedlichen physikalischen Systemkomponenten gewählt werden, z. B. ein Finite-Elemente-Modell für eine Festkörperstruktur und ein Rand-Elemente-Modell für eine umgebende Flüssigkeit. Dies ist ein typisches Beispiel aus dem Bereich der Fluid-Struktur-Interaktion (FSI).

Durch die Raumdiskretisierung ergibt sich ein System von gewöhnlichen Differentialgleichungen (ODE) in der Zeit, die im Fall großskaliger Probleme Millionen von Evolutionsgleichungen umfassen können, die numerisch integriert werden müssen. Im Prinzip stehen drei allgemeine Ansätze zur Verfügung, um die Zeitintegration gekoppelter Systeme durchzuführen:

(1) Monolithischer oder direkter Ansatz,

(2) Partitionierter oder iterativer Ansatz,

(3) Teil-Schritt-Methode (engl. *fractional-step method*).

Die geschickte Wahl eines der oben genannten Verfahren ist hierbei eng mit dem betrachteten Problem und insbesondere mit der Art der vorhandenen Wechselwirkung der abhängigen Feldgrößen verbunden. Es bietet sich daher an, die Anwendung der Integrationsstrategien ausgehend von einer einfachen Klassifizierung gekoppelter Probleme aufzuzeigen.

Einige gekoppelte Mehr-Feld-Probleme, wie z. B. die Fluid-Struktur- oder Struktur-Struktur-Interaktion, können anhand ihrer räumlichen Teilgebiete charakterisiert werden (z. B. Fluid und Struktur), in denen jeweils unterschiedliche Gruppen von abhängigen Variablen (z. B. Flüssigkeitsdruck und Strukturverschiebung) behandelt werden. In diesem Fall stehen die Teilsysteme nur über eine Grenzschicht (engl. *interface*) in Verbindung, so dass die Wechselwirkung lediglich mittels Nahwirkungs- bzw. Kontaktkräften an den Grenzflächen benachbarter Teilgebiete erfolgt. Es erscheint daher zweckmäßig, diese Problemklasse als *oberflächengekoppelt* oder *geometrisch gekoppelt* zu bezeichnen, wobei die Interaktion der räumlich getrennten Teilsysteme über Randbedingungen bzw. Interfacegesetze beschrie-

ben wird. Zur Lösung dieser Problemklasse bieten sich Partitionierungsstrategien geradezu an, da hierbei eine einfache räumliche Trennung des geometrisch gekoppelten Problems in lose gekoppelte Einheiten erfolgen kann. Die partitionierte oder iterative Vorgehensweise hat den Vorteil, dass sie aufgrund der günstigen algorithmischen Struktur einfach und flexibel umgesetzt werden kann, wobei die Verwendung verschiedener Modelle und Diskretisierungen problemlos möglich ist und Software-Modularität erhalten bleibt. Die Teilprobleme können auf ihren Gebieten mit maßgeschneiderten Programmpaketen unabhängig gelöst werden und je nach vorhandener Hardware flexibel im sequentiellen oder parallelen Betrieb synchronisiert werden. Allerdings erfordert der partitionierte Ansatz erhebliche Investitionen auf methodischer Seite, da sowohl die Genauigkeit als auch die Stabilität erheblich beeinträchtigt werden können, insbesondere wenn ein hoher Grad an nichtlinearer Wechselwirkung vorliegt, was teure Iterations- oder Stabilisierungsschritte nach sich ziehen kann.

Bei einer anderen Problemklasse, den sogenannten *volumengekoppelten* oder *materiell gekoppelten* Problemen, ist eine mögliche partitionierte Behandlung nicht sofort anwendbar und unter Umständen auch gar nicht sinnvoll. Volumetrisch gekoppelte Probleme zeichnen sich insbesondere dadurch aus, dass sich grundverschiedene physikalische Phänomene auf demselben räumlichen Gebiet gegenseitig beeinflussen (z. B. thermische und mechanische Wechselwirkung). Die beschreibenden physikalischen Felder interagieren somit an jedem materiellen Punkt des betrachteten Körpers, so dass sich eine Kontinuumstheorie zur theoretischen Beschreibung mittels einer gekoppelten Mehr-Feld-Formulierung anbietet. Im Grunde genommen steckt die Kopplung direkt in den beschreibenden Bilanzgleichungen, die natürlich über geeignete Konstitutivgesetze zur Modellierung der jeweiligen physikalischen Phänomene ertüchtigt werden müssen. Da diese Art der Kopplung oft zu hochgradig nichtlinearen Gleichungssystemen führt mit unter Umständen sehr steifen Anteilen (z. B. Reaktionsterme) und algebraischen Nebenbedingungen (z. B. Inkompressibilität), werden zu deren numerischer Lösung oft monolithische Methoden eingesetzt, die auf ausgefeilten impliziten Zeitverlaufsverfahren basieren (z. B. steif-genaue Runge-Kutta-Verfahren). Die simultane Integration erfordert jedoch spezielle Software-Module und Löser, die gleichzeitig unterschiedliche Arten von Differentialgleichungen (elliptisch, parabolisch, hyperbolisch) behandeln können. Darüber hinaus führen allgemeine dreidimensionale Probleme auf sehr große Matrixsysteme, die aufgrund enthaltener algebraischer Gleichungen auch indefinit sein können. Die monolithische Vorgehensweise zieht somit keinen wirklichen Vorteil aus dem Mehr-Physiken-Charakter eines Problems, so dass aufgrund der unvermeidbar großen Gleichungssysteme im allgemeinen nur iterative Verfahren für eine schnelle Lösung in Frage kommen. In diesem Zusammenhang haben sich Gebietszerlegungsverfahren (engl. *domain decomposition methods*) oder Substrukturmethoden als leistungsstarke Techniken herauskristallisiert, da sie parallele Hardware-Architekturen durch intelligente Aufteilung des Rechengebietes gekonnt ausnutzen. Es besteht jedoch auch für volumengekoppelte Probleme generell die Möglichkeit, einen gestaffelten Lösungsansatz zu wählen, wobei über eine geeignete (z. B. additive) Zerlegung von Differentialoperatoren (engl. *operator splitting*) die Möglichkeit für eine fraktionierte Zeitintegration geschaffen wird.

Dies umfasst in etwa den Themenkomplex, dem sich die vorliegende Arbeit widmet. Neben einer ausführlichen Einführung in die oben beschriebene Problematik, zielen die darauf

aufbauenden Ausführungen auf allgemeine materiell bzw. volumetrisch gekoppelte Mehr-Feld-Probleme ab, die zum einen theoretisch durchdrungen und zum anderen mittels geeigneter Methoden einer effizienten numerischen Lösung zugeführt werden sollen.

# Gliederung der Arbeit

Die vorliegende Arbeit untergliedert sich in zwei Teile:

*Teil I* führt den Leser an das Themengebiet der gekoppelten Probleme heran, indem die wesentlichen Begriffe eingeführt und die theoretischen Grundlagen volumengekoppelter Formulierungen geschaffen werden.

Hierzu wird in *Kapitel 1* das umfassende Gebiet der gekoppelten Mehr-Feld-Probleme erschlossen und mögliche Lösunsgsansätze für unterschiedliche Problemklassen diskutiert.

*Kapitel 2* gibt eine kompakte Einführung in die Mehr-Phasen-Kontinuumsmechanik basierend auf den allgemeinen Konzepten der Mischungstheorie und der Theorie Poröser Medien, wobei sowohl thermodynamische als auch elektrodynamische Effekte einbezogen werden.

*Teil II* der Arbeit ist der Anwendung der teilweise abstrakten theoretischen Grundlagen aus Teil I gewidmet. Hierbei werden konkrete Fragestellungen aus dem Bereich der volumengekoppelten Mehr-Feld-Probleme behandelt.

Hierzu wird in *Kapitel 3* zunächst eine kurze Einführung in die folgenden Anwendungsprobleme gegeben und die Verknüpfung zu den zuvor beschriebenen Methoden und Theorien aufgezeigt.

*Kapitel 4* diskutiert dann das Problem der Poroelastodynamik und vergleicht zwei numerische Lösungsstrategien, die in Kapitel 1 eingeführt wurden.

In *Kapitel 5* werden volumengekoppelte Formulierungen in Anlehnung an Kapitel 2 zur Behandlung von Problemen aus dem Bereich der Kontinuumsbiomechanik vorgestellt, die zur Simulation von Quell- und Wachstumsprozessen biologischer Gewebe verwendet werden.

Darüber hinaus beschäftigt sich *Kapitel 6* mit der theoretischen Untersuchung des Fluidpenetrationseffekts beim Kontakt fluidgesättigter poröser Medien.

Zum Schluss beschreibt *Kapitel 7* ein finites Viskoelastizitätsmodell für poröse Medien, das zur Beschreibung menschlichen Bandscheibengewebes unter Einbeziehung osmotischer Effekte und diverser Heterogenitäten herangezogen wird.

# Part I

# Introduction and Theoretical Fundamentals
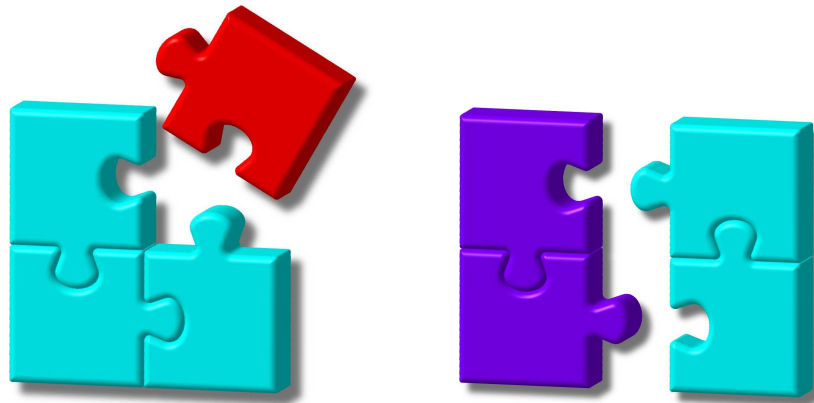
The jigsaw puzzle and the idea of
partitioning or splitting a coupled problem

# 1 Introduction to Coupled Problems

SUMMARY

This chapter aims at giving a concise introduction to the vast field of coupled problems, particularly to those of importance in engineering and physics. Therefore, the common terminology and an appropriate classification of coupled equation systems is presented accompanied by some mathematical and computational issues. Attention is focused on volumetrically coupled multifield formulations arising from the continuum mechanical treatment of multi-physics problems, but also geometrically coupled problems are addressed.

## 1.1 What is a Coupled Problem?

Following the comprehensive online dictionary `www.dictionary.com`, *coupled* means connected by a link, joined or associated together, and a *problem* is a statement requiring a solution, usually by mathematical operations.

Searching the internet for *coupled problem*, the popular search engines currently (June 2010) find about 35.000 hits, almost all of which are associated with some mathematical, physical, or computational background.

In daily life, we are permanently confronted with coupled phenomena, usually without recognizing or thinking about them. Consider, for instance, the fast cyclic bending of a paper clip until it breaks. What we observe, is that the clip is heated up around the break due to the dissipated plastic work in the material. Clearly, we have a coupled thermomechanical problem at hand where the deformation field is interacting with the temperature field and *vice versa*. Another example is always with us: The growth and remodeling processes going on in our body. Consider bone tissue as an example, which is constantly built and degraded, driven by external stimuli, chemical factors, and metabolic conditions. It is well known that astronauts lose bone mass while in space (up to 30% in 6 month) as no gravitational forces are present, and the bone tissue tries to adapt its structure to the new loading situation. From a modeling standpoint, this is a very complex example of a coupled multi-physics problem incorporating mechanical, chemical, and biological phenomena for which the interaction mechanisms, such as the bone cell mechanosensation controlling the biochemical process of growth, are not yet fully understood.

In science and engineering, we are commonly concerned with a certain kind of system (mechanical, chemical, biological etc.) for which we seek a response due to some excitation or change in the external conditions. This is what forms the type of problems, we are interested in. The different physical phenomena associated with the components that govern the system response possibly stay in mutual interaction, are nonlinear, and act on different time scales and spatial domains. In order to solve such problems, the components of the system have to be described by appropriate theoretical models additionally accounting for the inherent coupling mechanisms between dependent fields. In this regard

and geared by the terminology given by Park & Felippa [95] and Felippa *et al.* [45], the following definitions are proposed:

$$
\boxed{
\begin{array}{l}
\textbf{General definitions of coupled problems} \\[4pt]
\hline
\end{array}
}
$$

> **General definitions of coupled problems**
>
> (1) *Coupled problem:* A coupled problem is one in which physically or computationally heterogeneous components interact dynamically. The interaction is multi-way in the sense that the solution has to be obtained by a simultaneous analysis of the coupled equations which model the problem.
>
> (2) *Coupled multi-field problem:* A coupled multi-field problem is one in which the individual field equations are functions also of the other field variables governing the problem which requires the concurrent treatment of multiple dependent fields in a model. Every coupled problem is *per se* a coupled multi-field problem.
>
> (3) *Coupled multi-physics problem:* A coupled multi-physics problem is a coupled problem in which multiple physical models or phenomena are handled simultaneously. That is, if (1) different discretization techniques are used for individual subproblems on different (possibly coinciding) spatial domains or (2) individual field variables represent distinctly different but mutually interacting physical phenomena. A coupled multi-field problem is not *per se* a coupled multi-physics problem.

$$(1.1)$$

Typical examples of coupled multi-field problems are given by

- incompressible viscous flow (Navier-Stokes problem) described by a two-field formulation in the fluid velocity and the fluid pressure,

- saturated porous media (e. g. consolidation problem) modeled by a two-field formulation in the solid displacement and the pore-fluid pressure,

- acoustic-structure interaction treated as a two-field problem coupling the structural displacement field with the acoustic pressure field.

The following examples pose multi-physics problems:

- multi-scale models of granular matter (e. g. sand) where on the macro-scale a finite element model is used embedding a discrete particle model of the granular microstructure at integration point level,

- thermoelectricity (e. g. Peltier-Seebeck effect) as a two-physics problem combining heat conduction and electrodynamics,

- reaction-diffusion systems (e. g. pattern formation) as a two-physics problem combining local chemical reactions with diffusive spatial transport,

- multi-domain models of acoustic-structure interaction (e.g. aeroelasticity) by using different discretization schemes for the individual domains.

For a more comprehensive discussion of the notions *multi-scale* and *multi-domain* in the context of multi-physics systems, it is referred to the survey article of Michopoulos *et al.* [86].

## 1.2 Solution of Coupled Problems

The increasing necessity to solve complex problems in computational mechanics and physics accounting for all the coupling occurring on the different scales of the problem requires the ongoing development of new ideas and methods which can effectively provide accurate numerical solutions in affordable computing times. At this, challenges are given by coupled problems for which the computation of coupling phenomena are difficult to accomplish or with vastly different time constants (e.g. stiff problems) and long-time duration of transient responses. From a theoretical perspective, most of the individual physical processes are fairly understood and elaborated models exist for their mathematical description. For example, multi-functional and smart materials like piezo-ceramics, electroactive polymers (EAPs), etc. are treated since decades by mechanical theories. However, first the increasing power of modern computing systems in combination with sophisticated numerical algorithms exploiting the new hardware features allow the efficient solution of real-scale problems of practical relevance.

The theoretical models of coupled problems usually yield mathematical expressions of some conservation principle in form of coupled partial differential equations (PDEs) in space and time. Partial differential equations by their very nature deal with continuous functions, and hence, have to be discretized in space and time for the computational treatment. In particular, for computer simulations, the spatial semi-discretization is commonly done by the Finite Element Method (FEM) [12, 59, 144–146], the Finite Difference Method (FDM) [89, 92, 124], the Finite Volume Method (FVM) [69, 125, 131], or the Boundary Element Method (BEM) [10, 48, 138]. Considering coupled multi-physics problems, different spatial discretization schemes may be chosen for the different physical components, for instance, a finite element model of a structure linked to the boundary element model of a surrounding fluid, a typical example of fluid-structure interaction (FSI) [36, 91].

The space discretization results in a system of ordinary differential equations (ODEs) in time, which for real-scale problems may comprise millions of evolution equations that have to be integrated numerically. In principle, four approaches to the time integration of such coupled systems are feasible (cf. [45, 70, 95, 146]):

| **Time integration approaches for coupled systems** | |
| --- | --- |
| (1) *Monolithic or direct approach:* The whole problem is treated as a monolithic entity. All components are advanced simultaneously in time by the same, for stability reasons usually implicit, time-stepping scheme. | (1.2) |

(2) *Partitioned or iterative approach:* The physically or computationally heterogeneous system components are treated as isolated entities that are separately advanced in time, possibly by different integrators. Interaction effects are viewed as forcing effects that are communicated between the individual components using prediction, substitution, and synchronization techniques.

(3) *Fractional-step method:* Operator splitting is used to decompose unwieldy coupled systems into simpler integrable subproblems by advancing each time step in multiple (fractional) steps. The split parts are treated by special composition algorithms such as predictor-corrector or projection schemes, thereby accounting for specific geometric field properties.

(4) *Field variable elimination:* One or more field variables are eliminated by techniques such as reduction or integral transforms. The remaining field equations are treated by a monolithic time integration scheme.

(1.2)

Field variable elimination is a relict from the pre-computer era and restricted to special linear problems. Basically, the elimination destroys sparseness of matrix profiles leading to dense solution matrices. Consequently, this approach is of inferior importance from a computational perspective.

The other approaches are more general in nature. The monolithic or direct treatment is advantageous when the coupled field interaction is highly nonlinear and is best solved in a single solution using a coupled formulation. Examples of direct coupling include electro-magnetomechanical analysis, conjugate heat transfer with fluid flow, or multi-component porous media problems with chemical interactions. The simultaneous integration requires specialized software modules capable of treating different types of differential equations in a single solver which is not the standard in commercial software. Moreover, general three-dimensional (3-d) problems result in large matrix systems which may be indefinite due to included algebraic equations, additionally calling for a special solution procedure. Common methods for the simultaneous integration of such systems include implicit Runge-Kutta (IRK) methods [54, 55] and multi-step backward differentiation formulae (BDF) [19]. Examples for the effective application of the monolithic approach are reported for fluid-structure interaction [16, 56, 85, 115], open system growth models [65, 66], multi-field problems in structural dynamics [64], or inelastic and dynamic porous media problems [38, 79, 80] to name but a few.

There is no doubt that due to the huge linear systems generated by the monolithic treatment, which does not really take advantage of the multi-physics nature of the problem, iterative solvers are the key ingredient to fast solution. In this regard, domain decomposition (DD) or substructuring methods have proved to be a powerful technique. In particular, advancements of the non-overlapping DD methods, such as the balancing domain decomposition (BDD) method [30, 76] or the finite element tearing and intercon-

nect (FETI) method [41, 42], provide strong computational strategies, perfectly suited to modern computing hardware, see [47, 126]. The basic idea behind these methods is to substructure the computational domain thereby considering the problem on the interface between the subdomains to ensure the continuity of the primal unknowns and the equilibrium of fluxes. The underlying algorithms are built from a number of local solves of smaller systems on the subdomains where the interface problems are treated by some preconditioned iterative solver. In fact, such methods are believed to have a great potential to treat multi-field and multi-physics problems [15, 51, 111].

In contrast, partitioning and splitting follow a divide-and-conquer strategy in the sense of transforming the tightly coupled problem into loosely coupled entities. In particular, for coupling situations which do not exhibit a high degree of nonlinear interaction, the partitioned or iterative approach has the advantage of being more efficient and flexible. That is because of the favorable algorithmic structure which allows the independent analyzers for each partition to be synchronized to operate in sequential or parallel fashion such that the coupling of different discretization models is straightforward and software modularity is preserved. The coupling may be recursive where iterations between the different physics are performed until the desired level of convergence is achieved. In a sequential thermal-stress analysis, for instance, a performed nonlinear transient thermal analysis is followed by a linear static stress analysis. However, the partitioned approach requires considerable investment in methodology issues since accuracy and stability may be affected, particularly when couplings become very strong, which entails costly iteration or stabilization procedures. Difficulties may also arise if huge 3-d problems are considered and the dimensions of a distinct subproblem is far larger in comparison to others leading to unbalanced subsystems.

The development of partitioning methods was mainly driven in the 1970s by fluid-structure interaction problems since only specialized analysis codes tailored to independently treat either the structure or the fluid were available. The lack of a single analysis software for coupled FSI problems actually led to the first staggered procedures [98] where each subproblem was solved separately utilizing individual fluid and structure codes assuming that the field variables of one subproblem are known from an appropriate predictor and temporarily frozen while advancing the other subproblem. This paved the way to the more general partitioned approaches [43–45, 73, 94, 95, 97] applicable to a wider range of coupled multi-field problems, such as general FSI [82, 83, 100, 101, 106, 135], poroelasticity [116, 119, 128, 141], aeroelasticity [105, 114], and thermoelasticity [5, 37, 109].

In contrast to partitioning methods which imply a field-by-field decomposition of the space discretization, operator splitting or the fractional-step method is based on a decomposition of the time discretization of a field within its time-step interval. To be more precise, splitting refers to the decomposition of a differential operator underlying a particular time-stepping scheme denoted by fractional-step method. However, in the related literature both terms are often used synonymously. Both partitioning and splitting may be algebraic or differential. In the algebraic case, the complete coupled system is spatially discretized first and then decomposed. In the differential case, the decomposition is carried out first, and each field is then discretized separately. In this regard, algebraic operator splitting is associated with the segregated solution of already semi-discretized equations.

Differential operator splitting is rather used to decouple physical effects in complex and highly nonlinear initial boundary-value problems (IBVP), which is what we seek.

The historical development of splitting methods began somewhere in the late 1950s, but is hard to untangle because of its independent roots in different applied fields, see [84] for an overview. Here, we focus on operator-splitting techniques that have originally been applied to advection-diffusion-reaction (ADR) systems or the Navier-Stokes equations. Basically, operator-splitting methods proceed from the idea of writing some not necessarily linear differential operators in a PDE system at least as a linear sum of operator pieces. The solution in time is then advanced in a sequence of stages where each stage involves only one operator piece and an appropriate time-discretization scheme. At this, the time step of each stage in the sequence of updatings is only a fraction of the full time step in the sense of a fractional-step method, cf. [139] for details. Hence, operator splitting combines simple integration schemes for subproblems into an efficient scheme for the overall problem. Most naturally, semi-explicit-implicit strategies are convenient, for instance, an explicit scheme for the advection terms combined with an implicit scheme for the diffusion terms of a coupled advection-diffusion system. In this regard, operator splitting can be used to separate hyperbolic from parabolic parts or algebraic from differential equations of a system, where each is simpler to advance in time by some tailored scheme than the combined original system.

Unlike multi-step methods, operator splitting as one-step methods are not necessarily unstable. In fact, it is often sufficient to have a stable integrator only for the operator piece having the highest number of spatial derivatives in order to make the overall scheme stable [108]. Such methods are intended for time-accurate simulations rather than for quickly time-marching to steady-state solutions using large time steps [52]. However, it should be noted that the procedure introduces a splitting error on top of any additional errors in the time integration. Moreover, one has to be aware of order reductions when applied to systems which involve algebraic equations [133], and attention should be paid to the sequential order of the operators, where stiff operators must always be last in the splitting scheme [121].

Examples of successful applications are manifold and range from nonlinear thermomechanics [7, 118] via incompressible Navier-Stokes equations [26, 52, 110, 112, 127, 130] and porous media mechanics [6, 80, 102, 140] to general differential-algebraic equations (DAE) [133]. More recently, implementations try to automatically switch between monolithic and split integration in the sense of a hybrid scheme by recourse to some elaborate error control. For a nonlinear reaction-diffusion system such a hybrid strategy is presented by Vijalapura & Govindjee [132].

For the sake of completeness, it is also worth mentioning the so-called dimensional or Strang-splitting methods for parabolic PDEs such as the alternating direction implicit (ADI) method most notably used for the efficient solution of multi-dimensional heat and diffusion equations [35, 103, 122]. Basically, the ADI method proceeds from a split of the finite difference equations where in each only one dimension is taken implicitly yielding in combination a cheap to solve system. Roughly speaking, ADI methods aim at preserving the computational benefits of the related one-dimensional (1-d) problem also for the multi-dimensional problem. This however is not within the scope of this thesis as we

are interested in a physically motivated split of PDE systems rather than a simplifying breakdown in its space dimensions. For further particulars on splitting methods in general, the interested reader is referred to the review article by McLachlan & Quispel [84] and the quotations therein.

## 1.3 Coupled Problems at a Glance

### 1.3.1 Classification of Coupled Problems

Some coupled multi-field problems, such as fluid-structure or structure-structure interaction, can be characterized by distinct spatial subdomains (e.g. fluid and structure) with distinct sets of dependent variables (e.g. fluid pressure and solid displacement). In this case, the substructures are only linked along an interface with the interaction or coupling mechanisms representing actions at the immediate vicinity, i.e., contact or traction forces between the boundary or interface surfaces of the adjacent subdomains. Thus, it is convenient to refer to these problems as *surface-coupled* or *geometrically coupled*, where the interaction is governed by boundary conditions or interface equations. Clearly, geometrically coupled problems are well suited for partitioned solutions by untightening the coupling in space and solving each subproblem separately as outlined previously.

Other coupled problems are, in contrast, characterized by the immanent interaction of essentially different physical phenomena within the same spatial domain (e.g. thermal and mechanical interaction). The physical quantities interact at each material point of the body which gives rise to a continuum mechanical description by some coupled formulation. In fact, the coupling is inherent in the governing balance relations specified by some constitutive laws describing the different physical phenomena. Consequently, this class of problems will be denoted as *volume-coupled* or *materially coupled*[1]. It is actually the latter class of problems which is of primary concern in this thesis.

Proceeding from a standard numerical treatment of the governing PDE system underlying the physical model under study, each primal physical field is spatially discretized, here preferably by the FEM, into a finite number of degrees of freedom (DOFs), thus forming a semi-discrete subsystem of the original coupled problem. A system of equations which consists of two or more of such interconnected subsystems involving dependent variables that cannot be eliminated on equation level, where an independent solution of any subsystem is impossible without simultaneous solution of the others, is called a *coupled system*. Generally speaking, a coupled system is a system whose behavior is driven by the dynamic multi-way interaction of its functionally distinct or heterogeneous subsystem components [45]. The coupling strength is commonly classified from *weak* or *loose* to *strong* or *tight* depending on the degree of subsystem interaction [82, 143], where a coupling is regarded as strong if the solution depends significantly on the accuracy of the coupling term calculation [71]. In this connection, the course of interaction yields an additional indicator, where one-way coupling is considered as weak, for instance, between a thermal field and a

---

[1] Note that other authors use a different terminology. For instance, Zienkiewicz *et al.* [146] categorize the a.m. coupled problems into *Class I* and *Class II* problems.

structure, and two-way or multi-way coupling is considered as strong, such as in general FSI problems, because the overall state, in contrast to the former, has to be simultaneously updated over interacting subsystems. From a computational perspective, this biases the choice of a convenient combined method by which the individual time-discretized subsystems are algorithmically coupled, for instance, explicitly in the weak case using some staggering scheme and implicitly in the strong case applying a direct monolithic or an iterative partitioned approach [82].

However, to distinguish between weak and strong coupling, even on a numerical basis, is a very subjective classification which depends on the type of coupled problem as well as the physical properties and interdependencies controlled by the involved constitutive parameters. Especially, if nonlinearities come into play, such that material parameters nonlinearly depend on the primal field variables, the strength of coupling may change during the solution of the problem. As an illustrative example, consider a macroscopic, biphasic porous media model for the description of a flexible, high-porosity material such as an air-filled, open-celled polymer foam [77, 79]. It is beyond question that the coupling in the underlying solid displacement-pressure (u-p) formulation is driven by the mutual momentum exchange between the deforming polymer matrix and the streaming pore air governed by the intrinsic permeability and the fluid properties [78]. Let us suppose that in the undeformed state, the hydraulic conductivity is quite high such that the permeating air experiences almost no resistance. Accordingly, the frictional drag in the sense of a volume-specific interaction force between foam matrix and pore gas is comparatively small which connotes a weak coupling of the respective differential equations in the u-p formulation. However, if the flexible foam gets largely compressed, the cellular structure forming the interconnected pore space gets compacted, such that the porosity and likewise the permeability decreases. This gives rise to a nonlinear, deformation-dependent hydraulic conductivity which may change over several magnitudes, thereby provoking a transition from a weakly to a strongly coupled solid-fluid problem and *vice versa*.

Following this, it is generally wise to look at an abstract representation of the semi-discrete equation system and examine the coupling terms when extreme, but physically sound values of the involved constitutive parameters are assumed. Although this is very problem-specific and not straightforward, it is intended in this work to present a general framework that helps to grasp the coupling characteristics of primarily materially coupled problems and support the choice of a suitable numerical solution procedure.

Against this background, it is moreover convenient to distinguish between pure differential and differential-algebraic coupling depending on whether or not algebraic equations are present in the system, i. e., whether we have a PDE or a DAE system at hand. Algebraic equations usually represent some kind of side condition or constraint imposed on one or several primary variables, such as incompressibility, continuity, or some penalty or Lagrangean constraint at an interface. In the case of a highly nonlinear and strongly coupled DAE system, which we preferentially solve monolithically, the simultaneous approximation of the primary fields entails the usage of the mixed Finite Element Method with discrete approximation spaces for the individual unknowns. However, the multi-field variational principle yields a saddle-point type problem rather than an extremal problem, i. e., the solution corresponds simultaneously to a minimum w. r. t. the differential

variables and a maximum w. r. t. the algebraic variables. In general, minimization of an energy functional subject to a side condition, such as the continuity condition of the incompressible Stokes problem, results in a saddle-point problem, i. e., the discrete system is indefinite, so that a number of standard solution methods cannot be applied directly [14]. Moreover, the problem occurs that not all choices of finite element spaces will lead to convergent approximations, because the stability of mixed methods is by no means automatic [8]. Therefore, in mixed formulations, the inf-sup or Ladyzhenskaya-Babuška-Brezzi (LBB) condition is a crucial criterion for the stability of the numerical solution [20, 142]. Basically, the inf-sup condition compares the size of the approximation spaces and essentially serves as a compatibility condition in the sense that it keeps the balance between consistency error and approximation quality, see [18, 52] for references.

From a computational perspective, the further subclassification of coupled PDE or DAE systems into parabolic and hyperbolic is much less important, because many problems are of mixed type and most hyperbolic problems get parabolic pieces mixed into them when discussing practical numerical schemes [108]. It is rather more significant to consider the property of *stiffness* in this context. Stiff differential equations are equations which are ill-conditioned in a computational sense as they include some terms that can lead to rapid variations in the solution. In coupled systems, this is often the case if the physical components vary with different time scales, such as in slow diffusion-fast reaction systems. This usually entails that either the stability or the error bound or both can only, if at all possible be assured by unreasonable restrictions on the time-step size. However, the problem can be tackled by recourse to certain operator-splitting schemes or stiffly accurate implicit time integrators, see [24, 55, 88] for further details.

## 1.3.2   A Simple Example

To give an example, consider the mass-spring system depicted in Figure 1.1. From Newton's second law it is easy to find the motion equation of a point mass $m_n$ in a series of spring-mass elements:

$$m_n \ddot{u}_n + k_{n-1}(u_n - u_{n-1}) - k_n(u_{n+1} - u_n) = b_n \,. \tag{1.3}$$

Herein, $u_n(t)$ denotes the position of the $n$th mass, $k_{n-1}$ and $k_n$ are the elastic constants of the springs connected on the left and right sides to that mass, and $b_n(t)$ represents the time-dependent excitation force on $m_n$. The total (material) time derivative is defined as $(\cdot)^{\boldsymbol{\cdot}} := \mathrm{d}(\cdot)/\mathrm{d}t$, such that $\ddot{u}_n = \mathrm{d}^2 u_n/\mathrm{d}t^2$ is the acceleration of the considered point mass.
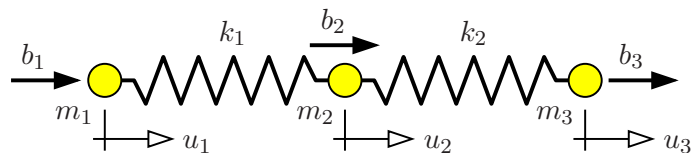


**Figure 1.1:** *Simple mass-spring system composed of three point masses $m_1, m_2, m_3$ loaded by time-dependent forces $b_1, b_2, b_3$ and connected via two massless elastic springs (spring constants $k_1, k_2$). The individual displacement coordinates of the masses are indicated by $u_1, u_2, u_3$.*

In matrix representation, for the system given in Figure 1.1, we obtain

$$\boldsymbol{M}\,\ddot{\boldsymbol{u}} + \boldsymbol{K}\,\boldsymbol{u} = \boldsymbol{b} \quad \text{with} \quad \begin{cases} \boldsymbol{u} = [u_n]^T\,, \\ \boldsymbol{b} = [b_n]^T\,, \\ \boldsymbol{M} = \operatorname{diag}[m_n]\,, \\ \boldsymbol{K} = \operatorname{tridiag}[-k_{n-1}, k_{n-1} + k_n, -k_n]\,, \end{cases} \tag{1.4}$$

and $n = 1, 2, 3$ which written out reads

$$\begin{bmatrix} m_1 & 0 & 0 \\ 0 & m_2 & 0 \\ 0 & 0 & m_3 \end{bmatrix} \begin{bmatrix} \ddot{u}_1 \\ \ddot{u}_2 \\ \ddot{u}_3 \end{bmatrix} + \begin{bmatrix} k_1 & -k_1 & 0 \\ -k_1 & k_1 + k_2 & -k_2 \\ 0 & -k_2 & k_2 \end{bmatrix} \begin{bmatrix} u_1 \\ u_2 \\ u_3 \end{bmatrix} = \begin{bmatrix} b_1 \\ b_2 \\ b_3 \end{bmatrix}. \tag{1.5}$$

From (1.5) it is obvious that the inertial forces of the individual point masses are decoupled, but their motions are coupled to each other via the interconnected springs. This reflects itself in the highlighted off-diagonal elements of the stiffness matrix $\boldsymbol{K}$. Thus, the above example yields a coupled system of ODEs of second order in time. Clearly, if the spring constants $k_n$ tend towards zero, we have three independent equations of motion, $m_n\,\ddot{u}_n = b_n$ ($n = 1, 2, 3$), and for $k_n \to \infty$ the point masses are rigidly connected and behave as a monolithic entity governed by a single equation, viz. $\overline{m}\,\ddot{u} = \overline{b}$ with $u := u_1 = u_2 = u_3$, $\overline{m} := \sum m_n$, and $\overline{b} := \sum b_n$. Within these theoretical limits of zero and full coupling, it is now left to the observer to define suitable thresholds or indicators that distinguish weak from strong interaction. This becomes even more difficult and also sometimes pointless if nonlinear interaction mechanisms (e.g. of Lennard-Jones type) are described by, for instance, motion-dependent stiffnesses $k_n = k_n(u_{n-1}, u_n, u_{n+1})$.

To continue, we recast the 2nd-order system (1.4) in a *state-space formulation* which provides the dynamics as a system of coupled first-order differential equations in a set of internal variables known as *state variables*. Basically, the concept of the state of a dynamic system refers to a minimum set of state variables, say $y_i(t)$ ($i = 1, ..., N$), together with respective initial conditions $y_i(t_0) = y_{0i}$ at some reference time $t_0$ that fully describe the system and its response to any given set of inputs for $t \geq t_0$, cf. [75, 120] among others. System models built of pure and ideal (linear) one-port elements (mass, spring, dashpot etc.) are state-determined system models. For such systems the number of state variables $N$ is equal to the number of independent energy storage elements in the system such that the values of the state variables specify the total system energy. In the considered example problem, we have two energy storage elements, viz. the elastic energy in the springs governed by the $u_n$ and the kinetic energy of the masses governed by their velocities $v_n = \dot{u}_n$. Together, they define the set of state variables which are collected in the *state vector* $\boldsymbol{y}(t) = [\boldsymbol{u}, \boldsymbol{v}]^T$. The corresponding *state equations* are easily found as[2]

$$\dot{\boldsymbol{u}} = \boldsymbol{v} \quad \text{and} \quad \dot{\boldsymbol{v}} = -\boldsymbol{M}^{-1}\boldsymbol{K}\,\boldsymbol{u} + \boldsymbol{M}^{-1}\boldsymbol{b}\,. \tag{1.6}$$

---

[2] An alternative choice of an auxiliary state variable would be $\boldsymbol{l} = \boldsymbol{M}\,\dot{\boldsymbol{u}}$ which is nothing else but the momentum vector such that $\dot{\boldsymbol{l}} = \boldsymbol{M}\,\ddot{\boldsymbol{u}}$ represents the inertial force, see [63] for details.

In matrix form, the initial-value problem (IVP) then reads

$$\underbrace{\begin{bmatrix} \boldsymbol{I} & 0 \\ 0 & \boldsymbol{M} \end{bmatrix}}_{\overline{\boldsymbol{M}}} \underbrace{\begin{bmatrix} \dot{\boldsymbol{u}} \\ \dot{\boldsymbol{v}} \end{bmatrix}}_{\dot{\boldsymbol{y}}} + \underbrace{\begin{bmatrix} 0 & -\boldsymbol{I} \\ \boldsymbol{K} & 0 \end{bmatrix}}_{\overline{\boldsymbol{K}}} \underbrace{\begin{bmatrix} \boldsymbol{u} \\ \boldsymbol{v} \end{bmatrix}}_{\boldsymbol{y}} = \underbrace{\begin{bmatrix} 0 \\ \boldsymbol{b} \end{bmatrix}}_{\overline{\boldsymbol{b}}}, \quad \boldsymbol{y}(t_0) = \boldsymbol{y}_0, \tag{1.7}$$

which is easily seen to yield the canonical equation of a state-space model system, viz.

$$\dot{\boldsymbol{y}} = \boldsymbol{A}\,\boldsymbol{y}(t) + \boldsymbol{B}\,\overline{\boldsymbol{b}}(t)\,. \tag{1.8}$$

Herein, $\boldsymbol{A} = -\overline{\boldsymbol{M}}^{-1}\overline{\boldsymbol{K}}$ represents the *state matrix* and $\boldsymbol{B} = \overline{\boldsymbol{M}}^{-1}$ is the input matrix, which both may be time-variant. For general nonlinear systems, the corresponding explicit and equivalent implicit representations of (1.8) are

$$\dot{\boldsymbol{y}} = \boldsymbol{f}(t, \boldsymbol{y}) \qquad \text{and} \qquad \boldsymbol{F}(t, \boldsymbol{y}, \dot{\boldsymbol{y}}) = \boldsymbol{0}\,. \tag{1.9}$$

These canonical formulations of first-order differential equation systems provide a suitable abstraction for the further discussion of coupled problems and are taken as basis in what follows.

**Remark:** In structural dynamics, Newmark-type schemes [93] are widely preferred for the solution of second-order dynamic problems, such as (1.4), instead of using common numerical methods that may be more efficient, of a higher order, or better for stiff equations. Actually, 2nd-order ODEs may alternatively be integrated by either recasting them as 1st-order ODEs, as in the above example, or by simply using explicit Runge-Kutta-Nyström (RKN) methods which are especially designed for 2nd-order, but originally non-stiff and non-dissipative systems [62, 129]. More recently stable RKN methods have been constructed particularly for the integration of stiff and non-conservative problems, see, e. g., [3]. Anyway, here, we will primarily focus on differential equation systems of first order in time in form of (1.9) in order to be able to apply established numerical integration schemes out of the class of implicit Runge-Kutta (IRK) methods (see Section 1.3.4). ■

## 1.3.3 Differential and Algebraic Coupling

To begin with, consider an initial-value problem given by a set of $N$ non-autonomous first-order differential equations in time accompanied by respective initial conditions:

$$\left.\begin{aligned} \dot{y}_1 &= f_1(t, y_1, y_2, \ldots, y_N), & y_1(t_0) &= y_{1\,0} \\ \dot{y}_2 &= f_2(t, y_1, y_2, \ldots, y_N), & y_2(t_0) &= y_{2\,0} \\ \vdots \quad &\quad \vdots \quad \vdots \quad \vdots \quad \vdots & \vdots \quad &\quad \vdots \\ \dot{y}_N &= f_N(t, y_1, y_2, \ldots, y_N), & y_N(t_0) &= y_{N0} \end{aligned}\right\} \quad \dot{\boldsymbol{y}} = \boldsymbol{f}(t, \boldsymbol{y}), \;\; \boldsymbol{y}(t_0) = \boldsymbol{y}_0\,. \tag{1.10}$$

Herein, each or several DEs together define some field problem possibly describing distinct physical phenomena on different time scales and not necessarily on coinciding spatial domains. The different $y_i$ can thereby be elements of some function spaces and the $f_i$ can represent some differential operator, such that (1.10) may describe some problem modeled

by partial differential equations. As the individual DEs may depend on the other field variables, the above equations are denoted as *coupled multi-field equations*. The contrary would be totally decoupled *singled field equations*, i.e., $\dot{y}_i = f_i(t, y_i)$ with $i = 1, ..., N$. Following the definitions in Box (1.1), if Equations (1.10) represent different physical processes (advection, diffusion, reaction etc.) or are treated by different physical models (e.g. FEM and BEM), $\dot{\boldsymbol{y}} = \boldsymbol{f}(t, \boldsymbol{y})$ defines a *coupled multi-physics problem*. Moreover, since for each variable a differential evolution equation exists, one refers to this case as pure *differential coupling*.

As we shall see later, this is not generally the case since the time evolution of physical state variables is often constrained by some algebraic side condition. They can have different origins, for instance, driven by physical properties like incompressibility and continuity-like conditions or incorporated for computational convenience in the sense of artificial subsystems such as interface constraints when using partitioning methods (see Section 1.4.1). To this end, consider the system in Hessenberg form

$$
\begin{aligned}
\dot{\boldsymbol{y}} &= \boldsymbol{f}(t, \boldsymbol{y}, \boldsymbol{z}), \\
\boldsymbol{0} &= \boldsymbol{g}(t, \boldsymbol{y}, \boldsymbol{z})
\end{aligned}
\tag{1.11}
$$

accompanied by consistent initial values such that $\boldsymbol{0} = \boldsymbol{g}(t_0, \boldsymbol{y}_0, \boldsymbol{z}_0)$. Clearly, we have no $\dot{\boldsymbol{z}}$, i.e., Equations (1.11) define a set of *differential-algebraic equations* (DAE) in time with $\boldsymbol{z}$ representing the algebraic variables, which imply an additional *algebraic coupling*. More precisely, (1.11) is a DAE system of *differentiation index* 1 (Hessenberg index-1), which is easily proven by differentiating (1.11)$_2$ to obtain

$$
\dot{\boldsymbol{z}} = -\left(\frac{\partial \boldsymbol{g}}{\partial \boldsymbol{z}}\right)^{-1} \left(\frac{\partial \boldsymbol{g}}{\partial t} + \frac{\partial \boldsymbol{g}}{\partial \boldsymbol{y}} \boldsymbol{f}(t, \boldsymbol{y}, \boldsymbol{z})\right).
\tag{1.12}
$$

This requires $\partial \boldsymbol{g}/\partial \boldsymbol{z}$ to be invertible, i.e., $\det(\partial \boldsymbol{g}/\partial \boldsymbol{z}) \neq 0$. As the number of differentiations needed to get an explicit differential equation for $\boldsymbol{z}$ defines the differentiation index [55], the DAE (1.11) is of index 1.

Next, consider the system

$$
\begin{aligned}
\dot{\boldsymbol{y}} &= \boldsymbol{f}(t, \boldsymbol{y}, \boldsymbol{z}), \\
\boldsymbol{0} &= \boldsymbol{g}(t, \boldsymbol{y}),
\end{aligned}
\tag{1.13}
$$

where the variable $\boldsymbol{z}$ is absent in the algebraic constraint, and thus, $\partial \boldsymbol{g}/\partial \boldsymbol{z}$ is singular. However, by time differentiation of (1.13)$_2$, one obtains the oblique constraint

$$
\boldsymbol{0} = \frac{\partial \boldsymbol{g}}{\partial t} + \frac{\partial \boldsymbol{g}}{\partial \boldsymbol{y}} \boldsymbol{f}(t, \boldsymbol{y}, \boldsymbol{z}) =: \widetilde{\boldsymbol{g}}(t, \boldsymbol{y}, \boldsymbol{z}),
\tag{1.14}
$$

which together with (1.13)$_1$ becomes again a DAE system of index 1 as given in (1.11). Accordingly, two differentiations are needed to find an explicit equation for $\dot{\boldsymbol{z}}$, such that (1.13) is of differentiation index 2 (Hessenberg index-2). In the same way, DAE systems with higher differential index can be introduced and discussed. From a computational perspective, it is desirable to have index-1 systems, which actually incloses the self-evident assumption of an invertible stiffness matrix associated with the mechanical unknowns involved in a coupled problem. Roughly speaking, the higher the differentiation index,

the more difficult the numerical solution of the initial-value problem at hand. However, higher index DAEs can be overcome by special *index reduction methods* (cf. [9]) which will not be discussed at this point. We will rather present application-dependent possibilities, such as augmenting particular field equations by inserting other field equations, in the second part of this thesis, see, e. g., Chapter 4. A more detailed discussion of DAE systems can be found in [19, 55] and the quotations therein.

## 1.3.4   Stiff and Higher-Order Differential Equations

To elucidate the term *stiffness* in the framework of initial-value problems, we start from the simple autonomous[3] differential equation system

$$\dot{\boldsymbol{y}} = \boldsymbol{f}(\boldsymbol{y})\,,\ \boldsymbol{y}(t_0) = \boldsymbol{y}_0 \quad \text{with} \quad \begin{bmatrix} \dot{y}_1 \\ \dot{y}_2 \end{bmatrix} = \begin{bmatrix} -y_1 \\ -k\,y_2 \end{bmatrix}. \tag{1.15}$$

If we interpret $\boldsymbol{y}(t) = [y_1, y_2]^T$ as the 2-d Cartesian coordinates of a particle, the above system describes its attraction to the origin of the coordinate system starting from an initial position $\boldsymbol{y}_0 \neq \boldsymbol{0}$. Let us further assume that $k$ is a large positive constant, so that the attraction to the $y_1$ axis ($y_2 = 0$) is much stronger than in the other direction. Solving the ODEs far enough forward in time, we expect the particles' location to converge towards $\boldsymbol{y} = \boldsymbol{0}$, but obviously more slowly towards $y_1 = 0$, and then stay there once it arrives.

To keep things simple, for the solution of the on the first view benign IVP (1.15), let us apply the Euler forward scheme with a constant time-step size $\Delta t = t_{n+1} - t_n$. In doing so, with the shortcut $\boldsymbol{y}_n := \boldsymbol{y}(t_n)$, one obtains the explicit update formula

$$\boldsymbol{y}_{n+1} = \boldsymbol{y}_n + \Delta t\,\dot{\boldsymbol{y}}_n = \begin{bmatrix} (1 - \Delta t)\,y_{1\,n} \\ (1 - k\Delta t)\,y_{2\,n} \end{bmatrix}. \tag{1.16}$$

Focusing on the $y_2$ component, it is easily seen that if $|1 - k\Delta t| > 1$, the newly computed $y_{2\,n+1}$ has an absolute value that is always greater than the previous one. In fact, as long as $\Delta t > 2/k$, we have $|y_{2\,n+1}| > |y_{2\,n}|$, i. e., Euler forward is unstable and will oscillate with increasing magnitude with increasing $n$, instead of converging to an answer for $n \to \infty$. An obvious remedy would be to take smaller time increments $0 < \Delta t < 2/k$. However, we assumed $k$ to be a large number which forces the particle to the $y_1$ axis, such that a convergent time-step size would be unbearably small even if $y_2 = 0$ is nearly satisfied from the start. This is exactly what constitutes a stiff problem.

A more general definition of stiffness[4] can hence be formulated following the idea of

---

[3] Note that for an autonomous ODE, which does not explicitly contain the independent time variable $t$, the solution is independent of the time at which the initial conditions are applied. Every non-autonomous system of $N$ 1st-order ODEs, such as (1.10), can be written as an autonomous system of $N + 1$ ODEs by letting $t := y_{N+1}$ and increasing the dimension of the system by one through adding the equation $\dot{y}_{N+1} \equiv 1$ to the system, see any textbook on differential equations.

[4] Please note that although the problem with stiff equations is clear to the specialists, who posed various verbal definitions with somewhat similar intuitive meaning, the formulation of a general mathematical criterion for stiffness is of controversial discussion, see, e. g., [57] for further particulars.

Lambert [67]:

| |
|---|
| **One feasible defintion of a stiff problem** |
| *If in a certain time interval of integration a numerical solution method is forced to use a time-step size which is excessively small in relation to the smoothness of the exact solution in that interval, then the problem is said to be stiff in that time interval.* |

(1.17)

Independent of the simple example, science and engineering are full of stiff problems as outlined by Hairer & Wanner [55] as, for instance, chemical reaction systems, diffusion, and electrical circuits to name but a few (see also [1]). Also mechanical mass-spring systems, as given in Section 1.3.2, may result in stiff ODEs if large spring constants occur, for instance, to model an almost rigid joint or connection [74]. Without going into the mathematical details, it becomes apparent from the above example that stiff initial-value problems demand certain stability requirements (viz. A-stability [31]) on the applied time-discretization scheme. In this regard, implicit Runge-Kutta (IRK) methods provide an elaborate possibility for the accurate and stable solution of stiff problems [2, 22, 32, 39, 55]. The drawback with implicit methods is that at each time step a system of nonlinear equations must be solved. This is usually achieved using a Newton-Raphson algorithm, but at the expense of many more function evaluations than are necessary in the explicit case. In particular, for a system of $N$ differential equations, a general $s$-stage fully implicit Runge-Kutta method requires the solution of a nonlinear equation system of dimension $s\,N$ which entails $\mathcal{O}(s^3 N^3)$ operations for matrix factorizations. This is what makes them costly and, on the first view, uneconomical compared to the rival linear multistep methods such as the backward differentiation formulae (BDF) also known as Gear's methods [49, 50], which require the simultaneous solution of only $N$ nonlinear equations per time step. However, a closer look reveals that RK methods in many cases attain the same accuracy as common BDF implementations, but with greater time increments. Moreover, they allow to build in the formal order of accuracy and an easy realization of an adaptive time-step control based on embedded error estimates, which is actually not possible for linear multistep methods [23]. It should also be noted that the computational overhead can be significantly reduced by recourse to diagonal-implicit Runge-Kutta (DIRK) schemes ($s\,\mathcal{O}(N^3)$ operations) and even further in the case of singly diagonal-implicit Runge-Kutta (SDIRK) methods ($\mathcal{O}(N^3) + (s-1)\,\mathcal{O}(N^2)$ operations), which are particularly advantageous for mildly nonlinear systems as they allow the reusability of previously factorized matrices. For further details on Runge-Kutta and linear multistep methods, we refer to [21, 22, 55].

However, the application of IRK methods demands the differential equations to be of 1st order. This is not a severe problem as we saw from the simple dynamics example of Section 1.3.2. Basically, each higher-order differential equation can easily be converted to a system of first-order equations by introducing auxiliary variables being aware of the

increased storage demand. Such an order reduction is simply accomplished, viz.

$$\ddot{\boldsymbol{y}} = \boldsymbol{f}(t, \boldsymbol{y}, \dot{\boldsymbol{y}}) \quad \longrightarrow \quad \begin{cases} \dot{\boldsymbol{y}} = \boldsymbol{x}\,, \\ \dot{\boldsymbol{x}} = \boldsymbol{f}(t, \boldsymbol{y}, \boldsymbol{x})\,. \end{cases} \tag{1.18}$$

We can proceed from the same idea in case of a prefixed non-constant matrix $\boldsymbol{H}(t, \boldsymbol{y})$ in order to avoid the inversion of $\boldsymbol{H}$ and preserve beneficial band structures,

$$\boldsymbol{H}(t, \boldsymbol{y})\, \dot{\boldsymbol{y}} = \boldsymbol{f}(t, \boldsymbol{y}) \quad \longrightarrow \quad \begin{cases} \dot{\boldsymbol{y}} = \boldsymbol{z}\,, \\ \boldsymbol{0} = \boldsymbol{H}(t, \boldsymbol{y})\, \boldsymbol{z} - \boldsymbol{f}(t, \boldsymbol{y})\,. \end{cases} \tag{1.19}$$

Combining both, we have

$$\boldsymbol{H}(t, \boldsymbol{y})\, \ddot{\boldsymbol{y}} = \boldsymbol{f}(t, \boldsymbol{y}, \dot{\boldsymbol{y}}) \quad \longrightarrow \quad \begin{cases} \dot{\boldsymbol{y}} = \boldsymbol{x}\,, \\ \dot{\boldsymbol{x}} = \boldsymbol{z}\,, \\ \boldsymbol{0} = \boldsymbol{H}(t, \boldsymbol{y})\, \boldsymbol{z} - \boldsymbol{f}(t, \boldsymbol{y}, \boldsymbol{x})\,. \end{cases} \tag{1.20}$$

## 1.4 Partitioning and Splitting

### 1.4.1 Spatial Partitioning

An illustrative motivation of *partitioning methods* can be given by reverting again to the simple mass-spring system of Figure 1.1. In order to treat the two springs and the attached masses as spatially separated but interacting subsystems, the mass $m_2$ in the middle as well as the excitation $b_2$ are equally (or in any other fashion) distributed on the left and the right subsystem, see Figure 1.2. In order to account for the mutual coupling, interface forces consistent with Newton's third law (*actio = reactio*) have to be introduced as it is well-known from free-body diagrams used in applied mechanics. Here, the so-called *localized Lagrangean multiplier method* (localized $\lambda$-method) is applied, which allows for a more modular treatment of coupled multi-physics problems than the classical $\lambda$-method, see [96, 99, 100] for details.
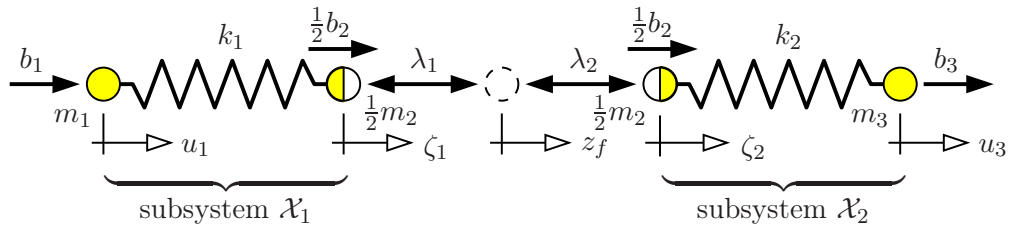


**Figure 1.2:** *Simple mass-spring system of Section 1.3.2 partitioned into two subsystems $\mathcal{X}_1$ and $\mathcal{X}_2$, which are coupled through interface forces $\lambda_1$ and $\lambda_2$.*

In doing so, one arrives at the partitioned equation systems,

$$
\mathcal{X}_1 : \begin{bmatrix} m_1 & 0 \\ 0 & \frac{1}{2}m_2 \end{bmatrix} \begin{bmatrix} \ddot{u}_1 \\ \ddot{\zeta}_1 \end{bmatrix} + \begin{bmatrix} k_1 & -k_1 \\ -k_1 & k_1 \end{bmatrix} \begin{bmatrix} u_1 \\ \zeta_1 \end{bmatrix} = \begin{bmatrix} b_1 \\ \frac{1}{2}b_2 \end{bmatrix} + \begin{bmatrix} 0 \\ \lambda_1 \end{bmatrix} ,
$$

$$
\mathcal{X}_2 : \begin{bmatrix} \frac{1}{2}m_2 & 0 \\ 0 & m_3 \end{bmatrix} \begin{bmatrix} \ddot{\zeta}_2 \\ \ddot{u}_3 \end{bmatrix} + \begin{bmatrix} k_2 & -k_2 \\ -k_2 & k_2 \end{bmatrix} \begin{bmatrix} \zeta_2 \\ u_3 \end{bmatrix} = \begin{bmatrix} \frac{1}{2}b_2 \\ b_3 \end{bmatrix} - \begin{bmatrix} \lambda_2 \\ 0 \end{bmatrix} ,
\tag{1.21}
$$

plus additional algebraic compatibility conditions, viz., the interface kinematic constraints

$$
\zeta_1 - z_f = 0 \quad \text{and} \quad \zeta_2 - z_f = 0 , \tag{1.22}
$$

and the interface force balance

$$
\lambda_1 - \lambda_2 = 0 . \tag{1.23}
$$

What is directly apparent from (1.21)–(1.23) is the fact that partitioning is accompanied by the introduction of additional unknowns (here: $\lambda_1, \lambda_2$ and, strictly speaking, also $\zeta_1, \zeta_2$) with the nature of the coupling being characterized by the algebraic compatibility constraints (1.22) and (1.23). Therein, the variable $z_f$ (originally $u_2$) is the so-called *frame displacement*, which represents the global displacement pertaining to the partition boundary. The interaction forces $\lambda_1$ and $\lambda_2$ are in general functions of the field variables, but in contrast to the classical $\lambda$-method, where the single interaction force represents a global variable that is common to both partitions, in the present case, they are local to the individual subsystems.

To continue, we recast the subsystems (1.21) in a state-space description as in Section 1.3.2 by introducing the state, input, and interface force vectors

$$
\left.\begin{array}{l} \boldsymbol{u}_1 = [u_1, \zeta_1]^T \\ \boldsymbol{v}_1 = \dot{\boldsymbol{u}}_1 \end{array}\right\} \quad \boldsymbol{y}_1 = \begin{bmatrix} \boldsymbol{u}_1 \\ \boldsymbol{v}_1 \end{bmatrix} , \quad \boldsymbol{b}_1 = \begin{bmatrix} f_1 \\ \frac{1}{2}f_2 \end{bmatrix} , \quad \boldsymbol{\lambda}_1 = \begin{bmatrix} 0 \\ -\lambda_1 \end{bmatrix} ,
$$

$$
\left.\begin{array}{l} \boldsymbol{u}_2 = [\zeta_2, u_3]^T \\ \boldsymbol{v}_2 = \dot{\boldsymbol{u}}_2 \end{array}\right\} \quad \boldsymbol{y}_2 = \begin{bmatrix} \boldsymbol{u}_2 \\ \boldsymbol{v}_2 \end{bmatrix} , \quad \boldsymbol{b}_2 = \begin{bmatrix} \frac{1}{2}f_2 \\ f_3 \end{bmatrix} , \quad \boldsymbol{\lambda}_2 = \begin{bmatrix} \lambda_2 \\ 0 \end{bmatrix} ,
\tag{1.24}
$$

the mass and stiffness matrices

$$
\boldsymbol{M}_1 = \begin{bmatrix} m_1 & 0 \\ 0 & \frac{1}{2}m_2 \end{bmatrix} , \quad \boldsymbol{K}_1 = \begin{bmatrix} k_1 & -k_1 \\ -k_1 & k_1 \end{bmatrix} ,
$$

$$
\boldsymbol{M}_2 = \begin{bmatrix} \frac{1}{2}m_2 & 0 \\ 0 & m_3 \end{bmatrix} , \quad \boldsymbol{K}_2 = \begin{bmatrix} k_2 & -k_2 \\ -k_2 & k_2 \end{bmatrix} ,
\tag{1.25}
$$

as well as the Boolean matrices

$$
\boldsymbol{D}_1 = \begin{bmatrix} 0 & 0 \\ 0 & 1 \end{bmatrix} , \quad \boldsymbol{D}_2 = \begin{bmatrix} 1 & 0 \\ 0 & 0 \end{bmatrix} , \quad \boldsymbol{L}_1 = \begin{bmatrix} 0 \\ 1 \end{bmatrix} , \quad \boldsymbol{L}_2 = \begin{bmatrix} 1 \\ 0 \end{bmatrix} . \tag{1.26}
$$

The canonical form of the generalized partitioned problem then finally reads

$$
\mathcal{X}_1 : \left\{ \begin{array}{l} \dot{\boldsymbol{u}}_1 = \boldsymbol{v}_1 \\ \dot{\boldsymbol{v}}_1 = \boldsymbol{A}_1 \boldsymbol{u}_1 + \boldsymbol{B}_1 \boldsymbol{b}_1 - \boldsymbol{C}_1 \boldsymbol{\lambda}_1 \end{array} \right\} \longrightarrow \dot{\boldsymbol{y}}_1 = \boldsymbol{f}_1(t, \boldsymbol{y}_1, \boldsymbol{\lambda}_1) ,
$$

$$
\mathcal{X}_2 : \left\{ \begin{array}{l} \dot{\boldsymbol{u}}_2 = \boldsymbol{v}_2 \\ \dot{\boldsymbol{v}}_2 = \boldsymbol{A}_2 \boldsymbol{u}_2 + \boldsymbol{B}_2 \boldsymbol{b}_2 - \boldsymbol{C}_2 \boldsymbol{\lambda}_2 \end{array} \right\} \longrightarrow \dot{\boldsymbol{y}}_2 = \boldsymbol{f}_2(t, \boldsymbol{y}_2, \boldsymbol{\lambda}_2)
\tag{1.27}
$$

with the generalized interface constraints subsumed as

$$\overline{\mathcal{I}}: \begin{cases} \boldsymbol{0} = \boldsymbol{D}_1^T \boldsymbol{u}_1 - \boldsymbol{L}_1 \boldsymbol{z}_f \\ \boldsymbol{0} = \boldsymbol{D}_2^T \boldsymbol{u}_2 - \boldsymbol{L}_2 \boldsymbol{z}_f \\ \boldsymbol{0} = \boldsymbol{L}_1^T \boldsymbol{\lambda}_1 + \boldsymbol{L}_2^T \boldsymbol{\lambda}_2 \end{cases} \longrightarrow \begin{cases} \boldsymbol{0} = \boldsymbol{g}_1(t, \boldsymbol{y}_1, \boldsymbol{z}_f) \\ \boldsymbol{0} = \boldsymbol{g}_2(t, \boldsymbol{y}_2, \boldsymbol{z}_f) \\ \boldsymbol{0} = \boldsymbol{h}(t, \boldsymbol{\lambda}_1, \boldsymbol{\lambda}_2) \end{cases}. \tag{1.28}$$

Herein, for the sake of clarity, the left-hand side equations are still given in terms of $\boldsymbol{u}_i$ and $\boldsymbol{v}_i$ rather than in the state vectors $\boldsymbol{y}_i$ with $i = \{1, 2\}$ indicating the respective subsystem $\mathcal{X}_i$. Moreover, the state, input, and interface matrices read $\boldsymbol{A}_i = -\boldsymbol{M}_i^{-1}\boldsymbol{K}_i$, $\boldsymbol{B}_i = \boldsymbol{M}_i^{-1}$, $\boldsymbol{C}_i = \boldsymbol{M}_i^{-1}\boldsymbol{D}_i$, and $\boldsymbol{z}_f$ denotes the general frame displacement vector (here: $\boldsymbol{z}_f = z_f$). If all algebraic variables are further collected in a vector $\boldsymbol{z}$ (in our example $\boldsymbol{z} = [\lambda_1, \lambda_2, z_f]^T$) and letting $\boldsymbol{y} = [\boldsymbol{y}_1, \boldsymbol{y}_2]^T$, one arrives at a system of coupled DAEs, which in general implicit form may be written as

$$\boldsymbol{F}(t, \boldsymbol{y}, \dot{\boldsymbol{y}}, \boldsymbol{z}) = \boldsymbol{0} \quad \text{with} \quad \det\left(\frac{\partial \boldsymbol{F}}{\partial \dot{\boldsymbol{y}}}\right) = 0. \tag{1.29}$$

At this, the zero determinant indicates a singular generalized mass matrix associated with the included set of algebraic equations (recall Section 1.3.3). However, we are not interested in a monolithic treatment at this point, but seek for a segregated solution of the partitioned problem. It is directly apparent from the subsystem equations (1.21) or (1.27) that they represent singled-field equations provided that the interface forces $\lambda_1$ and $\lambda_2$, respectively, are known. If so, the partitions can be treated in a modular fashion, i. e., independent of each other by some tailored solver as it would be desirable if, e. g., $\mathcal{X}_1$ refers to a solid structure and $\mathcal{X}_2$ to a fluid domain. In fact, the spatial breakdown of the coupled problem by the method of partitioning reduces the task to the determination of the interface forces consistent with the algebraic side conditions (1.28), while the solution of the decoupled and thus simpler subproblems is almost straightforward, however, by no means trivial.

**Interface Force Computation**

As pointed out before, the present interface forces are required in order to solve the partitioned equation systems. The computational effort required thereby depends on the time-discretization method applied to the individual subsystems and, of course, the general accuracy demands of the problem. To advance from time $t_n$ to $t_{n+1} = t_n + \Delta t_n$ let us first proceed from an explicit strategy for both subsystems by applying, for instance, the forward Euler method as in the example of Section 1.3.4. Following such an *explicit-explicit* approach, we need to compute

$$\dot{\boldsymbol{v}}_{in} = \boldsymbol{A}_i \boldsymbol{u}_{in} + \boldsymbol{B}_i \boldsymbol{b}_{in} - \boldsymbol{C}_i \boldsymbol{\lambda}_{in}. \tag{1.30}$$

Actually, the present state variables $\boldsymbol{u}_{in}$, $\boldsymbol{v}_{in}$, and the system inputs $\boldsymbol{b}_{in}$ are known, while the interface forces $\boldsymbol{\lambda}_{in}$ are not. To compute the latter, recall the interface kinematic constraints $(1.28)_{1,2}$ and differentiate them twice to obtain

$$\boldsymbol{D}_i^T \dot{\boldsymbol{v}}_{in} - \boldsymbol{L}_i \ddot{\boldsymbol{z}}_{fn} = \boldsymbol{0}. \tag{1.31}$$

Then, substitution of (1.30) into the above equation together with the interface force balance $(1.28)_3$ yields an independent equation system $\mathcal{I}$ for the computation of the $\boldsymbol{\lambda}_{in}$, viz.

$$
\mathcal{I}: \begin{bmatrix} \boldsymbol{D}_1^T \boldsymbol{M}_1^{-1} \boldsymbol{D}_1 & 0 & \boldsymbol{L}_1 \\ 0 & \boldsymbol{D}_2^T \boldsymbol{M}_2^{-1} \boldsymbol{D}_2 & \boldsymbol{L}_2 \\ \boldsymbol{L}_1^T & \boldsymbol{L}_2^T & 0 \end{bmatrix} \begin{bmatrix} \boldsymbol{\lambda}_{1n} \\ \boldsymbol{\lambda}_{2n} \\ \ddot{\boldsymbol{z}}_{fn} \end{bmatrix} = \begin{bmatrix} \overline{\boldsymbol{b}}_{1n} \\ \overline{\boldsymbol{b}}_{2n} \\ 0 \end{bmatrix} \tag{1.32}
$$

with the known right-hand side terms obviously given as

$$
\overline{\boldsymbol{b}}_{in} = \boldsymbol{D}_i^T (\boldsymbol{A}_i \boldsymbol{u}_{in} + \boldsymbol{B}_i \boldsymbol{b}_{in}). \tag{1.33}
$$

For the considered mass-spring example, the solution of the above system is trivially simple as the terms $\boldsymbol{D}_i^T \boldsymbol{M}_i^{-1} \boldsymbol{D}_i$ are diagonal. Even if not, the system is well-suited for mass matrix lumping (diagonalization), which is recommended as an economical numerical device generally paid for by some additional errors[5].

In summary, the modular explicit-explicit solution procedure of the overall partitioned problem is as follows (see also Figure 1.3):

(1) Compute the interface forces $\boldsymbol{\lambda}_{in}$ from (1.32) with known inputs $\overline{\boldsymbol{b}}_{in}$.

(2) Independently compute the present accelerations $\dot{\boldsymbol{v}}_{in}$ from (1.30).

(3) Update velocities and displacements to obtain $\boldsymbol{v}_{in+1}$ and $\boldsymbol{u}_{in+1}$
(here: $\boldsymbol{v}_{in+1} = \boldsymbol{v}_{in} + \Delta t\, \dot{\boldsymbol{v}}_{in}$ and $\boldsymbol{u}_{in+1} = \boldsymbol{u}_{in} + \Delta t\, \boldsymbol{v}_{in+1}$).
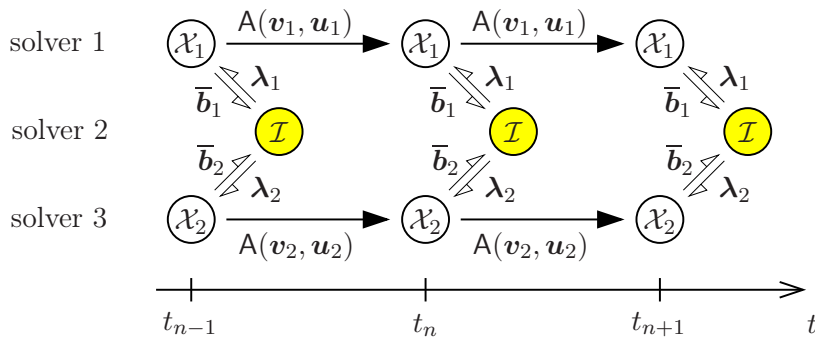


**Figure 1.3:** *Flow chart showing the modular treatment of the partitioned system based on the localized λ-method. The black arrows symbolize the advancement $\mathsf{A}(\boldsymbol{v}_i, \boldsymbol{u}_i)$ of the state variables in time and the opposed parallel arrows indicate the mutual data exchange of the subsystems $\mathcal{X}_i$ with the interface system $\mathcal{I}$.*

However, due to the explicit time stepping, one has to be aware of only conditional stability requiring that $\Delta t_n$ is restricted by a critical time step $\Delta t_{cr}$. In particular, the *Courant-Friedrichs-Lewy (CFL) condition* [29] has to be satisfied, which basically balances the propagation speed of the algorithmic solution with the physical solution speed of the

---

[5] It is worth noting that the lumping, mass conservation provided, may in some cases even improve the accuracy by error cancellation and can damp numerical oscillations in transient problems by introducing some additional dissipation of 'stiffness matrix form' [137, 146].

differential equation by limiting the maximal time increment. In fact, $\Delta t_{cr}$ is proportional to the grid or element size of the spatial discretization and varies inversely with the stiffness of the considered material such that fine resolution meshes of a partition or those describing a very stiff material entail an uneconomic global step size. Thus, it would be desirable to have unconditional stability with a moderate step size (e. g. controlled by a coarse mesh partition) in the partition, where the elements are small or mimic a stiff material. This motivates the often used *explicit-implicit* procedures [13, 60], which applied to our example means that, for instance, subsystem $\mathcal{X}_1$ is treated implicitly, while $\mathcal{X}_2$ is still advanced explicitly. The only difference is then in the computation of

$$\dot{\boldsymbol{v}}_{1\,n+1} = \boldsymbol{A}_1\,\boldsymbol{u}_{1\,n+1} + \boldsymbol{B}_1\,\boldsymbol{b}_{1\,n+1} - \boldsymbol{C}_1\,\boldsymbol{\lambda}_{1\,n+1}\,, \qquad (1.34)$$

which is now based on an implicit approach seeking equilibrium at time $t_{n+1}$, for instance, by use of the backward-Euler scheme[6], where

$$\begin{aligned} \boldsymbol{u}_{1\,n+1} &= \boldsymbol{u}_{1\,n} + \Delta t_n\,\boldsymbol{v}_{1\,n+1}\,, \\ \boldsymbol{v}_{1\,n+1} &= \boldsymbol{v}_{1\,n} + \Delta t_n\,\dot{\boldsymbol{v}}_{1\,n+1}\,. \end{aligned} \qquad (1.35)$$

Thus, proceeding in the same way as before, one arrives at the following modified system for the interface forces,

$$\mathcal{I}: \quad \begin{bmatrix} \boldsymbol{D}_1^T\,\overline{\boldsymbol{M}}_1^{-1}\,\boldsymbol{D}_1 & 0 & \boldsymbol{L}_1 \\ 0 & \boldsymbol{D}_2^T\,\boldsymbol{M}_2^{-1}\,\boldsymbol{D}_2 & \boldsymbol{L}_2 \\ \boldsymbol{L}_1^T & \boldsymbol{L}_2^T & 0 \end{bmatrix} \begin{bmatrix} \boldsymbol{\lambda}_{1\,n+1} \\ \boldsymbol{\lambda}_{2\,n} \\ \ddot{\boldsymbol{z}}_{f\,n} \end{bmatrix} = \begin{bmatrix} \overline{\overline{\boldsymbol{b}}}_{1\,n} \\ \overline{\boldsymbol{b}}_{2\,n} \\ 0 \end{bmatrix} \qquad (1.36)$$

with the modified terms (highlighted) given as

$$\begin{aligned} \overline{\boldsymbol{M}}_1 &= \boldsymbol{M}_1 + \Delta t_n^2\,\boldsymbol{K}_1\,, \\ \overline{\overline{\boldsymbol{b}}}_{1\,n} &= \boldsymbol{D}_i^T\,\overline{\boldsymbol{M}}_1^{-1}\big[\boldsymbol{b}_{1\,n+1} - \boldsymbol{K}_1(\boldsymbol{u}_{1\,n} + \Delta t_n\,\boldsymbol{v}_{1\,n})\big]\,, \end{aligned} \qquad (1.37)$$

where $\boldsymbol{b}_{1\,n+1}$ is supposed to be known. Clearly, in contrast to the explicit-explicit procedure, the semi-implicit solution now requires the factorization of the matrix $\overline{\boldsymbol{M}}_1$. However, due to the included explicit steps, the overall computational procedure still remains only conditionally stable with $\Delta t_{cr}$ dictated by the explicit scheme applied to subsystem $\mathcal{X}_2$.

In order to obtain an unconditionally stable algorithm, an *implicit-implicit* approach is feasible by treating also $\mathcal{X}_2$ implicitly. Such a fully-implicit partitioned strategy is the most costly as it requires two matrix factorizations, but may still be favored against an implicit monolithic approach, for instance, due to available hardware resources (particularly limited RAM storage), specialized modular solvers, or just to introduce different degrees of numerical damping for the individual subsystems [146].

---

[6] This choice is just for simplicity. In transient structural problems, it is generally more convenient to apply, for instance, the energy conserving, second-order accurate trapezoidal rule which corresponds to an implicit Newmark method [93] with the parameter choice $\beta = 0.25$ and $\gamma = 0.5$. In this regard, also the explicit time integration is better performed by the central difference scheme (Newmark method with $\beta = 0$ and $\gamma = 0.5$) rather than the simple forward Euler scheme.

## Staggering Procedures

From a computational point of view, partitioned explicit-implicit schemes, particularly those which do not involve explicit interface constraints like (1.28), are perfect candidates for staggered solution procedures as the independent solution of the explicit subsystem can serve as a predictor to progress with the implicit partition. Basically, the conventional serial staggered (CSS) method proceeds from an alternating integration of a partitioned system, where the first subsystem is individually solved with some assumed (predicted) values for the variables of the other. The result is then substituted in the second subsystem, which in turn is independently solved by some appropriate method. This is the standard procedure in the case of differential partitioning following the successive steps partition – predict – integrate. An illustrative example is given by the simple 1-d
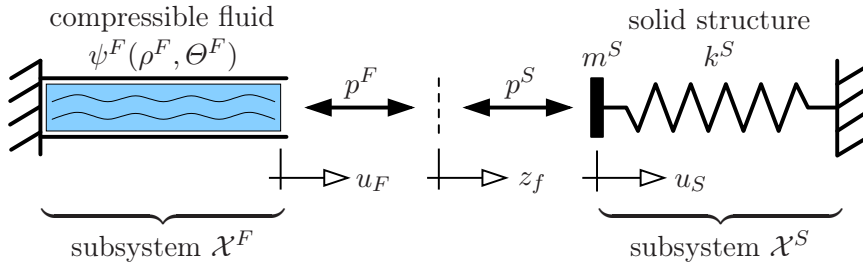


**Figure 1.4:** *The piston problem as a partitioned 1-d FSI problem of a compressible fluid (e. g. ideal gas with its free energy $\psi^F$ depending on density $\rho^F$ and temperature $\Theta^F$) with a non-dissipative solid structure represented by a mass-spring system.*

fluid-structure interaction problem depicted in Figure 1.4, where an elastic solid structure is geometrically coupled via a piston to a compressible fluid (e. g. ideal gas) that is trapped in a rigid cylinder. Without going into the modeling and discretization details (see [16, 17, 85]), a typical staggered FSI algorithm involves the following steps [40, 82, 104]:

(1) Predict the structural displacement, e. g., $u^P_{S\,n+1} = u_{S\,n} + \Delta t_n\, v_{S\,n}$.

(2) Update the fluid mesh according to the moving interface $u_{F\,n+1} = u^P_{S\,n+1}$.

(3) Advance the fluid subsystem to compute the new pressure field $p^F_{n+1}$.

(4) Convert the new fluid pressure into a structural load using $p^S_{n+1} = p^F_{n+1}$.

(5) Advance the solid structure under the fluid-induced load to obtain $u_{S\,n+1}$.

To simplify matters, but without loss of generality, now consider the partitioned system

$$\left.\begin{array}{ll} \mathcal{X}: & \dot{\boldsymbol{x}} = \boldsymbol{f}_x(t, \boldsymbol{x}, \boldsymbol{y}) \\ \mathcal{Y}: & \dot{\boldsymbol{y}} = \boldsymbol{f}_y(t, \boldsymbol{y}, \boldsymbol{x}) \end{array}\right\}\ \boldsymbol{F}(t, \dot{\boldsymbol{x}}, \dot{\boldsymbol{y}}, \boldsymbol{x}, \boldsymbol{y}) = \boldsymbol{0} \tag{1.38}$$

accompanied by respective initial conditions $\boldsymbol{x}_0$ and $\boldsymbol{y}_0$. If we would pursue an implicit monolithic strategy, we 'simply' need to solve the entire system

$$\boldsymbol{F}(t_{n+1}, \dot{\boldsymbol{x}}_{n+1}, \dot{\boldsymbol{y}}_{n+1}, \boldsymbol{x}_{n+1}, \boldsymbol{y}_{n+1}) = \boldsymbol{0} \tag{1.39}$$

in each time step, and this is the end of the story. In fact, the monolithic solution of the aggregated equations implies the synchronous treatment of the couplings (material or geometric) between the subsystems. Depending on the nonlinearity and strength of the mutual interactions, the discretized system is then typically solved by multiple iterations, where also the maintenance of conservation properties at interfaces in surface-coupled problems is possible, thus, guaranteeing unconditional stability. The admissible time-step size therefore appears to be limited only by the required accuracy.

Here, being inspired by the possibility that, for instance, subsystem $\mathcal{Y}$ can be very efficiently treated by some tailored explicit solver, while $\mathcal{X}$, for numerical convenience, is better advanced implicitly, we have a perfect prerequisite for a staggered solution of the coupled problem (1.38). Applying the previously mentioned CSS method in the sense of a Gauss-Seidel-like solution procedure, one proceeds from the simple-to-implement algorithm given in Box (1.40).

<div style="border:1px solid black; padding:10px;">

**Basic steps of an explicit-implicit serial staggered solution**

■ Algorithmic steps of a conventional serial staggered (CSS) solution

(1) *Predict*    $\mathsf{P}(\boldsymbol{y})$:    $\boldsymbol{y}_{n+1}^P = \boldsymbol{y}_n + \Delta t_n\,\dot{\boldsymbol{y}}_n$    (exemplary)

(2) *Advance*   $\mathsf{A}(\boldsymbol{x})$:    $\boldsymbol{x}_{n+1} = \boldsymbol{x}_n + \Delta t_n\,\boldsymbol{f}_x(t_{n+1}, \boldsymbol{x}_{n+1}, \boldsymbol{y}_{n+1}^P)$

(3) *Substitute* $\mathsf{S}(\boldsymbol{x})$:    $\boldsymbol{x}_{n+1} = \boldsymbol{x}_{n+1}$          (trivial case)

(4) *Advance*   $\mathsf{A}(\boldsymbol{y})$:    $\boldsymbol{y}_{n+1} = \boldsymbol{y}_n + \Delta t_n\,\boldsymbol{f}_y(t_n, \boldsymbol{y}_n, \boldsymbol{x}_{n+1})$

■ Flow chart of the two-system explicit-implicit CSS procedure



</div>

(1.40)
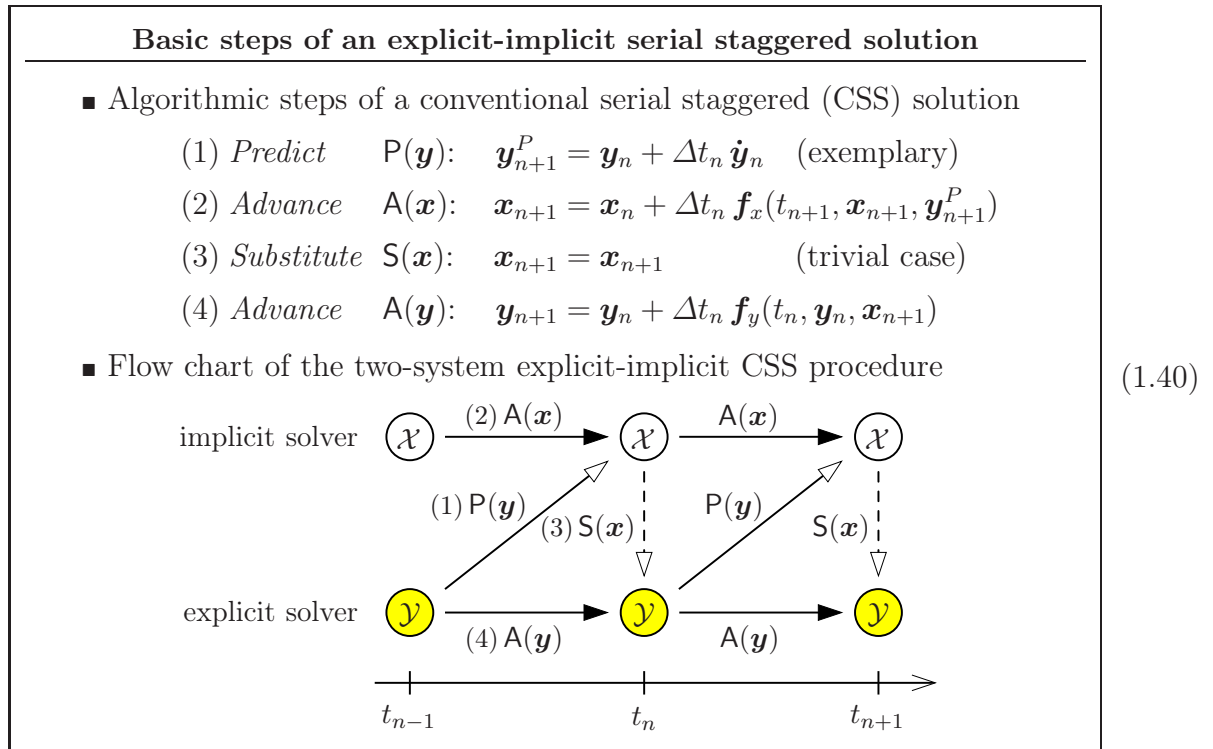
Besides the modularity benefit, the advantage of using the staggered process is obvious as the subsystem solving, even if both are advanced implicitly, is now confined to the magnitude of each partition, and thus, computationally more economic. However, the staggered procedure always induces a time lag between the integration of the partitioned subsystems such that conservation properties are lost[7]. We may therefore speak of a loosely coupled algorithmic treatment of some markedly coupled partitions. The accuracy can be increased if the interval between the information exchange is decreased, for example, by updating the interactions at intermediate time levels or after subiterations,

---

[7] In this regard, the destabilizing *artificial added-mass effect* in staggered solutions of FSI problems with incompressible fluids is worth mentioning. This sensitivity to violated continuity conditions becomes even more fatal for decreased time increments, see [25, 46, 61, 68, 134] for further particulars.

thereby making the algorithmic coupling more tight (cf. [16, 40, 73, 90]). In this regard, a variety of staggering procedures is feasible exploiting different time-stepping devices for the partitioned analysis, such as interfield iterations, correction steps, subcycling, and also parallel Jacobi-like staggered procedures, which are nicely outlined in the tutorial article by Felippa *et al.* [45].

Since the present work is primarily concerned with volume-coupled problems of continuum mechanics, where particular physical fields interact on the same spatial domain, a more comprehensive discussion of partitioning methods falls beyond its scope. For further reading, it is referred to [45, 81, 82, 90, 95, 100] and the quotations therein.

### 1.4.2 Time Splitting

To elucidate the principle idea of operator splitting, consider partial differential evolution equations of the form

$$\frac{\partial y}{\partial t} = f(t, y) =: f_A + f_D + f_R + f_b + f_\lambda, \quad y(t = 0) = y_0 \tag{1.41}$$

representing general advection-diffusion-reaction (ADR) equations, where in particular

$$
\begin{aligned}
f_A &= -\mathbf{v} \cdot \operatorname{grad} y && : \text{hyperbolic advection (convection}^8) \text{ term,} \\
f_D &= \operatorname{div}(\mathbf{D}(\mathbf{x}) \operatorname{grad} y) && : \text{parabolic diffusion term (slow process),} \\
f_R &= r(t, y) && : \text{source or reaction term (commonly very stiff),} && \tag{1.42} \\
f_b &= b(\mathbf{x}, t) && : \text{external excitations and forces,} \\
f_\lambda &= f_\lambda(\lambda) && : \text{Lagrange multiplier for any constraints.}
\end{aligned}
$$

Herein, $\mathbf{x}$ is the Cartesian position vector, $\mathbf{v} = \dot{\mathbf{x}}$ is the velocity vector, $\operatorname{grad}(\,\cdot\,) := \partial(\,\cdot\,)/\partial\mathbf{x}$ and $\operatorname{div}(\,\cdot\,) = \operatorname{grad}(\,\cdot\,) \cdot \mathbf{I}$ denote the gradient and the associated divergence operator with $\mathbf{I}$ being the identity tensor, $\mathbf{D}(\mathbf{x})$ is the diffusion tensor, and $\lambda$ some Lagrangean multiplier. It is quite obvious that the time integration of the separated operators, for example, the hyperbolic conservation laws $\partial y/\partial t = f_A$ or the equations $\partial y/\partial t = f_R$ describing potentially fast chemical reactions, are easier and by far more efficiently to accomplish by some tailored scheme than using some suboptimal integrator for the combined operator. This actually motivates the divide-and-conquer strategy termed *operator splitting*. In fact, various operator-splitting schemes have been proposed for equations similar to (1.41) depending on the combination of operators present in the system. Common to all schemes are the following basic steps [84]:

(1) Split the differential operator $f$ in operator pieces $f_i$ such that $f = \sum f_i$.

(2) Individually integrate either exactly or approximately each $f_i$.

(3) Combine the solutions to yield an integrator for $f$.

---

[8] Here, *advection* and *convection* are used synonymously. In other disciplines, such as oceanography or meteorology, advection is understood as horizontal transport by some distinct velocity field, while convection refers to vertical transport and mixing.

To set an example, consider a 1-d advection-diffusion equation describing some advection-dominated process,

$$\dot{y} = \frac{dy}{dt} = \frac{\partial y}{\partial t} + v\frac{\partial y}{\partial x} = D\frac{\partial^2 y}{\partial x^2}, \quad y(t_0) = y_0, \tag{1.43}$$

where $x$ is the Cartesian position coordinate, $v$ the velocity, and $D$ the homogeneous diffusion coefficient. Thus, (1.43) represents a linear evolution equation which may be rewritten as

$$\frac{\partial y}{\partial t} = -\mathcal{L}\,y \quad \text{with} \quad \mathcal{L} = \mathcal{L}_A + \mathcal{L}_D, \quad \text{where} \quad \begin{cases} \mathcal{L}_A = v\dfrac{\partial}{\partial x}, \\ \mathcal{L}_D = -D\dfrac{\partial^2}{\partial x^2} \end{cases} \tag{1.44}$$

are the linear advection and diffusion operators. A classical first-order or one-pass splitting scheme for the solution of (1.44) on the time interval $[t_n, t_{n+1}]$ with splitting time step $\Delta t = t_{n+1} - t_n$ is defined as follows:

(1) *Advection step:* Advance the hyperbolic part of (1.44) by some appropriate integrator $\varphi_A$ (e. g. explicit, 3rd-order Taylor-Galerkin (TG) scheme [33, 34]):

$$\frac{\partial y^*}{\partial t} = \mathcal{L}_A\, y^*, \quad y^*(t_n) = y_n \quad \text{on} \quad [t_n, t_{n+1}]. \tag{1.45}$$

(2) *Diffusion step:* Advance the parabolic part of (1.44) by some appropriate integrator $\varphi_D$ (e. g. implicit, 2nd-order trapezoidal rule (TR) [136, pp. 156–158]) using the result of (1) as initial condition:

$$\frac{\partial y}{\partial t} = \mathcal{L}_D\, y, \quad y(t_n) = y^*(t_{n+1}) \quad \text{on} \quad [t_n, t_{n+1}]. \tag{1.46}$$

From the sequence of successive integrations, the scheme may be named A-D splitting, which in terms of the respective integrators is usually written as $\varphi_{A,\Delta t} \circ \varphi_{D,\Delta t}$. In fact, the split treatment yields nothing else but a serial staggered-like solution of the problem, where the result of the advection step provides a 'predicted' initial condition for the diffusion equation, cf. Figure 1.5 (left). Strictly speaking, in the framework of differential operator splitting, the initial-value problem is solved by advancing each time step in multiple fractional steps, thereby introducing intermediate variables (here: $y^*$) which represent an approximation to the unknowns in the next time step. This partitioned time integration strategy actually suggests the notion *fractional-step method*, which for the considered problem proceeds from the evolution sequence $y_n \rightarrow y^* \rightarrow y_{n+1}$. As for partitioning methods, the subproblems can be discretized independently using different techniques and time-stepping devices. Moreover, the splitting scheme is unconditionally stable if the discrete counterparts of the separated operators $\mathcal{L}_A$ and $\mathcal{L}_D$ are positive definite. However, the simple and elegant this strategy is, it introduces a *splitting error* due to the uncoupling of the operators. According to that, the overall temporal accuracy of the above one-pass splitting scheme is only of first-order w. r. t. to the splitting time step, even if the

applied integrators $\varphi_A$ and $\varphi_D$ are of higher-order[9], consult, e. g., [117, 121, 123, 139] for details. An alternate first-order splitting scheme is conceivable, which is simply defined by reversing the order, i. e., the diffusion equation is evolved first followed by the advection equation yielding D-A splitting with $\varphi_{D,\Delta t} \circ \varphi_{A,\Delta t}$. In order to construct a second-order accurate time-splitting scheme, one may symmetrize the procedure in the sense of a two-pass algorithm, for instance, A-D-A splitting, where the integration of the advection operator is performed on a bisected interval $[t_n, t_{n+1/2}]$ before and $[t_{n+1/2}, t_{n+1}]$ after the diffusion step with half of the splitting time step $\Delta t/2$, which is briefly written as $\varphi_{A,\Delta t/2} \circ \varphi_{D,\Delta t} \circ \varphi_{A,\Delta t/2}$ (Figure 1.5, right). In this regard, it should be noted that the subproblem integrators must at least be of $\mathcal{O}(\Delta t^2)$ to obtain the desired accuracy in case of ODEs. Unfortunately, the second-order accuracy of the symmetric splitting scheme cannot be retained for differential-algebraic equations as shown by Vijalapura *et al.* [133].
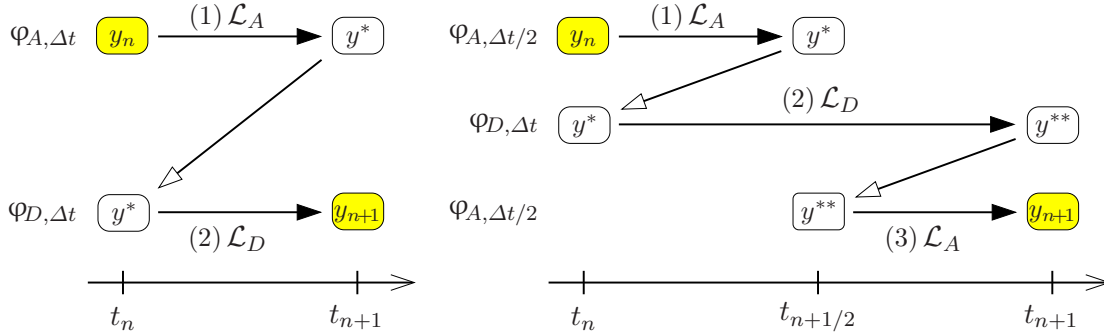


**Figure 1.5:** *Flow chart of the classical first-order (left) and a symmetric second-order splitting scheme (right) applied to the advection-diffusion problem (1.44).*

To continue, we generalize the operator-splitting strategy to coupled multi-field problems as introduced in Section 1.3.3. Therefore, consider a coupled system of first-order differential equations written in partitioned form, which is decoupled by splitting the differential operator in an additive fashion:

$$
\overbrace{\begin{bmatrix} \dot{\boldsymbol{y}} \\ \dot{\boldsymbol{z}} \end{bmatrix}}^{\mathcal{X}} = \underbrace{\begin{bmatrix} \boldsymbol{f}(t,\boldsymbol{y},\boldsymbol{z}) \\ \boldsymbol{g}(t,\boldsymbol{z},\boldsymbol{y}) \end{bmatrix}}_{\mathcal{F}} \longrightarrow \overbrace{\begin{bmatrix} \dot{\boldsymbol{y}} \\ \dot{\boldsymbol{z}} \end{bmatrix}}^{\mathcal{X}_{\boldsymbol{y}}} = \underbrace{\begin{bmatrix} \boldsymbol{f}(t,\boldsymbol{y},\boldsymbol{z}) \\ \boldsymbol{0} \end{bmatrix}}_{\mathcal{F}_{\boldsymbol{y}}}, \quad \overbrace{\begin{bmatrix} \dot{\boldsymbol{y}} \\ \dot{\boldsymbol{z}} \end{bmatrix}}^{\mathcal{X}_{\boldsymbol{z}}} = \underbrace{\begin{bmatrix} \boldsymbol{0} \\ \boldsymbol{g}(t,\boldsymbol{z},\boldsymbol{y}) \end{bmatrix}}_{\mathcal{F}_{\boldsymbol{z}}}. \quad (1.47)
$$

Clearly, it holds $\mathcal{F} = \mathcal{F}_{\boldsymbol{y}} + \mathcal{F}_{\boldsymbol{z}}$ in accordance with the splitting idea. Staying, for instance, with the first-order splitting scheme and supposing $\varphi_{\boldsymbol{y}}$ and $\varphi_{\boldsymbol{z}}$ to be appropriate integrators for the subsystems $\mathcal{X}_{\boldsymbol{y}}$ and $\mathcal{X}_{\boldsymbol{z}}$ on $[t_n, t_{n+1}]$, we may simply write $\varphi_{\boldsymbol{y},\Delta t} \circ \varphi_{\boldsymbol{z},\Delta t}$. In the terminology of the fractional-step method, the time-integration strategy can be expressed as $\{\boldsymbol{y}_n, \boldsymbol{z}_n\} \rightarrow \boldsymbol{y}^* \rightarrow \{\boldsymbol{y}_{n+1}, \boldsymbol{z}_{n+1}\}$, which is straightforward to implement in form of a

---

[9] This might also be seen positive since it implies that first-order time-stepping schemes are sufficient.

predictor-corrector algorithm obeying the following steps:

---

**Predictor-corrector algorithm of a splitting scheme**

(1) Make a prediction on $\boldsymbol{z}$ through extrapolation, e.g., $\boldsymbol{z}^P = \boldsymbol{z}_n + \Delta t\, \dot{\boldsymbol{z}}_n$.

(2) Advance $\boldsymbol{y}$ on $[t_n, t_{n+1}]$ while keeping $\boldsymbol{z} = \boldsymbol{z}^P$ fixed to obtain $\boldsymbol{y}^*$.    (1.48)

(3) Advance $\boldsymbol{z}$ on $[t_n, t_{n+1}]$ by substituting $\boldsymbol{y}^*$ to obtain $\boldsymbol{z}_{n+1}$.

(4) Perform a correction step using $\boldsymbol{z}_{n+1}$ to obtain $\boldsymbol{y}_{n+1}$ (optional).

---

In analogy to (1.47), a similar splitting procedure can be applied to DAE systems:

$$
\overbrace{\begin{bmatrix} \dot{\boldsymbol{y}} \\ \boldsymbol{0} \end{bmatrix} = \underbrace{\begin{bmatrix} \boldsymbol{f}(t, \boldsymbol{y}, \boldsymbol{z}) \\ \boldsymbol{g}(t, \boldsymbol{z}, \boldsymbol{y}) \end{bmatrix}}_{\mathcal{F}}}^{\mathcal{X}} \longrightarrow \overbrace{\begin{bmatrix} \dot{\boldsymbol{y}} \\ \dot{\boldsymbol{z}} \end{bmatrix} = \underbrace{\begin{bmatrix} \boldsymbol{f}(t, \boldsymbol{y}, \boldsymbol{z}) \\ \boldsymbol{0} \end{bmatrix}}_{\mathcal{F}_{\boldsymbol{y}}}}^{\mathcal{X}_{\boldsymbol{y}}}, \overbrace{\begin{bmatrix} \dot{\boldsymbol{y}} \\ \boldsymbol{0} \end{bmatrix} = \underbrace{\begin{bmatrix} \boldsymbol{0} \\ \boldsymbol{g}(t, \boldsymbol{z}, \boldsymbol{y}) \end{bmatrix}}_{\mathcal{F}_{\boldsymbol{z}}}}^{\mathcal{X}_{\boldsymbol{z}}}. \quad (1.49)
$$

The idea here is to decouple the differential from the unfavorable algebraic variables, which commonly act as Lagrangean multipliers to enforce some constraints, for instance, the pressure in the case of incompressibility (see Section 1.4.3). This is beneficial from a numerical perspective as the monolithic treatment of the coupled multi-field formulation in the framework of the mixed FEM normally induces restrictions to the choice of the spatial approximation spaces (LBB stability condition) or requires extra terms to stabilize the discretized equations. In the split approach, we gain stability even for linear equal-order interpolations, but on the expense of an additional splitting error. Furthermore, one needs to spatially discretize the intermediate variables (here: $\boldsymbol{y}^*$) and has to handle special boundary conditions (BCs) associated with the split equations. It is moreover obvious that if explicit time integrators are applied yielding some explicit-explicit or semi-explicit-implicit scheme, the CFL condition limits the global splitting time step. Concerning the reduced first-order accuracy of symmetric two-pass splitting schemes when applied to differential-algebraic equations [133], it should be mentioned that DAEs like $(1.49)_1$ can be recast into equivalent ODE systems as $(1.47)_1$ by use of (1.12) being aware of the computational overhead and possible loss of the strict observance of the constraints.

## 1.4.3   Two Illustrative Examples

To reveal the applicability of the time-splitting approach to volumetrically coupled multi-field systems, the principle procedure is illustrated for two examples relevant in computational mechanics and engineering.

**Thermomechanical Coupling**

The first canonical example is given by the problem of thermoelasticity. For simplicity and without going into the thermodynamical details, we adopt the dimensionless description

of 1-d linear thermoelasticity provided by Armero & Simo [7, Eq. (78)]:

$$
\begin{aligned}
\frac{\partial u}{\partial t} &= v & &: \text{displacement-velocity relation,} \\[2mm]
\frac{\partial v}{\partial t} &= \frac{\partial^2 u}{\partial x^2} - \frac{\partial \Theta}{\partial x} & &: \text{linear momentum balance,} \\[2mm]
\frac{\partial \Theta}{\partial t} &= \frac{\partial^2 \Theta}{\partial x^2} - C_{\theta u}\frac{\partial v}{\partial x} & &: \text{thermal conduction equation.}
\end{aligned}
\tag{1.50}
$$

Herein, $u, v$ and $\Theta$ represent the dimensionless displacement, velocity and temperature, and $x$ and $t$ are the dimensionless spatial coordinate and time. Moreover, $C_{\theta u} \geq 0$ is a dimensionless number governing the thermomechanical coupling strength. Clearly, $C_{\theta u} \equiv 0$ implies weak one-way coupling, i. e., the thermal part can be solved independently without any feedback from the mechanical subsystem. Here, we proceed from a marked coupling between the thermal and mechanical fields omitting body forces as well as radiation and seek for a stable partitioned solution of the system. In this context, note that $(1.50)_1$ is merely introduced to obtain first-order differential equations (cf. Section 1.3.4).

The most straightforward and therefore commonly used approach is to decouple the operators according to the evolution equations as in (1.47) and then pursue a conventional serial staggered solution strategy (recall Box (1.40)) [118]. Thus, with the shortcuts $a_{,b} := \partial a/\partial b$ and $a_{,bb} := \partial^2 a/\partial b^2$, we have

$$
\overbrace{\begin{bmatrix} u_{,t} \\ v_{,t} \\ \Theta_{,t} \end{bmatrix}}^{\mathcal{X}} = \underbrace{\begin{bmatrix} v \\ u_{,xx} - \Theta_{,x} \\ \Theta_{,xx} - C_{\theta u}\, v_{,x} \end{bmatrix}}_{\mathcal{F}} \longrightarrow \overbrace{\begin{bmatrix} u_{,t} \\ v_{,t} \\ \Theta_{,t} \end{bmatrix}}^{\mathcal{X}_u} = \underbrace{\begin{bmatrix} v \\ u_{,xx} - \Theta_{,x} \\ 0 \end{bmatrix}}_{\mathcal{F}_u}, \quad \overbrace{\begin{bmatrix} u_{,t} \\ v_{,t} \\ \Theta_{,t} \end{bmatrix}}^{\mathcal{X}_\theta} = \underbrace{\begin{bmatrix} 0 \\ 0 \\ \Theta_{,xx} - C_{\theta u}\, v_{,x} \end{bmatrix}}_{\mathcal{F}_\theta}.
$$
$$\tag{1.51}$$

Following the predictor-corrector algorithm in Box (1.48), first, the mechanical subsystem $\mathcal{X}_u$ is advanced under isothermal conditions with the temperature field kept constant $(\Theta_{,t} = 0)$. According to this, the procedure is termed *isothermal split*, where the constant temperature is commonly based on an extrapolated predictor, for instance, $\Theta^P = \Theta_n$ or $\Theta^P = \Theta_n + \Delta t\,(\Theta_{,t})_n$. Afterwards, $\mathcal{X}_\theta$ is integrated on $[t_n, t_{n+1}]$ at fixed configuration $(u_{,t}, v_{,t} = 0)$ and substitution of $v_{n+1} = v^*$. To meet the stability demands, one would intuitively choose the trapezoidal rule (implicit, $\mathcal{O}(\Delta t^2)$) for the time integration of the isothermal elastodynamic subproblem $\mathcal{X}_u$ and, for example, the backward-Euler scheme (implicit, $\mathcal{O}(\Delta t)$) for the heat conduction part $\mathcal{X}_\theta$. However, according to Armero & Simo [7], independent of the subsystem integrators, say $\varphi_{u,\Delta t}$ and $\varphi_{\theta,\Delta t}$, the combined solution algorithm $\varphi_{u,\Delta t} \circ \varphi_{\theta,\Delta t}$ is only conditionally stable with $C_{\theta u}$ governing the critical time step $\Delta t_{cr}$ of the CFL condition. Thus, Armero & Simo "conclude that the stronger the coupling, the less appropriate this algorithm becomes."

To overcome this deficiency, it needs just a slight modification (highlighted) of the split:

$$
\overbrace{\begin{bmatrix} u_{,t} \\ v_{,t} \\ \Theta_{,t} \end{bmatrix}}^{\mathcal{X}} = \underbrace{\begin{bmatrix} v \\ u_{,xx} - \Theta_{,x} \\ \Theta_{,xx} - C_{\theta u}\, v_{,x} \end{bmatrix}}_{\mathcal{F}} \longrightarrow \overbrace{\begin{bmatrix} u_{,t} \\ v_{,t} \\ \Theta_{,t} \end{bmatrix}}^{\mathcal{X}_u} = \underbrace{\begin{bmatrix} v \\ u_{,xx} - \Theta_{,x} \\ \boxed{-C_{\theta u}\, v_{,x}} \end{bmatrix}}_{\mathcal{F}_u}, \quad \overbrace{\begin{bmatrix} u_{,t} \\ v_{,t} \\ \Theta_{,t} \end{bmatrix}}^{\mathcal{X}_\theta} = \underbrace{\begin{bmatrix} 0 \\ 0 \\ \boxed{\Theta_{,xx}} \end{bmatrix}}_{\mathcal{F}_\theta}. \quad (1.52)
$$

From a thermodynamical perspective, this additional decomposition of the operator of the heat conduction equation $(1.50)_3$ is associated with an adiabatic evolution of the mechanical system at constant entropy (isentropic conditions). Therefore, this approach is called *adiabatic split* or *isentropic split*. Regarding the algorithmic treatment, the procedure is astonishingly not that different from the isothermal one. This is because of the fact that one easily finds an explicit expression for the intermediate temperature $\Theta^*$. For example, with the backward-Euler scheme, one obtains

$$
\frac{\Theta^* - \Theta_n}{\Delta t} = -C_{\theta u}\, \frac{(u_{n+1})_{,x} - (u_n)_{,x}}{\Delta t} \quad \longrightarrow \quad \Theta^* = \Theta_n - C_{\theta u}\left[ (u_{n+1})_{,x} - (u_n)_{,x} \right], \quad (1.53)
$$

which can directly be substituted into the time-discrete momentum balance letting $\Theta^P = \Theta^*$. Moreover, proceeding from an isentropic process, the evolution of the heat equation can be shown to be independent of the intermediate temperature [7], such that the actual temperature field may in turn be computed from the combined heat conduction equation as in the isothermal split (1.51). Actually, this means that $\Theta^*$ needs not to be spatially discretized because it is never computed. Roughly speaking, we may stay with the isothermal splitting scheme and just replace the temperature predictor through substitution of $(1.53)_2$ into the time-discrete momentum balance. This scheme has been proven to be unconditionally stable even for nonlinear thermoelasticity [7] appropriate (B-stable) subsystem integrators provided (cf. [4]). For further reading on thermomechanical problems in general, see [58, 72, 87, 113, 118] and the quotations therein.

**Incompressible Flow**

The second example concerns the fundamental equation of computational fluid dynamics (CFD), viz., the *Navier-Stokes equation* describing the nonlinear flow of commonly linear-viscous (Newtonian) continuum fluids [11, 28]. The nonlinearity due to the convective acceleration inherent to the momentum equation makes most problems difficult or impossible to solve and is the main contributor to turbulence [107]. The situation becomes even more complicated if incompressible flow problems are considered as in the course of the solution, the continuity equation has to be satisfied in the sense of an additional algebraic side condition. The incompressible viscous flow problem is modeled by the coupled two-field DAE system,

$$
\begin{aligned}
\frac{\partial \mathbf{v}}{\partial t} + (\mathrm{grad}\,\mathbf{v})\,\mathbf{v} &= -\mathrm{grad}\,p + \nu\, \mathrm{div}\,\mathrm{grad}\,\mathbf{v} \quad &: \text{Navier-Stokes equation,} \\
\mathrm{div}\,\mathbf{v} &= 0 \quad &: \text{continuity equation,}
\end{aligned}
\quad (1.54)
$$

formulated in the fluid velocity vector $\mathbf{v}$ (differential variable) and the mass-specific fluid pressure $p$ (algebraic variable). The only parameter that appears, is the kinematic viscosity $\nu$. For brevity, body forces have been neglected.

The algebraic continuity equation $(1.54)_2$ represents the incompressibility constraint, for which the pressure acts as a Lagrangean multiplier. The special thing about the constraint is that although it is used to determine the pressure field up to an additive constant defined through respective boundary conditions, the algebraic variable $p$ is absent in the equation. Accordingly, the DAE system is of differentiation index 2, recall (1.13) in Section 1.3.3 (see also [9]). This can be tackled by taking the divergence of the momentum equation $(1.54)_1$ and then exploiting $\text{div }\mathbf{v} = 0$. This leads to the so-called *pressure-Poisson equation* that equivalently replaces the continuity condition:

$$-\text{div grad}\, p = \text{div}\big[(\text{grad}\,\mathbf{v})\,\mathbf{v} - \nu\,\text{div grad}\,\mathbf{v}\big]. \qquad (1.55)$$

The satisfaction of this equation is a necessary and sufficient condition for a divergence-free (solenoidal) flow field to remain divergence-free. Clearly, the pressure variable is now explicitly included, such that in combination with the Navier-Stokes equation $(1.54)_1$, we obtain an index-1 DAE system similar to (1.11).

The pressure-Poisson equation (1.55) is widely used in *projection schemes* [53], which represent special two-stage fractional-step methods that target the separation of the momentum equation from the unfavorable incompressibility constraint by decoupling velocity and pressure, thereby providing stability. Here, we start with the classical semi-explicit-implicit projection scheme of Chorin [26, 27], which in notation of the fractional-step method reads $\mathbf{v}_n \rightarrow \mathbf{v}^* \rightarrow \{\mathbf{v}_{n+1}, p_{n+1}\}$. To continue, we first rewrite the DAE system (1.54) in concise mathematical form by means of the Nabla and Laplace operator, $\nabla(\,\cdot\,) = \text{grad}\,(\,\cdot\,)$, $\nabla \cdot (\,\cdot\,) = \text{div}\,(\,\cdot\,)$, and $\Delta(\,\cdot\,) = \text{div grad}\,(\,\cdot\,)$, yielding

$$\mathcal{X}:\ \begin{bmatrix} \mathbf{v}_{,t} \\ 0 \end{bmatrix} = \underbrace{\begin{bmatrix} -(\nabla\mathbf{v})\,\mathbf{v} - \nabla p + \nu\,\Delta\mathbf{v} \\ \nabla \cdot \mathbf{v} \end{bmatrix}}_{\mathcal{F}}. \qquad (1.56)$$

Then, one proceeds from the following operator split:

$$\mathcal{X} \longrightarrow \overbrace{\begin{bmatrix} \mathbf{v}_{,t} \\ p_{,t} \end{bmatrix} = \underbrace{\begin{bmatrix} -(\nabla\mathbf{v})\,\mathbf{v} + \nu\,\Delta\mathbf{v} \\ 0 \end{bmatrix}}_{\mathcal{F}_{\mathbf{v}}}}^{\mathcal{X}_{\mathbf{v}}},\ \overbrace{\begin{bmatrix} \mathbf{v}_{,t} \\ 0 \end{bmatrix} = \underbrace{\begin{bmatrix} -\nabla p \\ \nabla \cdot \mathbf{v} \end{bmatrix}}_{\mathcal{F}_p}}^{\mathcal{X}_p}. \qquad (1.57)$$

It is apparent that in subsystem $\mathcal{X}_{\mathbf{v}}$ the pressure gradient has been omitted resulting in the viscous Burgers' equation, which is advanced first on $[t_n, t_{n+1}]$, originally with the forward-Euler scheme, disregarding continuity to obtain $\mathbf{v}^*$ (velocity predictor step). In the second stage, the intermediate velocity is then projected onto the subspace of solenoidal functions by use of the pressure field (pressure correction step)[10]. In particular, this is accomplished

---

[10] More precisely, projection schemes are based on the *Helmholtz-Hodge decomposition* which states that any vector field can be uniquely decomposed into a solenoidal (divergence-free) part and an irrotational part, consult, e. g., Chorin & Marsden [28] for details.

by making the pressure subsystem $\mathcal{X}_p$ time discrete applying the backward-Euler method and recast it in form of the pressure-Poisson equation (1.55) to obtain $p_{n+1}$ and finally update the flow field:

$$\left\{\begin{array}{c} \dfrac{\mathbf{v}_{n+1} - \mathbf{v}^*}{\Delta t} = -\nabla p_{n+1} \\[2mm] \nabla \cdot \mathbf{v}_{n+1} = 0 \end{array}\right\} \quad \longrightarrow \quad \left\{\begin{array}{c} -\Delta p_{n+1} = -\frac{1}{\Delta t} \nabla \cdot \mathbf{v}^* \\[2mm] \mathbf{v}_{n+1} = \mathbf{v}^* - \Delta t\, \nabla p_{n+1} \end{array}\right\} . \tag{1.58}$$

Chorin's projection scheme is first-order accurate and stable for equal-order interpolations of $\mathbf{v}$ and $p$ if $\Delta t \leq \Delta t_{cr}$ according to the CFL condition. Note that the projection method shows spurious pressure boundary layers which might yield inaccurate solutions close to the boundaries [110].

A second-order accurate projection scheme à la van Kan [130] can be defined by 'enhancing' the split momentum equation through adding some approximation to the pressure gradient, say $-\nabla q$, and use a second-order time integrator (here: trapezoidal rule) to advance the system. The modified split reads

$$\mathcal{X} \; \longrightarrow \; \overbrace{\begin{bmatrix} \mathbf{v}_{,t} \\ p_{,t} \end{bmatrix} = \underbrace{\begin{bmatrix} -(\nabla \mathbf{v})\,\mathbf{v}\,\boxed{-\nabla q} + \nu\,\Delta \mathbf{v} \\ 0 \end{bmatrix}}_{\mathcal{F}_{\mathbf{v}}}}^{\mathcal{X}_{\mathbf{v}}}, \; \overbrace{\begin{bmatrix} \mathbf{v}_{,t} \\ 0 \end{bmatrix} = \underbrace{\begin{bmatrix} \boxed{-\nabla \widetilde{p}} \\ \nabla \cdot \mathbf{v} \end{bmatrix}}_{\mathcal{F}_p}}^{\mathcal{X}_p}, \tag{1.59}$$

where the highlighted terms meet $\nabla p = \nabla q + \nabla \widetilde{p}$. The method of van Kan is achieved by inserting the old pressure gradient in the sense of a predictor letting $\nabla q = \nabla p_n$ such that on the basis of the trapezoidal rule $\nabla \widetilde{p}_{n+1} = \frac{1}{2}(\nabla p_{n+1} - \nabla p_n)$. Thus, the solution is obtained in the fractional steps $\{\mathbf{v}_n, p_n\} \to \mathbf{v}^* \to \{\mathbf{v}_{n+1}, p_{n+1}\}$, where the predictor-corrector algorithm pursues the same stages as before: (1) solve the viscous Burgers' equation with known pressure gradient and (2) project the resulting intermediate velocity $\mathbf{v}^*$ to obtain a divergence-free flow field $\mathbf{v}_{n+1}$ via solution of the pressure-Poisson equation. In particular, we have

$$\left\{\begin{array}{c} \dfrac{\mathbf{v}_{n+1} - \mathbf{v}^*}{\Delta t} = -\nabla \widetilde{p}_{n+1} \\[2mm] \nabla \cdot \mathbf{v}_{n+1} = 0 \end{array}\right\} \quad \longrightarrow \quad \left\{\begin{array}{c} -\Delta \widetilde{p}_{n+1} = -\frac{1}{\Delta t} \nabla \cdot \mathbf{v}^* \\[1mm] \mathbf{v}_{n+1} = \mathbf{v}^* - \Delta t\, \nabla \widetilde{p}_{n+1} \\[1mm] p_{n+1} = p_n + 2\, \widetilde{p}_{n+1} \end{array}\right\} . \tag{1.60}$$

The only difference to (1.58) is in the additional step for the pressure update due to the split pressure gradient.

In fact, dozens of projection schemes for the incompressible Navier-Stokes equations (1.54) have been proposed in the related literature, which differ in the way the pressure gradient is split (i.e. how $\nabla q$ is defined), the momentum equation is advanced, the advection term is treated, and how the Poisson equation is approximated. However, it is neither in the scope of this work to review all possible variants nor to provide a statement, which of the methods is the most suitable. In this regard, it is rather referred to the works of Turek [127], Prohl [110], Guermond & Quartapelle [53], Rannacher [112], and Gresho & Sani [52] and to the quotations therein.

## 1.5 References

[1] Aiken, R. C. (ed.): *Stiff Computation.* Oxford University Press 1985.

[2] Alexander, R.: Diagonally implicit Runge-Kutta methods for stiff ODEs. *SIAM Journal on Numerical Analysis* **14** (1977), 1006–1021.

[3] Alonso-Mallo, I.; Cano, B. & Moreta, M. J.: Stable Runge-Kutta-Nyström methods for dissipative stiff problems. *Numerical Algorithms* **42** (2006), 193–203.

[4] Araújo, A.: A note on B-stability of splitting methods. *Computing and Visualization in Science* **6** (2004), 53–57.

[5] Argyris, J.; Doltsinis, I. S.; Pimenta, P. & Wüstenberg, H.: Thermomechanical response of solids at high strains – natural approach. *Computer Methods in Applied Mechanics and Engineering* **32** (1982), 3–57.

[6] Armero, F.: Formulation and finite element implementation of a multiplicative model of coupled poro-plasticity at finite strains under fully saturated conditions. *Computer Methods in Applied Mechanics and Engineering* **177** (1999), 205–241.

[7] Armero, F. & Simo, J. C.: A new unconditionally stable fractional step method for non-linear coupled thermomechanical problems. *International Journal for Numerical Methods in Engineering* **35** (1992), 737–766.

[8] Arnold, D. N.: Mixed finite element methods for elliptic problems. *Computer Methods in Applied Mechanics and Engineering* **82** (1990), 281–300.

[9] Ascher, U. M. & Petzold, L. R.: *Computer Methods for Ordinary Differential Equations and Differential-Algebraic Equations.* Society for Industrial and Applied Mathematics (SIAM), Philadelphia, PA 1998.

[10] Banerjee, P. K.: *The Boundary Element Methods in Engineering.* McGraw-Hill College 1994.

[11] Batchelor, G. K.: *An Introduction to Fluid Dynamics.* Cambridge University Press 1967.

[12] Bathe, K. J.: *Finite Element Procedures.* Prentice Hall, New Jersey 1996.

[13] Belytschko, T. & Mullen, R.: Stability of explicit-implicit time domain solution. *International Journal for Numerical Methods in Engineering* **12** (1978), 1575–1586.

[14] Benzi, M.; Golub, G. H. & Liesen, J.: Numerical solution of saddle point problems. *Acta Numerica* **14** (2005), 1–137.

[15] Bhardwaj, M.; Day, D.; Farhat, C.; Lesoinne, M.; Pierson, K. & Rixen, D.: Application of the feti method to asci problems – scalability results on 1000 processors and discussion of highly heterogeneous problems. *International Journal for Numerical Methods in Engineering* **47** (2000), 513–535.

[16] Blom, F. J.: A monolithical fluid-structure interaction algorithm applied to the piston problem. *Computer Methods in Applied Mechanics and Engineering* **167** (1998), 369–391.

[17] Blom, F. J. & Leyland, P.: Consistency analysis of fluid-structure interaction algorithms. In Papailiou, K. D.; Tsahalis, D.; Periaux, J. & Knoerzer, D. (eds.): *Proceedings of the 4th ECCOMAS Computational Fluid Dynamics Conference*. John Wiley & Sons, Chichester 1998, pp. 1026–1031.

[18] Boffi, D.; Brezzi, F.; Demkowicz, L. F.; Durán, R. G.; Falk, R. S. & Fortin, M.: *Mixed Finite Elements, Compatibility Conditions, and Applications: Lectures given at the C. I. M. E. Summer School held in Cetraro, Italy, June 26 - July 1, 2006*. Lecture Notes in Mathematics, Springer-Verlag 2008.

[19] Brenan, K. E.; Campbell, S. L. & Petzold, L. R.: *Numerical Solution of Initial-Value Problems in Differential-Algebraic Equations*, vol. 14 of *Classics in Applied Mathematics*. Society for Industrial and Applied Mathematics (SIAM), Philadelphia, PA 1996, revised and corrected reprint of the 1989 original, with an additional chapter and additional references.

[20] Brezzi, F. & Fortin, M.: *Mixed and Hybrid Finite Element Methods*. Springer-Verlag, New York 1991.

[21] Butcher, J. C.: *The Numerical Analysis of Ordinary Differential Equations: Runge-Kutta and General Linear Methods*. John Wiley & Sons, New York 1987.

[22] Butcher, J. C.: *Numerical Methods for Ordinary Differential Equations*. John Wiley & Sons, Chichester 2003.

[23] Butcher, J. C.: Runge-Kutta methods. *Scholarpedia* **2** (2007), 3147.

[24] Cash, J. R.: Efficient numerical methods for the solution of stiff initial-value problems and differential algebraic equations. *Proceedings of the Royal Society of London A* **459** (2003), 797–815.

[25] Causin, P.; Gerbeau, J.-F. & Nobile, F.: Added-mass effect in the design of partitioned algorithms for fluid-structure problems. *Computer Methods in Applied Mechanics and Engineering* **194** (2005), 4506–4527.

[26] Chorin, A. J.: A numerical method for solving incompressible viscous problems. *Journal of Applied Physics* **2** (1967), 12–26.

[27] Chorin, A. J.: Numerical solution of the Navier-Stokes equations. *Mathematics of Computation* **22** (1968), 745–762.

[28] Chorin, A. J. & Marsden, J. E.: *A Mathematical Introduction to Fluid Mechanics*. Springer-Verlag, New York 2000, 3rd edn.

[29] Courant, R.; Friedrichs, K. & Lewy, H.: Über die partiellen Differenzengleichungen der mathematischen Physik. *Mathematische Annalen* **100** (1928), 32–74.

[30] Cowsar, L. C.; Mandel, J. & Wheeler, M. F.: Balancing domain decomposition for mixed finite elements. *Mathematics of Computation* **64** (1995), 989–1015.

[31] Dahlquist, G.: A special stability problem for linear multistep methods. *BIT Numerical Mathematics* **3** (1963), 27–43.

[32] Dekker, K. & Verwer, J. G.: *Stability of Runge-Kutta Methods for Stiff Nonlinear Differential Equations.* North-Holland, Amsterdam 1984.

[33] Donea, J.: A Taylor-Galerkin method for convective transport problems. *International Journal for Numerical Methods in Engineering* **20** (1984), 101–120.

[34] Donea, J. & Quartapelle, L.: A Taylor-Galerkin method for convective transport problems. *Computer Methods in Applied Mechanics and Engineering* **95** (1992), 169–203.

[35] Douglas, J. & Jr., H. H. R.: On the numerical solution of the heat conduction problem in two and three space variables. *Transactions of the American Mathematical Society* **82** (1956), 421–439.

[36] Dowell, E. H. & Hall, K. C.: Modeling of fluid-structure interaction. *Annual Review of Fluid Mechanics* **33** (2001), 445–490.

[37] Dureisseix, D. & Bavestrello, H.: Information transfer between incompatible finite element meshes: Application to coupled thermo-viscoelasticity. *Computer Methods in Applied Mechanics and Engineering* **195** (2006), 6523–6541.

[38] Ehlers, W. & Ellsiepen, P.: Theoretical and numerical methods in environmental continuum mechanics based on the theory of porous media. In Schrefler, B. A. (ed.): *Environmental Geomechanics.* Springer-Verlag, Wien 2001, CISM Courses and Lectures No. 417, pp. 1–81.

[39] Ellsiepen, P.: *Zeit- und ortsadaptive Verfahren angewandt auf Mehrphasenprobleme poröser Medien.* Dissertation, Bericht Nr. II-3 aus dem Institut für Mechanik (Bauwesen), Universität Stuttgart 1999.

[40] Farhat, C. & Lesoinne, M.: Two efficient staggered algorithms for the serial and parallel solution of three-dimensional nonlinear transient aeroelastic problems. *Computer Methods in Applied Mechanics and Engineering* **182** (2000), 499–515.

[41] Farhat, C.; Mandel, J. & Roux, F.-X.: Optimal convergence properties of the feti domain decomposition method. *Computational Methods in Applied Mechanics and Engineering* **115** (1994), 365–385.

[42] Farhat, C. & Roux, F.-X.: A method of finite element tearing and interconnecting and its parallel solution algorithm. *International Journal for Numerical Methods in Engineering* **32** (1991), 1205–1227.

[43] Felippa, C. A. & Geers, T. L.: Partitioned analysis of coupled mechanical systems. *Engineering Computations* **5** (1988), 123–133.

[44] Felippa, C. A. & Park, K. C.: Staggered transient analysis procedures for coupled-field mechanical systems: Formulation. *Computer Methods in Applied Mechanics and Engineering* **24** (1980), 61–111.

[45] Felippa, C. A.; Park, K. C. & Farhat, C.: Partitioned analysis of coupled mechanical systems. *Computer Methods in Applied Mechanics and Engineering* **190** (2001), 3247–3270.

[46] Förster, C.; Wall, W. A. & Ramm, E.: Artificial added mass instabilities in sequential staggered coupling of nonlinear structures and incompressible viscous flows. *Computer Methods in Applied Mechanics and Engineering* **196** (2007), 1278–1293.

[47] Fragakis, Y. & Papadrakakis, M.: The mosaic of high performance domain decomposition methods for structural mechanics: Formulation, interrelation and numerical efficiency of primal and dual methods. *Computer Methods in Applied Mechanics and Engineering* **192** (2003), 3799–3830.

[48] Gaul, L.; Kögl, M. & Wagner, M.: *Boundary Element Methods for Engineers and Scientists.* Springer-Verlag, Berlin 2003.

[49] Gear, C. W.: The automatic integration of ordinary differential equations. *Communications of the ACM* **14** (1971), 176–179.

[50] Gear, C. W.: Simultaneous numerical solution of differential-algebraic equations. *IEEE Transactions on Circuit Theory* **18** (1971), 89–95.

[51] Gosselet, P.; Chiaruttini, V.; Rey, C. & Feyel, F.: A monolithic strategy based on an hybrid domain decomposition method for multiphysic problems: Application to poroelasticity. *Revue Européenne des Eléments Finis* **13** (2004), 523–534.

[52] Gresho, P. M. & Sani, R. L.: *Incompressible Flow and the Finite Element Method*, vol. 2. John Wiley & Sons, Chichester 2000, second corrected reprint of 1998.

[53] Guermond, J.-L. & Quartapelle, L.: On stability and convergence of projection methods based on pressure Poisson equation. *International Journal for Numerical Methods in Fluids* **26** (1998), 1039–1053.

[54] Hairer, E.; Lubich, C. & Roche, M.: *The Numerical Solution of Differential-Algebraic Equations by Runge-Kutta Methods.* Springer-Verlag 1989.

[55] Hairer, E. & Wanner, G.: *Solving Ordinary Differential Equations II: Stiff and Differential-Algebraic Problems.* Springer-Verlag, Berlin 1996, 2nd edn.

[56] Heil, M.: An efficient solver for the fully coupled solution of large-displacement fluid-structure interaction problems. *Computer Methods in Applied Mechanics and Engineering* **193** (2004), 1–23.

[57] Higham, D. J. & Trefethen, L. N.: Stiffness of odes. *BIT Numerical Mathematics* **33** (1993), 285–303.

[58] Holzapfel, G. A. & Simo, J. C.: A new viscoelastic constitutive model for continuous media at finite thermomechanical changes. *International Journal of Solids and Structures* **33** (1996), 3019–3034.

[59] Hughes, T. J. R.: *The Finite Element Method: Linear Static and Dynamic Finite Element Analysis.* Dover Publications, Mineola, New York 2000.

[60] Hughes, T. J. R. & Liu, W. K.: Implicit-explicit finite elements in transient analysis: Stability theory. *Journal of Applied Mechanics* **45** (1978), 371–374.

[61] Idelsohn, S. R.; Del Pin, F.; Rossi, R. & nate, E. O.: Fluid-structure interaction problems with strong added-mass effect. *International Journal for Numerical Methods in Engineering* **80** (2009), 1261–1294.

[62] J. R. Dormand, M. E. A. E.-M. & Prince, P. J.: Families of Runge-Kutta-Nystrom formulae. *IMA Journal of Numerical Analysis* **7** (1987), 235–250.

[63] Jensen, P. S.: Transient analysis of structures by stiffly stable methods. *Computers & Structures* **4** (1978), 615–626.

[64] Kuhl, D.: *Modellierung und Simulation von Mehrfeldproblemen der Strukturmechanik.* Habilitation thesis, Schriftenreihe des Instituts für Konstruktiven Ingenieurbau, Heft 2005-9, Ruhr-Universität Dortmund 2005.

[65] Kuhl, E.: *Theory and Numerics of Open System Continuum Thermodynamics - Spatial and Material Settings.* Habilitation thesis, Maschinenbau und Verfahrenstechnik, Technische Universität Kaiserslautern 2004.

[66] Kuhl, E. & Steinmann, P.: Theory and numerics of geometrically non-linear open system mechanics. *International Journal for Numerical Methods in Engineering* **58** (2003), 1593–1615.

[67] Lambert, J. D.: *Numerical Methods for Ordinary Differential Systems: The Initial Value Problem.* John Wiley & Sons, Chichester 1991.

[68] Le Tallec, P. & Mouro, J.: Fluid structure interaction with large structural displacements. *Computer Methods in Applied Mechanics and Engineering* **190** (2001), 3039–3067.

[69] LeVeque, R. J.: *Finite Volume Methods for Hyperbolic Problems.* Cambridge University Press 2002.

[70] Lewis, R. W.; Bettes, P. & Hinton, E. (eds.): *Numerical Methods in Coupled Systems.* John Wiley & Sons, Chichester 1984.

[71] Lewis, R. W. & Schrefler, B. A.: *The Finite Element Method in the Static and Dynamic Deformation and Consolidation of Porous Media.* John Wiley & Sons, Chichester 1998, 2nd edn.

[72] Lion, A.: A physically based method to represent the thermomechanical behaviour of elastomers. *Acta Mechanica* **123** (1997), 1–25.

[73] Lübbing, C.: *Zur Stabilität von gestaffelten Finite-Elemente Berechnungen*. Dissertation, Bericht Nr. 18Ð97 des Instituts für Statik und Dynamik der Luft- und Raumfahrtkonstruktionen, Universität Stuttgart 1997.

[74] Lubich, C.: Integration of stiff mechanical systems by Runge-Kutta methods. *Zeitschrift für angewandte Mathematik und Physik (ZAMP)* **44** (1993), 1022–1053.

[75] Luenberger, D. G.: *Introduction to Dynamic Systems, Theory, Models, and Applications*. John Wiley & Sons Inc., New York 1979.

[76] Mandel, J.: Balancing domain decomposition. *Communications in Numerical Methods in Engineering* **9** (1993), 233–241.

[77] Markert, B.: *Porous Media Viscoelasticity with Application to Polymeric Foams*. Dissertation, Report No. II-12 of the Institute of Applied Mechanics (CE), Universität Stuttgart, Germany 2005.

[78] Markert, B.: A constitutive approach to 3-d nonlinear fluid flow through finite deformable porous continua. *Transport in Porous Media* **70** (2007), 427–450.

[79] Markert, B.: A biphasic continuum approach for viscoelastic high-porosity foams: Comprehensive theory, numerics, and application. *Archives of Computational Methods in Engineering* **15** (2008), 371–446.

[80] Markert, B.; Heider, Y. & Ehlers, W.: Comparison of monolithic and splitting solution schemes for dynamic porous media problems. *International Journal for Numerical Methods in Engineering* **82** (2010), 1341–1383.

[81] Matthies, H. G.; Niekamp, R. & Steindorf, J.: *Strong Coupling Methods*. Informatikbericht Nr.:2002-06, Institute of Scientific Computing, Technical University Braunschweig, Brunswick, Germany 2002.

[82] Matthies, H. G.; Niekamp, R. & Steindorf, J.: Algorithms for strong coupling procedures. *Computer Methods in Applied Mechanics and Engineering* **195** (2006), 2028–2049.

[83] Matthies, H. G. & Steindorf, J.: Strong coupling methods. In Wendland, W. L. & Efendiev, M. (eds.): *Analysis and Simulation of Multifield Problems*. Springer-Verlag, Berlin 2003, pp. 13–36.

[84] McLachlan, R. I. & Quispel, G. R. W.: Splitting methods. *Acta Numerica* **11** (2002), 341–434.

[85] Michler, C.; Hulshoff, S. J.; van Brummelen, E. H. & de Borst, R.: A monolithic approach to fluid-structure interaction. *Computers & Fluids* **33** (2004), 839–848.

[86] Michopoulos, J. G.; Farhat, C. & Fish, J.: Modeling and simulation of multiphysics systems. *Journal of Computing and Information Science in Engineering* **5** (2005), 198–213.

[87] Miehe, C.: *Zur numerischen Behandlung thermomechanischer Prozesse.* Technischer Bericht Nr. F88/6, Institut für Baumechanik und Numerische Mechanik, Universität Hannover 1988.

[88] Miranker, W. L.: *The Computational Theory of Stiff Differential Equations.* Publication Mathématique d'Orsay, No 219 – 7667, Université Paris XI, U. E. R. Mathématique, Orsay, France 1975.

[89] Mitchell, A. R. & Griffiths, D. F.: *The Finite Difference Method in Partial Differential Equations.* John Wiley & Sons, Chichester 1980.

[90] Mok, D. P.: *Partitionierte Lösungsansätze in der Strukturdynamik und der Fluid-Struktur-Interaktion.* Ph. D. thesis, Bericht Nr. 36, Institut für Baustatik, Universität Stuttgart 2001.

[91] Morand, H. & Ohayon, R.: *Fluid-Structure Interaction: Applied Numerical Methods.* John Wiley & Sons, Chichester 1995.

[92] Morton, K. W. & Mayers, D. F.: *Numerical Solution of Partial Differential Equations, An Introduction.* Cambridge University Press 2005.

[93] Newmark, N. M.: A method for computation of structural dynamics. *ASCE Journal of the Engineering Mechanics Division* **67**–**94** (1959), 85.

[94] Park, K. C.: Partitioned transient analysis procedures for coupled-field problems: Stability analysis. *Journal of Applied Mechanics* **47** (1980), 370–376.

[95] Park, K. C. & Felippa, C. A.: Partitioned analysis of coupled systems. In Belytschko, T. & Hughes, T. J. R. (eds.): *Computational Methods for Transient Analysis.* North-Holland, Amsterdam 1983, pp. 157–219.

[96] Park, K. C. & Felippa, C. A.: A variational framework for solution method developments in structural mechanics. *Journal of Applied Mechanics* **65** (1998), 242–249.

[97] Park, K. C. & Felippa, C. A.: A variational principle for the formulation of partitioned structural systems. *International Journal for Numerical Methods in Engineering* **47** (2000), 359–418.

[98] Park, K. C.; Felippa, C. A. & DeRuntz, J. A.: Stabilization of staggered solution procedures for fluid-structure interaction analysis. In Belytschko, T. & Geers, T. L. (eds.): *Computational Methods for Fluid-Structure Interaction Problems.* American Society of Mechanical Engineers (ASME), New York 1977, vol. AMD Vol. 26, pp. 95–124.

[99] Park, K. C.; Felippa, C. A. & Gumaste, U. A.: Localized version of the method of Lagrange multipliers and its applications. *Computational Mechanics* **24** (2000), 463–475.

[100] Park, K. C.; Felippa, C. A. & Ohayon, R.: Partitioned formulation of internal fluid-structure interaction problems via localized Lagrange multipliers. *Computer Methods in Applied Mechanics and Engineering* **190** (2001), 2989–3007.

[101] Park, K. C.; Ohayon, R.; Felippa, C. A. & Gonzaález, J. A.: Partitioned formulation of internal and gravity waves interacting with flexible structures. *Computer Methods in Applied Mechanics and Engineering* **199** (2010), 723–733.

[102] Pastor, M.; Li, T.; Liu, X.; Zienkiewicz, O. C. & Quecedo, M.: A fractional step algorithm allowing equal order of interpolation for coupled analysis of saturated soil problems. *Mechanics of Cohesive-frictional Materials* **5** (2000), 511–534.

[103] Peaceman, D. W. & Jr., H. H. R.: The numerical solution of parabolic and elliptic differential equations. *Journal of the Society of Industrial and Applied Mathematics* **3** (1955), 28–41.

[104] Piperno, S. & Farhat, C.: *Design and evaluation of staggered partitioned procedures for fluid-structure interaction simulations.* Rapport de recherche No. 3241, Institute National de Recherche en Informatique et en Automatique, Centre de recherche Sophia Antipolis 1997.

[105] Piperno, S. & Farhat, C.: Partitioned procedures for the transient solution of coupled aeroelastic problems – Part ii: an energy transfer analysis and three-dimensional applications. *Computer Methods in Applied Mechanics and Engineering* **190** (2001), 3147–3170.

[106] Piperno, S. & Farhat, C.: Treatment of acoustic fluid-structure interaction by localized Lagrange multipliers: Formulation. *Computer Methods in Applied Mechanics and Engineering* **197** (2008), 3057–3079.

[107] Pope, S. B.: *Turbulent Flows.* Cambridge University Press 2000.

[108] Press, W. H.; Teukolsky, S. A.; Vetterling, W. T. & Flannery, B. P.: *Numerical Recipes: The Art of Scientific Computing.* Cambridge University Press 2007, 3rd edn.

[109] Prevost, J. H.: Partitioned solution procedure for simultaneous integration of coupled-field problems. *Communications in Numerical Methods in Engineering* **13** (1997), 239–247.

[110] Prohl, A.: *Projection and Quasi-Compressibility Methods for Solving the Incompressible Navier-Stokes Equations.* Teubner, Stuttgart 1997.

[111] Quarteroni, A. & Valli, A.: *Domain Decomposition Methods for Partial Differential Equations.* Oxford Science Publications 1999.

[112] Rannacher, R.: Finite element methods for the incompressible Navier-Stokes equations. In Galdi, P.; Heywood, J. & Rannacher, R. (eds.): *Fundamental Directions in Mathematical Fluid Mechanics.* Birkhäuser, Basel 2000, pp. 191–293.

[113] Reese, S. & Govindjee, S.: Theoretical and numerical aspects in the thermo-viscoelastic material behaviour of rubber-like polymers. *Mechanics of Time-dependent Materials* **1** (1998), 357–396.

[114] Rifai, S. M.; Johan, Z.; Wang, W.-P.; Grisval, J.-P.; Hughes, T. J. R. & Ferencz, R. M.: Multiphysics simulation of flow-induced vibrations and aeroelasticity on parallel computing platforms. *Computer Methods in Applied Mechanics and Engineering* **173** (1999), 393–417.

[115] Rugonyi, S. & Bathe, K. J.: On the analysis of fully-coupled fluid flows with structural interactions – a coupling and condensation procedure. *International Journal for Computational Civil and Structural Engineering* **1** (2000), 29–41.

[116] Saetta, A. V. & Vitaliani, R. V.: Unconditionally convergent partitioned solution procedure for dynamic coupled mechanical systems. *International Journal for Numerical Methods in Engineering* **33** (1992), 1975–1996.

[117] Sanz-Serna, J. M.: Geometric integration. In Duff, I. S. & Watson, G. A. (eds.): *The State of the Art in Numerical Analysis.* Clarendon Press, Oxford 1997, pp. 121–143.

[118] Simo, J. C. & Miehe, C.: Associative coupled thermoplasticity at finite strains: Formulation, numerical analysis and implementation. *Computer Methods in Applied Mechanics and Engineering* **98** (1992), 41–104.

[119] Simoni, L. & Schrefler, B. A.: A staggered finite-element solution for water and gas flow in deforming porous media. *Communications in Applied Numerical Methods* **7** (1991), 213–223.

[120] Skelton, R. E.: *Dynamic Systems Control - Linear Systems Analysis and Synthesis.* John Wiley & Sons Inc., New York 1988.

[121] Sportisse, B.: An analysis of operator splitting techniques in the stiff case. *Journal of Computational Physics* **161** (2000), 140–168.

[122] Strang, G.: Accurate partial difference methods I: Linear Cauchy problems. *Archive for Rational Mechanics and Analysis* **12** (1963), 392–402.

[123] Strang, G.: On the construction and comparison of difference schemes. *SIAM Journal on Numerical Analysis* **5** (1968), 506–517.

[124] Thomas, J. W.: *Numerical Partial Differential Equations: Finite Difference Methods.* Springer-Verlag, Berlin 1998.

[125] Toro, E. F.: *Riemann Solvers and Numerical Methods for Fluid Dynamics: A Practical Introduction.* Springer-Verlag, Berlin 2009, 3rd edn.

[126] Toselli, A. & Widlund, O.: *Domain Decomposition Methods – Algorithms and Theory.* Springer-Verlag 2005.

[127] Turek, S.: A comparative study of time-stepping techniques for the incompressible Navier-Stokes equations: From fully implicit non-linear schemes to semi-implicit projection methods. *International Journal for Numerical Methods in Fluids* **22** (1996), 987–1011.

[128] Turska, E. & Schrefler, B. A.: On convergence conditions of partitioned solution procedures for consolidation problems. *Computer Methods in Applied Mechanics and Engineering* **106** (1993), 51–63.

[129] Van der Houwen, P. J. & Sommeijer, B. P.: Explicit Runge-Kutta (-Nystrom) methods with reduced phase errors for computing oscillating solutions. *SIAM Journal on Numerical Analysis* **24** (1987), 595–617.

[130] van Kan, J.: A second-order accurate pressure-correction scheme for viscous incompressible flow. *SIAM Journal on Scientific and Statistical Computing* **7** (1986), 870–891.

[131] Versteeg, H. & Malalasekra, W.: *An Introduction to Computational Fluid Dynamics: The Finite Volume Method.* Prentice Hall 2007, 2nd edn.

[132] Vijalapura, P. K. & Govindjee, S.: An adaptive hybrid time-stepping scheme for highly non-linear strongly coupled problems. *International Journal for Numerical Methods in Engineering* **64** (2005), 819–848.

[133] Vijalapura, P. K.; Strain, J. & Govindjee, S.: Fractional step methods for index-1 differential-algebraic equations. *Journal of Computational Physics* **203** (2005), 305–320.

[134] Wall, W. A.: *Fluid-Struktur-Interaktion mit stabilisierten Finiten Elementen.* Ph. D. thesis, Bericht Nr. 31, Institut für Baustatik, Universität Stuttgart 1999.

[135] Wall, W. A.; Genkinger, S. & Ramm, E.: A strong coupling partitioned approach for fluid-structure interaction with free surfaces. *Computers & Fluids* **36** (2007), 169–183.

[136] Whittaker, E. T. & Robinson, G.: *The Calculus of Observations: A Treatise on Numerical Mathematics.* Dover Publications, New York 1967, 4th edn.

[137] Wood, W. L.: *Practical Time Stepping Schemes.* Clarendon Press, Oxford 1990.

[138] Wrobel, L. C. & Aliabadi, M. H.: *The Boundary Element Method.* John Wiley & Sons, New Jersey 2002.

[139] Yanenko, N. N.: *The Method of Fractional Steps: The solution of problems of mathematical physics in several variables.* Springer-Verlag, New-York 1971.

[140] Zienkiewicz, O. C.; Huang, M.; Wu, J. & Wu, S.: A new algorithm for coupled soil-pore fluid problem. *Shock and Vibration* **1** (1993), 3–14.

[141] Zienkiewicz, O. C.; Paul, D. K. & Chan, A. H. C.: Unconditionally stable staggered solution procedure for soil-pore fluid interaction problems. *International Journal for Numerical Methods in Engineering* **26** (1988), 1039–1055.

[142] Zienkiewicz, O. C.; Qu, S.; Taylor, R. L. & Nakazawa, S.: The patch test for mixed formulations. *International Journal for Numerical Methods in Engineering* **23** (1986), 1873–1883.

[143] Zienkiewicz, O. C. & Taylor, R. L.: *The Finite Element Method. The Basis*, vol. 1. Butterworth Heinemann, Oxford 2000, 5th edn.

[144] Zienkiewicz, O. C. & Taylor, R. L.: *The Finite Element Method for Solid and Structural Mechanics.* Elsevier Butterworth-Heinemann 2005, 6th edn.

[145] Zienkiewicz, O. C.; Taylor, R. L. & Nithiarasu, P.: *The Finite Element Method for Fluid Dynamics.* Elsevier Butterworth-Heinemann 2005, 6th edn.

[146] Zienkiewicz, O. C.; Taylor, R. L. & Zhu, J. Z.: *The Finite Element Method: Its Basis and Fundamentals.* Elsevier Butterworth-Heinemann 2005, 6th edn.

# 2 Fundamentals of Volume-Coupled Formulations

SUMMARY

The objective of this chapter is to give a compact introduction into multi-field continuum mechanics by recourse to the general concepts of mixture and porous media theories, which naturally embrace a diversity of multi-physics phenomena. For this purpose, starting with some basics of the macroscopic mixture approach, the kinematics and the stress concept are reviewed, and the axiomatic conservation laws of thermodynamics and electrodynamics are presented within a combined framework.

## 2.1 Mixture and Porous Media Theories

From the last two examples of the previous chapter, it becomes clear that materially coupled problems with the coupling inherent in the governing multi-field equations may emerge in solids as well as in fluids and *a fortiori* in multiphasic materials constituted of both. Therefore, it suggests itself to start from a more general theoretical framework that allows to address solids and fluids solely or interacting together, additionally having the possibility to account for thermal, chemical, and electrical effects in a modular fashion. However, it is beyond the scope of this work to start from scratch and derive all concepts, theories, or constitutive laws from a microscopic level. It is rather envisaged to follow a macroscopic approach on a phenomenological basis without getting lost in the 'real' physics of the processes and material habits that are governed on the atomic, molecular, or some other lower scale.

### 2.1.1 The Macroscopic Mixture Approach

In the framework of continuum physics, a mixture $\varphi$ is understood as an idealized macroscopic model of superimposed continua of miscellaneous constituents $\varphi^\alpha$ without restriction to be solid, liquid, or gas [67]. Here, we limit the presentation to solid-fluid aggregates with the solid-phase forming some interconnected porous matrix or skeleton[1], whereas the intrinsic fluid (pore fluid) itself may be a real mixture of sundry components $\varphi^\beta$. Such fluid-saturated porous solids can very elegantly be treated by the Theory of Porous Media (TPM) [7, 19], where the material is represented as a *de facto* immiscible binary mixture of constituents $\varphi^S$ (solid skeleton) and $\varphi^F$ (pore-fluid mixture), which are assumed to be in a state of ideal disarrangement. Following this, the prescription of a real or a virtual averaging process over a representative elementary volume (REV) leads to a model $\varphi$ of

---

[1] Actually, we want to exclude suspensions of solid particles in a fluid. The cases of pure solid or fluid are however naturally included as special simplifications of the mixture model.
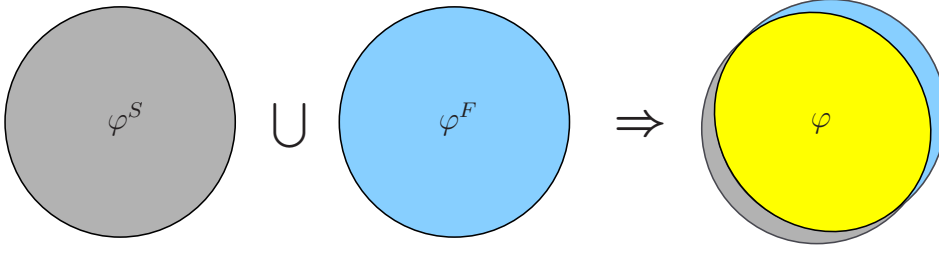
**Figure 2.1:** *The mixture $\varphi$ as superimposed continuum of constituents $\varphi^\alpha$ with $\alpha = \{S, F\}$.*

overlayed and interacting continua (Figure 2.1), viz.

$$\varphi = \bigcup_\alpha \varphi^\alpha = \varphi^S \cup \varphi^F \qquad \text{with} \qquad \varphi^F = \bigcup_\beta \varphi^\beta. \tag{2.1}$$

In the arising macroscopic model, the incorporated physical quantities are then understood as the local averages of their microscopic representatives. In this regard, note that also $\varphi^S$ may further be subdivided in the sense of mixture theories, for instance, if fixed charges or other attached reactive species are to be considered (cp. Chapter 5 and 7).

### 2.1.2 Volume Fractions, Saturation, and Density

In order to account for the local composition of the mixture, local volumetric ratios are introduced according to the concept of volume fractions. The volume $V$ of the overall medium $\mathcal{B}$ results from the sum of the partial volumes $V^\alpha$ of the constituent bodies $\mathcal{B}^\alpha$:

$$V = \int_\mathcal{B} \mathrm{d}v = \sum_\alpha V^\alpha \qquad \text{with} \qquad V^\alpha = \int_{\mathcal{B}^\alpha} \mathrm{d}v = \int_\mathcal{B} \mathrm{d}v^\alpha =: \int_\mathcal{B} n^\alpha \, \mathrm{d}v. \tag{2.2}$$

Following this, the volume fractions $n^\alpha$ of $\varphi^\alpha$ are defined as the local ratios of the partial volume elements $\mathrm{d}v^\alpha$ with respect to the volume element $\mathrm{d}v$ of the whole mixture $\varphi$:

$$n^\alpha := \frac{\mathrm{d}v^\alpha}{\mathrm{d}v}, \qquad \text{where} \qquad \begin{cases} n^S & : \text{solidity}, \\ n^F & : \text{porosity}. \end{cases} \tag{2.3}$$

As a further consequence of Equations (2.2), assuming fully saturated conditions, i.e., avoiding any vacant space within the porous medium, the saturation constraint yields

$$\sum_\alpha n^\alpha = n^S + n^F = 1 \qquad \text{with} \qquad n^F = \sum_\beta n^\beta, \tag{2.4}$$

where $n^\beta$ is the volume fraction of the not further specified components $\varphi^\beta$ of $\varphi^F$. Note that for some specific applications, where the pore fluid does not affect the mechanical properties of the porous medium, such as a pore gas in a stiff metal foam, an empty (non-saturated) solid matrix can be assumed, where $\varphi = \varphi^S$ yielding $\sum_\alpha n^\alpha = n^S < 1$.

In presence of a pore-fluid mixture, it is moreover convenient to introduce the saturation of a fluid component $\varphi^\beta$ as the quotient of its volume fraction and the porosity [32]:

$$s^\beta := \frac{n^\beta}{n^F}, \qquad \text{where} \qquad \sum_\beta s^\beta = 1. \tag{2.5}$$

Proceeding from the definition of the volume fractions (2.3), associated with each constituent $\varphi^\alpha$ is a material (realistic or effective) density $\rho^{\alpha R}$ defined as the local mass $\mathrm{d}m^\alpha$ of $\varphi^\alpha$ per unit of $\mathrm{d}v^\alpha$, and a partial density $\rho^\alpha$, where the local mass element $\mathrm{d}m^\alpha$ is related to the bulk volume element $\mathrm{d}v$. Moreover, the so-called mixture density can be introduced as the sum of the partial densities $\rho^\alpha$. In particular, the density functions read

$$\rho^{\alpha R} := \frac{\mathrm{d}m^\alpha}{\mathrm{d}v^\alpha}, \quad \rho^\alpha := \frac{\mathrm{d}m^\alpha}{\mathrm{d}v}, \quad \rho := \sum_\alpha \rho^\alpha, \quad \text{where} \quad \rho^\alpha = n^\alpha \rho^{\alpha R}. \tag{2.6}$$

Moreover, one finds for the pore-fluid mixture

$$\rho^{FR} = \sum_\beta s^\beta \rho^{\beta R} \quad \text{and} \quad \rho^F = \sum_\beta \rho^\beta \quad \text{with} \quad \rho^\beta = n^\beta \rho^{\beta R}. \tag{2.7}$$

According to Equations (2.6), it is obvious that the property of material incompressibility of a constituent $\varphi^\alpha$, defined by $\rho^{\alpha R} = \text{const.}$, does not lead to macroscopic incompressibility as the partial density $\rho^\alpha$, and thus, $\rho$ can still change through changes in the volume fractions $n^\alpha$.

Following the above, additional quantities can be introduced relevant for specific fields of application. For example, the local mass fraction $x_M^\alpha$ (or likewise $x_M^\beta$), which is used in phase-field models and chemical applications [8, 55], relates the constituent mass element to the bulk mass element:

$$x_M^\alpha := \frac{\mathrm{d}m^\alpha}{\mathrm{d}m}, \qquad \text{where} \qquad \sum_\alpha x_M^\alpha = 1. \tag{2.8}$$

Further chemical measures are the molar concentration $c_m^\beta$ given by the local amount of substance in moles $\mathrm{d}n_m^\beta$ per volume of pore-fluid mixture $\mathrm{d}v^F$ and the mole fraction $x_m^\beta$ as the amount of a fluid component $\varphi^\beta$ in solution, cf. Chapter 5 and [1, 20]:

$$c_m^\beta := \frac{\mathrm{d}n_m^\beta}{\mathrm{d}v^F}, \quad x_m^\beta := \frac{\mathrm{d}n_m^\beta}{\sum_\beta \mathrm{d}n_m^\beta} = \frac{c_m^\beta}{\sum_\beta c_m^\beta}, \quad \text{where} \quad \sum_\beta x_m^\beta = 1. \tag{2.9}$$

## 2.2 Kinematical Relations

### 2.2.1 Mixture Kinematics

Concerning the kinematics of mixtures, the idea of superimposed and interacting continua implies that, starting from different reference positions $\mathbf{X}_\alpha$ at time $t_0$, each constituent follows its individual Lagrangean motion function and has its own velocity and acceleration fields:

$$\mathbf{x} = \boldsymbol{\chi}_\alpha(\mathbf{X}_\alpha, t), \quad \overset{\prime}{\mathbf{x}}_\alpha = \frac{\mathrm{d}\boldsymbol{\chi}_\alpha(\mathbf{X}_\alpha, t)}{\mathrm{d}t}, \quad \overset{\prime\prime}{\mathbf{x}}_\alpha = \frac{\mathrm{d}^2\boldsymbol{\chi}_\alpha(\mathbf{X}_\alpha, t)}{\mathrm{d}t^2}. \tag{2.10}$$
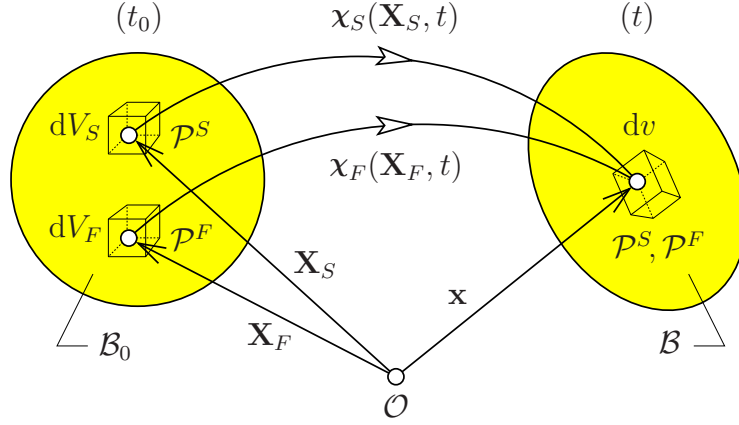
**Figure 2.2:** *Motion of a biphasic mixture.*

Following this, each spatial point $\mathbf{x}$ of the current configuration at time $t$ is simultaneously occupied by material points $\mathcal{P}^\alpha$ of both constituents (Figure 2.2)[2]. For the sake of convenience, the presentation is restricted to standard Boltzmann continua without equipping the individual material points with more than the classical three translational degrees of freedom (see also remark on Page 64).

Unique individual motions $\boldsymbol{\chi}_\alpha$ of the material points $\mathcal{P}^\alpha$ require the existence of unique inverse motion functions based on non-singular functional determinants (Jacobians) $J_\alpha$[3]:

$$\mathbf{X}_\alpha = \boldsymbol{\chi}_\alpha^{-1}(\mathbf{x}, t)\,, \quad \text{if} \quad J_\alpha := \det \frac{\partial \boldsymbol{\chi}_\alpha(\mathbf{X}_\alpha, t)}{\partial \mathbf{X}_\alpha} \neq 0\,. \tag{2.11}$$

Thus, using the inverse motion functions $\boldsymbol{\chi}_\alpha^{-1}$, the Eulerian description of the velocity and the acceleration fields from (2.10) are given by

$$\overset{\prime}{\mathbf{x}}_\alpha = \overset{\prime}{\mathbf{x}}_\alpha(\mathbf{x}, t)\,, \quad \overset{\prime\prime}{\mathbf{x}}_\alpha = \overset{\prime\prime}{\mathbf{x}}_\alpha(\mathbf{x}, t)\,. \tag{2.12}$$

Furthermore, by use of the mixture density $\rho$ from (2.6), the so-called mixture velocity $\dot{\mathbf{x}}$ describing the barycentric velocity of the overall medium and the diffusion velocity $\mathbf{d}_\alpha$ describing the relative velocity of $\varphi^\alpha$ with respect to $\varphi$ can be introduced as

$$\dot{\mathbf{x}} = \frac{1}{\rho} \sum_\alpha \rho^\alpha \overset{\prime}{\mathbf{x}}_\alpha\,, \quad \mathbf{d}_\alpha = \overset{\prime}{\mathbf{x}}_\alpha - \dot{\mathbf{x}} \quad \text{with} \quad \sum_\alpha \rho^\alpha \mathbf{d}_\alpha = \mathbf{0}\,. \tag{2.13}$$

In analogy, one finds for the pore-fluid mixture

$$\overset{\prime}{\mathbf{x}}_F = \frac{1}{\rho^F} \sum_\beta \rho^\beta \overset{\prime}{\mathbf{x}}_\beta\,, \quad \mathbf{d}_{\beta F} = \overset{\prime}{\mathbf{x}}_\beta - \overset{\prime}{\mathbf{x}}_F \quad \text{with} \quad \sum_\beta \rho^\beta \mathbf{d}_{\beta F} = \mathbf{0}\,, \tag{2.14}$$

---

[2] Concerning the notation, there is a break in the conventions declared on Page i. Following the tradition, the reference position vectors are denoted by capital letters defined as $\mathbf{X}_\alpha := \mathbf{x}_{0\alpha}$ with $(\,\boldsymbol{\cdot}\,)_{0\alpha}$ indicating an arbitrary initial state of the motion of $\varphi^\alpha$ at time $t_0$. Moreover, the common choice of capitals to indicate reference values is retained for line, area, and volume elements, e. g., $\mathrm{d}V_S := \mathrm{d}v_{0S}$ is the reference bulk volume element with respect to an initial (normally undeformed) solid state.

[3] Strictly speaking, the motion functions $\boldsymbol{\chi}_\alpha$ are supposed to be local diffeomorphisms, i. e., maps that are differentiable and have a differentiable inverse.

where $\mathbf{d}_{\beta F}$ is the diffusion velocity of the components within the moving pore-fluid mixture. In the above equations, $(\,\cdot\,)'_\alpha$ (and likewise $(\,\cdot\,)'_\beta$) indicates the material time derivative following the motion of $\varphi_\alpha$ (or $\varphi_\beta$) and $(\,\cdot\,)^{\displaystyle\cdot}$ denotes the material time derivative following the barycentric motion of the whole mixture $\varphi$ (mixture derivative). Suppose that $\varPsi$ and $\boldsymbol{\Psi}$ are arbitrary, steady and sufficiently steadily differentiable scalar- and vector-valued field functions. Then, the respective derivatives are computed as follows:

$$
\begin{aligned}
\overset{'}{\varPsi}_\alpha &= \frac{\mathrm{d}_\alpha \varPsi}{\mathrm{d}t} = \frac{\partial \varPsi}{\partial t} + \operatorname{grad}\varPsi \cdot \overset{'}{\mathbf{x}}_\alpha\,, \quad
\overset{'}{\boldsymbol{\Psi}}_\alpha = \frac{\mathrm{d}_\alpha \boldsymbol{\Psi}}{\mathrm{d}t} = \frac{\partial \boldsymbol{\Psi}}{\partial t} + (\operatorname{grad}\boldsymbol{\Psi})\,\overset{'}{\mathbf{x}}_\alpha\,, \\[2mm]
\dot{\varPsi} &= \frac{\mathrm{d}\varPsi}{\mathrm{d}t} = \frac{\partial \varPsi}{\partial t} + \operatorname{grad}\varPsi \cdot \dot{\mathbf{x}}\,, \quad
\dot{\boldsymbol{\Psi}} = \frac{\mathrm{d}\boldsymbol{\Psi}}{\mathrm{d}t} = \frac{\partial \boldsymbol{\Psi}}{\partial t} + (\operatorname{grad}\boldsymbol{\Psi})\,\dot{\mathbf{x}}\,.
\end{aligned}
\tag{2.15}
$$

Therein, the differential operator $\operatorname{grad}(\,\cdot\,) := \partial(\,\cdot\,)/\partial\mathbf{x}$ denotes the partial derivative with respect to the actual position vector $\mathbf{x}$.

In porous media theories, it is generally convenient to proceed from a Lagrangean description of the solid matrix via the solid displacement vector $\mathbf{u}_S$ as the primary kinematical variable. In contrast, according to Gibson *et al.* [25], the pore-fluid flow is better expressed in a modified Eulerian setting via the seepage velocity $\mathbf{w}_{FS}$ describing the fluid motion relative to the deforming skeleton. Moreover, relating $\mathbf{w}_{FS}$ only to the fluid part of the mixture, the so-called filter or superficial velocity $\mathbf{w}_F$ can be introduced. Thus,

$$
\mathbf{u}_S = \mathbf{x} - \mathbf{X}_S\,, \quad \mathbf{w}_{FS} = \mathbf{v}_F - \mathbf{v}_S \quad \text{with} \quad \mathbf{v}_\alpha := \overset{'}{\mathbf{x}}_\alpha\,, \quad \mathbf{w}_F = n^F \mathbf{w}_{FS}\,.
\tag{2.16}
$$

The movement of the fluid components $\varphi^\beta$ may likewise be expressed w.r.t. the motion of the fluid mixture via $\mathbf{d}_{\beta F}$ $(2.14)_2$ or analogously to $(2.16)_2$ w.r.t. the solid motion via

$$
\mathbf{w}_{\beta S} := \mathbf{v}_\beta - \mathbf{v}_S = \mathbf{d}_{\beta F} + \mathbf{w}_{FS}\,.
\tag{2.17}
$$

Given Equations $(2.10)_1$ and $(2.11)_1$, the material deformation gradients and their inverses are defined by

$$
\mathbf{F}_\alpha = \frac{\partial \mathbf{x}}{\partial \mathbf{X}_\alpha} =: \operatorname{Grad}_\alpha \mathbf{x}\,, \quad \mathbf{F}_\alpha^{-1} = \frac{\partial \mathbf{X}_\alpha}{\partial \mathbf{x}} = \operatorname{grad} \mathbf{X}_\alpha\,,
\tag{2.18}
$$

where the gradient operator $\operatorname{Grad}_\alpha(\,\cdot\,) := \partial(\,\cdot\,)/\partial\mathbf{X}_\alpha$ denotes the partial derivative w.r.t. the reference position vector $\mathbf{X}_\alpha$. Particularly, the solid deformation gradient $\mathbf{F}_S$, as a basic kinematical quantity, can be expressed in terms of the solid displacement using Equation $(2.16)_1$:

$$
\mathbf{F}_S = \frac{\partial \mathbf{x}}{\partial \mathbf{X}_S} = \operatorname{Grad}_S \mathbf{x} = \mathbf{I} + \operatorname{Grad}_S \mathbf{u}_S\,.
\tag{2.19}
$$

By virtue of (2.11), the existence of uniquely invertible motions requires non-zero Jacobians $J_\alpha$. Starting the deformation process from an undeformed (natural) state at time $t_0$, the initial condition $\mathbf{F}_\alpha(t_0) = \mathbf{I}$ restricts the domain of $\det \mathbf{F}_\alpha$ to positive values,

$$
\det \mathbf{F}_\alpha = J_\alpha > 0 \quad \text{with} \quad \det \mathbf{F}_\alpha(t_0) = 1\,.
\tag{2.20}
$$

Moreover, the assumption of solid incompressibility ($\rho^{SR} = \text{const.}$) implies that volumetric compression is only possible until the pore space is completely closed ($n^F = 0$). Therefore,

the lower limit of the finite volume dilatation $\mathrm{e}_{VS}$ of the solid matrix is predefined by the initial porosity $n_{0S}^F$, viz.

$$\mathrm{e}_{VS} = \frac{\mathrm{d}v - \mathrm{d}V_S}{\mathrm{d}V_S} = \det \mathbf{F}_S - 1 > -n_{0S}^F \,, \tag{2.21}$$

thus, directly yielding the stronger restriction

$$\det \mathbf{F}_S = J_S > n_{0S}^S \quad \text{with} \quad n_{0S}^S = 1 - n_{0S}^F \,. \tag{2.22}$$

Therein, the transport property, $\mathrm{d}v = (\det \mathbf{F}_S)\,\mathrm{d}V_S$, of $\det \mathbf{F}_S$ is used (cf. Equations (2.25)) describing the finite volume change of the reference volume element $\mathrm{d}V_S = \mathrm{d}v_{0S}$ to the volume element $\mathrm{d}v$ of the current configuration (Figure 2.2). Furthermore, $(\,\cdot\,)_{0S}$ indicates initial values with respect to an undeformed solid state at time $t_0$. In particular, $n_{0S}^S = \mathrm{d}V_S^S/\mathrm{d}V_S$ and $n_{0S}^F = \mathrm{d}V_S^F/\mathrm{d}V_S$ are the initial solidity and porosity consistent with the saturation constraint (2.4).

## 2.2.2 Deformation and Strain Measures

In the framework of a finite deformation theory of general fluid-saturated porous materials, where the constituents can exhibit intrinsic non-dissipative (elastic) as well as inelastic properties, it is common practice, particularly for the solid phase, to proceed from a local multiplicative split of the deformation gradient

$$\mathbf{F}_\alpha = \mathbf{F}_\alpha^{el}\,\mathbf{F}_\alpha^{in} \tag{2.23}$$

into an elastic part $\mathbf{F}_\alpha^{el}$ and an inelastic part $\mathbf{F}_\alpha^{in}$. In principle, $\mathbf{F}_\alpha^{in}$ may be used to describe any type of deformation-related dissipative process conceivable for the constituent $\varphi^\alpha$, such as viscosity [34, 44, 48, 58, 64], plasticity [5, 15, 16, 30, 39, 43], or even biological growth [40, 59] to name but a few. Basically, the multiplicative geometric concept can be phenomenologically introduced without insisting on somehow abstract and somewhat controversial interpretations. Instead, it can be understood as constitutive definition that will consequently yield a favorable structure of finite strain measures and their spatiotemporal derivatives.[4] The theoretical description of the inelastic processes is commonly accomplished by introducing internal state variables associated with $\mathbf{F}_\alpha^{in}$ [10, 68], which are nothing but additional fields that govern the inelastic evolution by some constitutive rate equations. Strictly speaking, in combination with, for instance, the momentum equation, this constitutes a coupled multi-field problem. However, for the rest of this chapter, we leave intrinsic inelastic properties aside and rather concentrate on multi-phase and multi-physics problems, where the dependent variables are commonly treated as primal unknowns to be determined from a conservation principle and do not just represent history variables that are treated by some collocation method on integration-point level.

To continue, we stay with the material deformation gradient $\mathbf{F}_\alpha$, which is known to be a mixed-variant, two-field or two-point tensor with identity metric in terms of a curvilinear

---

[4] Note that the multiplicative geometric concept was subject of diverse discussions before it became established [26, 29, 62]. In this regard, other authors follow different concepts, cf. [4, 51–53, 63].

(natural) basis[5]. This directly implies its special property of acting as a transport mechanism between configurations (cf. [21, Sec. III]). To show this, let us apply $\mathbf{F}_\alpha$ and $\mathbf{F}_\alpha^{-1}$ and their transposes as linear mappings to some covariant vectors $\boldsymbol{\Psi}_{ref}^\sharp$ and $\boldsymbol{\Psi}_{act}^\sharp$ as well as contravariant vectors $\boldsymbol{\Psi}_{ref}^\flat$ and $\boldsymbol{\Psi}_{act}^\flat$ of the reference and the actual configuration[6]:

$$
\boldsymbol{\Psi}_{ref}^\sharp \;\; \underset{\mathbf{F}_\alpha^{-1}}{\overset{\mathbf{F}_\alpha}{\rightleftharpoons}} \;\; \boldsymbol{\Psi}_{act}^\sharp \,, \qquad
\boldsymbol{\Psi}_{ref}^\flat \;\; \underset{\mathbf{F}_\alpha^{T}}{\overset{\mathbf{F}_\alpha^{T-1}}{\rightleftharpoons}} \;\; \boldsymbol{\Psi}_{act}^\flat \,.
\tag{2.24}
$$

The transformations $(2.24)_1$ and $(2.24)_2$ are commonly known as co- and contravariant *push-forward* (reference $\rightarrow$ actual) and *pull-back* (actual $\rightarrow$ reference) operations. Following this, the transport mechanisms of material line, oriented area, and scalar volume elements of $\varphi^\alpha$ can be formulated:

$$
\mathrm{d}\mathbf{x}_{(k)} = \mathbf{F}_\alpha \, \mathrm{d}\mathbf{X}_{\alpha(k)} \,,
$$
$$
\begin{aligned}
\mathrm{d}\mathbf{a}_{(k)} &= \mathrm{d}\mathbf{x}_{(l)} \times \mathrm{d}\mathbf{x}_{(m)} = (\mathbf{F}_\alpha \, \mathrm{d}\mathbf{X}_{(l)}) \times (\mathbf{F}_\alpha \, \mathrm{d}\mathbf{X}_{(m)}) \\
&= \tfrac{1}{2} \left( \mathbf{F}_\alpha \divideontimes \mathbf{F}_\alpha \right) (\mathrm{d}\mathbf{X}_{(l)} \times \mathrm{d}\mathbf{X}_{(m)}) = \mathrm{cof} \, \mathbf{F}_\alpha \, \mathrm{d}\mathbf{A}_{\alpha(k)} \,,
\end{aligned}
\tag{2.25}
$$
$$
\begin{aligned}
\mathrm{d}v &= (\mathrm{d}\mathbf{x}_{(k)} \times \mathrm{d}\mathbf{x}_{(l)}) \cdot \mathrm{d}\mathbf{x}_{(m)} = [(\mathbf{F}_\alpha \, \mathrm{d}\mathbf{X}_{(k)}) \times (\mathbf{F}_\alpha \, \mathrm{d}\mathbf{X}_{(l)})] \cdot (\mathbf{F}_\alpha \, \mathrm{d}\mathbf{X}_{(m)}) \\
&= \tfrac{1}{6} [(\mathbf{F}_\alpha \divideontimes \mathbf{F}_\alpha) \cdot \mathbf{F}_\alpha] (\mathrm{d}\mathbf{X}_{\alpha(k)} \times \mathrm{d}\mathbf{X}_{\alpha(l)}) \cdot \mathrm{d}\mathbf{X}_{\alpha(m)} = \det \mathbf{F}_\alpha \, \mathrm{d}V_\alpha \,.
\end{aligned}
$$

Herein, $\mathrm{d}\mathbf{X}_{\alpha(k)} := \mathrm{d}\mathbf{x}_{0\alpha(k)}$ and $\mathrm{d}\mathbf{x}_{(k)}$ as well as $\mathrm{d}\mathbf{A}_{\alpha(k)} := \mathrm{d}\mathbf{a}_{0\alpha(k)}$ and $\mathrm{d}\mathbf{a}_{(k)}$ denote the covariant line and the contravariant area elements of the reference and the actual configuration. Moreover,

$$
\mathrm{d}\mathbf{A}_{\alpha(k)} = \mathbf{n}_{0\alpha(k)} \, \mathrm{d}A_{\alpha(k)} \,, \quad \mathrm{d}\mathbf{a}_{(k)} = \mathbf{n}_{(k)} \, \mathrm{d}a_{(k)} \quad \textstyle\sum k
\tag{2.26}
$$

with $\mathrm{d}A_{\alpha(k)} := \mathrm{d}a_{0\alpha(k)}$ and $\mathrm{d}a_{(k)}$ as the scalar area elements, and $\mathbf{n}_{0\alpha(k)}$ and $\mathbf{n}_{(k)}$ as the corresponding reference and actual outward-oriented unit surface normals. Furthermore, use was made of the outer (double cross) tensor product of tensors $(\cdot) \divideontimes (\cdot)$, which allows a concise representation of cofactor tensors and of determinants [6], for instance,

$$
\mathrm{cof} \, \mathbf{F}_\alpha = \tfrac{1}{2} \left( \mathbf{F}_\alpha \divideontimes \mathbf{F}_\alpha \right), \quad \det \mathbf{F}_\alpha = \tfrac{1}{6} \left( \mathbf{F}_\alpha \divideontimes \mathbf{F}_\alpha \right) \cdot \mathbf{F}_\alpha \,.
\tag{2.27}
$$

Concerning the transport properties of the gradient operator, the following contravariant mechanisms are apparent [17]:

$$
\mathrm{Grad}_\alpha \Psi = \frac{\partial \Psi}{\partial \mathbf{X}_\alpha} \;\; \underset{\mathbf{F}_\alpha^{T}}{\overset{\mathbf{F}_\alpha^{T-1}}{\rightleftharpoons}} \;\; \frac{\partial \Psi}{\partial \mathbf{x}} = \mathrm{grad} \, \Psi \,,
$$
$$
\mathrm{Grad}_\alpha \boldsymbol{\Psi} = \frac{\partial \boldsymbol{\Psi}}{\partial \mathbf{X}_\alpha} \;\; \underset{(\mathbf{I} \otimes \mathbf{F}_\alpha^{T})^{\overset{23}{T}}}{\overset{(\mathbf{I} \otimes \mathbf{F}_\alpha^{T-1})^{\overset{23}{T}}}{\rightleftharpoons}} \;\; \frac{\partial \boldsymbol{\Psi}}{\partial \mathbf{x}} = \mathrm{grad} \, \boldsymbol{\Psi} \,.
\tag{2.28}
$$

---

[5] An arbitrary vector or tensor can be expressed with respect to a co- or contravariant (local) basis in a curvilinear frame, i. e., admits a co- and a contravariant representation. Here, in contrast to, e. g., [33, p. 35], vectors and tensors are called co- or contravariant depending on the variant type of the basis vectors included in the vectorial and tensorial components [6, 27].

[6] The identifiers $(\cdot)^\sharp$ and $(\cdot)^\flat$ are used to distinguish co- and contravariant vectors and tensors.

Herein, $(\,\cdot\,)^{\overset{kl}{T}}$ indicates an exchange of the $k$th and the $l$th basis vector included in the polyadic components of higher-order tensors.

Next, by means of $\mathbf{F}_\alpha$ as the basic kinematical quantity, the right and left Cauchy-Green deformation tensors are defined as usual:

$$\mathbf{C}_\alpha = \mathbf{F}_\alpha^T\,\mathbf{F}_\alpha\,, \quad \mathbf{B}_\alpha = \mathbf{F}_\alpha\,\mathbf{F}_\alpha^T\,. \tag{2.29}$$

The corresponding inverse relations read

$$\mathbf{C}_\alpha^{-1} = \mathbf{F}_\alpha^{-1}\,\mathbf{F}_\alpha^{T-1}\,, \quad \mathbf{B}_\alpha^{-1} = \mathbf{F}_\alpha^{T-1}\,\mathbf{F}_\alpha^{-1}\,. \tag{2.30}$$

Given the definitions for the contravariant Green-Lagrangean and Almansian strains[7], one obtains

$$\mathbf{E}_\alpha = \tfrac{1}{2}\,(\mathbf{C}_\alpha - \mathbf{I}) \quad \underset{(\mathbf{F}_\alpha^T \otimes \mathbf{F}_\alpha^T)^{\overset{23}{T}}}{\overset{(\mathbf{F}_\alpha^{T-1} \otimes \mathbf{F}_\alpha^{T-1})^{\overset{23}{T}}}{\rightleftarrows}} \quad \tfrac{1}{2}\,(\mathbf{I} - \mathbf{B}_\alpha^{-1}) = \mathbf{A}_\alpha\,. \tag{2.31}$$

Analogously, the covariant Karni-Reiner strain tensors can be introduced by definition[8]:

$$\overset{R}{\mathbf{K}}_\alpha = \tfrac{1}{2}\,(\mathbf{I} - \mathbf{C}_\alpha^{-1}) \quad \underset{(\mathbf{F}_\alpha^{-1} \otimes \mathbf{F}_\alpha^{-1})^{\overset{23}{T}}}{\overset{(\mathbf{F}_\alpha \otimes \mathbf{F}_\alpha)^{\overset{23}{T}}}{\rightleftarrows}} \quad \tfrac{1}{2}\,(\mathbf{B}_\alpha - \mathbf{I}) = \mathbf{K}_\alpha\,. \tag{2.32}$$

In order to formulate rate equations, time derivatives of the introduced deformation and strain measures are required. To begin with, the material velocity gradient is given as

$$(\mathbf{F}_\alpha)'_\alpha = \frac{\mathrm{d}_\alpha}{\mathrm{d}t}\left(\frac{\partial \mathbf{x}}{\partial \mathbf{X}_\alpha}\right) = \frac{\partial \mathbf{v}_\alpha}{\partial \mathbf{X}_\alpha} = \mathrm{Grad}_\alpha \mathbf{v}_\alpha \tag{2.33}$$

and the corresponding spatial velocity gradient is defined by

$$\mathbf{L}_\alpha := \mathrm{grad}\,\mathbf{v}_\alpha = \frac{\partial \mathbf{v}_\alpha}{\partial \mathbf{x}} = \frac{\partial \mathbf{v}_\alpha}{\partial \mathbf{X}_\alpha}\frac{\partial \mathbf{X}_\alpha}{\partial \mathbf{x}} = (\mathbf{F}_\alpha)'_\alpha\,\mathbf{F}_\alpha^{-1}\,. \tag{2.34}$$

By use of $\mathbf{L}_\alpha$, the material time derivatives of the infinitesimal line, area, and volume elements given in Equations (2.25) take the compact form

$$(\mathrm{d}\mathbf{x})'_\alpha = \mathbf{L}_\alpha\,\mathrm{d}\mathbf{x}\,, \quad (\mathrm{d}\mathbf{a})'_\alpha = (\mathbf{L}_\alpha \divideontimes \mathbf{I})\,\mathrm{d}\mathbf{a}\,, \quad (\mathrm{d}v)'_\alpha = (\mathbf{L}_\alpha \cdot \mathbf{I})\,\mathrm{d}v\,. \tag{2.35}$$

The symmetric and skew-symmetric parts of $\mathbf{L}_\alpha$, commonly termed stretching or deformation rate tensor and spin or vorticity tensor, read

$$\mathbf{D}_\alpha = \tfrac{1}{2}\,(\mathbf{L}_\alpha + \mathbf{L}_\alpha^T) = \mathbf{D}_\alpha^T\,, \quad \mathbf{W}_\alpha = \tfrac{1}{2}\,(\mathbf{L}_\alpha - \mathbf{L}_\alpha^T) = -\mathbf{W}_\alpha^T\,. \tag{2.36}$$

---

[7] From the common definition by the differences of squares of line elements, e.g., with the squared lengths of the actual and reference line elements $\mathrm{d}s^2 = \mathrm{d}\mathbf{x} \cdot \mathrm{d}\mathbf{x}$ and $\mathrm{d}S_\alpha^2 = \mathrm{d}\mathbf{X}_\alpha \cdot \mathrm{d}\mathbf{X}_\alpha$, one finds

$$\mathrm{d}s^2 - \mathrm{d}S_\alpha^2 = (\mathbf{F}_\alpha\,\mathrm{d}\mathbf{X} \cdot \mathbf{F}_\alpha\,\mathrm{d}\mathbf{X} - \mathrm{d}\mathbf{X} \cdot \mathrm{d}\mathbf{X}) = \mathrm{d}\mathbf{X} \cdot (\mathbf{F}_\alpha^T\,\mathbf{F}_\alpha - \mathbf{I})\,\mathrm{d}\mathbf{X} = \mathrm{d}\mathbf{X} \cdot (2\,\mathbf{E}_\alpha)\,\mathrm{d}\mathbf{X}$$
$$= (\mathrm{d}\mathbf{x} \cdot \mathrm{d}\mathbf{x} - \mathbf{F}_\alpha^{-1}\,\mathrm{d}\mathbf{x} \cdot \mathbf{F}_\alpha^{-1}\,\mathrm{d}\mathbf{x}) = \mathrm{d}\mathbf{x} \cdot (\mathbf{I} - \mathbf{F}_\alpha^{T-1}\,\mathbf{F}_\alpha^{-1})\,\mathrm{d}\mathbf{x} = \mathrm{d}\mathbf{x} \cdot (2\,\mathbf{A}_\alpha)\,\mathrm{d}\mathbf{x}\,.$$

[8] Commonly, based on the polar decomposition of the solid material deformation gradient, they are introduced by the differences of squares of rotated line elements. Alternatively, this second family of strain tensors can also be motivated through the differences of squares of weighted vectorial area elements [31].

In this regard, it can be shown that the deformation velocity tensor $\mathbf{D}_\alpha$ admits a co- and a contravariant representation in the frame of convected curvilinear coordinates (cf. e. g. [47]), which by implication means that the material time derivative acts only on the time-dependent metric coefficients but not on the natural basis vectors. Accordingly, it holds

$$\mathbf{D}_\alpha = -\tfrac{1}{2}\,\mathbf{F}_\alpha\,(\mathbf{C}_\alpha^{-1})'_\alpha\,\mathbf{F}_\alpha^T = \tfrac{1}{2}\,\mathbf{F}_\alpha^{T-1}\,(\mathbf{C}_\alpha)'_\alpha\,\mathbf{F}_\alpha^{-1}\,. \tag{2.37}$$

The above motivates the introduction of a special class of *objective* time derivatives. In continuum mechanics, the most familiar is the *convective* or Oldroyd derivative [56], which applied to a tensor field is essentially its Lie derivative along the velocity vector [35, 69]. The procedure is to compute a pull-back to the reference configuration, take the material time derivative, and push-forward the result back to the actual configuration. Thus, one defines the *lower* (covariant) and the *upper* (contravariant) Lie or Oldroyd derivatives via

$$
\begin{aligned}
(\,\cdot\,)^\triangledown_\alpha &:= \mathcal{L}_{\mathbf{v}_\alpha}(\,\cdot\,)^\sharp = \mathbf{F}_\alpha\left(\frac{\mathrm{d}_\alpha}{\mathrm{d}t}\big[\mathbf{F}_\alpha^{-1}(\,\cdot\,)\,\mathbf{F}_\alpha^{T-1}\big]\right)\mathbf{F}_\alpha^T = (\,\cdot\,)'_\alpha - \mathbf{L}_\alpha\,(\,\cdot\,) - (\,\cdot\,)\,\mathbf{L}_\alpha^T\,, \\
(\,\cdot\,)^\triangle_\alpha &:= \mathcal{L}_{\mathbf{v}_\alpha}(\,\cdot\,)^\flat = \mathbf{F}_\alpha^{T-1}\left(\frac{\mathrm{d}_\alpha}{\mathrm{d}t}\big[\mathbf{F}_\alpha^T(\,\cdot\,)\,\mathbf{F}_\alpha\big]\right)\mathbf{F}_\alpha^{-1} = (\,\cdot\,)'_\alpha + \mathbf{L}_\alpha^T\,(\,\cdot\,) + (\,\cdot\,)\,\mathbf{L}_\alpha\,.
\end{aligned}
\tag{2.38}
$$

In essence, the lower and upper Lie time derivatives are material time derivatives of the tensorial components while keeping the co- and contravariant tensorial bases fixed. Thus, it is obvious that the Lie time derivative of a scalar field $\Psi(\mathbf{x}, t)$ coincides with the material time derivative, i. e., $(\Psi)^\triangledown_\alpha = (\Psi)^\triangle_\alpha = (\Psi)'_\alpha$.

Applying the Lie time derivative to the Karni-Reiner and Almansian strains, it is easily concluded that

$$(\mathbf{K}_\alpha)^\triangledown_\alpha = \mathbf{D}_\alpha\,, \quad (\mathbf{A}_\alpha)^\triangle_\alpha = \mathbf{D}_\alpha\,. \tag{2.39}$$

Then, consistent with the co- and contravariant transport mechanisms, the corresponding strain rates of the reference configuration read

$$(\overset{\mathrm{R}}{\mathbf{K}}_\alpha)'_\alpha = -\tfrac{1}{2}\,(\mathbf{C}_\alpha^{-1})'_\alpha\,, \quad (\mathbf{E}_\alpha)'_\alpha = \tfrac{1}{2}\,(\mathbf{C}_\alpha)'_\alpha\,. \tag{2.40}$$

A further convective time derivative that accounts for volume changes is given by the so-called *flux derivative*. It is of major importance for the treatment of the surface balances required in elastodynamics. It is easily derived by regarding the temporal change of a flux of a partial vector field $\boldsymbol{\Psi}^\alpha(\mathbf{x}, t)$ through the material surface $\mathcal{S}$ of $\varphi$:

$$\frac{\mathrm{d}_\alpha}{\mathrm{d}t}\int_\mathcal{S}\boldsymbol{\Psi}^\alpha\cdot\mathrm{d}\mathbf{a} = \int_\mathcal{S}\frac{\mathrm{d}_\alpha}{\mathrm{d}t}(\boldsymbol{\Psi}^\alpha\cdot\mathrm{d}\mathbf{a}) = \int_\mathcal{S}\big[(\boldsymbol{\Psi}^\alpha)'_\alpha\cdot\mathrm{d}\mathbf{a} + \boldsymbol{\Psi}^\alpha\cdot(\mathrm{d}\mathbf{a})'_\alpha\big]\,. \tag{2.41}$$

With the material time derivative of the oriented area element $(2.35)_2$ and the identity

$$\mathbf{L}_\alpha \mathbin{\text{\Large※}} \mathbf{I} = (\mathbf{L}_\alpha\cdot\mathbf{I})\,\mathbf{I} - \mathbf{L}_\alpha^T\,, \quad\text{where}\quad \mathbf{L}_\alpha\cdot\mathbf{I} = \operatorname{div}\mathbf{v}_\alpha\,, \tag{2.42}$$

one directly obtains

$$\frac{\mathrm{d}_\alpha}{\mathrm{d}t}\int_\mathcal{S}\boldsymbol{\Psi}^\alpha\cdot\mathrm{d}\mathbf{a} = \int_\mathcal{S}(\boldsymbol{\Psi}^\alpha)^*_\alpha\cdot\mathrm{d}\mathbf{a} \quad\text{with}\quad (\boldsymbol{\Psi}^\alpha)^*_\alpha := (\boldsymbol{\Psi}^\alpha)'_\alpha + \boldsymbol{\Psi}^\alpha\operatorname{div}\mathbf{v}_\alpha - (\operatorname{grad}\mathbf{v}_\alpha)\,\boldsymbol{\Psi}^\alpha \tag{2.43}$$

being the flux derivative. Alternate representations of $(\boldsymbol{\Psi}^\alpha)^*_\alpha$ can be obtained by expanding the material time derivative $(\boldsymbol{\Psi}^\alpha)'_\alpha$ according to $(2.15)_2$, extend the equation by $\mathbf{v}_\alpha \operatorname{div} \boldsymbol{\Psi}^\alpha$, and exploit the following rule for the rotation operator:

$$-\operatorname{rot}(\mathbf{b} \times \mathbf{a}) = \mathbf{a} \operatorname{div} \mathbf{b} + (\operatorname{grad} \mathbf{a})\,\mathbf{b} - \mathbf{b} \operatorname{div} \mathbf{a} - (\operatorname{grad} \mathbf{b})\,\mathbf{a}\,. \qquad (2.44)$$

In particular, we have

$$
\begin{aligned}
(\boldsymbol{\Psi}^\alpha)^*_\alpha &= \frac{\partial \boldsymbol{\Psi}^\alpha}{\partial t} + (\operatorname{grad} \boldsymbol{\Psi}^\alpha)\,\mathbf{v}_\alpha + \boldsymbol{\Psi}^\alpha \operatorname{div} \mathbf{v}_\alpha - (\operatorname{grad} \mathbf{v}_\alpha)\,\boldsymbol{\Psi}^\alpha \\
&= \frac{\partial \boldsymbol{\Psi}^\alpha}{\partial t} + (\operatorname{grad} \boldsymbol{\Psi}^\alpha)\,\mathbf{v}_\alpha + \boldsymbol{\Psi}^\alpha \operatorname{div} \mathbf{v}_\alpha - (\operatorname{grad} \mathbf{v}_\alpha)\,\boldsymbol{\Psi}^\alpha + \mathbf{v}_\alpha \operatorname{div} \boldsymbol{\Psi}^\alpha - \mathbf{v}_\alpha \operatorname{div} \boldsymbol{\Psi}^\alpha \\
&= \frac{\partial \boldsymbol{\Psi}^\alpha}{\partial t} + \mathbf{v}_\alpha \operatorname{div} \boldsymbol{\Psi}^\alpha - \operatorname{rot}(\mathbf{v}_\alpha \times \boldsymbol{\Psi}^\alpha)\,.
\end{aligned}
$$
$$(2.45)$$

In terms of mixture quantities, one obtains analogously

$$\frac{\mathrm{d}}{\mathrm{d}t} \int_{\mathcal{S}} \boldsymbol{\Psi} \cdot \mathrm{d}\mathbf{a} = \int_{\mathcal{S}} \overset{*}{\boldsymbol{\Psi}} \cdot \mathrm{d}\mathbf{a} \quad \text{with} \quad \overset{*}{\boldsymbol{\Psi}} = \begin{cases} \dot{\boldsymbol{\Psi}} + \boldsymbol{\Psi} \operatorname{div} \dot{\mathbf{x}} - (\operatorname{grad} \dot{\mathbf{x}})\,\boldsymbol{\Psi}\,, \\ \dfrac{\partial \boldsymbol{\Psi}}{\partial t} + \dot{\mathbf{x}} \operatorname{div} \boldsymbol{\Psi} - \operatorname{rot}(\dot{\mathbf{x}} \times \boldsymbol{\Psi})\,. \end{cases} \qquad (2.46)$$

## 2.3　Some Aspects of Electrodynamics

Hitherto, we just introduced some basic quantities and notions of mixture and porous media mechanics, which would be sufficient to continue with the stress concept and the thermodynamical balance laws. However, we started with the objective to provide a more general framework of volume-coupled formulations, which also consider electromagnetic phenomena. Obviously, this makes it necessary to introduce additional fields and notions of electrodynamics before continuing with a universal representation of conservation principles.

### 2.3.1　Preliminaries

Electrodynamics is a classical field theory dealing with electromagnetic phenomena, which in contrast to Newtonian mechanics is consistent with the theory of relativity. The modern form of electrodynamics is based on the four equations formulated in 1864 by and named after the Scottish physicist James Clerk Maxwell [50], from which all electromagnetic effects can be deduced. The additional Lorentz-force equation formally establishes the link between electrodynamics and mechanics. In principle, Maxwell's equations are valid in vacuum as well as in matter of any kind. When dealing with electrodynamics in continuous media, which naturally imply a huge number of charged particles over several atomic length scales, such as bound electrons, protons, and neutrons plus freely moving charges, it is sensible to proceed from reformulated Maxwell's equations in terms of macroscopic fields, see, e.g., the classical article by Lorentz [46].

The macroscopic electromagnetic theory is based on a spatial averaging procedure, which guarantees that, on the one hand, atomic fluctuations are averaged out and, on the other

hand, the interesting spatial dependencies on the macro scale remain unaffected. For an arbitrary microscopic field quantity $\mathbf{a}_m(\mathbf{x}, t)$, the averaging can be carried out by [49][9]

$$\mathbf{A} = \langle \mathbf{a}_m \rangle := \int \mathbf{a}_m \, f_m \, \mathrm{d}v_m \,, \quad \text{where} \quad \begin{cases} \dfrac{\partial \langle \mathbf{a}_m \rangle}{\partial t} = \left\langle \dfrac{\mathrm{d}_m \mathbf{a}_m}{\mathrm{d}t} \right\rangle , \\[2ex] \operatorname{grad} \langle \mathbf{a}_m \rangle = \langle \operatorname{grad} \mathbf{a}_m \rangle . \end{cases} \quad (2.47)$$

Herein, $f_m$ is a statistical distribution function of point-like particles of electric charge and $\mathrm{d}v_m$ is the microscopic volume element (fluxion or phase-space element) such that $f_m \, \mathrm{d}v_m$ represents the probability of finding the particle system in $\mathrm{d}v_m$. Moreover, the averaging $\langle ( \cdot ) \rangle$ commutes with the spatial and temporal derivatives, where $\mathrm{d}_m( \cdot )/\mathrm{d}t$ is a total time derivative in the sense of statistical mechanics. Following this, in Table 2.1, we introduce the macroscopic fields obtained through averaging from their atomic representatives.

**Table 2.1:** *Macroscopic electromagnetic quantities.*

| Symbol | Unit[10] | Name |
|---|---|---|
| $\rho_e$ | $\mathrm{C/m^3}$ | electric charge density |
| $\mathbf{E}$ | $\mathrm{V/m}$ | electric field strength vector |
| $\mathbf{B}$ | $\mathrm{V\,s/m^2}$ | magnetic induction field vector (magnetic flux) |
| $\mathbf{D}$ | $\mathrm{C/m^2}$ | electric displacement vector (charge potential) |
| $\mathbf{H}$ | $\mathrm{A/m}$ | magnetic field strength vector (current potential) |
| $\mathbf{J}$ | $\mathrm{A/m^2}$ | electric current density vector |
| $\mathbf{P}$ | $\mathrm{C/m^2}$ | mean polarization field vector |
| $\mathbf{M}$ | $\mathrm{A/m}$ | mean (Minkowski) magnetization field vector |

In this context, it can further be shown [49] that the following relationships hold:

$$\mathbf{D} = \epsilon_0 \, \mathbf{E} + \mathbf{P} \,, \quad \mathbf{H} = \frac{1}{\mu_0} \, \mathbf{B} - \mathbf{M} \,, \quad (2.48)$$

where $\epsilon_0$ and $\mu_0$ represent universal constants, namely the permittivity and the permeability of free space (vacuum)[11]. Moreover, $\mathbf{P}$ and $\mathbf{M}$ describe the neutral charge and current density distributions bound in the material, and thus, represent matter-dependent macroscopic quantities, which are related to the fields $\mathbf{E}$ and $\mathbf{B}$ via phenomenological material equations. For instance, proceeding from isotropic and homogeneous properties and further disregarding hysteretic effects as they are observed for ferroelectric and ferromagnetic materials, the following approximate linear relations are valid:

$$\mathbf{P} = \epsilon_0 \, \chi_e \, \mathbf{E} \,, \quad \mathbf{M} = \chi_m \, \mathbf{H} \quad \longrightarrow \quad \mathbf{D} = \epsilon \, \mathbf{E} \,, \quad \mathbf{B} = \mu \, \mathbf{H} \,. \quad (2.49)$$

---

[9] In view of the common notation in continuum electrodynamics, the macroscopic vector fields obtained through averaging will be indicated by boldface small capitals.

[10] Besides the SI base unit Ampère A, the coherent SI derived units Coulomb $\mathrm{C = A\,s}$ and Volt $\mathrm{V = kg\,m^2/A\,s^3}$ have been used. Please note that all electromagnetic quantities and equations in this work are given in the rationalized MKS (meter-kilogram-second) system of units [9].

[11] In particular, $\epsilon_0 = 8.854187817... \cdot 10^{-12} \, \mathrm{C/V\,m}$ and $\mu_0 = 4\,\pi \cdot 10^{-7} \, \mathrm{kg\,m/A^2\,s^2}$.

Herein, $\chi_e$ and $\chi_m$ are the electric and magnetic suspectibilities, $\epsilon = \epsilon_0 (1 + \chi_e)$ is the permittivity and $\mu = \mu_0 (1 + \chi_m)$ the permeability. A further celebrated phenomenological relation for isotropic conductors is given by Ohm's law

$$\mathbf{J} = \sigma \, \mathbf{E} \tag{2.50}$$

with $\sigma$ in A/V m representing the electrical conductivity or specific conductance.

## 2.3.2 The Macroscopic Maxwell Equations

The four macroscopic Maxwell equations are formulated in the averaged macroscopic fields of Table 2.1 and obey a similar structure as their microscopic counterparts. It should however be noted that they are phenomenological inspired rather than of fundamental nature. In particular, they read:

$$
\begin{aligned}
\operatorname{div} \mathbf{D} &= \rho_e & &: \text{Gauss's law (Gauss's flux theorem),}\\[4pt]
\operatorname{div} \mathbf{B} &= 0 & &: \text{Gauss's law for magnetism,}\\[4pt]
\operatorname{rot} \mathbf{E} &= -\frac{\partial \mathbf{B}}{\partial t} & &: \text{Maxwell-Faraday equation (Faraday's law of induction),}\\[4pt]
\operatorname{rot} \mathbf{H} &= \mathbf{J} + \frac{\partial \mathbf{D}}{\partial t} & &: \text{Maxwell-Ampère equation (corrected Ampère's law).}
\end{aligned}
\tag{2.51}
$$

From the above equations, one easily derives the principle of charge conservation. To this end, take the divergence of Ampère's law $(2.51)_4$, exploit the identity $\operatorname{div} \operatorname{rot} \mathbf{H} = 0$, and substitute the Gauss's law $(2.51)_1$ to obtain the continuity equation

$$\operatorname{div} \mathbf{J} = -\frac{\partial \rho_e}{\partial t} \qquad : \text{conservation of charge.} \tag{2.52}$$

In order to be able to formulate a general system of balance equations relative to inertial frames, Galilean invariance must be regarded as a fundamental requirement [60]. In fact, the thermodynamical balance laws in the sense of Newtonian mechanics are Galilean invariant as they admit the same expression in any co-moving frame, say $\{\overline{\mathbf{x}}, \overline{t}\}$, related to an inertial reference frame $\{\mathbf{x}, t\}$ by a Galilean transformation given through

$$\overline{\mathbf{x}} = \mathbf{Q}_0 \, \mathbf{x} + \mathbf{v}_0 \, t + \mathbf{c}_0 \,, \quad \overline{t} = t \,. \tag{2.53}$$

Herein, $\mathbf{Q}_0$ is a constant proper orthogonal tensor (rotation tensor), $\mathbf{v}_0$ a constant non-relativistic velocity, and $\mathbf{c}_0$ some constant vector. Basically, the requirement of Galilean invariance imposes a specific dependence of the flux and supply terms on the velocity field [45]. Now, verifying the macroscopic electromagnetic quantities in respect of (2.53), it can be shown that $\mathbf{B}, \mathbf{D}, \mathbf{P}$, and $\rho_e$ fulfill the invariance requirement but the others do not [41]. Suppose $\dot{\mathbf{x}}$ to be the velocity of a moving continuum representing a Galilean frame according to (2.53). Then, with $\mathbf{v}_0 = -\dot{\mathbf{x}}$, one obtains the remaining electromagnetic quantities in a proper co-moving reference frame as

$$
\begin{aligned}
\boldsymbol{\mathcal{E}} &= \mathbf{E} + \dot{\mathbf{x}} \times \mathbf{B} & &: \text{electromotive intensity vector,}\\[4pt]
\boldsymbol{\mathcal{H}} &= \mathbf{H} - \dot{\mathbf{x}} \times \mathbf{D} & &: \text{magnetomotive intensity vector,}\\[4pt]
\boldsymbol{\mathcal{J}} &= \mathbf{J} - \rho_e \, \dot{\mathbf{x}} & &: \text{conduction current density vector,}\\[4pt]
\boldsymbol{\mathcal{M}} &= \mathbf{M} + \dot{\mathbf{x}} \times \mathbf{P} & &: \text{Lorentz magnetization field vector.}
\end{aligned}
\tag{2.54}
$$

Herein, in the conduction current $(2.54)_3$, $\rho_e \, \dot{\mathbf{x}}$ is commonly termed convection current density. Following this, in order to have Maxwell's equations Galilean invariant, $(2.51)_{3,4}$ and the charge conservation (2.52) are rewritten in terms of (2.54) and the flux derivative (2.46) yielding

$$
\begin{aligned}
\operatorname{rot} \boldsymbol{\mathcal{E}} &= -\overset{*}{\mathbf{B}} \,, \\
\operatorname{rot} \boldsymbol{\mathcal{H}} &= \boldsymbol{\mathcal{J}} + \overset{*}{\mathbf{D}} \,, \\
\operatorname{div} \boldsymbol{\mathcal{J}} &= -\dot{\rho}_e - \rho_e \operatorname{div} \dot{\mathbf{x}} \,.
\end{aligned}
\tag{2.55}
$$

### 2.3.3 Fusion of Electrodynamics and Thermodynamics

As long as our considerations are restricted to terrestrial problems, it is not a serious limitation to assume the involved velocity fields to be much smaller than the speed of light since macroscopic ponderable bodies cannot be accelerated to relativistic speeds. Thus, proceeding from non-relativistic mechanics, the fusion of the thermodynamic and electrodynamic balance laws can be carried out equivalently in three different ways [23, 41]:

(1) *Continuum-like approach:* Consider the electromagnetic effects as an action from the distance in analogy to gravitation.

(2) *Relativistic approach:* Consider electromagnetic fields to exhibit inertia and contact actions.

(3) *Alternate approach:* Assume electromagnetic fields to produce surface and volume forces but not inertia.

Here, we will follow the continuum-like way of linking the electromagnetic relations to the thermomechanical equations. To this end, it is necessary to introduce the respective electromagnetic force, couple, and energy, which will later represent the supply and source terms in the combined set of general balance equations. Without presenting the derivation, they read (consult Eringen & Maugin [23] for details):

- Electromagnetic force density (electromagnetic body force):

$$
\begin{aligned}
\mathbf{b}_e &= \rho_e \, \mathbf{E} + \mathbf{J} \times \mathbf{B} + (\operatorname{grad} \mathbf{E}) \, \mathbf{P} + (\operatorname{grad} \mathbf{B}) \, \mathbf{M} + \operatorname{div}[(\mathbf{P} \times \mathbf{B}) \otimes \dot{\mathbf{x}}] + \frac{\partial}{\partial t}(\mathbf{P} \times \mathbf{B}) \\
&= \rho_e \, \boldsymbol{\mathcal{E}} + (\boldsymbol{\mathcal{J}} + \overset{*}{\mathbf{P}}) \times \mathbf{B} + (\operatorname{grad} \boldsymbol{\mathcal{E}}) \, \mathbf{P} + (\operatorname{grad} \mathbf{B}) \, \boldsymbol{\mathcal{M}} \,.
\end{aligned}
\tag{2.56}
$$

- Electromagnetic momentum couple density:

$$
\begin{aligned}
\mathbf{c}_e &= \mathbf{P} \times \mathbf{E} + \mathbf{M} \times \mathbf{B} + \dot{\mathbf{x}} \times (\mathbf{P} \times \mathbf{B}) \\
&= \mathbf{P} \times \boldsymbol{\mathcal{E}} + \boldsymbol{\mathcal{M}} \times \mathbf{B} \,.
\end{aligned}
\tag{2.57}
$$

- Total electromagnetic energy:

$$
\begin{aligned}
\varepsilon_e &= \mathbf{J} \cdot \mathbf{E} + \frac{\partial \mathbf{P}}{\partial t} \cdot \mathbf{E} - \mathbf{M} \cdot \frac{\partial \mathbf{B}}{\partial t} + \operatorname{div}[\dot{\mathbf{x}} \, (\mathbf{P} \cdot \mathbf{E})] \\
&= \dot{\mathbf{x}} \cdot \mathbf{b}_e + \boldsymbol{\mathcal{J}} \cdot \boldsymbol{\mathcal{E}} + \rho \, \boldsymbol{\mathcal{E}} \cdot \dot{\boldsymbol{\pi}} - \boldsymbol{\mathcal{M}} \cdot \dot{\mathbf{B}} \,,
\end{aligned}
\tag{2.58}
$$

  where $\boldsymbol{\pi} = \mathbf{P}/\rho$ is the polarization per unit mass.

The second identities in the above equations are the respective Galilean invariant forms w.r.t. a co-moving inertial frame.

Please note that the above just represents an incomplete summary of the basic quantities and equations of electrodynamics without giving a detailed interpretation of their mathematical meaning and phenomenological implications. Of course, there exists a bunch of excellent textbooks, which comprehensively elucidate the electrodynamic theory from the microscopic electromagnetism of point charges up to the electrodynamics of continua, see Jackson [37] among others. Of particular relevance for this thesis, we see the books of Landau *et al.* [42], Maugin [49], Eringen & Maugin [23, 24], Müller [54], and Kovetz [41].

## 2.4   Balance Relations

In this section, the fundamental balance laws of continuum thermodynamics and elastodynamics applied to mixtures are summarized within a general framework. Therefore, the basic stress measures are introduced and the specific balances of the overall mixture as well as of the individual constituents are discussed in the context of the master balance principle. For a more detailed discussion of the continuum mechanical basics, the reader should refer to the classical works of Truesdell & Toupin [67], Coleman & Noll [11], as well as Truesdell & Noll [66]. Concerning mixture theories, a comprehensive description of the thermodynamical balance principles can be found in the works of Ehlers [18, 19] and Hutter & Jöhnk [36]. Regarding the fusion of electrodynamics and thermodynamics, it is referred to the books cited at the end of the previous section and in the context of mixtures to the articles of Kelly [38] and Bennethum & Cushman [2].

### 2.4.1   Stress Concept and Dual Variables

According to the intersection (free-body) principle, each partial body $\mathcal{B}^\alpha \subset \mathcal{B}$ of the mixture $\varphi$ is subjected to an external mass-specific body (volume) force $\mathbf{b}^\alpha = \mathbf{b}^\alpha(\mathbf{x}, t)$ (normally gravitation) and an external traction (contact) force $\mathbf{t}^\alpha = \mathbf{t}^\alpha(\mathbf{x}, t, \mathbf{n})$ acting on parts or the whole of the boundary surface $\mathcal{S}^\alpha \subset \mathcal{S}$ with orientation $\mathbf{n}$. Now, in consideration of electrodynamics, according to (2.56), additional volume-specific electromagnetic body forces $\mathbf{b}_e^\alpha = \mathbf{b}_e^\alpha(\mathbf{x}, t)$ are present. Then, the whole mixture body $\mathcal{B} = \bigcup_\alpha \mathcal{B}^\alpha$ is exposed to the mechanical body force $\rho\,\mathbf{b} = \sum_\alpha \rho^\alpha\,\mathbf{b}^\alpha$, the electromagnetic body force $\mathbf{b}_e = \sum_\alpha \mathbf{b}_e^\alpha$, and the total surface traction $\mathbf{t} = \sum_\alpha \mathbf{t}^\alpha$ on the entire surface $\mathcal{S} = \bigcup_\alpha \mathcal{S}^\alpha$. In conclusion, one finds the resultant force vectors $\mathbf{f}$ and $\mathbf{f}^\alpha$ acting on the overall medium $\varphi$ and on the constituents $\varphi^\alpha$ as

$$\mathbf{f} = \underbrace{\int_\mathcal{B} \rho\,\mathbf{b}\,\mathrm{d}v}_{\mathbf{f}_{vm}} + \underbrace{\int_\mathcal{B} \mathbf{b}_e\,\mathrm{d}v}_{\mathbf{f}_{ve}} + \underbrace{\int_\mathcal{S} \mathbf{t}\,\mathrm{d}a}_{\mathbf{f}_a}, \quad \mathbf{f}^\alpha = \underbrace{\int_\mathcal{B} \rho^\alpha\,\mathbf{b}^\alpha\,\mathrm{d}v}_{\mathbf{f}_{vm}^\alpha} + \underbrace{\int_\mathcal{B} \mathbf{b}_e^\alpha\,\mathrm{d}v}_{\mathbf{f}_{ve}^\alpha} + \underbrace{\int_\mathcal{S} \mathbf{t}^\alpha\,\mathrm{d}a}_{\mathbf{f}_a^\alpha}. \quad (2.59)$$

Applying Cauchy's theorem, one recovers the total Cauchy stress tensor of the mixture $\mathbf{T} = \mathbf{T}(\mathbf{x}, t)$ and the partial Cauchy stress tensor $\mathbf{T}^\alpha = \mathbf{T}^\alpha(\mathbf{x}, t)$ of $\varphi^\alpha$ from

$$\mathbf{t}(\mathbf{x}, t, \mathbf{n}) = \mathbf{T}(\mathbf{x}, t)\,\mathbf{n}, \quad \mathbf{t}^\alpha(\mathbf{x}, t, \mathbf{n}) = \mathbf{T}^\alpha(\mathbf{x}, t)\,\mathbf{n}. \quad (2.60)$$

The total Cauchy stress may also be expressed by means of partial quantities, viz.

$$\mathbf{T} = \sum_\alpha \left( \mathbf{T}^\alpha - \rho^\alpha \mathbf{d}_\alpha \otimes \mathbf{d}_\alpha \right), \tag{2.61}$$

where $\rho^\alpha \mathbf{d}_\alpha \otimes \mathbf{d}_\alpha$ represents an apparent stress comparable to the Reynolds stress in turbulent flows (cf. [57, 61]), which is caused by fluctuations of the entire velocity field due to the diffusion velocities $\mathbf{d}_\alpha$ superimposed on the averaged velocity of the whole mixture $\dot{\mathbf{x}}$ given in Equations (2.13).

Following the above, the Cauchy stresses as the true stresses represent the current stress state at material points by describing the surface force acting on an area element in the actual configuration. Proceeding from the partial incremental surface force on $\mathcal{S}$, additional stress tensors are introduced via

$$\mathrm{d}\mathbf{f}^\alpha_a = \mathbf{t}^\alpha\,\mathrm{d}a = \mathbf{T}^\alpha\,\mathrm{d}\mathbf{a} = \mathbf{T}^\alpha \operatorname{cof} \mathbf{F}_\alpha\,\mathrm{d}\mathbf{A}_\alpha = \underbrace{\overbrace{\mathbf{T}^\alpha\left(\det \mathbf{F}_\alpha\right)}^{\boldsymbol{\tau}^\alpha} \mathbf{F}^{T-1}_\alpha}_{\mathbf{P}^\alpha}\,\mathrm{d}\mathbf{A}_\alpha\,, \tag{2.62}$$

where in particular

$$\begin{aligned} \mathbf{T}^\alpha &\quad : \text{Cauchy stress (true stress)}, \\ \boldsymbol{\tau}^\alpha = \left(\det \mathbf{F}_\alpha\right) \mathbf{T}^\alpha &\quad : \text{Kirchhoff stress (weighted Cauchy stress)}, \\ \mathbf{P}^\alpha = \boldsymbol{\tau}^\alpha \mathbf{F}^{T-1}_\alpha &\quad : \text{1st Piola-Kirchhoff stress (nominal stress)}. \end{aligned} \tag{2.63}$$

Moreover, it is of considerable assistance to formally introduce a further stress tensor operating on the reference configuration, viz.

$$\mathbf{S}^\alpha = \mathbf{F}^{-1}_\alpha \mathbf{P}^\alpha = \mathbf{F}^{-1}_\alpha \boldsymbol{\tau}^\alpha \mathbf{F}^{T-1}_\alpha \quad : \text{2nd Piola-Kirchhoff stress.} \tag{2.64}$$

Note that the above stress measures represent covariant tensors, which is a direct consequence of the contravariant nature of the oriented area element (recall Equation $(2.25)_2$). Thus, in analogy to the covariant strain rates $(2.39)_1$ and $(2.40)_1$, by use of the lower Oldroyd derivative (2.38), convenient stress rates, which obey the same transport mechanisms as the corresponding stresses, can be introduced. In summary, we have

$$\mathbf{S}^\alpha \;\; \overset{(\mathbf{F}_\alpha \otimes \mathbf{F}_\alpha)^{\frac{23}{T}}}{\underset{(\mathbf{F}^{-1}_\alpha \otimes \mathbf{F}^{-1}_\alpha)^{\frac{23}{T}}}{\rightleftarrows}} \;\; \boldsymbol{\tau}^\alpha, \qquad (\mathbf{S}^\alpha)'_\alpha \;\; \overset{(\mathbf{F}_\alpha \otimes \mathbf{F}_\alpha)^{\frac{23}{T}}}{\underset{(\mathbf{F}^{-1}_\alpha \otimes \mathbf{F}^{-1}_\alpha)^{\frac{23}{T}}}{\rightleftarrows}} \;\; (\boldsymbol{\tau}^\alpha)^\triangledown_\alpha\,. \tag{2.65}$$

The natural bond between certain stresses and strains is best described by the concept of *dual variables* stating that physically relevant scalar products between associated (conjugate) stress-strain pairs, such as the rate of internal mechanical work (stress power), stay invariant due to any transport operation between configurations [30]. One finds,

$$\begin{aligned} \mathbf{S}^\alpha \cdot \mathbf{E}_\alpha &= \boldsymbol{\tau}^\alpha \cdot \mathbf{A}_\alpha\,, \\ \mathbf{S}^\alpha \cdot (\mathbf{E}_\alpha)'_\alpha &= \boldsymbol{\tau}^\alpha \cdot (\mathbf{A}_\alpha)^\triangle_\alpha\,, \\ (\mathbf{S}^\alpha)'_\alpha \cdot \mathbf{E}_\alpha &= (\boldsymbol{\tau}^\alpha)^\triangledown_\alpha \cdot \mathbf{A}_\alpha\,, \\ (\mathbf{S}^\alpha)'_\alpha \cdot (\mathbf{E}_\alpha)'_\alpha &= (\boldsymbol{\tau}^\alpha)^\triangledown_\alpha \cdot (\mathbf{A}_\alpha)^\triangle_\alpha\,. \end{aligned} \tag{2.66}$$

Note that the scalar products of equations (2.66) including strain rates may also be expressed by means of the 1st Piola-Kirchhoff stress. For example, assuming that $\boldsymbol{\tau}^\alpha = (\boldsymbol{\tau}^\alpha)^T$ (see remark on Page 64), the volume-specific stress power can be rewritten as

$$\boldsymbol{\tau}^\alpha \cdot (\mathbf{A}_\alpha)^\triangle_\alpha = \boldsymbol{\tau}^\alpha \cdot \mathbf{D}_\alpha = \boldsymbol{\tau}^\alpha \cdot \mathbf{L}_\alpha = (\mathbf{P}^\alpha \mathbf{F}^T_\alpha) \cdot [(\mathbf{F}_\alpha)'_\alpha \mathbf{F}^{-1}_\alpha] = \mathbf{P}^\alpha \cdot (\mathbf{F}_\alpha)'_\alpha \qquad (2.67)$$

with $\{\mathbf{P}^\alpha, (\mathbf{F}_\alpha)'_\alpha\}$ as a so-called work conjugate pair, which is obviously not consistent with all of the invariance conditions of dual variables (2.66).

## 2.4.2 Master Balance Principle for Mixtures

According to Truesdell's *metaphysical principles* given in Box (2.68), each constituent can be described by individual balance equations accounting for mutual interactions with the other $\varphi^\alpha$ by additional production terms. The balance equations of the whole mixture are then obtained as the sum of the balance equations of the constituents and must have the same form as the respective balance equations of a single-phase material. Due to the fact that the mathematical structure of the fundamental thermodynamical balance laws, namely of mass, linear momentum, moment of momentum (m. o. m.), energy, and entropy, is in principle identical, they can be formulated within the concise shape of a master balance. The same applies to the basic electromagnetic relations in form of the Galilean invariant Maxwell equations $(2.51)_{1,2}$ and $(2.55)$.

<div style="border:1px solid">

**Truesdell's metaphysical principles**

*(1) All properties of the mixture must be mathematical consequences of properties of the constituents.*

*(2) So as to describe the motion of a constituent, we may in imagination isolate it from the rest of the mixture, provided we allow properly for the actions of the other constituents upon it.*

*(3) The motion of a mixture is governed by the same equations as is a single body.*

(Truesdell, 1984, p. 221 [65])

</div>

(2.68)

To begin with, let $\Psi$ and $\boldsymbol{\Psi}$ be arbitrary scalar- and vector-valued densities of some physical quantity to be balanced. Then, proceeding from classical continuum mechanics of single-phase materials, the general volumetric balance relations of a multiphasic mixture $\varphi = \bigcup_\alpha \varphi^\alpha$ take the global (integral) form:

$$\frac{\mathrm{d}}{\mathrm{d}t} \int_{\mathcal{B}} \Psi \, \mathrm{d}v = \int_{\mathcal{S}} (\boldsymbol{\phi} \cdot \mathbf{n}) \, \mathrm{d}a + \int_{\mathcal{B}} \sigma \, \mathrm{d}v + \int_{\mathcal{B}} \hat{\Psi} \, \mathrm{d}v \, ,$$
$$\frac{\mathrm{d}}{\mathrm{d}t} \int_{\mathcal{B}} \boldsymbol{\Psi} \, \mathrm{d}v = \int_{\mathcal{S}} (\boldsymbol{\Phi} \, \mathbf{n}) \, \mathrm{d}a + \int_{\mathcal{B}} \boldsymbol{\sigma} \, \mathrm{d}v + \int_{\mathcal{B}} \hat{\boldsymbol{\Psi}} \, \mathrm{d}v \, . \qquad (2.69)$$

Herein, $\boldsymbol{\phi} \cdot \mathbf{n}$ and $\boldsymbol{\Phi} \, \mathbf{n}$ are the surface densities defined per unit current area representing the efflux of the physical quantity over the surface $\mathcal{S}$ of $\mathcal{B}$, $\sigma$ and $\boldsymbol{\sigma}$ are the volume densities

describing the supply (external source) of the physical quantity, and $\hat{\psi}$ and $\hat{\boldsymbol{\Psi}}$ represent the productions of the physical quantity due to couplings of $\varphi$ with its environment.

Analogously to (2.69), one defines a global surface balance,

$$\frac{\mathrm{d}}{\mathrm{d}t} \int_{\mathcal{S}} (\boldsymbol{\Psi} \cdot \mathbf{n}) \, \mathrm{d}a = \oint_{\mathcal{L}} (\boldsymbol{\phi} \cdot \mathbf{n}_t) \, \mathrm{d}s + \int_{\mathcal{S}} (\boldsymbol{\sigma} \cdot \mathbf{n}) \, \mathrm{d}a + \int_{\mathcal{S}} (\hat{\boldsymbol{\Psi}} \cdot \mathbf{n}) \, \mathrm{d}a \,, \qquad (2.70)$$

in which $\mathcal{L}$ is a closed material curve (line) bounding $\mathcal{S}$ and $\mathbf{n}_t$ is the unit tangent vector along $\mathcal{L}$. Moreover, the other terms have a similar intuitive meaning as in the volume balance, that is, $\boldsymbol{\phi} \cdot \mathbf{n}_t$ is the flux of lines through $\mathcal{S}$, and $(\boldsymbol{\sigma} \cdot \mathbf{n})$ and $(\hat{\boldsymbol{\Psi}} \cdot \mathbf{n})$ are the supply and the production of $\boldsymbol{\Psi}$ on $\mathcal{S}$.

Supposing adequate continuity properties for all occurring fields, the equivalent local (differential) form of the master balance equations (2.69) results from differentiation of the left-hand sides and transformation of the surface integrals into volume integrals on the right-hand sides of (2.69):

$$\begin{aligned} \dot{\psi} + \psi \operatorname{div} \dot{\mathbf{x}} &= \operatorname{div} \boldsymbol{\phi} + \sigma + \hat{\psi} \,, \\ \dot{\boldsymbol{\Psi}} + \boldsymbol{\Psi} \operatorname{div} \dot{\mathbf{x}} &= \operatorname{div} \boldsymbol{\Phi} + \boldsymbol{\sigma} + \hat{\boldsymbol{\Psi}} \,. \end{aligned} \qquad (2.71)$$

From (2.70), one respectively obtains with the aid of the flux derivative (2.46) the local form of the surface balance

$$\overset{*}{\boldsymbol{\Psi}} = \operatorname{rot} \boldsymbol{\phi} + \boldsymbol{\sigma} + \hat{\boldsymbol{\Psi}} \,. \qquad (2.72)$$

Next, proceeding from the axiomatically introduced balance principles, namely of mass, linear momentum, moment of momentum (m. o. m.), energy, and entropy, as well as the macroscopic Maxwell equations, one identifies the quantities in Equations (2.69) and (2.70), as well as (2.71) and (2.72), respectively, according to Table 2.2.

**Table 2.2:** *Identified physical quantities of the volume and surface master balances for the mixture $\varphi$.*

| Balance | $\psi, \boldsymbol{\Psi}$ | $\phi, \boldsymbol{\Phi}$ | $\sigma, \boldsymbol{\sigma}$ | $\hat{\psi}, \hat{\boldsymbol{\Psi}}$ |
|---|---|---|---|---|
| mass | $\rho$ | $\mathbf{0}$ | $0$ | $0$ |
| momentum | $\rho \dot{\mathbf{x}}$ | $\mathbf{T}$ | $\rho \mathbf{b} + \mathbf{b}_e$ | $\mathbf{0}$ |
| m. o. m. | $\mathbf{x} \times (\rho \dot{\mathbf{x}})$ | $\mathbf{x} \times \mathbf{T}$ | $\mathbf{x} \times (\rho \mathbf{b} + \mathbf{b}_e) + \mathbf{c}_e$ | $\mathbf{0}$ |
| energy | $\rho \varepsilon + \frac{1}{2} \dot{\mathbf{x}} \cdot (\rho \dot{\mathbf{x}})$ | $\mathbf{T}^T \dot{\mathbf{x}} - \mathbf{q}$ | $\dot{\mathbf{x}} \cdot (\rho \mathbf{b}) + \rho r + \varepsilon_e$ | $0$ |
| entropy | $\rho \eta$ | $\phi_\eta$ | $\sigma_\eta$ | $\hat{\eta}$ |
| charge | $\rho_e$ | $-\boldsymbol{\mathcal{J}}$ | $0$ | $0$ |
| Gauss's law (elec.) | $0$ | $-\mathbf{D}$ | $\rho_e$ | $0$ |
| Gauss's law (magn.) | $0$ | $-\mathbf{B}$ | $0$ | $0$ |
| Faraday's law | $\mathbf{B}$ | $-\boldsymbol{\mathcal{E}}$ | $0$ | $0$ |
| Ampère's law | $-\mathbf{D}$ | $-\boldsymbol{\mathcal{H}}$ | $\boldsymbol{\mathcal{J}}$ | $0$ |

Therein, $\rho \dot{\mathbf{x}}$ is the momentum of the entire mixture and $\mathbf{x} \times (\rho \dot{\mathbf{x}})$ is the corresponding moment of momentum. Concerning the energy balance, $\varepsilon$ is the internal energy, $\mathbf{q}$ is

the heat influx vector, and $r$ is the external heat supply. The additional electromagnetic contributions are the electromagnetic body force, couple, and energy $\mathbf{b}_e, \mathbf{c}_e$, and $\varepsilon_e$ given through Equations (2.56)–(2.58). The separated middle three and last two lines represent the electromagnetic volume and surface conservation laws according to Maxwell's equations given in Section 2.3.2. Moreover, $\eta$ is the entropy, $\boldsymbol{\phi}_\eta$ and $\sigma_\eta$ are the efflux of entropy and the external entropy supply, and $\hat{\eta} \geq 0$ is the non-negative entropy production, which considers the irreversibility of the overall thermodynamical process. Furthermore, regarding the mixture as a closed system, all remaining production terms are equal to zero. Then, by inserting the respective quantities of Table 2.2 into the local master balances (2.71) and (2.72), respectively, one recovers the specific balance relations of continuum electro-magneto-thermomechanics as for singlephasic materials [23]. The complete set of equations is depicted in Box (2.73), where $\mathbf{L} = \operatorname{grad} \dot{\mathbf{x}}$ is the spatial velocity gradient of the mixture in analogy to (2.34).

$$
\begin{array}{ll}
\textbf{Specific conservation laws for the mixture} & \\[1em]
\textit{mass:} \quad \dot{\rho} + \rho \operatorname{div} \dot{\mathbf{x}} = 0 & \\[0.5em]
\textit{momentum:} \quad \rho \ddot{\mathbf{x}} = \operatorname{div} \mathbf{T} + \rho \mathbf{b} + \mathbf{b}_e & \\[0.5em]
\textit{m. o. m.:} \quad \mathbf{0} = \mathbf{I} \times \mathbf{T} + \mathbf{c}_e \quad \longrightarrow \quad \mathbf{T} \neq \mathbf{T}^T & \\[0.5em]
\textit{energy:} \quad \rho \dot{\varepsilon} = \mathbf{T} \cdot \mathbf{L} - \operatorname{div} \mathbf{q} + \rho r + \varepsilon_e - \dot{\mathbf{x}} \cdot \mathbf{b}_e & \\[0.5em]
\textit{entropy:} \quad \rho \dot{\eta} \geq \operatorname{div} \boldsymbol{\phi}_\eta + \sigma_\eta & \\[1em]
\textit{charge:} \quad \dot{\rho}_e + \rho_e \operatorname{div} \dot{\mathbf{x}} = -\operatorname{div} \boldsymbol{\mathcal{J}} \quad \longrightarrow \quad \operatorname{div} \mathbf{J} = -\dfrac{\partial \rho_e}{\partial t} & \\[0.5em]
\textit{Gauss's law (elec.):} \quad 0 = \operatorname{div} \mathbf{D} - \rho_e & \\[0.5em]
\textit{Gauss's law (magn.):} \quad 0 = \operatorname{div} \mathbf{B} & \\[1em]
\textit{Faraday's law:} \quad \overset{*}{\mathbf{B}} = -\operatorname{rot} \boldsymbol{\mathcal{E}} \quad \longrightarrow \quad \operatorname{rot} \mathbf{E} = -\dfrac{\partial \mathbf{B}}{\partial t} & \\[0.5em]
\textit{Ampère's law:} \quad -\overset{*}{\mathbf{D}} = -\operatorname{rot} \boldsymbol{\mathcal{H}} + \boldsymbol{\mathcal{J}} \quad \longrightarrow \quad \operatorname{rot} \mathbf{H} = \mathbf{J} + \dfrac{\partial \mathbf{D}}{\partial t} &
\end{array} \tag{2.73}
$$

Moreover, regarding the total Cauchy stress tensor, which from $(2.73)_3$ is obviously not symmetric for general electromagnetic materials, it is of considerable assistance to proceed from a constitutive split $\mathbf{T} = \mathbf{T}_m + \mathbf{T}_e$ into a thermomechanical part $\mathbf{T}_m$ and an electromagnetic part $\mathbf{T}_e$, for both of which further material-dependent equations must be provided. Here, we introduce the electromagnetic stress tensor of the form [23, Sect. 3.6]

$$
\mathbf{T}_e = \mathbf{T}_e^M + \overline{\mathbf{T}}_e \quad \text{with} \quad \begin{cases} \mathbf{T}_e^M = \mathbf{E} \otimes \mathbf{E} + \mathbf{B} \otimes \mathbf{B} - \frac{1}{2}\left(\mathbf{E} \cdot \mathbf{E} + \mathbf{B} \cdot \mathbf{B}\right)\mathbf{I}, \\ \overline{\mathbf{T}}_e = \mathbf{P} \otimes \boldsymbol{\mathcal{E}} - \mathbf{B} \otimes \boldsymbol{\mathcal{M}} + \left(\boldsymbol{\mathcal{M}} \cdot \mathbf{B}\right)\mathbf{I}, \end{cases} \tag{2.74}
$$

which is decomposed into the symmetric Maxwell stress $\mathbf{T}_e^M = (\mathbf{T}_e^M)^T$ and another stress tensor $\overline{\mathbf{T}}_e$ depending on the polarization and magnetization. Then, it is easily proven that the electromagnetic momentum couple is related to the skew-symmetric part of $\mathbf{T}_e$, viz.

$$
\mathbf{c}_e = -\mathbf{I} \times \operatorname{skw} \mathbf{T}_e = \overset{3}{\mathbf{E}} \operatorname{skw} \mathbf{T}_e = \overset{3}{\mathbf{E}} \operatorname{skw} \overline{\mathbf{T}}_e, \tag{2.75}
$$

where $\overset{3}{\mathbf{E}}$ is the rank-3 Ricci permutation tensor (cf. remark and footnote on Page 64). In this context, it might also be convenient to express the electromagnetic volume force $\mathbf{b}_e$ in some divergence form dependent on the electromagnetic stress field. This can be accomplished with the aid of the volume- and mass-specific electromagnetic momentum vectors

$$\mathbf{G} = \mathbf{E} \times \mathbf{B} \qquad \text{and} \qquad \boldsymbol{\gamma} = \frac{\mathbf{G}}{\rho} \tag{2.76}$$

describing the momentum carried by electromagnetic radiation, by which one finds [49]

$$\mathbf{b}_e = \operatorname{div} \mathbf{T}_e - \frac{\partial \mathbf{G}}{\partial t} = \operatorname{div}\left(\mathbf{T}_e + \dot{\mathbf{x}} \otimes \mathbf{G}\right) - \rho\,\dot{\boldsymbol{\gamma}}\,. \tag{2.77}$$

Note that this gives rise to an alternate representation of the momentum balance when linking thermo- and electrodynamics as mentioned in Section 2.3.3.[12]

To continue with the derivation of the partial balance relations in consideration of electrodynamics, we proceed from the most general ansatz proposed by Kelly [38] and split-up all the electromagnetic fields into pieces to be associated with each constituent. Thus, following Truesdell's principles (2.68), the general balances of the individual constituents yield, in analogy to (2.69), the global form

$$\begin{aligned}
\frac{\mathrm{d}_\alpha}{\mathrm{d}t} \int_{\mathcal{B}} \Psi^\alpha \, \mathrm{d}v &= \int_{\mathcal{S}} (\boldsymbol{\phi}^\alpha \cdot \mathbf{n}) \, \mathrm{d}a + \int_{\mathcal{B}} \sigma^\alpha \, \mathrm{d}v + \int_{\mathcal{B}} \hat{\psi}^\alpha \, \mathrm{d}v\,, \\
\frac{\mathrm{d}_\alpha}{\mathrm{d}t} \int_{\mathcal{B}} \boldsymbol{\Psi}^\alpha \, \mathrm{d}v &= \int_{\mathcal{S}} (\boldsymbol{\Phi}^\alpha \mathbf{n}) \, \mathrm{d}a + \int_{\mathcal{B}} \boldsymbol{\sigma}^\alpha \, \mathrm{d}v + \int_{\mathcal{B}} \hat{\boldsymbol{\Psi}}^\alpha \, \mathrm{d}v\,,
\end{aligned} \tag{2.78}$$

and according to (2.71) the local form

$$\begin{aligned}
(\Psi^\alpha)'_\alpha + \Psi^\alpha \operatorname{div} \overset{\prime}{\mathbf{x}}_\alpha &= \operatorname{div} \boldsymbol{\phi}^\alpha + \sigma^\alpha + \hat{\psi}^\alpha\,, \\
(\boldsymbol{\Psi}^\alpha)'_\alpha + \boldsymbol{\Psi}^\alpha \operatorname{div} \overset{\prime}{\mathbf{x}}_\alpha &= \operatorname{div} \boldsymbol{\Phi}^\alpha + \boldsymbol{\sigma}^\alpha + \hat{\boldsymbol{\Psi}}^\alpha\,.
\end{aligned} \tag{2.79}$$

In the same way, one adopts the global and local structure of the surface balance (2.70) and (2.72) to obtain

$$\frac{\mathrm{d}}{\mathrm{d}t} \int_{\mathcal{S}} (\boldsymbol{\Psi}^\alpha \cdot \mathbf{n}) \, \mathrm{d}a = \oint_{\mathcal{L}} (\boldsymbol{\phi}^\alpha \cdot \mathbf{n}_t) \, \mathrm{d}s + \int_{\mathcal{S}} (\boldsymbol{\sigma}^\alpha \cdot \mathbf{n}) \, \mathrm{d}a + \int_{\mathcal{S}} (\hat{\boldsymbol{\Psi}}^\alpha \cdot \mathbf{n}) \, \mathrm{d}a\,, \tag{2.80}$$

$$(\boldsymbol{\Psi}^\alpha)^*_\alpha = \operatorname{rot} \boldsymbol{\phi}^\alpha + \boldsymbol{\sigma}^\alpha + \hat{\boldsymbol{\Psi}}^\alpha\,,$$

where $(\,\cdot\,)^*_\alpha$ represents the flux derivative according to (2.43). In the above equations, the partial quantities $(\,\cdot\,)^\alpha$ have the same physical meaning as the quantities included in the master balances of the overall mixture. However, they have to satisfy additional conditions such that summation of a partial balance of all $\varphi^\alpha$ yields the respective fields of the multiphasic continuum $\varphi$. For the constituent volume balances (2.78), they read:

$$\begin{aligned}
\Psi &= \sum_\alpha \Psi^\alpha\,, \quad \boldsymbol{\phi} \cdot \mathbf{n} = \sum_\alpha (\boldsymbol{\phi}^\alpha - \Psi^\alpha \, \mathbf{d}_\alpha) \cdot \mathbf{n}\,, \qquad \sigma = \sum_\alpha \sigma^\alpha\,, \quad \hat{\psi} = \sum_\alpha \hat{\psi}^\alpha\,, \\
\boldsymbol{\Psi} &= \sum_\alpha \boldsymbol{\Psi}^\alpha\,, \quad \boldsymbol{\Phi}\,\mathbf{n} = \sum_\alpha (\boldsymbol{\Phi}^\alpha - \boldsymbol{\Psi}^\alpha \otimes \mathbf{d}_\alpha)\,\mathbf{n}\,, \quad \boldsymbol{\sigma} = \sum_\alpha \boldsymbol{\sigma}^\alpha\,, \quad \hat{\boldsymbol{\Psi}} = \sum_\alpha \hat{\boldsymbol{\Psi}}^\alpha\,.
\end{aligned} \tag{2.81}$$

---

[12] In fact, following the master balance approach, one may proceed from an equivalent representation of the momentum balance based on the identification $\boldsymbol{\Psi} = \rho\dot{\mathbf{x}} + \mathbf{G}$, $\boldsymbol{\Phi} = \mathbf{T} + \mathbf{T}_e + \dot{\mathbf{x}} \otimes \mathbf{G}$, and $\boldsymbol{\sigma} = \rho\,\mathbf{b}$.

Respective constraints apply also to the partial surface balances (2.80) [38]:

$$\mathbf{\Psi} = \sum_\alpha \mathbf{\Psi}^\alpha, \quad \boldsymbol{\phi} \cdot \mathbf{n}_t = \sum_\alpha (\boldsymbol{\phi}^\alpha - \mathbf{\Psi}^\alpha \times \mathbf{d}_\alpha) \cdot \mathbf{n}_t,$$

$$(\boldsymbol{\sigma} + \hat{\mathbf{\Psi}}) \cdot \mathbf{n} = \sum_\alpha (\boldsymbol{\sigma}^\alpha + \hat{\mathbf{\Psi}}^\alpha - \mathbf{d}_\alpha \operatorname{div} \mathbf{\Psi}^\alpha) \cdot \mathbf{n}. \tag{2.82}$$

In this regard, it should be noted that the supply $\boldsymbol{\sigma}^\alpha$ and the production $\hat{\mathbf{\Psi}}^\alpha$ of $\mathbf{\Psi}^\alpha$ on $\mathcal{S}$ can only hardly be distinguished. Hence, it is convenient to formally treat them together.

Next, the specific balance equations of the constituents are derived in analogy to those of single-phase materials except that one needs to account for the interaction mechanisms by additional production terms. Strictly speaking, the local partial continua represent open systems, which stay in thermo- and electrodynamical exchange with one another. In particular, one identifies the partial physical quantities according to the following table:

**Table 2.3:** *Identified physical quantities of the volume and surface master balances for the constituent $\varphi^\alpha$.*

| Balance | $\Psi^\alpha$, $\mathbf{\Psi}^\alpha$ | $\phi^\alpha$, $\mathbf{\Phi}^\alpha$ | $\sigma^\alpha$, $\boldsymbol{\sigma}^\alpha$ | $\hat{\Psi}^\alpha$, $\hat{\mathbf{\Psi}}^\alpha$ |
|---|---|---|---|---|
| mass | $\rho^\alpha$ | $\mathbf{0}$ | $0$ | $\hat{\rho}^\alpha$ |
| momentum | $\rho^\alpha \overset{'}{\mathbf{x}}_\alpha$ | $\mathbf{T}^\alpha$ | $\rho^\alpha \mathbf{b}^\alpha + \mathbf{b}_e^\alpha$ | $\hat{\mathbf{s}}^\alpha$ |
| m. o. m. | $\mathbf{x} \times (\rho^\alpha \overset{'}{\mathbf{x}}_\alpha)$ | $\mathbf{x} \times \mathbf{T}^\alpha$ | $\mathbf{x} \times (\rho^\alpha \mathbf{b}^\alpha + \mathbf{b}_e^\alpha) + \mathbf{c}_e^\alpha$ | $\hat{\mathbf{h}}^\alpha$ |
| energy | $\rho^\alpha \varepsilon^\alpha + \frac{1}{2} \overset{'}{\mathbf{x}}_\alpha \cdot (\rho^\alpha \overset{'}{\mathbf{x}}_\alpha)$ | $(\mathbf{T}^\alpha)^T \overset{'}{\mathbf{x}}_\alpha - \mathbf{q}^\alpha$ | $\overset{'}{\mathbf{x}}_\alpha \cdot (\rho^\alpha \mathbf{b}^\alpha) + \rho^\alpha r^\alpha + \varepsilon_e^\alpha$ | $\hat{e}^\alpha$ |
| entropy | $\rho^\alpha \eta^\alpha$ | $\phi_\eta^\alpha$ | $\sigma_\eta^\alpha$ | $\hat{\eta}^\alpha$ |
| charge | $\rho_e^\alpha$ | $-\boldsymbol{\mathcal{J}}^\alpha$ | $0$ | $\hat{\rho}_e^\alpha$ |
| Gauss's law (elec.) | $0$ | $-\mathbf{D}^\alpha$ | $\rho_e^\alpha$ | $\hat{\sigma}^\alpha$ |
| Gauss's law (magn.) | $0$ | $-\mathbf{B}^\alpha$ | $0$ | $\hat{\lambda}^\alpha$ |
| Faraday's law | $\mathbf{B}^\alpha$ | $-\boldsymbol{\mathcal{E}}^\alpha$ | $0$ | $\hat{\boldsymbol{\xi}}^\alpha$ |
| Ampère's law | $-\mathbf{D}^\alpha$ | $-\boldsymbol{\mathcal{H}}^\alpha$ | $\boldsymbol{\mathcal{J}}^\alpha$ | $\hat{\boldsymbol{\mathcal{J}}}^\alpha$ |

Herein, $\hat{\rho}^\alpha$ is the mass production describing mass exchanges or phase transitions between a particular $\varphi^\alpha$ and the other constituents, $\hat{\mathbf{s}}^\alpha$ is the total momentum production of $\varphi^\alpha$, and $\hat{\mathbf{h}}^\alpha$ is the total production of angular momentum. Moreover, $\hat{e}^\alpha$ and $\hat{\eta}^\alpha$ represent the total energy and entropy productions of $\varphi^\alpha$. Concerning the electromagnetic terms, $\hat{\rho}_e^\alpha$ is the production of electric charge (e. g. through reaction), $\hat{\sigma}^\alpha$ and $\hat{\boldsymbol{\mathcal{J}}}^\alpha$ account for the fact that charge and current are not necessarily conserved for the individual $\varphi^\alpha$, and $\hat{\lambda}^\alpha$ and $\hat{\boldsymbol{\xi}}^\alpha$ are additionally introduced productions associated with the magnetic flux and the electric field.

In mixture theories, it is moreover convenient to split the total production terms of the thermodynamical balances into direct parts and parts including productions of the pre-

ceding (lower) balances:

$$\hat{\mathbf{s}}^\alpha = \hat{\mathbf{p}}^\alpha + \hat{\rho}^\alpha \overset{'}{\mathbf{x}}_\alpha, \quad \hat{\mathbf{h}}^\alpha = \hat{\mathbf{m}}^\alpha + \mathbf{x} \times (\hat{\mathbf{p}}^\alpha + \hat{\rho}^\alpha \overset{'}{\mathbf{x}}_\alpha),$$
$$\hat{e}^\alpha = \hat{\varepsilon}^\alpha + \hat{\mathbf{p}}^\alpha \cdot \overset{'}{\mathbf{x}}_\alpha + \hat{\rho}^\alpha (\varepsilon^\alpha + \tfrac{1}{2} \overset{'}{\mathbf{x}}_\alpha \cdot \overset{'}{\mathbf{x}}_\alpha), \quad \hat{\eta}^\alpha = \hat{\zeta}^\alpha + \hat{\rho}^\alpha \eta^\alpha. \tag{2.83}$$

In Equations (2.83), $\hat{\mathbf{p}}^\alpha$ denotes the direct momentum production, which can be interpreted as the volume-specific local interaction force between $\varphi^\alpha$ and the other constituents of $\varphi$, and $\hat{\mathbf{m}}^\alpha$ represents the direct moment of momentum production describing the angular momentum couplings between the constituents. Moreover, $\hat{\varepsilon}^\alpha$ and $\hat{\zeta}^\alpha$ are the direct terms of the energy and the entropy productions. As is usual in the framework of single-phase continua, one proceeds from an *a priori* constitutive assumption for the partial entropy efflux and the external entropy supply, viz.

$$\phi_\eta^\alpha = -\frac{1}{\Theta^\alpha} \mathbf{q}^\alpha, \quad \sigma_\eta^\alpha = \frac{1}{\Theta^\alpha} \rho^\alpha r^\alpha, \tag{2.84}$$

where different absolute Kelvin's temperatures $\Theta^\alpha > 0$ allow for an individual temperature field for each constituent. Following this, the final form of the specific partial balance relations is obtained in analogy to those of the whole mixture (2.73):

---

**Specific constituent balance relations**

*mass:* $\quad (\rho^\alpha)'_\alpha + \rho^\alpha \operatorname{div} \overset{'}{\mathbf{x}}_\alpha = \hat{\rho}^\alpha$

*momentum:* $\quad \rho^\alpha \overset{''}{\mathbf{x}}_\alpha = \operatorname{div} \mathbf{T}^\alpha + \rho^\alpha \mathbf{b}^\alpha + \mathbf{b}_e^\alpha + \hat{\mathbf{p}}^\alpha$

*m. o. m.:* $\quad \mathbf{0} = \mathbf{I} \times \mathbf{T}^\alpha + \mathbf{c}_e^\alpha + \hat{\mathbf{m}}^\alpha$

*energy:* $\quad \rho^\alpha (\varepsilon^\alpha)'_\alpha = \mathbf{T}^\alpha \cdot \mathbf{L}_\alpha - \operatorname{div} \mathbf{q}^\alpha + \rho^\alpha r^\alpha +$
$\qquad\qquad\qquad + \varepsilon_e^\alpha - \overset{'}{\mathbf{x}}_\alpha \cdot \mathbf{b}_e^\alpha + \hat{\varepsilon}^\alpha$

*entropy:* $\quad \rho^\alpha (\eta^\alpha)'_\alpha = \operatorname{div} (-\dfrac{1}{\Theta^\alpha} \mathbf{q}^\alpha) + \dfrac{1}{\Theta^\alpha} \rho^\alpha r^\alpha + \hat{\zeta}^\alpha$

*charge:* $\quad (\rho_e^\alpha)'_\alpha + \rho_e^\alpha \operatorname{div} \overset{'}{\mathbf{x}}_\alpha = -\operatorname{div} \boldsymbol{\mathcal{J}}^\alpha + \hat{\rho}_e^\alpha$

*Gauss's law (elec.):* $\quad 0 = -\operatorname{div} \mathbf{D}^\alpha + \rho_e^\alpha + \hat{\sigma}^\alpha$

*Gauss's law (magn.):* $\quad 0 = -\operatorname{div} \mathbf{B}^\alpha + \hat{\lambda}^\alpha$

*Faraday's law:* $\quad (\mathbf{B}^\alpha)_\alpha^* = -\operatorname{rot} \boldsymbol{\mathcal{E}} + \hat{\boldsymbol{\xi}}^\alpha$

*Ampère's law:* $\quad -(\mathbf{D}^\alpha)_\alpha^* = -\operatorname{rot} \boldsymbol{\mathcal{H}}^\alpha + \boldsymbol{\mathcal{J}}^\alpha + \hat{\boldsymbol{\mathcal{J}}}^\alpha$

$$\tag{2.85}$$

---

According to the sum relations (2.81), the physical quantities of the mixture can be expressed by means of the respective partial quantities extended by a diffusion term in the case of the surface densities. As an example, recall the previously introduced total Cauchy stress tensor $\mathbf{T}$ of equation (2.61). Moreover, one finds the following restrictions on the partial production terms:

$$\sum_\alpha \hat{\rho}^\alpha = 0, \quad \sum_\alpha \hat{\mathbf{s}}^\alpha = \mathbf{0}, \quad \sum_\alpha \hat{\mathbf{h}}^\alpha = \mathbf{0}, \quad \sum_\alpha \hat{e}^\alpha = 0, \quad \sum_\alpha \hat{\eta}^\alpha \geq 0. \tag{2.86}$$

The partial Maxwell equations are easily recovered from Box (2.85), from which, through summation over all $\varphi^\alpha$, the respective mixture relations must be obtained. In doing so, one finds the constraints for the electromagnetic productions consistent with (2.82):

$$
\begin{aligned}
\operatorname{div} \mathbf{J}^\alpha &= -\frac{\partial \rho_e^\alpha}{\partial t} + \hat{\rho}_e^\alpha
&&\longrightarrow \quad \sum_\alpha \hat{\rho}_e^\alpha = 0\,, \\[2mm]
\operatorname{div} \mathbf{B}^\alpha &= \hat{\lambda}^\alpha
&&\longrightarrow \quad \sum_\alpha \hat{\lambda}^\alpha = 0\,, \\[2mm]
\operatorname{div} \mathbf{D}^\alpha &= \rho_e^\alpha + \hat{\sigma}^\alpha
&&\longrightarrow \quad \sum_\alpha \hat{\sigma}^\alpha = 0\,, \\[2mm]
\operatorname{rot} \mathbf{E}^\alpha &= -\frac{\partial \mathbf{B}^\alpha}{\partial t} + \hat{\boldsymbol{\xi}}^\alpha - \overset{'}{\mathbf{x}}_\alpha\, \hat{\lambda}^\alpha
&&\longrightarrow \quad \sum_\alpha \left( \hat{\boldsymbol{\xi}}^\alpha - \mathbf{d}_\alpha\, \hat{\lambda}^\alpha \right) = \mathbf{0}\,, \\[2mm]
\operatorname{rot} \mathbf{H}^\alpha &= \mathbf{J}^\alpha + \frac{\partial \mathbf{D}^\alpha}{\partial t} + \hat{\boldsymbol{\mathcal{J}}}^\alpha + \overset{'}{\mathbf{x}}_\alpha\, \hat{\sigma}^\alpha
&&\longrightarrow \quad \sum_\alpha \left( \hat{\boldsymbol{\mathcal{J}}}^\alpha + \mathbf{d}_\alpha\, \hat{\sigma}^\alpha \right) = \mathbf{0}\,.
\end{aligned} \tag{2.87}
$$

**Remark:** In this contribution, only non-polar materials (Boltzmann continua) are considered, where the motion does not possess independent degrees of freedom for translation and rotation. Thus, proceeding from non-polar mixtures, evaluation of the mixture balance of angular momentum yields the symmetry of the thermomechanical part of the total Cauchy stress tensor $\mathbf{T}_m = \mathbf{T}_m^T$. However, since the electromagnetic phenomena in general induce an additional momentum couple $\mathbf{c}_e$ (see Box $(2.73)_3$) caused by electric and magnetic multipole moments, the combined stress tensor $\mathbf{T} = \mathbf{T}_m + \mathbf{T}_e$ is not symmetric, recall Equation (2.74). Now, regarding the partial moment of momentum balances of the non-polar $\varphi^\alpha$ $(2.85)_3$, direct angular momentum couplings $\hat{\mathbf{m}}^\alpha$ must additionally be considered yielding together with the partial electromagnetic couples to non-symmetric partial Cauchy stresses, $\mathbf{T}^\alpha \neq (\mathbf{T}^\alpha)^T$, where it is likewise assumed that $\mathbf{T}^\alpha = \mathbf{T}_m^\alpha + \mathbf{T}_e^\alpha$.[13] Nevertheless, proceeding from intrinsically non-polar materials associated with symmetric thermomechanical Cauchy stresses on the micro scale, it can be shown by homogenization that on the macroscopic level $\hat{\mathbf{m}}^\alpha \equiv \mathbf{0}$ [19, 28]. Then, if we further proceed from almost linear electromagnetic materials, for which Equations (2.49) are valid implying that skw $\mathbf{T}_e^\alpha \equiv \mathbf{0}$ or equivalently $\mathbf{c}_e^\alpha \equiv \mathbf{0}$, also the electromagnetic stress tensor, and thus, the combined stress becomes symmetric. Consequently, the combined partial Kirchhoff and 2nd Piola-Kirchhoff stresses would also be symmetric, while the 1st Piola-Kirchhoff stress is generally not (cf. (2.63) and (2.64)). For specific extensions of the balance principles for single- and multiphasic materials to micropolarity (Cosserat continua), the interested reader is referred to [12–14, 19, 22] and the quotations therein.   ■

The specific local balance relations for the mixture (or likewise a singlephasic material) given in Box (2.73) as well as the respective partial conservation laws of Box (2.85) can now

---

[13] The direct or intrinsic spin production $\hat{\mathbf{m}}^\alpha$ represents twice the negative axial vector $\overset{\mathrm{A}}{\mathbf{t}}{}^\alpha$ associated with the skew-symmetric properties of $\mathbf{T}_m^\alpha$. It can be shown that [6]

$$
\hat{\mathbf{m}}^\alpha = -\mathbf{I} \times \operatorname{skw} \mathbf{T}_m^\alpha = \overset{3}{\mathbf{E}} \operatorname{skw} \mathbf{T}_m^\alpha = -2\, \overset{\mathrm{A}}{\mathbf{t}}{}^\alpha\,, \quad \operatorname{skw} \mathbf{T}_m^\alpha = -\tfrac{1}{2}\left( \hat{\mathbf{m}}^\alpha \times \mathbf{I} \right) = -\tfrac{1}{2}\, [\overset{3}{\mathbf{E}}\,(\hat{\mathbf{m}}^\alpha \otimes \mathbf{I})]^{\underline{2}}\,.
$$

be combined to form a system of volume-coupled PDEs governing some region of interest. Accompanied by respective material-dependent constitutive equations, problem-specific assumptions, as well as boundary and initial conditions, this is what constitutes an initial boundary-value problem in strong form. Basically, one ends up with a volumetrically coupled formulation in the primal variables of choice, such as displacement, pressure, temperature, electric or magnetic potential among others, which can be made accessible to numerical solution by some variational method.

However, at this point, we waive further continuative details, such as a serious discussion of the entropy principle for mixtures, which would be of interest when deriving a thermodynamically admissible constitutive setting for the description of a specific material, see, e.g., [3, 13, 16, 19, 48]. Moreover, due to the manifold possibilities of physical processes involved, which essentially guide the sensible choice of the primary fields, it is virtually impossible to provide an all-embracing presentation of the numerical treatment, for instance, in the framework of the FEM by a general variational formulation in analogy to the master balance principle from above. Therefore, it is rather intended to continue in Part 2 of this thesis with the application-dependent treatment of coupled problems based on specific volume-coupled formulations. In particular, staying with the porous media approach, in Chapter 4, the problem of poro-elastodynamics will be discussed in detail and its numerical solution will be presented applying some strategies outlined in Section 1.2. Chapter 5 is devoted to the continuum biomechanics of living matter dealing with the swelling of charged hydrated tissues and the biological growth process of tumor spheroids. Moreover, Chapter 6 presents a theoretically investigation of fluid penetration effects in porous media contact, and finally, Chapter 7 applies finite porous media viscoelasticity for the description of human intervertebral discs as ionized, fluid-saturated, and collagen-reinforced porous materials.

## 2.5 References

[1] Acartürk, A.: *Simulation of Charged Hydrated Porous Materials*. Dissertation, Report No. II-18 of the Institute of Applied Mechanics (CE), Universität Stuttgart, Germany 2009.

[2] Bennethum, L. S. & Cushman, J. H.: Multicomponent, multiphase thermodynamics of swelling porous media with electroquasistatics: I. Macroscale field equations. *Transport in Porous Media* **47** (2002), 309–336.

[3] Bennethum, L. S. & Cushman, J. H.: Multicomponent, multiphase thermodynamics of swelling porous media with electroquasistatics: II. Constitutive theory. *Transport in Porous Media* **47** (2002), 337–362.

[4] Bertram, A.: An alternative approach to finite plasticity based on material isomorphisms. *International Journal of Plasticity* **15** (1999), 353–374.

[5] Bluhm, J.: *Ein Modell zur Berechnung geometrisch nichtlinearer Probleme der Elastoplastizität mit Anwendung auf ebene Stabtragwerke*. Dissertation, Fortschritt-Berichte VDI, Reihe 18, Nr. 94, VDI-Verlag, Düsseldorf 1991.

[6] de Boer, R.: *Vektor- und Tensorrechnung für Ingenieure.* Springer-Verlag, Berlin 1982.

[7] de Boer, R.: *Theory of Porous Media.* Springer-Verlag, Berlin 2000.

[8] Bowen, R. M.: Theory of mixtures. In Eringen, A. C. (ed.): *Continuum Physics.* Academic Press, New York 1976, vol. III, pp. 1–127.

[9] Chapman, S.: Rationalized mks system of units. *American Journal of Physics* **24** (1956), 162–166.

[10] Coleman, B. D. & Gurtin, M. E.: Thermodynamics with internal state variables. *Journal of Chemical Physics* **47** (1967), 597–613.

[11] Coleman, B. D. & Noll, W.: The thermodynamics of elastic materials with heat conduction and viscosity. *Archives for Rational Mechanics and Analysis* **13** (1963), 167–178.

[12] Cosserat, E. & Cosserat, F.: *Théorie des corps déformables.* A. Hermann et fils, Paris 1909, (Theory of Deformable Bodies, NASA TT F-11 561, 1968).

[13] Diebels, S.: *Mikropolare Zweiphasenmodelle: Formulierung auf der Basis der Theorie Poröser Medien.* Habilitation, Bericht Nr. II-4 aus dem Institut für Mechanik (Bauwesen), Universität Stuttgart 2000.

[14] Diebels, S. & Ehlers, W.: On fundamental concepts of multiphase micropolar materials. *Technische Mechanik* **16** (1996), 77–88.

[15] Ehlers, W.: Toward finite theories of liquid-saturated elasto-plastic porous media. *International Journal of Plasticity* **7** (1991), 443–475.

[16] Ehlers, W.: Constitutive equations for granular materials in geomechanical context. In Hutter, K. (ed.): *Continuum Mechanics in Environmental Sciences and Geophysics.* Springer-Verlag, Wien 1993, CISM Courses and Lectures No. 337, pp. 313–402.

[17] Ehlers, W.: *Vector and Tensor Calculus: An Introduction.* Lecture notes, Institute of Applied Mechanics (Chair of Continuum Mechanics), Universität Stuttgart, Germany 1995–2010, URL `http://www.mechbau.de`.

[18] Ehlers, W.: Grundlegende Konzepte in der Theorie Poröser Medien. *Technische Mechanik* **16** (1996), 63–76.

[19] Ehlers, W.: Foundations of multiphasic and porous materials. In Ehlers, W. & Bluhm, J. (eds.): *Porous Media: Theory, Experiments and Numerical Applications.* Springer-Verlag, Berlin 2002, pp. 3–86.

[20] Ehlers, W.: Challenges of porous media models in geo- and biomechanical engineering including electro-chemically active polymers and gels. *International Journal of Advances in Engineering Sciences and Applied Mathematics* **1** (2009), 1–24.

[21] Ericksen, J. L.: Tensor fields. In Flügge, S. (ed.): *Handbuch der Physik*. Springer-Verlag, Berlin 1960, vol. III/1, pp. 794–858.

[22] Eringen, A. C. & Kafadar, C. B.: Polar field theories. In Eringen, A. C. (ed.): *Continuum Physics*. Academic Press, New York 1976, vol. VI, pp. 1–73.

[23] Eringen, A. C. & Maugin, G. A.: *Electrodynamics of Continua I: Foundations and Solid Media*. Springer-Verlag, New-York 1990.

[24] Eringen, A. C. & Maugin, G. A.: *Electrodynamics of Continua II: Fluids and Complex Media*. Springer-Verlag, New-York 1990.

[25] Gibson, R. E.; England, G. L. & Hussey, M. J. L.: The theory of one-dimensional consolidation of saturated clays. *Géotechnique* **17** (1967), 261–273.

[26] Green, A. E. & Naghdi, P. M.: Some remarks on elastic-plastic deformation at finite strain. *International Journal of Engineering Sciences* **9** (1971), 1219–1229.

[27] Green, A. E. & Zerna, W.: *Theoretical Elasticity*. Oxford University Press 1968, 2nd edn.

[28] Hassanizadeh, S. M. & Gray, W. G.: General conservation equations for multi-phase-systems: 2. mass, momenta, energy and entropy equations. *Advances in Water Resources* **2** (1979), 191–203.

[29] Haupt, P.: On the concept of an intermediate configuration and its application to a representation of viscoelastic-plastic material behavior. *International Journal of Plasticity* **1** (1985), 303–316.

[30] Haupt, P.: *Continuum Mechanics and Theory of Materials*. Springer-Verlag, Berlin 2000.

[31] Haupt, P. & Tsakmakis, Ch.: On the application of dual variables in continuum mechanics. *Journal of Continuum Mechanics and Thermodynamics* **1** (1985), 165–196.

[32] Helmig, R.: *Multiphase Flow and Transport Processes in the Subsurface*. Springer-Verlag, Berlin 1997.

[33] Holzapfel, G. A.: *Nonlinear Solid Mechanics: A Continuum Approach for Engineering*. John Wiley & Sons, Chichester 2000.

[34] Huber, N. & Tsakmakis, Ch.: Finite deformation viscoelasticity laws. *Mechanics of Materials* **32** (2000), 1–18.

[35] Hughes, T. J. R. & Pister, K. S.: Consistent linearization in mechanics of solids and structures. *Computers and Structures* **8** (1978), 391–397.

[36] Hutter, K. & Jöhnk, K.: *Continuum Methods of Physical Modeling*. Springer-Verlag, Berlin 2004.

[37] Jackson, J. D.: *Classical Electrodynamics*. John Wiley & Sons, New York 1975, 2nd edn.

[38] Kelly, P. D.: A reacting continuum. *International Journal of Engineering Science* **2** (1964), 129–153.

[39] Kleiber, M.: Kinematics of deformation processes in materials subjected to finite elastic-plastic strains. *International Journal of Engineering Sciences* **13** (1975), 513–525.

[40] Klisch, S. M. & Hoger, A.: Volumetric growth of thermoelastic materials and mixtures. *Mathematics and Mechanics of Solids* **8** (2003), 377–402.

[41] Kovetz, A.: *Electromagnetic Theory*. Oxford University Press 2000.

[42] Landau, L. D.; Pitaevskii, L. P. & Lifshitz, E. M.: *Electrodynamics of Continuous Media*, vol. 8 of *Course of Theoretical Physics*. Elsevier Butterworth-Heinemann 1984, 2nd edn.

[43] Lee, E. H.: Elastic-plastic deformation at finite strains. *Journal of Applied Mechanics* **36** (1969), 1–6.

[44] Lion, A.: A physically based method to represent the thermomechanical behaviour of elastomers. *Acta Mechanica* **123** (1997), 1–25.

[45] Liu, I.-S.: *Continuum Mechanics*. Springer-Verlag, Berlin 2002.

[46] Lorentz, H. A.: The fundamental equations for electromagnetic phenomena in ponderable bodies deduced from the theory of electrons. *Proceedings of the Royal Netherlands Academy of Arts and Science, Amsterdam* **5** (1902), 254–266.

[47] Markert, B.: *Porous Media Viscoelasticity with Application to Polymeric Foams*. Dissertation, Report No. II-12 of the Institute of Applied Mechanics (CE), Universität Stuttgart, Germany 2005.

[48] Markert, B.: A biphasic continuum approach for viscoelastic high-porosity foams: Comprehensive theory, numerics, and application. *Archives of Computational Methods in Engineering* **15** (2008), 371–446.

[49] Maugin, G. A.: *Continuum Mechanics of Electromagnetic Solids*. North Holland - Elsevier, Amsterdam 1988.

[50] Maxwell, J. C.: A dynamical theory of the electromagnetic field. *Philosophical Transactions of the Royal Society of London* **155** (1865), 459–512, submitted in 1964.

[51] Miehe, C.: A constitutive frame of elastoplasticity at large strains based on the notion of a plastic metric. *International Journal of Solids and Structures* **35** (1998), 3859–3897.

[52] Miehe, C.: A formulation of finite elastoplasticity based on dual co- and contra-variant eigenvector triads normalized with respect to a plastic metric. *Computer Methods in Applied Mechanics and Engineering* **159** (1998), 223–260.

[53] Miehe, C. & Keck, J.: Superimposed finite elastic-viscoelastic-plastoelastic stress response with damage in filled rubbery polymers. Experiments, modelling and algorithmic implementation. *Journal of the Mechanics and Physics of Solids* **48** (2000), 323–365.

[54] Müller, I.: *Thermodynamics*. Pitman Publishing, Boston 1985.

[55] Müller, I.: Thermodynamics of mixtures and phase field theory. *International Journal of Solids and Structures* **38** (2001), 1105–1113.

[56] Oldroyd, J. G.: On the formulation of rheological equations of state. In *Proceedings of the Royal Society of London Series A*. 1950, vol. 200, pp. 523–541.

[57] Prandtl, L.: *Strömungslehre*. Friedrich Vieweg & Sohn, Braunschweig 1965.

[58] Reese, S. & Govindjee, S.: A theory of finite viscoelasticity and numerical aspects. *International Journal of Solids and Structures* **35** (1998), 3455–3482.

[59] Rodriguez, E. K.; Hoger, A. & McCulloch, A. D.: Stress-dependent finite growth in soft elastic tissues. *Journal of Biomechanics* **27** (1994), 455–467.

[60] Ruggeri, T.: Galilean invariance and entropy principle for systems of balance laws. The structure of extended thermodynamics. *Continuum Mechanics and Thermodynamics* **1** (1989), 3–20.

[61] Schlichting, H.: *Grenzschicht-Theorie*. G. Braun GmbH, Karlsruhe 1965, 5th edn.

[62] Sidoroff, F.: The geometrical concept of intermediate configuration and elastic-plastic finite strain. *Archives of Mechanics* **25** (1973), 299–308.

[63] Svendsen, B.: A thermodynamic formulation of finite-deformation elastoplasticity with hardening based on the concept of material isomorphism. *International Journal of Plasticity* **14** (1998), 473–488.

[64] le Tallec, P.; Rahier, C. & Kaiss, A.: Three-dimensional incompressible viscoelasticity in large strains: Formulation and numerical approximation. *Computer Methods in Applied Mechanics and Engineering* **109** (1993), 133–258.

[65] Truesdell, C.: Thermodynamics of diffusion. In Truesdell, C. (ed.): *Rational Thermodynamics*. Springer-Verlag, New York 1984, 2nd edn., pp. 219–236.

[66] Truesdell, C. & Noll, W.: In Antman, S. S. (ed.): *The Non-linear Field Theories of Mechanics*. Springer, Berlin 2004, 3rd edn.

[67] Truesdell, C. & Toupin, R. A.: The classical field theories. In Flügge, S. (ed.): *Handbuch der Physik*. Springer-Verlag, Berlin 1960, vol. III/1, pp. 226–902.

[68] Valanis, K. C.: Internal variable theory. In Valanis, K. C. (ed.): *Irreversible Thermodynamics of Continous Media.* Springer-Verlag, Wien 1971, CISM Courses and Lectures No. 77.

[69] Wriggers, P.: *Konsistente Linearisierung in der Kontinuumsmechanik und ihre Anwendung auf die Finite-Elemente-Methode.* Technischer Bericht Nr. F88/4, Forschungs- und Seminarberichte aus dem Bereich der Mechanik der Universität Hannover 1988.

# Part II

# A Selection of Coupled Problems
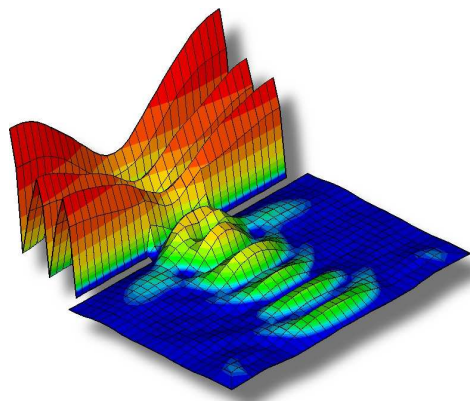


**Wave diffraction in
poroelastodynamics**
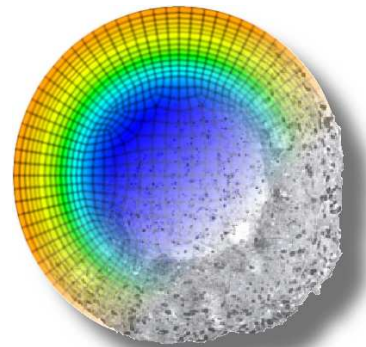
**Avascular growth
of a tumor spheroid**

# 3    Introductory Notes to Part II

SUMMARY

This chapter aims at giving a brief introduction to the selfcontained application problems collected in Part II of this thesis by establishing the link to the fundamental methods and approaches that are presented in Part I. Out of the many issues that can be addressed in the broad field of continuum physics, attention is exclusively called to specific multi-field and multi-physics problems being of topical interest in porous media mechanics, for which the general theoretical frame has been provided in Chapter 2.

## 3.1    The Strongly Coupled Problem of Poroelastodynamics

In Chapter 4, the numerical solution of wave propagation problems in porous media dynamics is investigated. The presentation proceeds from a saturated biphasic solid-fluid material with intrinsically incompressible constituents. The governing conservation laws and the constitutive equations are introduced in the framework of the Theory of Porous Media (TPM), see Sections 2.1 and 2.4.2, accounting for an elastic solid matrix and lingering flow conditions based on a geometrically and materially linear description. In particular, the natural set of equations comprises the solid and fluid momentum balances and the mixture volume balance as a continuity-like constraint for the determination of the primary unknowns, viz. solid displacement, fluid velocity, and pore-fluid pressure, plus the solid velocity-displacement relation, which is merely used for an order reduction in time, cf. Section 1.3.4. Due to the inherent solid-fluid momentum interactions, one is concerned with the class of volumetrically coupled problems (Section 1.3.1) involving a potentially strong coupling of the momentum equations and the algebraic incompressibility constraint in form of the volume balance. In fact, different formulations (uvp, uwp, and up) relying on different primal variables and governing equations are feasible, of which not all exhibit a computationally favorable structure, for instance, entailing a system of higher differential index, see Section 1.3.3. This is actually one of the reasons why an all-embracing numerical treatment of coupled problems by a general formalism is hard to accomplish.

For the numerical solution, the achieved sets of coupled partial differential equations (PDEs) are cast into a variational form yielding a general three-field initial boundary-value problem. The spatial semi-discretization is carried out by the mixed Finite Element Method (FEM) resulting in a stiff system of coupled differential-algebraic equations (DAEs) of first order in time (cf. Section 1.3.4) with the coupling strength mainly controlled by the permeability. For the further treatment of the time-continuous DAEs, two time-integration strategies out of the four introduced in Box (1.2) are applied: (1) an unconditionally stable implicit monolithic approach, where the equations are first discretized in space using stable mixed finite elements consistent with the LBB condition and sec-

ond in time using stiffly accurate implicit time integrators (Sections 1.2 and 1.3.4); (2) a conditionally stable semi-explicit-implicit splitting scheme as discussed in Section 1.4.2, which is implemented in form of a fractional-step method using a predictor-corrector algorithm according to Box (1.48). To this end, the DAEs are first discretized in time, split by means of intermediate variables, and then discretized in space using linear equal-order approximations for all primary unknowns.

Finally, a one- and a two-dimensional wave propagation example serve to reveal the pros and cons in regard to accuracy and stability of both solution strategies and their algorithmic implementations. Therefore, several test cases differing in the used multi-field formulation, the monolithic time-stepping method, and the approximation order of the individual unknowns are analyzed for varying degrees of coupling controlled by the permeability parameter.

## 3.2 Intrinsic Interactions in Hydrated Multi-Component Bio-Tissues

Chapter 5 is concerned with the description of the complex material behavior of biological tissues on the basis of the TPM, thus allowing for a detailed consideration of solid deformation, interstitial fluid flow, ion diffusion, and growth and degradation processes. In this regard, at first, charged hydrated bio-tissues or respective artificial substitutes, which show distinct swelling properties, are addressed and modeled as biphasic, four-component aggregates accounting for Donnan osmotic and electrostatic effects. In particular, this is accomplished by incorporating additional fields, namely the molar concentrations (see Section 2.1.2) of the fixed charges attached to the solid matrix and the mobile anions and cations of a dissolved salt in the pore-fluid solution. These are governed by concentration balances deduced from partial mass balances (cf. Box $(2.85)_1$) accompanied by appropriate constitutive laws describing the osmotic pressure contributions and the ion diffusion. Moreover, a scalar electric potential is introduced to enforce electroneutrality in the sense of a Lagrangean multiplier, where the Gauss's law for the mixture according to $(2.73)_7$ and the linear constitutive relation $(2.49)_3$ are exploited. The presented FE simulations of a free swelling hydrogel sample and a bulging nucleus pulposus out of a sagittally cut human intervertebral disc (IVD) are based on a straightforward monolithic solution strategy applying the scientific FE package PANDAS[1] tailored for the computation of strongly coupled DAE systems.

The second part of the chapter is then devoted to the modeling and simulation of the avascular stages of tumor growth. With respect to the complex metabolic processes governed by nutrient, angiogenic, and growth factors, it proves again to be expedient to continue with the macroscopic porous media approach instead of getting lost in the description of the physiochemical mechanisms at the cellular level. Thus, the hydrated organic tissue is treated as a biphasic aggregate constituted by a porous solid (tumor cells and extra-

---

[1] Porous media Adaptive Nonlinear finite element solver based on Differential Algebraic Systems, see http://www.get-pandas.com.

cellular matrix) which is permeated by an organic interstitial fluid mixture. Since the imbalances of production and degradation of the individual constituents associated with growth and necrosis of the tumor tissue are strongly influenced by several chemical factors (nutrients, enzymes etc.), the model incorporates two additional caloric state variables. These new variables are introduced as the "growth energies" compared to the thermodynamic temperatures and their energetically conjugate terms, the "configurational growth entropies" compared to the thermodynamic entropies. This actually represents a further consistent extension of the classical thermodynamic setting provided in Section 2.4 and is in the same way accessible to numerical solution by a variational FE approach. However, the couplings inherent in the arising five-field PDE system can only hardly be untangled, such that it is sensible to apply again an implicit monolithic solution procedure without really exploiting the multi-physics nature of the complex growth problem. How far it is possible to take algorithmically and computationally advantage of the different time scales involved, for instance, using operator splitting (Section 1.4.2) to separate the slow growth process from the fast biochemical reactions, is, however, out of the scope and not discussed in detail, thus remaining some area of unexplored space for further investigations.

# 3.3 Surface Interactions in Porous Media Contact

The objective of Chapter 6 is to derive convenient boundary conditions at the interface between two contacting fluid-saturated porous bodies on the basis of a discontinuity analysis in the framework of the TPM approach. In this regard, the special focus lies in the effects resulting from interstitial fluid penetration from one body into the other. Due to the fluid flux across the interface, the mated bodies interact and interchange by mass, linear momentum, and energy, thereby strongly influencing the coupling characteristics. Actually, this represents a generalization of the geometrically coupled problems discussed in Section 1.3.1. Here, two solid-fluid mixtures stay in mutual interaction via an interface region similar to the known structure-structure and fluid-structure interaction problems, which are naturally included as special cases in the presented porous media formalism. However, following such a macroscopic approach, the microtopography of the contact surface is not distinguished. More precisely, the surface microstructure of the contacting porous boundaries is only taken into account by limit boundary values of the volume fractions in the sense of an average macrocharacteristic of the real surface topography.

The derived jump conditions at the contact interface represent formal extensions of the thermodynamic balance principles given in Section 2.4.2 by describing the change of a physical quantity across a moving material discontinuity surface. In fact, the discontinuities are caused by the penetration of the pore fluid from one porous body into the other, where the order of the jumps is defined by products of the constituent velocities. For completeness, corresponding jump relations in the context of electrodynamics can be found in the references provided at the end of Section 2.3.3.

From a computational perspective, the efficient numerical solution of such surface-coupled problems suggests the application of a spatial partitioning strategy as discussed in Section 1.4.1. In this context, based on the derived jump condition for the total traction

force between the contacting mixture bodies incorporating the seepage flow across the interface together with respective kinematic constraints, a modular interface system can be formulated, for instance, using the localized $\lambda$-method similar to Equation (1.32).

## 3.4   Materially Coupled Phenomena in Cartilage

The last Chapter 7 pertains again to soft hydrated biological tissues, particularly cartilage, but in contrast to Chapter 5 puts more emphasize on the modeling of viscoelastic solid properties, anisotropic fiber reinforcements, and general tissue heterogeneities. In this regard, a model is presented which includes several levels of complexity, thereby having the advantage of meaningful and identifiable material parameters on the one hand and the possibility to describe arbitrary material behavior on the other hand. In particular, the presentation proceeds from a consistent biphasic TPM model in the realm of a geometrically and materially nonlinear description, which in a modular, nevertheless, general manner mimics all relevant habits of cartilaginous tissues. At this, polyconvex Ogden-type material formulations build the corner stone for the description of the anisotropic, collagen-reinforced, and intrinsically viscoelastic behavior of the extracellular solid matrix. The finite solid viscoelasticity model proceeds from a differential representation on the basis of the generalized Maxwell body as rheological analog. Moreover, other features such as a deformation-dependent permeability, the possibility to consider inhomogeneities like varying collagen-fiber alignment and behavior, as well as basic osmotic effects are also included. Accordingly, any complexity level concerning the mechanical behavior of the solid skeleton, i.e., viscoelasticity, elasticity, and anisotropy is possible. However, in view of the fact that the model is to be used on complex anatomic geometries in combination with other materials (e.g. hard bone tissue), simplifications are accepted regarding the electro-chemical coupling phenomena. Based on the assumption that biological tissues are instantaneously in chemical equilibrium (Lanir's assumption), the separate consideration of ion diffusion and the electric potential as in Chapter 5 is not required. Thus, a biphasic description suffices as the osmotic pressure can be determined depending on the salt concentration of the external solution and the deformation state of the tissue.

Finally, the human intervertebral disc is chosen as a representative for complex soft biological tissue behavior. In this regard, two numerical examples are presented with focus on the viscoelastic and osmotic capacity of the model. In regard of accuracy and stability issues, such a nonlinear and inelastic analysis is best performed by an implicit monolithic solution algorithm in combination with an efficient solver that exploits the capabilities of modern hardware architectures, cf. Section 1.2. Moreover, the fully coupled approach negates the need to transfer data from one solver to another, which helps to achieve good scalability on parallel systems. The procedure is also beneficial in the considered case of viscoelastic skeleton properties since the elaborate implicit Runge-Kutta (IRK) methods applied for the time stepping of the global FE system can as well be used for the time integration of the associated viscous rate equations, which are commonly evaluated at integration point level. In fact, as briefly addressed in Section 2.2.2, inelasticity can also be viewed as an inherent multi-field problem closely intertwined with the FE system.

# 4 Monolithic vs. Splitting Solutions in Porous Media Dynamics

## SUMMARY

Proceeding from the governing equations describing a saturated poroelastic material with intrinsically incompressible solid and fluid constituents, we compare the monolithic and splitting solution of the different multi-field formulations feasible in porous media dynamics. Due to the inherent solid-fluid momentum interactions, one is concerned with the class of volumetrically coupled problems involving a potentially strong coupling of the momentum equations and the algebraic incompressibility constraint. Here, the resulting set of differential-algebraic equations (DAEs) is solved by the Finite Element Method (FEM) following two different strategies: (1) an implicit monolithic approach, where the equations are first discretized in space using stable mixed finite elements and second in time using stiffly accurate implicit time integrators; (2) a semi-explicit-implicit splitting scheme in the sense of a fractional-step method, where the DAEs are first discretized in time, split using intermediate variables, and then discretized in space using linear equal-order approximations for all primary unknowns. Finally, a one- and a two-dimensional wave propagation example serve to reveal the pros and cons in regard to accuracy and stability of both solution strategies. Therefore, several test cases differing in the used multi-field formulation, the monolithic time-stepping method, and the approximation order of the individual unknowns are analyzed for varying degrees of coupling controlled by the permeability parameter. In the end, we provide a reliable recommendation which of the presented strategies and formulations is the most suitable for which particular dynamic porous media problem.

## 4.1  Introduction

The mechanical behavior of saturated porous solids, such as geomaterials like soil, is largely governed by the mutual interaction between the solid skeleton and the pore fluid. This interaction is particularly strong in dynamic problems and in the case of soils may lead to hazardous softening of the material known as liquefaction which is caused by a destabilizing pore-pressure increase and frequently occurs under earthquake loading. In essence, saturated porous materials represent biphasic aggregates consisting of interplaying solid and fluid constituents with individual states of deformation. Such multi-phase materials can properly be described within the thermodynamical consistent Theory of Porous Media (TPM) where all constituents are assumed to simultaneously occupy the spatial points in a representative elementary volume (REV). Hence, choosing the REV in a

way that allows the macroscopic characterization of the material, the averaged treatment of physical field variables in the TPM yields a volume-coupled continuum formulation. This is accomplished by recourse to Bowen's Theory of Mixtures (TM) [11] and the concept of volume fractions [58], where Drumheller [26] seems to be the first who applied this idea for the description of an empty porous medium. Later, Bowen [12, 13] extended this approach to fluid-saturated porous solids considering both compressible and incompressible constituents. Subsequent developments were mainly driven by geomechanical problems and have substantially been contributed by the works of de Boer and Ehlers, see [7, 27] for detailed references. It is worth mentioning that independent of these developments, the TM early found application also in other disciplines such as soft tissue biomechanics [47].

An alternative phenomenological approach that originates more from engineering deduction rather than from thermodynamic evaluation goes back to the pioneering works of Biot [5, 6], who described saturated soil as a binary porous medium and identified the coupling terms between the solid and the fluid phase under static and dynamic loading. In fact, Biot's Theory (BT) is basically confirmed by Bowen's TM and serves as the basis for a lot of research works on the general behavior of saturated and partially saturated porous materials, see Coussy [22] for particulars. It is interesting to note that under linear model assumptions, the TPM and BT proceed from almost identical governing equations except for some constitutive details [29, 55].

In regard to saturated porous media dynamics, the theoretical modeling and the numerical treatment have considerably been put forward by Zienkiewicz and coworkers [60, 61, 64], but also by Diebels & Ehlers [24], Breuer [15], and Li *et al.* [42] to name but a few. Analytical solutions for one-dimensional (1-d) wave propagation in saturated poroelastic media are given in [9, 53]. A recent review on poroelastodynamics can be found in Schanz [54].

Independent of the origin of the equations, the volume-averaged solid-fluid interaction in the biphasic macro model is described by a mutual momentum exchange resulting in a coupled set of conservation laws formulated either for the individual constituents or the entire mixture. However, against the background of an accurate and stable numerical solution of the multi-field problem, the choice of the primary variables and the associated conditional balance relations is neither evident nor unique. Commonly, so-called u-v-p, u-w-p, or reduced u-p formulations[1] are used which proceed from slightly different sets of governing partial differential equations (PDEs). Here, without at first insisting on a preferred formulation, we will start with the natural set of PDEs, namely the partial solid and fluid momentum balances and the volume balance of the mixture representing a continuity-like constraint for the considered saturated porous medium with incompressible constituents. Necessary modifications and possible variations will be discussed in the framework of the numerical solution procedure, where the Finite Element Method (FEM) is used as a convenient technique for the treatment of coupled problems, cf. [41]. In doing so, the spatial FE discretization of the general three-field (u-v-p or u-w-p) variational problem yields a stiff system of differential-algebraic equations (DAEs) in time. In fact,

---

[1] The abbreviations indicate the primary unknowns of the problem: u = solid displacement, v = fluid velocity, w = seepage velocity, p = pore-fluid pressure.

the semi-discrete volume balance as an algebraic side condition makes the problem ill-conditioned in a computational sense. In the literature, several works exist, however, mainly related to fluid-structure interaction, where coupled equation systems are defined or classified and suitable solution procedures are introduced, see, e. g., [31, 46].

In this contribution, two solution strategies for the strongly coupled dynamic problem are presented and compared, viz. a monolithic and a splitting solution scheme. In the monolithic approach, the system of equations is solved by one common strategy, where first the spatial FE discretization is carried out as described before yielding a time-continuous DAE system with a singular generalized mass matrix. Thus, only implicit time-integration schemes are appropriate, which in addition must account for the stiffness of the coupled equation system. This is accomplished by an efficient diagonal implicit Runge-Kutta (DIRK) time-stepping algorithm, for which different stiffly accurate integration rules are discussed. For more details on the solution of DAE systems in general and those arising from porous media problems in particular, see [25, 30, 35] and the quotations therein. One of the major disadvantages of the implicit monolithic procedure is the crucial requirement of stable mixed finite element formulations in order to avoid oscillations in the pressure variable originating from the inherent algebraic equations. In fact, the mixed elements must fulfill the Ladyzhenskaya-Babuška-Brezzi (LBB) condition [14, 16, 48] or the patch test of Zienkiewicz *et al.* [63].

The second strategy is out of the popular class of operator-splitting techniques, for which several aliases exist, e. g., fractional-step, projection, and pressure-correction method. The basic idea is to decouple the unfavorable volume balance from the momentum equations by advancing each time step via intermediate steps, which allows to separate the pore pressure solution from the kinematical unknowns, thereby providing stability. This demands the discretization in time to be carried out before that in space, but permits a continuous and equal-order interpolation of all primary variables. For the considered dynamic problem, we proceed from a semi-explicit-implicit approach, in which some of the advantages of the pure explicit and pure implicit schemes are realized and the disadvantages are reduced. However, due to the explicit steps, the method is only conditionally stable with the time-step size restricted by the Courant-Friedrichs-Lewy (CFL) condition [21], which depends on the mesh size and the wave speed in the considered medium. One of the first semi-explicit-implicit methods has been proposed by Chorin [20] followed by manifold enhancements in order to solve the incompressible Navier-Stokes equations in computational fluid dynamics (CFD). In this regard, we refer to the works of van Kan [56], Prohl [50], Rannacher [51], and Gresho & Sani [33]. Meanwhile, the splitting schemes have also been adopted by Zienkiewicz *et al.* [62] for the solution of saturated soil dynamic problems, where several solution algorithms have been proposed for the reduced u-p formulation. In particular, they differ in the way the pressure variable is treated in the split equations from a conditionally stable explicit to a stabilized implicit manner, see [38, 39] for details.

For the sake of completeness, we additionally refer to another class of solution procedures that are applied to porous media dynamics, viz. the time- and coupled space-time discontinuous Galerkin methods, which, however, seem not to be widespread. In fact, such methods are able to reproduce physically discontinuous phenomena occurring in

pore-fluid flow problems and show a wide potential to develop both coupled space-time adaptive strategies and simple decoupled adaptive methods based on residual- and/or gradient-based error estimation techniques, cf. [18, 19].

In summary, this chapter discusses the numerical solution of strongly coupled DAE systems arising from dynamic saturated porous media models with incompressible solid and fluid constituents. Without any limitations on the permeability controlling the strength of coupling, our investigations proceed from a general three-field (u-v-p) formulation based on the Theory of Porous Media. For convenience, the presentation is restricted to linear elastic skeleton properties and lingering flow conditions in the realm of a geometrically linear theory. The numerical treatment is based on a Galerkin variational finite element formulation of the governing balance relations. At this, particular focus is drawn to the structure of the resulting space-discrete DAE system and the inherent coupling terms, where modifications in the set of equations and primary unknowns are discussed concerning their influence on the numerical solution behavior. In this regard, two types of solution strategies with associated algorithms are presented: (1) an implicit monolithic scheme, where a stiffly accurate DIRK time-stepping algorithm is applied to the different semi-discrete formulations based on an equal- or mixed-order interpolation of the respective unknowns; (2) a semi-explicit-implicit splitting scheme which is realized in form of a predictor-corrector algorithm proceeding from a uniform linear FE approximation of the unknowns. Then, on the basis of two canonical wave propagation examples, we compile a comprehensive comparison of the accuracy and stability habits of the given algorithms and formulations for large and small values of the permeability parameter. As far as the authors are aware, neither a detailed discussion of monolithic and splitting solutions applied to the general three-field formulation nor a quantitative comparison of these methods and formulations exists in the related literature. In conclusion, our investigations clearly expose the merits and drawbacks of the presented approaches and provide a valuable decision support to find the appropriate solution strategy for a particular dynamic porous media problem.

To give an overview, in Section 2, the basics of the biphasic TPM model and the governing equations are presented. Section 3 is concerned with the variational formulation and the spatial semi-discretization by use of the FEM. The major contribution is in Section 4, which is devoted to the time discretization of the coupled problem giving a detailed description of the monolithic and splitting solution algorithms. The presented formulations and solution schemes are compared in Section 5 on a 1-d and 2-d wave propagation example followed by the conclusions in the last section.

## 4.2   Theoretical Basics

In preparation for a comprehensible introduction of the numerical solution procedures for dynamic porous media problems, some fundamentals of multiphasic continuum theories are briefly recapitulated including the basic concepts of the TPM approach, the mixture kinematics, and the governing balance and constitutive relations required in the sequel.

## 4.2.1  Theory of Porous Media (TPM)

For the purpose of this work but without loss of generality, we study the dynamic excitation of a biphasic porous body consisting of a solid skeleton saturated by a single interstitial fluid (pore fluid). The theoretical framework is provided by the macroscopic Theory of Porous Media (TPM), where a biphasic porous body is treated as a de facto immiscible mixture $\varphi$ of superimposed and interacting solid and fluid constituents $\varphi^\alpha$ ($\alpha = S$ : solid skeleton; $\alpha = F$ : pore fluid). In the macroscopic model, $\varphi = \varphi^S \cup \varphi^F$, the incorporated physical quantities are then understood as the local averages of their microscopic representatives, and the microstructural composition of the mixture is captured by local volumetric ratios (Figure 4.1). In particular, the volume fractions $n^\alpha := \mathrm{d}v^\alpha/\mathrm{d}v$ of $\varphi^\alpha$ are defined as the local ratios of the partial volume elements $\mathrm{d}v^\alpha$ with respect to the bulk volume element $\mathrm{d}v$ of $\varphi$. Apparently, assuming fully saturated conditions implies the saturation constraint to hold:

$$\sum_\alpha n^\alpha = n^S + n^F = 1 \quad \text{with} \quad \left\{ \begin{array}{ll} n^S & : \text{solidity}\,, \\ n^F & : \text{porosity}\,. \end{array} \right. \tag{4.1}$$

Here, we additionally proceed from $0 < n^\alpha < 1$, i.e., the transition of $\varphi$ to a singlephasic material (pure solid or fluid) is not considered. The introduction of the $n^\alpha$ is furthermore associated with two density functions, namely a material (effective or intrinsic) density $\rho^{\alpha R}$ and a partial density $\rho^\alpha$ relating the local mass of $\varphi^\alpha$ to the partial or the bulk volume element, respectively. It is easily concluded that $\rho^\alpha = n^\alpha \rho^{\alpha R}$, which underlines the general compressibility of porous solids through possible changes of the volume fractions.
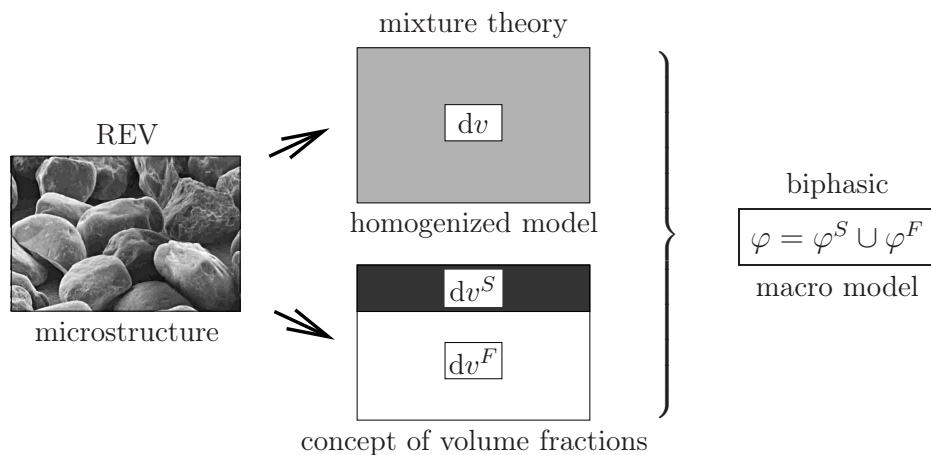


**Figure 4.1:** *REV with the granular microstructure of sand and the biphasic TPM macro model.*

## 4.2.2  Mixture Kinematics

Concerning the kinematics of mixtures, the idea of superimposed and interacting continua implies that, starting from different reference positions $\mathbf{X}_\alpha$ at time $t_0$, each constituent is

supposed to follow its unique individual Lagrangean (material) motion function $\boldsymbol{\chi}_\alpha$ and has its own velocity and acceleration fields, viz.:

$$\mathbf{x} = \boldsymbol{\chi}_\alpha(\mathbf{X}_\alpha, t) \;\Leftrightarrow\; \mathbf{X}_\alpha = \boldsymbol{\chi}_\alpha^{-1}(\mathbf{x}, t)\,, \quad \mathbf{v}_\alpha := \overset{\prime}{\mathbf{x}}_\alpha = \frac{\mathrm{d}_\alpha \mathbf{x}}{\mathrm{d}t}\,, \quad (\mathbf{v}_\alpha)_\alpha' = \overset{\prime\prime}{\mathbf{x}}_\alpha = \frac{\mathrm{d}_\alpha^2 \mathbf{x}}{\mathrm{d}t^2}\,. \quad (4.2)$$

Therein, supposing that $\boldsymbol{\chi}_\alpha$ is a local diffeomorphism, $\boldsymbol{\chi}_\alpha^{-1}$ represents the inverse (Eulerian or spatial) motion function and

$$(\,\cdot\,)_\alpha' := \frac{\mathrm{d}_\alpha(\,\cdot\,)}{\mathrm{d}t} = \frac{\partial(\,\cdot\,)}{\partial t} + \mathrm{grad}\,(\,\cdot\,)\,\mathbf{v}_\alpha \qquad \text{with} \qquad \mathrm{grad}\,(\,\cdot\,) = \frac{\partial(\,\cdot\,)}{\partial \mathbf{x}} \quad (4.3)$$

indicates the material time derivative following the motion of $\varphi^\alpha$. By virtue of $(4.2)_1$, each spatial point $\mathbf{x}$ of the current configuration at time $t$ is simultaneously occupied by material points of both constituents reflecting the overlay of the partial continua (Figure 4.2).
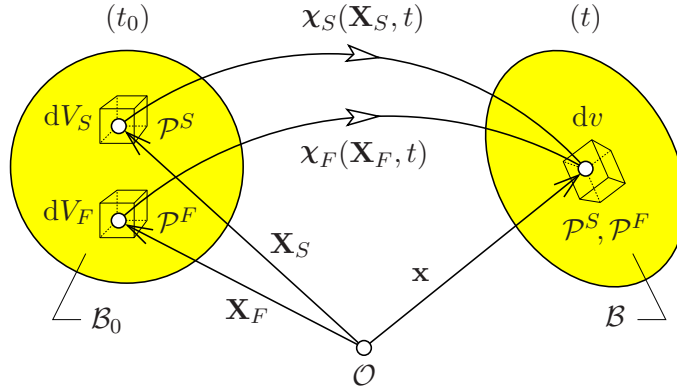


**Figure 4.2:** *Motion of a biphasic mixture.* $\mathrm{d}V_\alpha := \mathrm{d}v_{0\alpha}$ *is the reference bulk volume element with respect to an arbitrary initial state of the motion of* $\varphi^\alpha$ *at time* $t_0$.

In porous media theories, it is moreover convenient to proceed from a Lagrangean description of the solid matrix via the solid displacement $\mathbf{u}_S$ and velocity $\mathbf{v}_S$ as the kinematical variables. However, the pore-fluid flow is expressed either in a modified Eulerian setting via the seepage velocity vector $\mathbf{w}_{FR}$ describing the fluid motion relative to the deforming skeleton or by using the fluid velocity $\mathbf{v}_F$ itself. In detail, we have

$$\mathbf{u}_S = \mathbf{x} - \mathbf{X}_S\,, \quad \mathbf{v}_S = (\mathbf{u}_S)_S' = \overset{\prime}{\mathbf{x}}_S\,, \quad \mathbf{v}_F = \overset{\prime}{\mathbf{x}}_F\,, \quad \mathbf{w}_{FR} = \mathbf{v}_F - \mathbf{v}_S\,. \quad (4.4)$$

### 4.2.3   Governing Balance and Constitutive Relations

With regard to a clear and concise representation, the biphasic model excludes thermal effects as well as any mass exchanges (inert $\varphi^\alpha$) and proceeds from intrinsically incompressible constituents associated with $\rho^{\alpha R} = \mathrm{const}$. In particular, the arising purely mechanical binary model is governed by the following constituent balance equations $\forall\, \mathbf{x} \in \mathcal{B}$ and $\alpha = \{S, F\}$:

- Partial mass balance $\longrightarrow$ partial volume balance:

$$(\rho^\alpha)'_\alpha + \rho^\alpha \operatorname{div} \mathbf{v}_\alpha = 0 \quad \longrightarrow \quad (n^\alpha)'_\alpha + n^\alpha \operatorname{div} \mathbf{v}_\alpha = 0\,, \tag{4.5}$$

- Partial momentum balance:

$$\rho^\alpha (\mathbf{v}_\alpha)'_\alpha = \operatorname{div} \mathbf{T}^\alpha + \rho^\alpha\, \mathbf{b} + \hat{\mathbf{p}}^\alpha\,. \tag{4.6}$$

Herein, proceeding from materially incompressible $\varphi^\alpha$, the mass balance degenerates to a volume balance as $(n^\alpha \rho^{\alpha R})'_\alpha = (n^\alpha)'_\alpha\, \rho^{\alpha R}$ due to $(\rho^{\alpha R})'_\alpha \equiv 0$. In (4.6), $\mathbf{T}^\alpha = (\mathbf{T}^\alpha)^T$ is the symmetric partial Cauchy stress assuming non-polar materials and $\mathbf{b}$ is the mass-specific body force (here: constant gravitational acceleration) acting on the mixture. Moreover, $\hat{\mathbf{p}}^\alpha$ denotes the direct momentum production which can be interpreted as the volume-specific local interaction force between the percolating fluid and the solid skeleton, where, proceeding from a closed mixture system, $\hat{\mathbf{p}}^S + \hat{\mathbf{p}}^F = \mathbf{0}$ must hold due to the overall conservation of momentum. From $(4.5)_2$ with $\alpha = S$, one directly obtains the solidity as a secondary variable by analytical integration:

$$(n^S)'_S = -n^S \operatorname{div} \mathbf{v}_S \quad \longrightarrow \quad n^S = n^S_{0S}\, \det \mathbf{F}_S^{-1} \approx n^S_{0S}\, (1 - \operatorname{div} \mathbf{u}_S)\,. \tag{4.7}$$

Therein, $n^S_{0S}$ denotes the initial volume fraction of $\varphi^S$ at time $t_0$ and $\mathbf{F}_S = \partial \mathbf{x} / \partial \mathbf{X}_S$ is the solid deformation gradient. The second identity is valid in the geometrically linear case.

To continue, according to the principle of effective stresses, see [8] for references, $\mathbf{T}^\alpha$ and $\hat{\mathbf{p}}^F$ are split into effective field quantities, the so-called extra terms indicated by the subscript $(\,\cdot\,)_E$, and parts that are governed by the excess pore-fluid pressure $p$:

$$\mathbf{T}^\alpha = \mathbf{T}^\alpha_E - n^\alpha p\, \mathbf{I}\,, \quad \hat{\mathbf{p}}^F = \hat{\mathbf{p}}^F_E + p \operatorname{grad} n^F \tag{4.8}$$

with $\mathbf{I}$ as the 2nd-order identity tensor. Actually, (4.8) can be deduced from thermodynamic considerations, where $p$ enters the entropy principle for mixtures as a Lagrangean multiplier to preserve the saturation constraint (4.1) in the sense of a penalty per violation of a continuity-like condition. More precisely, the volume balance of the incompressible biphasic model,

$$-(n^S + n^F)'_S = \operatorname{div}(n^S \mathbf{v}_S + n^F \mathbf{v}_F) = \operatorname{div}(\mathbf{v}_S + n^F \mathbf{w}_{FR}) = 0\,, \tag{4.9}$$

takes over the role of an algebraic constraint of the coupled problem noting that

$$(\,\cdot\,)'_S = (\,\cdot\,)'_F - \operatorname{grad}(\,\cdot\,) \cdot \mathbf{w}_{FR}\,. \tag{4.10}$$

Next, against the background of a thermodynamically consistent model, admissible constitutive equations for the response functions $\mathbf{T}^\alpha_E$ and $\hat{\mathbf{p}}^F_E$ must be provided. For convenience, confining to the small strain regime, the solid extra stress is determined by the Hookean elasticity law,

$$\mathbf{T}^S_E = 2\mu^S\, \boldsymbol{\varepsilon}_S + \lambda^S\, (\boldsymbol{\varepsilon}_S \cdot \mathbf{I})\, \mathbf{I} \qquad \text{with} \qquad \boldsymbol{\varepsilon}_S = \tfrac{1}{2}\,(\operatorname{grad} \mathbf{u}_S + \operatorname{grad}^T \mathbf{u}_S) \tag{4.11}$$

as the geometrically linear solid strain tensor and $\mu^S$ and $\lambda^S$ as the macroscopic Lamé constants of the porous solid matrix. Moreover, it follows from a dimensional analysis that in a macroscopic porous media approach $\mathrm{div}\,\mathbf{T}_E^F \ll \hat{\mathbf{p}}_E^F$ (cf. [44]), i.e., $\mathbf{T}_E^F$ can a priori be neglected such that $\mathbf{T}^F = -n^F p\,\mathbf{I}$. Then, assuming isotropic, lingering flow conditions at low Reynolds numbers, the percolation process is appropriately described by a linear filter law (Darcy's law) which can be traced back to the simple but thermodynamically consistent ansatz

$$\hat{\mathbf{p}}_E^F = -\frac{(n^F)^2\,\gamma^{FR}}{k^F}\,\mathbf{w}_{FR}\,, \tag{4.12}$$

where $k^F > 0$ denotes the conventional hydraulic conductivity (Darcy permeability) in m/s and $\gamma^{FR} = \rho^{FR}g$ is the effective fluid weight with $g = |\mathbf{b}| = $ const. as the scalar gravitational acceleration. For continuative details see, e.g., [27] and the quotations therein.

In summary, inserting the above constitutive relations into (4.6) and using (4.10) to express the material time derivatives with respect to the solid motion, one obtains the natural set of coupled partial differential equations for the determination of the fields $\mathbf{u}_S, \mathbf{v}_S, \mathbf{v}_F$, and $p$:

- Solid displacement-velocity relation:

$$(\mathbf{u}_S)_S' = \mathbf{v}_S\,, \tag{4.13}$$

- Solid momentum balance:

$$\rho^S(\mathbf{v}_S)_S' = \mathrm{div}\,(\mathbf{T}_E^S - n^S p\,\mathbf{I}) + \rho^S\,\mathbf{b} + \frac{(n^F)^2\,\gamma^{FR}}{k^F}\,\mathbf{w}_{FR} - p\,\mathrm{grad}\,n^F\,, \tag{4.14}$$

- Fluid momentum balance:

$$\rho^F(\mathbf{v}_F)_S' + \rho^F(\mathrm{grad}\,\mathbf{v}_F)\,\mathbf{w}_{FR} = -n^F\mathrm{grad}\,p + \rho^F\,\mathbf{b} - \frac{(n^F)^2\,\gamma^{FR}}{k^F}\,\mathbf{w}_{FR}\,, \tag{4.15}$$

- Mixture volume balance:

$$\mathrm{div}\,(\mathbf{v}_S + n^F\mathbf{w}_{FR}) = 0\,. \tag{4.16}$$

Please note that depending on the choice of the primary unknowns, this set of equations is referred to as $\mathbf{u}_S$-$\mathbf{v}_F$-$p$ or $\mathbf{u}_S$-$\mathbf{w}_{FR}$-$p$ formulation. Thus, $\mathbf{v}_S(\mathbf{u}_S)$ as well as $\mathbf{T}_E^S(\mathbf{u}_S)$, $n^S(\mathbf{u}_S)$, $n^F(\mathbf{u}_S)$, and $\mathbf{w}_{FR}(\mathbf{v}_F)$ or $\mathbf{v}_F(\mathbf{w}_{FR})$, respectively, represent secondary variables.

In this context, it is worth mentioning that the general three-field description in some cases may be boiled down to a special bivariate formulation. For low and moderate frequencies, say below about 30 Hz[2], it is particularly for geomechanical problems convenient to assume the fluid acceleration almost identical to the solid acceleration, $(\mathbf{v}_F)_S' \approx (\mathbf{v}_S)_S'$, i.e.,

---

[2] Biot [6, Eq. (6.11)] introduced a critical frequency depending on the pore-fluid properties and the size of the pores in order to distinguish the low from the higher frequency range. Roughly speaking, as long as the apparent wavelength is considerably larger than the pore size, we are in the low frequency range associated with Poiseuille-type flow on the microscale.

$(\mathbf{w}_{FR})'_S \approx \mathbf{0}$, and revert instead to a simpler consolidation model based on the primary unknowns $\mathbf{u}_S$ and $p$, thereby accepting some additional error [41, 61]. In this case, the fluid momentum balance (4.15) just serves as an explicit equation for the filter velocity $n^F \mathbf{w}_{FR}$ which is then substituted into the other balances. In doing so, (4.14–4.16) are replaced by:

- Modified solid (or mixture) momentum balance:

$$(\rho^S + \rho^F)(\mathbf{v}_S)'_S = \operatorname{div}(\mathbf{T}_E^S - p\,\mathbf{I}) + (\rho^S + \rho^F)\,\mathbf{b}\,, \qquad (4.17)$$

- Modified mixture volume balance:

$$\operatorname{div}\left(\mathbf{v}_S - \frac{k^F}{g}\left[(\mathbf{v}_S)'_S - \mathbf{b}\right]\right) - \frac{k^F}{\gamma^{FR}}\Delta p = 0\,. \qquad (4.18)$$

Therein, $\Delta(\,\cdot\,) = \operatorname{div}\operatorname{grad}(\,\cdot\,)$ denotes the Laplace operator and the convective term and the porosity gradient were neglected as usual in linear analysis (cf. Section 4.4.1). In fact, for low permeability conditions with the pore fluid almost trapped in the solid matrix, this is a reasonable possibility to reduce the number of unknowns. Nevertheless, here we will proceed with the more general three-field description but the presented solution procedures can in the same way be applied to the simpler $\mathbf{u}_S$-$p$ formulation.

# 4.3 Weak Formulation and Spatial Discretization

## 4.3.1 Governing Weak Formulations

Following the idea of the FEM, (4.13 – 4.16) are transferred to weak formulations, where the weak form of (4.13) is merely introduced for a coherent representation of the subsequent discretization procedure. Therefore, the balance relations are weighted by independent test functions and integrated over the spatial domain $\Omega$ occupied by the mixture body $\mathcal{B}$. As usual, the surface $\Gamma = \partial\Omega$ is split into a *Dirichlet* (essential) and a *Neumann* (natural) boundary yielding $\Gamma = \Gamma_{\mathbf{u}_S} \cup \Gamma_{\mathbf{t}^S}$ and $\Gamma = \Gamma_{\mathbf{v}_F} \cup \Gamma_{\mathbf{t}^F}$ for the solid and fluid momentum balances, and $\Gamma = \Gamma_p \cup \Gamma_v$ for the mixture volume balance. Then, applying the product rule and the *Gauß*ian integral theorem, one obtains the weak forms as

$$\mathcal{G}_{(\mathbf{v}_S)}(\delta\mathbf{u}_S, \mathbf{u}_S, \mathbf{v}_S) \equiv \int_\Omega \delta\mathbf{u}_S \cdot [(\mathbf{u}_S)'_S - \mathbf{v}_S]\,\mathrm{d}v = 0\,, \qquad (4.19)$$

$$\mathcal{G}_{\mathbf{u}_S}(\delta\mathbf{u}_S, \mathbf{u}_S, \mathbf{v}_S, \mathbf{v}_F, p) \equiv \int_\Omega \operatorname{grad}\delta\mathbf{u}_S \cdot (\mathbf{T}_E^S - n^S p\,\mathbf{I})\,\mathrm{d}v - \int_{\Gamma_{\mathbf{t}^S}} \delta\mathbf{u}_S \cdot \overline{\mathbf{t}}^S\,\mathrm{d}a + $$
$$+ \int_\Omega \delta\mathbf{u}_S \cdot \left\{n^S \rho^{SR}\left[(\mathbf{v}_S)'_S - \mathbf{b}\right] - \frac{(n^F)^2\,\gamma^{FR}}{k^F}\left(\mathbf{v}_F - \mathbf{v}_S\right) + p\operatorname{grad}n^F\right\}\mathrm{d}v = 0\,, \qquad (4.20)$$

$$\mathcal{G}_{\mathbf{v}_F}(\delta\mathbf{v}_F, \mathbf{u}_S, \mathbf{v}_S, \mathbf{v}_F, p) \equiv -\int_\Omega \operatorname{div}\delta\mathbf{v}_F\, n^F p\,\mathrm{d}v - \int_{\Gamma_{\mathbf{t}^F}} \delta\mathbf{v}_F \cdot \overline{\mathbf{t}}^F\,\mathrm{d}a + $$
$$+ \int_\Omega \delta\mathbf{v}_F \cdot \left\{n^F \rho^{FR}\left[(\mathbf{v}_F)'_S - \mathbf{b} + \left(\operatorname{grad}\mathbf{v}_F + \frac{n^F g}{k^F}\,\mathbf{I}\right)(\mathbf{v}_F - \mathbf{v}_S)\right]\right\}\mathrm{d}v = 0\,, \qquad (4.21)$$

$$\mathcal{G}_p(\delta p, \mathbf{v}_S, \mathbf{v}_F) \equiv \int_{\Omega} \delta p \operatorname{div} \mathbf{v}_S \, \mathrm{d}v - \int_{\Omega} \operatorname{grad} \delta p \cdot n^F (\mathbf{v}_F - \mathbf{v}_S) \, \mathrm{d}v + \int_{\Gamma_v} \delta p \, \overline{v} \, \mathrm{d}a = 0 \,. \quad (4.22)$$

Herein, $\delta \mathbf{u}_S$, $\delta \mathbf{v}_F$, and $\delta p$ are the test functions which can be interpreted as virtual fields corresponding to the primary variables $\mathbf{u}_S$, $\mathbf{v}_F$, and $p$. In this context, note that $\mathbf{u}_S = \overline{\mathbf{u}}_S$ on $\Gamma_{\mathbf{u}_S}$, $\mathbf{v}_F = \overline{\mathbf{v}}_F$ on $\Gamma_{\mathbf{v}_F}$, and $p = \overline{p}$ on $\Gamma_p$ exactly fulfill the *Dirichlet* boundary conditions, whereas the test functions $\delta \mathbf{u}_S$, $\delta \mathbf{v}_F$, and $\delta p$ identically vanish on *Dirichlet* boundaries. Moreover, $\overline{\mathbf{t}}^S = (\mathbf{T}_E^S - n^S p \, \mathbf{I}) \, \mathbf{n}$ and $\overline{\mathbf{t}}^F = -n^F p \, \mathbf{n}$ are the external solid and fluid load vectors acting on the *Neumann* boundaries $\Gamma_{\mathbf{t}^S}$ and $\Gamma_{\mathbf{t}^F}$ with outward-oriented unit surface normal $\mathbf{n}$, and $\overline{v} = n^F \mathbf{w}_{FR} \cdot \mathbf{n}$ denotes the volume efflux of the incompressible fluid draining through the *Neumann* boundary $\Gamma_v$ of the mixture body. In this context, it seems at first sight to be more convenient to proceed also from the momentum balance of the whole mixture instead of using (4.20) as the surface traction $\overline{\mathbf{t}} = \overline{\mathbf{t}}^S + \overline{\mathbf{t}}^F$ would then concurrently act on both the solid and the fluid phase such that no separation of the boundary conditions is needed. However, in this case, the mass matrix of the semi-discrete system contains additional off-diagonal elements, which causes additional complexities and expenses when splitting solution schemes are to be used. Here, we substitute $\overline{\mathbf{t}}^S = \overline{\mathbf{t}} - \overline{\mathbf{t}}^F$ in (4.20) noting that $\overline{\mathbf{t}}^F = \overline{\mathbf{t}}^F(\mathbf{u}_S, p)$ represents an implicit boundary term which depends on the solution of the coupled problem. It is moreover apparent that in the case of a fully drained boundary $\overline{\mathbf{t}}^F \equiv \mathbf{0}$ as $\overline{p} \equiv 0$ on that boundary. It should also be noted that the boundary conditions in general cannot be chosen independent from each other as on overlapping boundaries, such as $\Gamma_p \cap \Gamma_{\mathbf{t}^F}$, the related *Dirichlet* and *Neumann* boundary conditions must be compatible.

Next, for the sake of a clear and compact representation, the weak formulations (4.19–4.22) are collected in a function vector $\boldsymbol{\mathcal{G}_u}$ and the unknown field variables are summarized in a vector of unknowns $\boldsymbol{u} = \boldsymbol{u}(\mathbf{x}, t)$:

$$\boldsymbol{\mathcal{G}_u} = \begin{bmatrix} \mathcal{G}_{(\mathbf{v}_S)} \\ \mathcal{G}_{\mathbf{u}_S} \\ \mathcal{G}_{\mathbf{v}_F} \\ \mathcal{G}_p \end{bmatrix} , \quad \boldsymbol{u} = \begin{bmatrix} \mathbf{u}_S \\ \mathbf{v}_S \\ \mathbf{v}_F \\ p \end{bmatrix} , \quad \delta \boldsymbol{u} = \begin{bmatrix} \delta \mathbf{u}_S \\ \delta \mathbf{v}_F \\ \delta p \end{bmatrix} , \quad (\boldsymbol{u})'_S = \begin{bmatrix} (\mathbf{u}_S)'_S \\ (\mathbf{v}_S)'_S \\ (\mathbf{v}_F)'_S \\ (p)'_S \end{bmatrix} , \quad \boldsymbol{u}_0 = \begin{bmatrix} \mathbf{u}_{S0} \\ \mathbf{v}_{S0} \\ \mathbf{v}_{F0} \\ p_0 \end{bmatrix} . \quad (4.23)$$

In this connection, one additionally introduces the corresponding vector of test functions $\delta \boldsymbol{u}$, the solid time derivative of the vector of unknowns $(\boldsymbol{u})'_S$, and its initial value $\boldsymbol{u}_0 = \boldsymbol{u}(\mathbf{x}, t_0)$. Actually, $\mathbf{v}_S = (\mathbf{u}_S)'_S$ will be strongly fulfilled and, just as the terms in $(\boldsymbol{u})'_S$, represents as secondary variable no additional degree of freedom (DOF) in the proper sense of a weak formulation. They only serve to transform the global set of equations into a system of first-order differential equations in time. Consequently, the three-field variational problem ($\mathbf{u}_S$-$\mathbf{v}_F$-$p$ formulation) can be rewritten in abstract form as follows:

$$\boxed{\text{Find} \quad \boldsymbol{u} \in \mathcal{S}_{\boldsymbol{u}}(t) \quad \text{such that} \quad \boldsymbol{\mathcal{G}_u}(\delta \boldsymbol{u}, \boldsymbol{u}) = \boldsymbol{0} \quad \forall \, \delta \boldsymbol{u} \in \mathcal{T}_{\boldsymbol{u}}, \ t \in [t_0, T] \,.} \quad (4.24)$$

Herein, $\mathcal{S}_{\boldsymbol{u}}(t)$ is the trial space for the external variables $\boldsymbol{u}$, $\mathcal{T}_{\boldsymbol{u}}$ is the test space for the corresponding test functions $\delta \boldsymbol{u}$, and $[t_0, T]$ is the considered time interval. Without going into mathematical details, the function spaces $\mathcal{S}_{\boldsymbol{u}}$ and $\mathcal{T}_{\boldsymbol{u}}$ must be chosen in such a way that the integrals involved in the definition of $\boldsymbol{\mathcal{G}_u}$ 'make sense'.

### 4.3.2 Finite Element Discretization

Now, for the solution of the variational problem (4.24), the Finite Element Method (FEM) is applied. Therefore, the spatial domain occupied by the mixture body $\mathcal{B}$ is subdivided into $N_e$ finite elements yielding an approximation of the continuous domain $\Omega$ by the discrete domain $\Omega^h$. This spatial semi-discretization yields a finite element mesh with $N_\mathbf{x}$ nodes for the geometry approximation, on which the following discrete trial and test functions are defined:

$$\boldsymbol{u}^h(\mathbf{x}, t) = \overline{\boldsymbol{u}}^h(\mathbf{x}, t) + \sum_{i=1}^{N_{\boldsymbol{u}}} \boldsymbol{N}_{\boldsymbol{u}(i)}(\mathbf{x})\, \boldsymbol{u}_{(i)}(t) \in \mathcal{S}_{\boldsymbol{u}}^h(t)\,,$$

$$\delta\boldsymbol{u}^h(\mathbf{x}) = \sum_{i=1}^{M_{\boldsymbol{u}}} \boldsymbol{M}_{\boldsymbol{u}(i)}(\mathbf{x})\, \delta\boldsymbol{u}_{(i)} \in \mathcal{T}_{\boldsymbol{u}}^h\,. \tag{4.25}$$

Therein, $\overline{\boldsymbol{u}}^h$ represents the approximated *Dirichlet* boundary conditions of the considered problem, $N_{\boldsymbol{u}}$ denotes the number of FE nodes used for the approximation of the respective fields in $\boldsymbol{u}$, and $\boldsymbol{N}_{\boldsymbol{u}(i)}$ represents the global basis functions at node $i$ which depend only on the spatial position $\mathbf{x}$, whereas the degrees of freedom $\boldsymbol{u}_{(i)}$ are the time-dependent nodal coefficients. Moreover, $M_{\boldsymbol{u}}$ is the number of FE nodes used for the test functions $\delta\mathbf{u}_S$, $\delta\mathbf{v}_F$, and $\delta p$, respectively, $\boldsymbol{M}_{\boldsymbol{u}(i)}$ denotes the global basis functions, and $\delta\boldsymbol{u}_{(i)}$ represents the corresponding nodal values of the test functions. Furthermore, $\mathcal{S}_{\boldsymbol{u}}^h(t)$ and $\mathcal{T}_{\boldsymbol{u}}^h$ are the discrete, finite-dimensional trial and test spaces. In this context, the *Bubnov-Galerkin* procedure is applied using the same basis functions $\boldsymbol{N}_{\boldsymbol{u}(i)} \equiv \boldsymbol{M}_{\boldsymbol{u}(i)}$ for the approximation of $\boldsymbol{u}$ and $\delta\boldsymbol{u}$, which implies that the trial and test spaces coincide except for the shift through the *Dirichlet* boundary conditions $\mathcal{S}_{\boldsymbol{u}}^h(t) = \overline{\boldsymbol{u}}^h + \mathcal{T}_{\boldsymbol{u}}^h$. However, the individual approximation spaces usually differ in the sense of a mixed method meaning that in general not all interpolation functions $\boldsymbol{N}_{\boldsymbol{u}(i)}$ coincide.

To continue, in the course of the FE discretization, the semi-discrete FE-*Galerkin* formulation of the variational problem (4.24) reads:

$$\boxed{\text{Find}\quad \boldsymbol{u}^h \in \mathcal{S}_{\boldsymbol{u}}^h(t) \quad \text{such that}\quad \boldsymbol{\mathcal{G}}_{\boldsymbol{u}}^h(\delta\boldsymbol{u}^h, \boldsymbol{u}^h) = \boldsymbol{0} \quad \forall\, \delta\boldsymbol{u}^h \in \mathcal{T}_{\boldsymbol{u}}^h,\ t \in [t_0, T]\,.} \tag{4.26}$$

To complete the spatial discretization procedure, the discrete trial and test functions must be specified by choosing an appropriate mixed finite element formulation. However, the suitable choice in regard to accuracy, stability, and computational costs is by no means trivial. Actually, it depends, inter alia, on the applied time-stepping algorithm and will therefore be revisited later. For some general particulars on mixed methods, where multiple discretization spaces are used to approximate the multiple primal variables of a problem, we refer to [1, 10, 14, 16, 33] among others.

## 4.4 Time Discretization of the Coupled Problem

A system of equations which consists of two or more interconnected subsystems, where an independent solution of any subsystem is impossible without simultaneous solution of

the others is called a coupled system. The coupling can be classified from weak to strong depending on the degree of subsystem interaction [46, 66], where a coupling is commonly regarded as strong if the solution depends significantly on the accuracy of the coupling term calculation [41]. In this context, an obvious coupled problem is that of dynamics in saturated porous materials, where neither the fluid nor the solid motion can be solved independently due to the mutual momentum exchanges governed by (4.12).

### 4.4.1   The Time-Continuous Coupled Problem

To make the inherent coupling of the problem more visible, we first rewrite (4.26) in descriptive matrix form. Therefore, (4.25) is given in a shortened representation using the following abbreviations for the approximated fields and related quantities:

$$
\boldsymbol{u}^h = \begin{bmatrix} \boldsymbol{U}\,\mathsf{u}_S \\ \boldsymbol{U}\,\mathsf{v}_S \\ \boldsymbol{V}\,\mathsf{v}_F \\ \boldsymbol{P}\,\mathsf{p} \end{bmatrix}, \quad (\boldsymbol{u}^h)'_S = \begin{bmatrix} \boldsymbol{U}\,\dot{\mathsf{u}}_S \\ \boldsymbol{U}\,\dot{\mathsf{v}}_S \\ \boldsymbol{V}\,\dot{\mathsf{v}}_F \\ \boldsymbol{P}\,\dot{\mathsf{p}} \end{bmatrix}, \quad \operatorname{grad}\boldsymbol{u}^h = \begin{bmatrix} \nabla\boldsymbol{U}\,\mathsf{u}_S \\ \nabla\boldsymbol{U}\,\mathsf{v}_S \\ \nabla\boldsymbol{V}\,\mathsf{v}_F \\ \nabla\boldsymbol{P}\,\mathsf{p} \end{bmatrix},
$$

$$
\delta\boldsymbol{u}^h = \begin{bmatrix} \boldsymbol{U}\,\delta\mathsf{u}_S \\ \boldsymbol{V}\,\delta\mathsf{v}_F \\ \boldsymbol{P}\,\delta\mathsf{p} \end{bmatrix}, \quad \operatorname{grad}\delta\boldsymbol{u}^h = \begin{bmatrix} \nabla\boldsymbol{U}\,\delta\mathsf{u}_S \\ \nabla\boldsymbol{V}\,\delta\mathsf{v}_F \\ \nabla\boldsymbol{P}\,\delta\mathsf{p} \end{bmatrix}.
$$

(4.27)

Herein, $\boldsymbol{U},\boldsymbol{V},\boldsymbol{P}$ represent the interpolation functions corresponding to the nodal unknowns of the FE mesh $\mathsf{u}_S,\mathsf{v}_S = \dot{\mathsf{u}}_S,\mathsf{v}_F$, and $\mathsf{p}$ with associated test functions $\delta\mathsf{u}_S,\delta\mathsf{v}_F$, and $\delta\mathsf{p}$. Moreover, we define $(\,\cdot\,)^{\boldsymbol{\cdot}} := (\,\cdot\,)'_S$ and $\nabla(\,\cdot\,) := \operatorname{grad}(\,\cdot\,)$. Note that the Dirichlet boundary conditions $\overline{\boldsymbol{u}}^h$ in (4.25) are explicitly fulfilled during the assembling of the FE system and need not to be considered in the sequel. Thus, the space-discrete system (4.26) yields in matrix form

$$
\boldsymbol{\mathcal{G}}_{\boldsymbol{u}}^h = \underbrace{\begin{bmatrix} \boldsymbol{I} & 0 & 0 & 0 \\ 0 & \boldsymbol{M}_{22} & 0 & 0 \\ 0 & 0 & \boldsymbol{M}_{33} & 0 \\ 0 & 0 & 0 & 0 \end{bmatrix}}_{\boldsymbol{M}} \underbrace{\begin{bmatrix} \dot{\mathsf{u}}_S \\ \dot{\mathsf{v}}_S \\ \dot{\mathsf{v}}_F \\ \dot{\mathsf{p}} \end{bmatrix}}_{\dot{\boldsymbol{y}}} + \underbrace{\begin{bmatrix} 0 & -\boldsymbol{I} & 0 & 0 \\ \boldsymbol{K}_{21} & \boldsymbol{K}_{22} & \boldsymbol{K}_{23} & \boldsymbol{K}_{24} \\ 0 & \boldsymbol{K}_{32} & \boldsymbol{K}_{33} & \boldsymbol{K}_{34} \\ 0 & \boldsymbol{K}_{42} & \boldsymbol{K}_{43} & 0 \end{bmatrix}}_{\boldsymbol{K}} \underbrace{\begin{bmatrix} \mathsf{u}_S \\ \mathsf{v}_S \\ \mathsf{v}_F \\ \mathsf{p} \end{bmatrix}}_{\boldsymbol{y}} - \underbrace{\begin{bmatrix} 0 \\ \boldsymbol{b}_2 + \boldsymbol{f}_S \\ \boldsymbol{b}_3 + \boldsymbol{f}_F \\ \boldsymbol{f}_p \end{bmatrix}}_{\boldsymbol{f}} = \boldsymbol{0}\,.
$$

(4.28)

Herein, the semi-discrete momentum balances build the first two differential subsystems (2nd and 3rd row), whereas the mixture volume balance (4th row) enters (4.28) as an algebraic subsystem leading to a system of coupled differential-algebraic equations (DAEs) in time. It is quite evident that the stiffness submatrices $\boldsymbol{K}_{ij}$ can easily be distinguished into coupling terms (highlighted) and non-coupling or internal terms. Focusing on the

coupling expressions only, they read:

$$
\boldsymbol{K}_{23} = -\int_{\Omega^h} \boldsymbol{U}^T \frac{(n^F)^2 \gamma^{FR}}{k^F} \boldsymbol{V} \, \mathrm{d}v \, , \quad \boldsymbol{K}_{24} = -\int_{\Omega^h} \nabla \boldsymbol{U}^T n^S \boldsymbol{P} \, \mathrm{d}v \, ,
$$

$$
\boldsymbol{K}_{32} = -\int_{\Omega^h} \boldsymbol{V}^T \frac{(n^F)^2 \gamma^{FR}}{k^F} \boldsymbol{U} \, \mathrm{d}v \, , \quad \boldsymbol{K}_{34} = -\int_{\Omega^h} \nabla \boldsymbol{V}^T n^F \boldsymbol{P} \, \mathrm{d}v \, , \tag{4.29}
$$

$$
\boldsymbol{K}_{42} = \int_{\Omega^h} \boldsymbol{P}^T \nabla \boldsymbol{U} \, \mathrm{d}v + \int_{\Omega^h} \nabla \boldsymbol{P}^T n^F \boldsymbol{U} \, \mathrm{d}v \, , \quad \boldsymbol{K}_{43} = -\int_{\Omega^h} \nabla \boldsymbol{P}^T n^F \boldsymbol{V} \, \mathrm{d}v \, .
$$

It is obvious that the subsystem interaction is very sensitive to changes in the permeability parameter, where small values of $k^F$ provoke a strong coupling and increase the stiffness of the problem. The remaining terms are not directly affected by rough parameter values and in the geometrically linear regime are only subjected to mild changes. In this regard, by virtue of $(4.7)_2$ with $\mathbf{u}_S := \epsilon \, \mathbf{u}_S$ and small values $\epsilon \geq 0$, we have $n^\alpha(\mathbf{u}_S) \approx n^\alpha_{0S} = \mathrm{const.}$, $\mathrm{grad}\, n^\alpha \approx \mathbf{0}$, and thus, no direct contribution to $\boldsymbol{K}$. By the same arguments, the nonlinear convective term $\mathrm{grad}\, \mathbf{v}_F \, (\mathbf{v}_F - \mathbf{v}_S)$ is omitted, which actually corresponds to a formal linearization of the model. Essentially, it is convenient to consider $\boldsymbol{M}$ and $\boldsymbol{K}$ as almost constant under infinitesimal conditions being aware of the fact that they in general are implicit functions of the nodal unknowns. Moreover, in (4.28), $\boldsymbol{K}_{21}$ contains the constant elastic solid tangent, $\boldsymbol{K}_{22}, \boldsymbol{K}_{33}$ and $\boldsymbol{M}_{22}, \boldsymbol{M}_{33}$ are non-coupling stiffness and mass submatrices, $\boldsymbol{b}_2, \boldsymbol{b}_3$ represent the apparent body force contributions, and $\boldsymbol{f}_S, \boldsymbol{f}_F, \boldsymbol{f}_p$ are the space-discrete Neumann boundary terms.

Next, in preparation for the time discretization, let $\boldsymbol{y} = [\mathbf{u}_S, \mathbf{v}_S, \mathbf{v}_F, \mathbf{p}]^T \in \mathbb{R}^m$ with $m = \dim(\boldsymbol{y})$ represent all nodal degrees of freedom $\boldsymbol{u}_{(i)}(t)$ of the FE mesh (recall (4.25)). Then, the DAE system (4.28) takes the abstract form

$$
\boldsymbol{F}(t, \boldsymbol{y}, \dot{\boldsymbol{y}}) \equiv \boldsymbol{\mathcal{G}}^h_{\boldsymbol{u}}(t, \boldsymbol{y}, \dot{\boldsymbol{y}}) \equiv \boldsymbol{M} \, \dot{\boldsymbol{y}} + \boldsymbol{K} \, \boldsymbol{y} - \boldsymbol{f} \overset{!}{=} \boldsymbol{0} \tag{4.30}
$$

with $\boldsymbol{M}$ and $\boldsymbol{K}$ as generalized mass and stiffness matrices, and $\boldsymbol{f}$ as generalized external force vector. In the considered case of a materially incompressible description, $\boldsymbol{M}$ (and for the moment also $\boldsymbol{K}$) does not possess the full rank as no evolution equation for the pore pressure exists and, as a consequence, $\boldsymbol{M}$ has no entry corresponding to $\dot{\mathbf{p}}$ (algebraic coupling). Accordingly, an explicit monolithic solution is not possible such that proceeding from a strongly coupled problem (realistic values $0 < k^F \ll 1$ provided) only some implicit monolithic or splitting time integration scheme is appropriate. Following this, for the solution of the time-continuous initial-value problem

$$
\boxed{\text{Find} \quad \boldsymbol{y}(t) \in \mathbb{R}^m \quad \text{such that} \quad \boldsymbol{F}\big[t, \boldsymbol{y}, \dot{\boldsymbol{y}}\big] = \boldsymbol{0} \, , \quad \boldsymbol{y}(t_0) = \boldsymbol{y}_0 \quad \forall \, t \in [t_0, T]} \tag{4.31}
$$

the considered time interval is divided into a finite number of subintervals $[t_n, t_{n+1}]$ with time-step size $\Delta t_n = t_{n+1} - t_n > 0$, on which (4.31) is successively solved according to the time-stepping algorithms discussed in the following subsections.

### 4.4.2    Implicit Monolithic Time-Integration Scheme

In (4.28), the algebraic equation, i.e., the space-discrete volume balance, is independent of the pressure variable. This causes problems for the monolithic time integration as it makes (4.28) a DAE system of higher differential index [30]. An order reduction to an index-1 DAE is achieved by solving the fluid momentum balance (4.15) with respect to the filter velocity $n^F \mathbf{w}_{FR}$ on the right hand side and replacing it into the weak form of the mixture volume balance (4.22) yielding

$$
\mathcal{G}_p(\delta p, \mathbf{v}_S, \mathbf{v}_F, p) \equiv \int_\Omega \delta p \, \mathrm{div} \, \mathbf{v}_S \, \mathrm{d}v + \int_{\Gamma_v} \delta p \, \overline{v} \, \mathrm{d}a +
$$
$$
+ \int_\Omega \mathrm{grad} \, \delta p \cdot \frac{k^F}{g} \Big( \frac{1}{\rho^{FR}} \mathrm{grad} \, p + (\mathbf{v}_F)'_S - \mathbf{b} \Big) \, \mathrm{d}v = 0 \, ,
\tag{4.32}
$$

where the convective term was directly omitted. Moreover, the fluid traction $\overline{\mathbf{t}}^F = -n^F p \, \mathbf{n}$ in the boundary term of the solid momentum balance $\overline{\mathbf{t}}^S = \overline{\mathbf{t}} - \overline{\mathbf{t}}^F$ is treated implicitly within the domain and, as before, the fluid momentum balance (4.15) is inserted such that (4.20) yields the suitable form of a ('convectiveless') mixture momentum balance:

$$
\mathcal{G}_{\mathbf{u}_S}(\delta\mathbf{u}_S, \mathbf{u}_S, \mathbf{v}_S, \mathbf{v}_F, p) \equiv \int_\Omega \mathrm{grad} \, \delta\mathbf{u}_S \cdot (\mathbf{T}_E^S - p\,\mathbf{I}) \, \mathrm{d}v - \int_{\Gamma_{\mathbf{t}^S}} \delta\mathbf{u}_S \cdot \overline{\mathbf{t}} \, \mathrm{d}a +
$$
$$
+ \int_\Omega \delta\mathbf{u}_S \cdot \big\{ n^S \rho^{SR} [(\mathbf{v}_S)'_S - \mathbf{b}] + n^F \rho^{FR} [(\mathbf{v}_F)'_S - \mathbf{b}] \big\} \, \mathrm{d}v = 0 \, .
\tag{4.33}
$$

This manipulation removes the destabilizing off-diagonal entry $\boldsymbol{K}_{23}$ containing the factor $1/k^F$, which has a favorable effect on the condition of the system. In fact, proceeding with the original solid momentum balance (4.20) would yield oscillations and even wrong numerical solutions of the pressure field for low values of the permeability (see Section 4.5). Note that (4.33) could also be directly achieved by first adding the solid and fluid momentum balances (4.14) and (4.15) and then building the weak form (cf. [24]). The resulting changes to the structure of the DAE system are again best displayed in matrix form,

$$
\mathcal{G}_{\boldsymbol{u}}^h = \underbrace{\begin{bmatrix} \boldsymbol{I} & 0 & 0 & 0 \\ 0 & \boldsymbol{M}_{22} & \boldsymbol{M}_{23} & 0 \\ 0 & 0 & \boldsymbol{M}_{33} & 0 \\ 0 & 0 & \boldsymbol{M}_{43} & 0 \end{bmatrix}}_{\boldsymbol{M}} \underbrace{\begin{bmatrix} \dot{\mathbf{u}}_S \\ \dot{\mathbf{v}}_S \\ \dot{\mathbf{v}}_F \\ \dot{\mathbf{p}} \end{bmatrix}}_{\dot{\boldsymbol{y}}} + \underbrace{\begin{bmatrix} 0 & -\boldsymbol{I} & 0 & 0 \\ \boldsymbol{K}_{21} & 0 & 0 & \boldsymbol{K}_{24} \\ 0 & \boldsymbol{K}_{32} & \boldsymbol{K}_{33} & \boldsymbol{K}_{34} \\ 0 & \boldsymbol{K}_{42} & 0 & \boldsymbol{K}_{44} \end{bmatrix}}_{\boldsymbol{K}} \underbrace{\begin{bmatrix} \mathbf{u}_S \\ \mathbf{v}_S \\ \mathbf{v}_F \\ \mathbf{p} \end{bmatrix}}_{\boldsymbol{y}} - \underbrace{\begin{bmatrix} 0 \\ \boldsymbol{b}_2 + \boldsymbol{f}_S \\ b_3 + f_F \\ \boldsymbol{b}_4 + f_p \end{bmatrix}}_{\boldsymbol{f}} = \boldsymbol{0} \, ,
\tag{4.34}
$$

where the new or modified terms are highlighted. The affected coupling submatrices read:

$$
\boldsymbol{M}_{23} = \int_{\Omega^h} \boldsymbol{U}^T n^F \rho^{FR} \boldsymbol{V} \, \mathrm{d}v \, , \quad \boldsymbol{M}_{43} = -\int_{\Omega^h} \nabla \boldsymbol{P}^T \frac{k^F}{g} \boldsymbol{V} \, \mathrm{d}v \, ,
$$
$$
\boldsymbol{K}_{24} = -\int_{\Omega^h} \nabla \boldsymbol{U}^T \boldsymbol{P} \, \mathrm{d}v \, , \quad \boldsymbol{K}_{42} = \int_{\Omega^h} \boldsymbol{P}^T \nabla \boldsymbol{U} \, \mathrm{d}v \, , \quad \boldsymbol{K}_{44} = \int_{\Omega^h} \nabla \boldsymbol{P}^T \frac{k^F}{\gamma^{FR}} \nabla \boldsymbol{P} \, \mathrm{d}v \, .
\tag{4.35}
$$

In this regard, it is worth mentioning that a change in the primary unknowns from $\mathbf{v}_F$ to $\mathbf{w}_{FR}$ would, on the one hand, further 'enhance' the generalized stiffness matrix in (4.34) as $1/k^F$ then solely occurs in the diagonal term $\boldsymbol{K}_{33}$. However, on the other hand, this would yield additional entries $\boldsymbol{M}_{32}$ and $\boldsymbol{M}_{42}$ in the generalized mass matrix, where it is observed that the $\mathbf{u}_S$-$\mathbf{w}_{FR}$-$p$ formulation is more vulnerable to instabilities in the pressure variable. In fact, $\boldsymbol{M}_{42}$ depends on $k^F$ yielding an additional source for instabilities particularly under high permeability conditions if marginally stable time integrators are used (see Section 4.5 and also [49]). Therefore, we stick to the presented $\mathbf{u}_S$-$\mathbf{v}_F$-$p$ formulation and keep tabs on the $1/k^F$ expression in $\boldsymbol{K}_{32}$.

Coming back to the spatial semi-discretization, the simultaneous approximation of the primary unknowns $\mathbf{u}_S$, $\mathbf{v}_F$, and $p$ entails the usage of the mixed FEM, which is known to exhibit a great robustness with respect to the roughness of the coefficients of the equations. However, the considered three-field variational principle yields a saddle-point problem rather than an extremal problem. More precisely, the minimization of the energy functionals is subject to a side condition, namely the saturation constraint in form of the volume balance, such that the space-discrete system is indefinite, which excludes the direct application of standard solution methods. To furthermore overcome the instability problem of mixed formulations [1], i.e., to avoid non-physical oscillations in the pore pressure caused by spurious pressure modes [16], in case of the monolithic solution, we choose Taylor-Hood-like elements with a quadratic approximation of $\mathbf{u}_S$ and $\mathbf{v}_S$ and linear approximations of $\mathbf{v}_F$ and $p$ which fulfill the discrete version of the inf-sup or *Ladyzhenskaya-Babuška-Brezzi* (LBB) condition (cf. [33] for references) or the more pragmatic patch test for mixed formulations of Zienkiewicz *et al.* [63], respectively. In the context of stable mixed FE approximations, it is moreover worth to mention the MINI element of Arnold [1] which in lieu of a quadratic approximation proceeds from a linear interpolation of $\mathbf{u}_S$ and $\mathbf{v}_S$ extended by barycentric bubble nodes in triangular or tetrahedral elements. Basically, the additional bubble functions enrich the corresponding trial space thereby guaranteeing stability [14, 48]. For a comparative study of the MINI element applied to porous media problems, see [45].

An alternative approach which proceeds from uniform linear interpolation functions is feasible if the overall volume balance is extended in the sense of adding some artificial compressibility to the mixture[3]. It is apparent from $(4.35)_5$ that the $\boldsymbol{K}_{44}$ entry in (4.34) tends towards zero if $k^F$ becomes very small, which is the root cause for the pressure instability. In a reverse conclusion, for large enough permeabilities $\boldsymbol{K}_{44}$ stabilizes the pressure solution even in the case of a linear equal-order approximation. In this regard, to overcome the instability problem for the more interesting low permeability case, one extends the original volume balance (4.16), viz.

$$\operatorname{div}\left(\mathbf{v}_S + n^F \mathbf{w}_{FR}\right) - \epsilon \, \Delta p = 0 \qquad (4.36)$$

with $\epsilon \geq 0$ being a small parameter controlling the influence of the Laplacian. In fact,

---

[3] Note that the instability problem can be totally avoided by reverting to porous media models with a compressible fluid phase. This entails an additional constitutive law that uniquely assigns the effective fluid density to the present pressure state and vice versa, e.g., $\rho^{FR} = \rho^{FR}(p)$ in the case of a barotropic fluid [45]. Thus, additional terms $\boldsymbol{M}_{44}$ and $\boldsymbol{K}_{44}$, which are independent of $k^F$, enter the semi-discrete system (4.34) that consequently boils down to an ODE system.

this is comparable to the pressure stabilization or quasi-compressibility methods used in computational fluid dynamics (CFD) [50, 51]. Proceeding with (4.36) in the same way as before, the sensitive stiffness term now becomes

$$\boldsymbol{K}_{44} = \int_{\Omega^h} \nabla \boldsymbol{P}^T \alpha \, \nabla \boldsymbol{P} \, \mathrm{d}v \quad \text{with} \quad \alpha := \left( \frac{k^F}{\gamma^{FR}} + \epsilon \right) \geq \alpha_{\min} \,. \tag{4.37}$$

Herein, $\alpha_{\min} > 0$ is associated with a 'moderately small' permeability large enough to prevent oscillations in the pressure variable. Its magnitude can be estimated against the poroelastic pressure wave speed in the discretized domain. A detailed discussion on that will be presented in the context of the splitting method in the next section. It should further be noted that the stabilization term $\epsilon \, \Delta p$ also causes an additional boundary term $\operatorname{grad} p \cdot \mathbf{n}$ which vanishes on impermeable boundaries. For further reading on stabilized monolithic schemes in porous media dynamics, we refer to [39].

To continue, in order to integrate large DAE systems of index 1, one-step $s$-stage diagonally-implicit *Runge-Kutta* (DIRK) methods provide suitable means at moderate storage and computational costs as they allow the solution of the stage equations in a decoupled fashion [25, 30]. In this connection, with regard to a proper treatment of the included algebraic equations, stiffly accurate methods are appropriate being aware of certain stability requirements to guarantee the accurate time integration with large time steps. A straightforward method would be the implicit (backward) Euler (IE) scheme which, however, is deemed as inappropriate for the time stepping of dynamic problems due to its considerable artificial numerical damping. Another common possibility would be the 2nd-order accurate trapezoidal rule (TR) which shows no damping but is only marginally stable (no L-stability) so that the time-step size has to be limited, e. g., by tightening the error tolerances. Therefore, the method of choice is the TR-BDF2 method [3] as a composite integration scheme combining the advantages of both the trapezoidal rule and the 2nd-order backward difference formula (BDF2) which can be easily recast in the framework of Runge-Kutta (RK) methods [37]. The representation in Butcher tableaus [17] yields:

$$
\begin{array}{c|ccc}
c_1 & a_{11} & \cdots & a_{1s} \\
\vdots & \vdots & \ddots & \vdots \\
c_s & a_{s1} & \cdots & a_{ss} \\
\hline
& b_1 & \cdots & b_s
\end{array}
\qquad
\begin{array}{c|c}
0 & 0 \\
1 & 1 \\
\hline
& 1
\end{array}
\qquad
\begin{array}{c|cc}
0 & 0 & 0 \\
1 & \frac{1}{2} & \frac{1}{2} \\
\hline
& \frac{1}{2} & \frac{1}{2}
\end{array}
\qquad
\begin{array}{c|ccc}
0 & 0 & 0 & 0 \\
\theta & \frac{\theta}{2} & \frac{\theta}{2} & 0 \\
1 & \frac{3\theta - \theta^2 - 1}{2\theta} & \frac{1-\theta}{2\theta} & \frac{\theta}{2} \\
\hline
& \frac{3\theta - \theta^2 - 1}{2\theta} & \frac{1-\theta}{2\theta} & \frac{\theta}{2}
\end{array}
\tag{4.38}
$$

$$\text{Butcher tableau} \qquad\qquad \text{IE} \qquad\qquad \text{TR} \qquad\qquad \text{TR-BDF2 with } \theta = 2 - \sqrt{2}$$

In fact, TR-BDF2 (and also TR) is almost a singly diagonal-implicit Runge-Kutta (SD-IRK) method, which is advantageous for mildly nonlinear systems as it allows the reusability of previously factorized matrices, which may drastically reduce the required solution time. Hence, applying a stiffly accurate $s$-stage DIRK method, the initial-value problem (4.31) with the modifications as per (4.34) is successively solved according to the following

time-step algorithm:

---

**Time-step algorithm of a stiffly accurate $s$-stage DIRK method**

*Given:* coefficients $c_i, a_{ij}, b_j = a_{sj}$ of a stiffly accurate $s$-stage DIRK method, approximate solution $\boldsymbol{y}_n \approx \boldsymbol{y}(t_n)$ at time $t_n$, time-step size $\Delta t_n$

*Find:* approximate solution $\boldsymbol{y}_{n+1} \approx \boldsymbol{y}(t_{n+1})$ at time $t_{n+1}$

*Step 1:* for each *Runge-Kutta* stage $i = 1, ..., s$

(a) set stage time $T_{ni} := t_n + c_i\, \Delta t_n$ and
accumulated stage derivative $\overline{\boldsymbol{Y}}_{ni} := \Delta t_n \sum\limits_{j=1}^{i-1} a_{ij} \dot{\boldsymbol{Y}}_{nj}$

(b) solve nonlinear system for stage increments $\Delta\boldsymbol{Y}_{ni}$
$$\boldsymbol{R}_{ni}(\Delta\boldsymbol{Y}_{ni}) \equiv \boldsymbol{F}\left(T_{ni},\ \boldsymbol{y}_n + \Delta\boldsymbol{Y}_{ni},\ \frac{1}{\Delta t_n\, a_{ii}}\left[\Delta\boldsymbol{Y}_{ni} - \overline{\boldsymbol{Y}}_{ni}\right]\right) = \boldsymbol{0}$$

(c) set stage derivative $\dot{\boldsymbol{Y}}_{ni} := \dfrac{1}{\Delta t_n\, a_{ii}}\left[\Delta\boldsymbol{Y}_{ni} - \overline{\boldsymbol{Y}}_{ni}\right]$

*Step 2:* set $\boldsymbol{y}_{n+1} := \boldsymbol{Y}_{ns} = \boldsymbol{y}_n + \Delta\boldsymbol{Y}_{ns}$ and $t_{n+1} := T_{ns}$

(4.39)

---

In this context, it is evident from the Butcher tableaus (4.38) that TR-BDF2 and TR have a singular coefficient matrix $[a_{ij}]$. Nevertheless, they can be treated by the DIRK algorithm (4.39) by simply skipping the first RK stage as $c_1 = a_{11} = 0$, and thus, $T_{n1} = t_n$, $\boldsymbol{Y}_{n1} = \boldsymbol{y}_n$ and $\Delta\boldsymbol{Y}_{n1} = \dot{\boldsymbol{Y}}_{n1} = \boldsymbol{0}$. It should further be noted that for a current time step $n$, instead of the stage solutions $\boldsymbol{Y}_{ni}$, the stage increments $\Delta\boldsymbol{Y}_{ni} := \boldsymbol{Y}_{ni} - \boldsymbol{y}_n$ are used as unknowns to reduce round-off errors during the solution of the time-discrete system in step 1(b) [35, IV.8]. In contrast, the accumulated stage derivatives $\overline{\boldsymbol{Y}}_{ni}$ depend only on previously computed quantities, and thus, are constant for the current *Runge-Kutta* stage $i$. Apparently, the main computational effort is in the solution of the generally nonlinear system in step 1(b) of (4.39). For its efficient solution with the *Newton-Raphson* method, the derivative of the nonlinear vector function $\boldsymbol{R}_{ni}(\Delta\boldsymbol{Y}_{ni})$ with respect to the stage increments $\Delta\boldsymbol{Y}_{ni}$ is required. The *Jacobi*an matrix takes the form

$$\boldsymbol{J}_{ni} := \frac{\mathrm{d}\boldsymbol{R}_{ni}}{\mathrm{d}\Delta\boldsymbol{Y}_{ni}} = \frac{1}{\Delta t_n\, a_{ii}} \left.\frac{\partial\boldsymbol{F}}{\partial\dot{\boldsymbol{y}}}\right|_{\boldsymbol{z}} + \left.\frac{\partial\boldsymbol{F}}{\partial\boldsymbol{y}}\right|_{\boldsymbol{z}}, \tag{4.40}$$

where $\boldsymbol{z} = \{T_{ni}, \boldsymbol{Y}_{ni}, \boldsymbol{Y}'_{ni}\}$ denotes the current set of arguments of $\boldsymbol{F}$ in $\boldsymbol{R}_{ni}$. However, the biphasic model under study proceeds from geometrical as well as material linearities, so that

$$\left.\frac{\partial\boldsymbol{F}}{\partial\dot{\boldsymbol{y}}}\right|_{\boldsymbol{z}} = \boldsymbol{M} \approx \text{const.}, \quad \left.\frac{\partial\boldsymbol{F}}{\partial\boldsymbol{y}}\right|_{\boldsymbol{z}} = \boldsymbol{K} \approx \text{const.} \quad \longrightarrow \quad \boldsymbol{J}_{ni} = \frac{1}{\Delta t_n\, a_{ii}}\boldsymbol{M} + \boldsymbol{K}, \tag{4.41}$$

and thus, the discrete sparse FEM system, $\boldsymbol{R}_{ni}(\Delta\boldsymbol{Y}_{ni}) = \boldsymbol{0}$, is already linear and can be solved by common means. For the general nonlinear case, in the Newton iteration procedure, for each Newton step $k$ of the current RK stage $i$ of the current time step $n$, $\Delta\boldsymbol{Y}_{ni}^k = -(\boldsymbol{J}_{ni}^k)^{-1}\boldsymbol{R}_{ni}^k$ has to be solved until a suitable convergence criterion, such

as $\|\boldsymbol{R}_{ni}^k\| < TOL_{\boldsymbol{R}}$ or $\|\Delta \boldsymbol{Y}_{ni}^k\| < TOL_{\boldsymbol{y}}$, is met. For further particulars on embedded and error-controlled DIRK methods applied to the solution of inelastic and geometrically nonlinear problems, see, e.g., [25, 28, 30, 36, 45] and the quotations therein.

### 4.4.3  Semi-Explicit-Implicit Splitting Scheme

In dynamic problems, small time steps are usually needed in order to get a correct description of the applied dynamic load. This situation coincides with explicit time-integration schemes or those strategies including explicit steps which for stability reasons are subject to crucial time-step size restrictions. However, as already mentioned, due to the algebraic coupling, the holistic application of explicit time integrators to the entire space-discrete system (4.28) is not possible. To overcome this problem, splitting methods can be used to separate the constituent momentum balances from the algebraic saturation constraint by decoupling the displacement and velocity fields $\mathbf{u}_S, \mathbf{v}_S$, and $\mathbf{v}_F$ from the pore-fluid pressure $p$. The splitting is accomplished by introducing constituent intermediate velocities $\mathbf{v}_\alpha^*$ which represent an approximation to the velocities in the next time step. In contrast to the monolithic scheme, the differential operator-splitting technique, which allows the decoupling of physical phenomena in complex initial boundary-value problems (IBVP), first demands the time discretization and second the spatial FE discretization of the decoupled equations.

**Time Discretization and Splitting**

Starting from the governing set of balance equations $(4.13-4.16)$ and adopting the established splitting algorithms used to solve the incompressible Navier-Stokes equations [20, 33, 34, 50], the splitting is carried out by advancing each time step in multiple steps (fractional-step method), such that $\{\mathbf{v}_{\alpha n}, p_n, \mathbf{u}_{S n}\} \to \mathbf{v}_\alpha^* \to \{\mathbf{v}_{\alpha n+1}, p_{n+1}, \mathbf{u}_{S n+1}\}$. Similar strategies have already been successfully applied to soil dynamic problems based on the reduced $\mathbf{u}_S$-$p$ formulation, see, e.g., [38, 39]. In porous media dynamics, it is furthermore rational to perform the time discretization of the decoupled subproblems on the basis of a semi-explicit-implicit approach. To this end, we begin with a standard implicit time discretization of the solid displacement-velocity relation (4.13) by applying the trapezoidal rule:

$$\frac{(\mathbf{u}_{S n+1} - \mathbf{u}_{S n})}{\Delta t_n} = \tfrac{1}{2} \left(\mathbf{v}_{S n+1} + \mathbf{v}_{S n}\right). \tag{4.42}$$

Next, in the solid momentum balance (4.14) with $n^\alpha \approx n_{0S}^\alpha$, $\operatorname{grad} n^F \approx \mathbf{0}$ (cf. Section 4.4.1), and $\mathbf{b} = \text{const.}$, the extra stress is treated explicitly, $\mathbf{T}_{E n}^S := \mathbf{T}_E^S(\mathbf{u}_{S n})$ according to (4.11), the pressure term is considered implicitly, and the seepage velocity is discretized in time with the aid of the intermediate velocities, i.e., $\mathbf{w}_{FR}^* = \mathbf{v}_F^* - \mathbf{v}_S^*$:

$$\rho^S \frac{(\mathbf{v}_{S n+1} - \mathbf{v}_{S n})}{\Delta t_n} = \operatorname{div} \mathbf{T}_{E n}^S - n^S \operatorname{grad} p_{n+1} + \rho^S \mathbf{b} + \frac{(n^F)^2 \gamma^{FR}}{k^F} \mathbf{w}_{FR}^* . \tag{4.43}$$

Then, exploiting the solid intermediate velocity $\mathbf{v}_S^*$ enables the splitting of (4.43) into

$$\rho^S \frac{(\mathbf{v}_S^* - \mathbf{v}_{S n})}{\Delta t_n} = \operatorname{div} \mathbf{T}_{E n}^S - n^S \operatorname{grad} p_n + \rho^S \mathbf{b} + \frac{(n^F)^2 \gamma^{FR}}{k^F} \left(\mathbf{v}_F^* - \mathbf{v}_S^*\right), \tag{4.44}$$

$$\rho^S \frac{(\mathbf{v}_{Sn+1} - \mathbf{v}_S^*)}{\Delta t_n} = -n^S \mathrm{grad}(p_{n+1} - p_n) \,. \tag{4.45}$$

Applying the same procedure to the fluid momentum balance (4.15) with omitted convective term (cf. Section 4.4.1), we have

$$\rho^F \frac{(\mathbf{v}_{Fn+1} - \mathbf{v}_{Fn})}{\Delta t_n} = -n^F \mathrm{grad}\, p_{n+1} + \rho^F \mathbf{b} - \frac{(n^F)^2 \gamma^{FR}}{k^F} \mathbf{w}_{FR}^* \,, \tag{4.46}$$

such that with the fluid intermediate velocity $\mathbf{v}_F^*$, one obtains

$$\rho^F \frac{(\mathbf{v}_F^* - \mathbf{v}_{Fn})}{\Delta t_n} = -n^F \mathrm{grad}\, p_n + \rho^F \mathbf{b} - \frac{(n^F)^2 \gamma^{FR}}{k^F} (\mathbf{v}_F^* - \mathbf{v}_S^*) \,, \tag{4.47}$$

$$\rho^F \frac{(\mathbf{v}_{Fn+1} - \mathbf{v}_F^*)}{\Delta t_n} = -n^F \mathrm{grad}(p_{n+1} - p_n) \,. \tag{4.48}$$

The remaining mixture volume balance (4.16) is again treated fully implicitly:

$$\mathrm{div}\,(n^S \mathbf{v}_{Sn+1} + n^F \mathbf{v}_{Fn+1}) = 0 \,. \tag{4.49}$$

Note that the intermediate treatment of the seepage velocity gives (4.44) and (4.47) an implicit character in the respective intermediate velocity and makes the choice of the time-step size independent of the actual permeability. If instead $\mathbf{w}_{FR}$ is considered explicitly, additional improvements for the low permeability case are necessary as, e. g., described by Li *et al.* [43]. Moreover, the consideration of $\mathrm{grad}\, p_n$ in the sense of a predictor in (4.44) and (4.47) is commonly referred to as Chorin-Uzawa scheme [50] which is in line with the incremental projection schemes à la Goda [32], van Kan [56], or Rannacher [51], see also [34]. Essentially, inserting (4.45) and (4.48) into the volume balance (4.49) results in a Poisson-like equation for the pore-fluid pressure. It is also worth mentioning that a reformulation of (4.49) such as for the monolithic scheme (cf. Section 4.4.2) has no beneficial effect on the solution behavior.

**Weak Formulation**

To continue, the above time discrete relations except for the solid displacement-velocity relation (4.42) are transferred to weak formulations as in Section 4.3.1. They finally read:

- Split solid momentum balance:

$$\int_\Omega \delta\mathbf{u}_S \cdot \left\{ n^S \rho^{SR} \left[ \frac{(\mathbf{v}_S^* - \mathbf{v}_{Sn})}{\Delta t_n} - \mathbf{b} \right] - \frac{(n^F)^2 \gamma^{FR}}{k^F} (\mathbf{v}_F^* - \mathbf{v}_S^*) \right\} \mathrm{d}v +$$
$$+ \int_\Omega \mathrm{grad}\, \delta\mathbf{u}_S \cdot (\mathbf{T}_{En}^S - n^S p_n \mathbf{I})\, \mathrm{d}v - \int_{\Gamma_{\mathbf{t}^S}} \delta\mathbf{u}_S \cdot \overline{\mathbf{t}}_n^S\, \mathrm{d}a = 0 \,, \tag{4.50}$$

$$\int_\Omega \delta\mathbf{u}_S \cdot \left[ \rho^{SR} \frac{(\mathbf{v}_{Sn+1} - \mathbf{v}_S^*)}{\Delta t_n} + \mathrm{grad}(p_{n+1} - p_n) \right] \mathrm{d}v = 0 \,, \tag{4.51}$$

■ Split fluid momentum balance:

$$\int_{\Omega} \delta\mathbf{v}_F \cdot n^F \rho^{FR} \Big[ \frac{(\mathbf{v}_F^* - \mathbf{v}_{F\,n})}{\Delta t_n} - \mathbf{b} + \frac{n^F g}{k^F}(\mathbf{v}_F^* - \mathbf{v}_S^*) + \frac{1}{\rho^{FR}}\operatorname{grad} p_n \Big] \mathrm{d}v = 0\,,$$
(4.52)

$$\int_{\Omega} \delta\mathbf{v}_F \cdot n^F \rho^{FR} \frac{(\mathbf{v}_{F\,n+1} - \mathbf{v}_F^*)}{\Delta t_n} \mathrm{d}v -$$
$$- \int_{\Omega} \operatorname{div} \delta\mathbf{v}_F \, n^F (p_{n+1} - p_n) \, \mathrm{d}v - \int_{\Gamma_{\mathbf{t}^F}} \delta\mathbf{v}_F \cdot \widetilde{\mathbf{t}}_{n+1}^F \, \mathrm{d}a = 0\,,$$
(4.53)

■ Mixture volume balance:

$$\int_{\Omega} \delta p \operatorname{div} \mathbf{v}_S^* \, \mathrm{d}v + \int_{\Gamma_v} \delta p\, \widetilde{v}_{n+1} \, \mathrm{d}a -$$
$$- \int_{\Omega} \operatorname{grad} \delta p \cdot \Big[ n^F(\mathbf{v}_F^* - \mathbf{v}_S^*) - \Delta t_n \Big(\frac{n^F}{\rho^{FR}} + \frac{n^S}{\rho^{SR}}\Big) \operatorname{grad}(p_{n+1} - p_n) \Big] \mathrm{d}v = 0\,.$$
(4.54)

Herein, the weak form of the mixture volume balance has been reformulated by use of (4.9) and substitution of $\mathbf{v}_{S\,n+1}$ and $\mathbf{v}_{F\,n+1}$ as given by (4.45) and (4.48), respectively. The included time discrete boundary terms read as follows:

$$\overline{\mathbf{t}}_n^S = (\mathbf{T}_{E\,n}^S - n^S p_n \, \mathbf{I})\,\mathbf{n}\,, \quad \widetilde{\mathbf{t}}_{n+1}^F = -n^F(p_{n+1} - p_n)\,\mathbf{n}\,,$$
$$\widetilde{v}_{n+1} = \Big[ n^F(\mathbf{v}_{F\,n+1} - \mathbf{v}_{S\,n+1}) - \frac{\Delta t_n}{\rho^{SR}} \operatorname{grad}(p_{n+1} - p_n) \Big] \cdot \mathbf{n}\,.$$
(4.55)

Apparently, the treatment of the volume efflux $\widetilde{v}_{n+1}$ is not that straight-forward as for the monolithic case. However, the majority of initial boundary-value problems proceeds either from undrained (no-flow) boundaries with $n^F \mathbf{w}_{FR} \cdot \mathbf{n} \equiv 0$ and $\operatorname{grad} p \cdot \mathbf{n} \equiv 0$ or fully permeable conditions with $p \equiv 0$, such that (4.55) simplify accordingly (recall Section 4.3.1).

## Spatial Discretization

For the spatial discretization, the strong form (4.42) and the weak forms (4.50 – 4.54) are treated in the same way as before using again the concise notations (4.27) of Section 4.4.1. As the splitting procedure requires also the approximation of the intermediate velocities, we additionally proceed from $(\mathbf{v}_S^*)^h = \boldsymbol{U}\, \mathbf{v}_S^*$ and $(\mathbf{v}_F^*)^h = \boldsymbol{V}\, \mathbf{v}_F^*$. Herein, the nodal values $\mathbf{v}_S^*$ and $\mathbf{v}_F^*$ must not be regarded as genuine DOFs of the problem as for them no boundary conditions exist and the associated conditional equations (4.50) and (4.52) just represent fractions of the physical balance relations. Finally, the discrete equations read as follows:

■ Solid displacement-velocity relation:

$$\frac{\mathbf{u}_{S\,n+1} - \mathbf{u}_{S\,n}}{\Delta t_n} - \tfrac{1}{2}(\mathbf{v}_{S\,n+1} - \mathbf{v}_{S\,n}) = \boldsymbol{0}\,.$$
(4.56)

- Split solid momentum balance:

$$M_{22} \frac{\mathsf{v}_S^* - \mathsf{v}_{S\,n}}{\Delta t_n} + K_{21}\,\mathsf{u}_{S\,n} + K_{22}\,\mathsf{v}_S^* + K_{23}\,\mathsf{v}_F^* + K_{24}\,\mathsf{p}_n - b_2 - f_{S\,n} = 0\,, \quad (4.57)$$

$$M_{22} \frac{\mathsf{v}_{S\,n+1} - \mathsf{v}_S^*}{\Delta t_n} + \widetilde{K}_{24}\,(\mathsf{p}_{n+1} - \mathsf{p}_n) = 0\,. \qquad (4.58)$$

- Split fluid momentum balance:

$$M_{33} \frac{\mathsf{v}_F^* - \mathsf{v}_{F\,n}}{\Delta t_n} + K_{32}\,\mathsf{v}_S^* + K_{33}\,\mathsf{v}_F^* + \widetilde{K}_{34}\,\mathsf{p}_n - b_3 = 0\,, \qquad (4.59)$$

$$M_{33} \frac{\mathsf{v}_{F\,n+1} - \mathsf{v}_F^*}{\Delta t_n} + K_{34}\,(\mathsf{p}_{n+1} - \mathsf{p}_n) - \widetilde{f}_{F\,n+1} = 0\,. \qquad (4.60)$$

- Mixture volume balance:

$$K_{42}\,\mathsf{v}_S^* + K_{43}\,\mathsf{v}_F^* + \widetilde{K}_{44}\,(\mathsf{p}_{n+1} - \mathsf{p}_n) - \widetilde{f}_{p\,n+1} = 0\,. \qquad (4.61)$$

Herein, the mass and stiffness matrices $M_{ik}$ and $K_{ik}$ as well as the load vectors $b_i$ and $f_S$ coincide with those in (4.28). In addition, the splitting procedure induces the following terms:

$$\widetilde{K}_{24} = \int_{\Omega^h} U^T \nabla P \,\mathrm{d}v\,, \quad \widetilde{K}_{34} = \int_{\Omega^h} V^T n^F \nabla P \,\mathrm{d}v\,,$$

$$\widetilde{K}_{44} = \int_{\Omega^h} \nabla P^T \Delta t_n \Big( \frac{n^F}{\rho^{FR}} + \frac{n^S}{\rho^{SR}} \Big) \nabla P \,\mathrm{d}v\,, \qquad (4.62)$$

$$\widetilde{f}_{F\,n+1} = \int_{\Gamma_{\mathbf{t}^F}^h} V^T \widetilde{\mathbf{t}}_{n+1}^F \,\mathrm{d}a\,, \quad \widetilde{f}_{p\,n+1} = \int_{\Gamma_v^h} P^T \widetilde{v}_{n+1} \,\mathrm{d}a\,.$$

For the further treatment, we exploit the beneficial property of splitting methods which permit a continuous and equal-order interpolation to be used for all occurring fields. Thus, proceeding from uniform linear interpolation functions, i.e., $U = V = P$ and $\nabla U = \nabla V = \nabla P$, it is easily deduced that $K_{22} = -K_{23} = -K_{32} = K_{33} =: \overline{K}$ and that the discrete equations (4.57) and (4.59) simplify accordingly:

$$M_{22} \frac{\mathsf{v}_S^* - \mathsf{v}_{S\,n}}{\Delta t_n} + K_{21}\,\mathsf{u}_{S\,n} + \overline{K}\,\mathsf{v}_S^* - \overline{K}\,\mathsf{v}_F^* + K_{24}\,\mathsf{p}_n - b_2 - f_{S\,n} = 0\,, \qquad (4.63)$$

$$M_{33} \frac{\mathsf{v}_F^* - \mathsf{v}_{F\,n}}{\Delta t_n} - \overline{K}\,\mathsf{v}_S^* + \overline{K}\,\mathsf{v}_F^* + \widetilde{K}_{34}\,\mathsf{p}_n - b_3 = 0\,. \qquad (4.64)$$

By some simple algebraic manipulations, equations (4.63) and (4.64) can now be solved with respect to the intermediate velocities yielding the explicit relations

$$\begin{aligned}
\mathsf{v}_S^* &= \mathsf{v}_{S\,n} + h_1(\mathsf{u}_{S\,n}, \mathsf{v}_{S\,n}, \mathsf{v}_{F\,n}, \mathsf{p}_n, \Delta t_n)\,, \\
\mathsf{v}_F^* &= \mathsf{v}_{F\,n} + h_2(\mathsf{u}_{S\,n}, \mathsf{v}_{S\,n}, \mathsf{v}_{F\,n}, \mathsf{p}_n, \Delta t_n)\,,
\end{aligned} \qquad (4.65)$$

where for a concise representation the remainder expressions are collected in the auxiliary functions $h_1$ and $h_2$ which only depend on known quantities of time $t_n$.

**Predictor-Corrector Algorithm**

The semi-explicit-implicit splitting scheme can be very conveniently implemented in form of the predictor-corrector (P-C) algorithm given in box (4.67). This algorithm is well-suited for mass matrix lumping, which is recommended as an economical numerical device generally paid for by some additional errors. However, it is noticed that the lumping, mass conservation provided, can improve the accuracy of some problems by error cancellation [59, 65]. Moreover, it is proven that in transient problems the lumping process introduces some additional dissipation of 'stiffness matrix form' which can help in case of numerical oscillations. Here, we proceed from the classical row-sum procedure which diagonalizes the mass matrix by adding all entries in a row to the diagonal element of that row. Thus, the lumped mass matrix is given as

$$\widetilde{\boldsymbol{M}} = \mathrm{diag}(\widetilde{M}_i) \quad \text{with} \quad \widetilde{M}_i = \sum_{k=1}^{m} M_{ik}\,, \quad i = 1, ..., m\,, \tag{4.66}$$

where $m$ represents the number of columns (or rows) related to the number of nodal DOFs of the FE mesh. In particular, mass lumping is applied on $\boldsymbol{M}_{22}$ and $\boldsymbol{M}_{33}$ which need to be inverted in Steps 2 and 4 of the P-C algorithm (4.67).

---

**Predictor-corrector algorithm of the semi-explicit-implicit scheme**

*Given:* approximate solution $\boldsymbol{y}_n \approx \boldsymbol{y}(t_n)$ at time $t_n$, time-step size $\Delta t_n$

*Find:* approximate solution $\boldsymbol{y}_{n+1} \approx \boldsymbol{y}(t_{n+1})$ at time $t_{n+1}$

*Step 1:* set predictor values

$$\mathsf{v}_S^P := \mathsf{v}_{S\,n}\,, \quad \mathsf{v}_F^P := \mathsf{v}_{F\,n}\,, \quad \mathsf{p}^P := \mathsf{p}_n\,, \quad \mathsf{u}_S^P := \mathsf{u}_{S\,n} + \Delta t_n\,\mathsf{v}_S^P$$

*Step 2:* compute intermediate velocities

$$\mathsf{v}_S^* = \mathsf{v}_S^P + \boldsymbol{h}_1(\mathsf{u}_S^P, \mathsf{v}_S^P, \mathsf{v}_F^P, \mathsf{p}^P, \Delta t_n)\ ,$$
$$\mathsf{v}_F^* = \mathsf{v}_F^P + \boldsymbol{h}_2(\mathsf{u}_S^P, \mathsf{v}_S^P, \mathsf{v}_F^P, \mathsf{p}^P, \Delta t_n)$$

*Step 3:* calculate the pore-fluid pressure (pressure projection)

$$\mathsf{p}_{n+1} = \mathsf{p}^P - \widetilde{\boldsymbol{K}}_{44}^{-1}\left(\boldsymbol{K}_{42}\,\mathsf{v}_S^* + \boldsymbol{K}_{43}\,\mathsf{v}_F^* - \widetilde{\boldsymbol{f}}_{p\,n+1}\right)$$

*Step 4:* compute velocity correctors and solid displacement

$$\mathsf{v}_{S\,n+1} = \mathsf{v}_S^* - \Delta t_n\,\boldsymbol{M}_{22}^{-1}\,\widetilde{\boldsymbol{K}}_{24}\,(\mathsf{p}_{n+1} - \mathsf{p}^P)$$
$$\mathsf{v}_{F\,n+1} = \mathsf{v}_F^* - \Delta t_n\,\boldsymbol{M}_{33}^{-1}\left[\boldsymbol{K}_{34}\,(\mathsf{p}_{n+1} - \mathsf{p}^P) - \boldsymbol{f}_{F\,n+1}\right]$$
$$\mathsf{u}_{S\,n+1} = \mathsf{u}_{S\,n} + \tfrac{1}{2}\,\Delta t_n\,(\mathsf{v}_{S\,n+1} - \mathsf{v}_{S\,n})$$

*Step 5:* update $\quad \boldsymbol{y}_n := \boldsymbol{y}_{n+1}\quad$ and advance in time $\quad t_{n+1} = t_n + \Delta t_n$

internal iteration loop                 (4.67)

---

Moreover, before the update in Step 5, the convergence can be checked by comparing the results of subsequent internal iteration loops (Steps 1 to 4) within the same time step.

That is, repeat the iteration loop $i$ of the current time step $n$ until a suitable convergence criterion, such as $\|\boldsymbol{y}_{n+1}^{i+1} - \boldsymbol{y}_{n+1}^i\| < TOL_{\boldsymbol{y}}$, is met. For the numerical examples presented in Section 4.5, we found it sufficient to pass only once through the internal loop in each time step of the implemented P-C algorithm.

The major drawback of the presented splitting procedure is the restriction to a critical time-step size $\Delta t_{cr}$ due to the included explicit steps. In particular, the Courant-Friedrichs-Lewy (CFL) condition has to be satisfied which limits the maximal time-step size depending on the minimal discrete element dimensions and the speed of poroelastic pressure wave propagation in the solid domain [39, 43]. Basically, the CFL condition balances the propagation speed of the algorithmic solution with the physical solution speed of the differential equation. For 1-d two-node and 2-d four-node linear elements, the critical time-step size is estimated as

$$\Delta t_{cr}^I = \frac{\Delta h_x}{c_p^x}, \quad \Delta t_{cr}^{II} = \frac{\Delta h_x \, \Delta h_y}{c_p^x \Delta h_y + c_p^y \Delta h_x} \, . \tag{4.68}$$

Herein, $\Delta h_x$ and $\Delta h_y$ are the minimal discrete element dimensions in $x$ and $y$ direction, $c_p^x$ and $c_p^y$ represent the speed of elastic pressure wave propagation in $x$ and $y$ direction, respectively, which for a drained, isotropic poroelastic medium with incompressible constituents is[4]

$$c_p = \sqrt{\frac{2\mu^S + \lambda^S}{\rho^S}} \, . \tag{4.69}$$

In general, numerical studies reveal that the stability of the implemented P-C algorithm (4.67) depends very strongly on the chosen time-step size. Although the CFL condition requires that $\Delta t_n \leq \Delta t_{cr}$, an optimal solution is obtained just for $\Delta t_n \approx \Delta t_{cr}$, whereas significant oscillations in the pressure variable can be observed when $\Delta t_n \ll \Delta t_{cr}$. Because of that, the presented algorithm is not feasible in cases where non-uniform FE meshes are required, e. g., when space adaptive strategies are to be used, as the whole dynamic problem is advanced with the same global time step. However, the time-step restriction can be partly overcome by taking recourse to staggered implicit-implicit schemes with stabilizing parameters, cf. [33, 38, 39] for details. In fact, the instability due to $\Delta t_n \ll \Delta t_{cr}$ is in contrast to standard explicit methods and is inherent to the splitting procedure. This becomes apparent from the additional stiffness term $\widetilde{\boldsymbol{K}}_{44}$ in $(4.62)_1$ which tends towards zero in the limit of an infinitely small time-step size causing a pressure 'overshoot' in the projection step (Step 3) of the P-C algorithm (4.67). This problem can be tackled by adding some artificial compressibility to the mixture in analogy to (4.36). This manipulation yields a semi-explicit quasi-compressibility strategy, which in CFD is known

---

[4] In fact, there are three apparent types of bulk waves in a saturated porous medium (cf. [6, 57]): (1) the fast and only weakly damped longitudinal pressure wave (P1-wave, Biot wave of 1st kind) with in-phase motion of solid and fluid mainly governed by the constituent compressibility, (2) the slow and strongly damped longitudinal pressure wave (P2-wave, Biot wave of 2nd kind) with anti-phase motion of solid and fluid mainly determined by the solid skeleton deformability, and (3) the even slower transverse shear wave (S-wave) transmitted only in the solid governed by its shear stiffness. In the considered case of materially incompressible constituents, the theoretical speed of the 1st Biot wave is infinite.

as artificial compressibility or modified Chorin-Uzawa method [50]. Following this, we extend (4.49),

$$\text{div}\,(n^S \mathbf{v}_{S\,n+1} + n^F \mathbf{v}_{F\,n+1}) - \epsilon\,\Delta(p_{n+1} - p_n) = 0\,, \tag{4.70}$$

where again $\epsilon \geq 0$ is a small parameter and $\Delta(\,\cdot\,)$ is the Laplace operator. Then, proceeding through all steps, one finally arrives at

$$\widetilde{\boldsymbol{K}}_{44} = \int_{\Omega^h} \nabla \boldsymbol{P}^T \beta \,\nabla \boldsymbol{P}\,\mathrm{d}v \quad \text{with} \quad \beta := \left[\Delta t_n\big(\frac{n^F}{\rho^{FR}} + \frac{n^S}{\rho^{SR}}\big) + \epsilon\,\right] \geq \beta_{\min}\,, \tag{4.71}$$

where $\beta_{\min}$ is associated with a critical time-step size. As the CFL condition suggests, the optimal solution is obtained for $\Delta t_n \approx \Delta t_{cr}$, so that it is natural to choose

$$\beta_{\min} = \beta_0\,\Delta t_{cr}\big(\frac{n^F}{\rho^{FR}} + \frac{n^S}{\rho^{SR}}\big)\,. \tag{4.72}$$

It is obvious that the parameter $\beta_0 > 0$ controls the imposed artificial compressibility (see numerical examples), and thus, the deviation from the volume preserving solution of a mixture with materially incompressible constituents. Moreover, in analogy to $\beta_{\min}$, (4.72) can also provide as a good estimate for $\alpha_{\min}$ to stabilize the monolithic scheme if uniform equal-order elements are used, although $\alpha$ is independent of the FE mesh size (recall (4.37)), cf. [39].

## 4.5   Numerical Examples

For the numerical examples, the monolithic solution scheme using the DIRK time-stepping algorithm (4.39) is implemented in the FE package PANDAS[5] and the splitting procedure using the predictor-corrector algorithm (4.67) is realized in the free software Scilab[6]. As the coding in Scilab using built-in functions is not that optimized and high-performance as the C-based routines in PANDAS, we waive an efficiency contest in regard to the required net computing times and memory demands. We rather compare the accuracy and stability habits of the different formulations and algorithms. Therefore, to keep an overview, unique abbreviations for each distinct test case are introduced according to Table 4.1.

### 4.5.1   Saturated Poroelastic Column under Harmonic Load

In this example, the response of a homogeneous and isotropic, water-saturated, poroelastic column (height: $10\,\mathrm{m}$, width: $2\,\mathrm{m}$) is analyzed under plane-strain, confined compression conditions. Therefore, the mixture domain is surrounded by impermeable, frictionless but rigid boundaries except for the loaded top side which is perfectly drained. The geometry with boundary conditions and the loading path are illustrated in Figure 4.3.

---

[5] Porous media Adaptive Nonlinear finite element solver based on Differential Algebraic Systems, see http://www.get-pandas.com

[6] Scientific software package for numerical computations, see http://www.scilab.org

**Table 4.1:** *Abbreviations used in the examples. For instance, uvp(2)-TB2-QL stands for the monolithic solution of the $\mathbf{u}_S$-$\mathbf{v}_F$-$p$ formulation based on the weak forms $(4.19, 4.33, 4.21, 4.32)$ using the TR-BDF2 time-integration scheme and mixed quadratic-linear finite elements.*

| Abbr. | Prim. vars. | Governing equations | Solution algorithm |
|---|---|---|---|
| uvp(1) | $\mathbf{u}_S, \mathbf{v}_F, p$ | $(4.19, 4.20, 4.21, 4.32)$ | monolithic implicit $(4.39)$ |
| uvp(2) | $\mathbf{u}_S, \mathbf{v}_F, p$ | $(4.19, 4.33, 4.21, 4.32)$ | monolithic implicit $(4.39)$ |
| uwp | $\mathbf{u}_S, \mathbf{w}_{FR}, p$ | $(4.19, 4.33, 4.21, 4.32) + (4.4)_4$ | monolithic implicit $(4.39)$ |
| uvp($\alpha$) | $\mathbf{u}_S, \mathbf{v}_F, p$ | $(4.19, 4.33, 4.21, 4.32) + (4.37)$ | monolithic implicit $(4.39)$ |
| uvp(pc) | $\mathbf{u}_S, \mathbf{v}_F, p$ | $(4.19, 4.20, 4.21, 4.22)$ | semi-explicit-implicit $(4.67)$ |
| uvp($\beta$) | $\mathbf{u}_S, \mathbf{v}_F, p$ | $(4.19, 4.20, 4.21, 4.22) + (4.72)$ | semi-explicit-implicit $(4.67)$ |
| up | $\mathbf{u}_S, p$ | $(4.19) +$ weak forms of $(4.17, 4.18)$ | monolithic implicit $(4.39)$ |

| Abbr. | Time integration | Abbr. | Approximation of primary variables |
|---|---|---|---|
| IE | implicit Euler | QL | $\mathbf{u}_S, \mathbf{v}_S$: quadratic; $\mathbf{v}_F/\mathbf{w}_{FR}, p$: linear |
| TR | trapezoidal rule | LL | $\mathbf{u}_S, \mathbf{v}_S$: linear; $\mathbf{v}_F/\mathbf{w}_{FR}, p$: linear |
| TB2 | TR-BDF2 | QQ | $\mathbf{u}_S, \mathbf{v}_S$: quadratic; $\mathbf{v}_F/\mathbf{w}_{FR}, p$: quadratic |

The constitutive material parameters are adopted from the related literature [9] and listed in Table 4.2. The objective of this simple benchmark problem is to principally compare the different cases of Table 4.1 with existing (semi-)analytical solutions for the solid displacement and the pore-fluid pressure of an infinite half-space under dynamic loading obtained via Laplace transform [9]. In particular, two scenarios are tested: (1) a high permeability case with $k^F = 10^{-2}$ m/s and (2) a moderately low permeability case with $k^F = 10^{-5}$ m/s which is the lowest permeability for which we achieved the (semi-)analytical solutions using Maple.
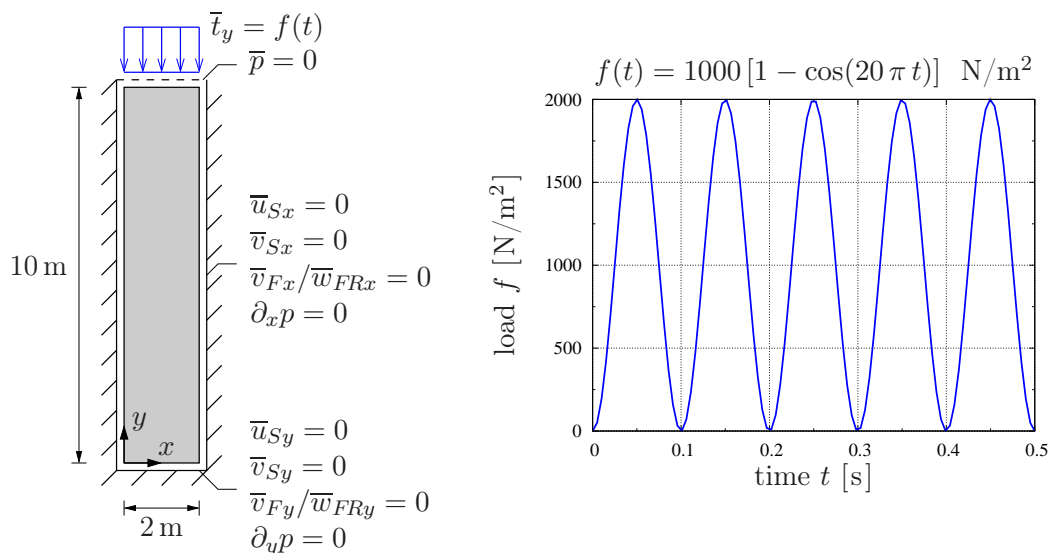


**Figure 4.3:** *Geometry and boundary conditions (left) and loading path (right) of the dynamic confined compression of a saturated poroelastic column.*

**Table 4.2:** *Material parameters for elastic soil used in the example problems [9].*

| Parameter | Symbol | Value | SI unit |
|---|---|---|---|
| 1st *Lamé* constant of solid skeleton | $\mu^S$ | $5.583 \cdot 10^6$ | N/m$^2$ |
| 2nd *Lamé* constant of solid skeleton | $\lambda^S$ | $8.375 \cdot 10^6$ | N/m$^2$ |
| effective density of dense solid | $\rho^{SR}$ | 2000 | kg/m$^3$ |
| effective density of pore fluid | $\rho^{FR}$ | 1000 | kg/m$^3$ |
| initial volume fraction of solid | $n_{0S}^S$ | 0.67 | – |
| Darcy permeability | $k^F$ | $10^{-2}, 10^{-5}, 10^{-10}$ | m/s |

The 1-d wave propagation example mainly serves to compare uvp(2)-TB2 as the best combination for solving the coupled problem monolithically (see Section 4.5.2) with the splitting solution uvp(pc). In addition, we provide the results for the monolithic solution of the reduced $\mathbf{u}_S$-$p$ formulation up-TB2. All computations proceed from isotropic meshes with uniform and fully integrated quadrilateral elements, where several refinement levels from 1 to 50 elements per meter of column height are considered. This entails a respective choice of the time-step size ($\Delta t \approx \Delta t_{cr}$) for the semi-explicit-implicit scheme by virtue of the CFL condition (4.68). For the monolithic scheme, we waive time adaptive strategies and proceed from a constant $\Delta t$ of $10^{-3}$ s. Essentially, for reasonably chosen time steps, the monolithic solution of the uniaxial dynamic consolidation problem is not very sensitive to the applied time-integration scheme, so that only TR-BDF2 (TB2) is used. Further details are provided in Table 4.3.

**Table 4.3:** *Used time-step sizes and number of nodal unknowns for different quadrilateral FE discretizations of the column problem. Note that uvp(pc)-LL requires additional expenses for the discretization of the intermediate velocities (recall Section 4.4.3).*

| #elements/meter | 1 | 5 | 10 | 15 | 20 | 30 | 40 | 50 |
|---|---|---|---|---|---|---|---|---|
| $\Delta t_{cr}$ (CFL)　$[10^{-3}\,\mathrm{s}]$ | 5.5 | 1.5 | 0.78 | 0.53 | 0.4 | 0.27 | 0.2 | 0.16 |
| $\Delta t$　(pc)　$[10^{-3}\,\mathrm{s}]$ | 5.0 | 1.0 | 0.5 | 0.25 | 0.25 | 0.2 | 0.1 | 0.1 |
| $\Delta t$　(monol.) $[10^{-3}\,\mathrm{s}]$ | 1.0 | 1.0 | 1.0 | 1.0 | 1.0 | 1.0 | 1.0 | 1.0 |
| #DOFs uvp-LL | 154 | 714 | 1414 | 2114 | 2814 | 4214 | 5614 | 7014 |
| #DOFs uvp-QL | 278 | 1318 | 2618 | 3918 | 5218 | 7818 | 10418 | 13018 |
| #DOFs uvp-QQ | 371 | 1771 | 3521 | 5271 | 7021 | 10521 | 14021 | 17521 |
| #DOFs up-QL | 234 | 1114 | 2214 | 3314 | 4414 | 6614 | 8814 | 11014 |

To begin with the high permeability case ($k^F = 10^{-2}$ m/s), there is no need for a pressure stabilization of the monolithic scheme for equal-order approximations as in (4.37). On the first view, all formulations yield convergent approximations of the solid displacement field following the analytical reference solution $u_{ref}$ of a point at the top of the column (Figure 4.4, left). However, regarding the relative displacement error $ERR_u = |(u_{Sy} - u_{ref})/u_{ref}|$ in Figure 4.4 (right), one observes an unforeseen inadequate solution of the often praised

quadratic-linear Taylor-Hood elements (QL) in comparison to the linear equal-order approximation (LL). The same holds for the splitting solution uvp(pc)-LL. Obviously, the reduced $\mathbf{u}_S$-$p$ formulation up-TB2-QL shows the highest deficiency as expected for large values of $k^F$.
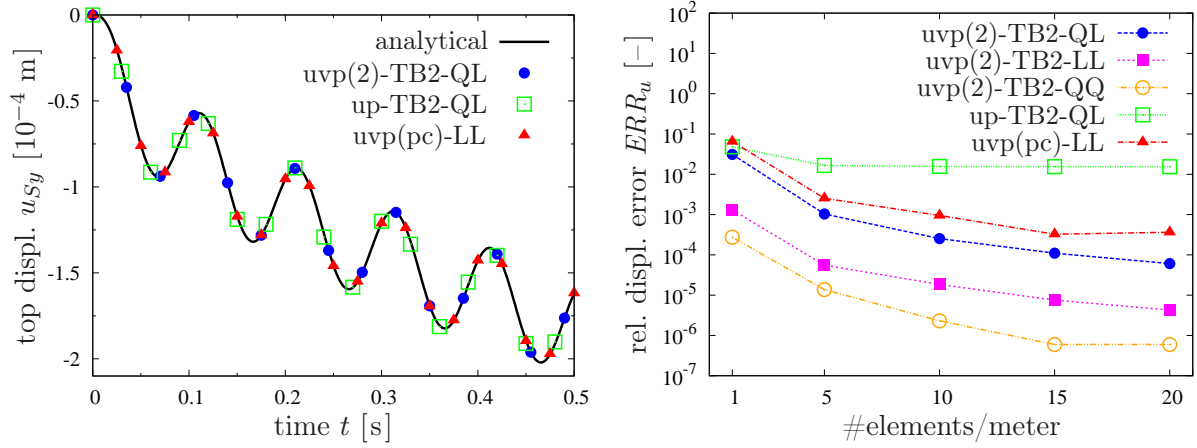


**Figure 4.4:** *Top displacement history (left) for $k^F = 10^{-2}$ m/s, $t = [0, 0.5]$ s, 5 elements/meter and corresponding relative error (right, logarithmic scale) over mesh size at $t = 0.15$ s.*
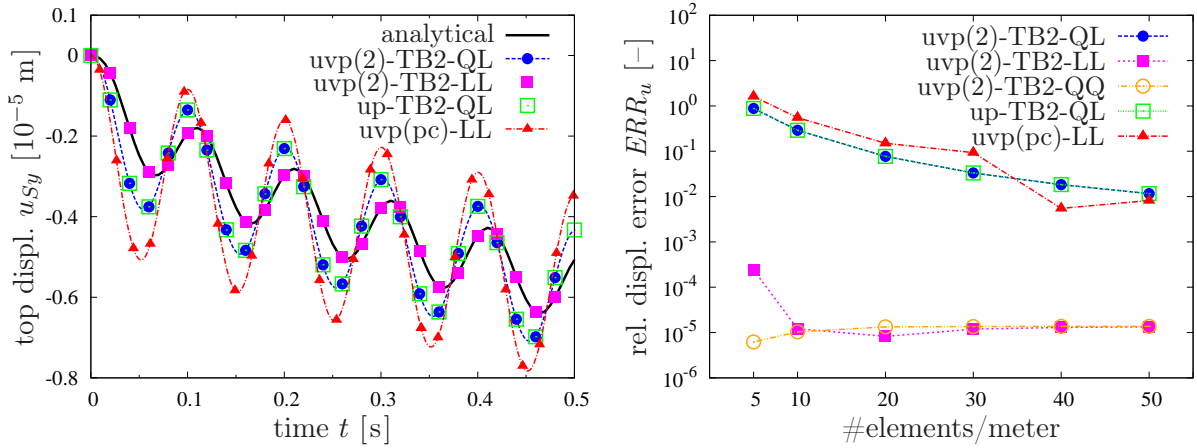


**Figure 4.5:** *Top displacement history (left) for $k^F = 10^{-5}$ m/s, $t = [0, 0.5]$ s, 10 elements/ meter and corresponding relative error (right, logarithmic scale) over mesh size at $t = 0.15$ s.*

This finding becomes even more prominent for the lower permeability case with $k^F = 10^{-5}$ m/s. Comparing again the displacement history of a point on top of the column (Figure 4.5, left), one now directly sees the faulty approximation of $\mathbf{u}_S$. Only uvp(2)-TB2-LL and uvp(2)-TB2-QQ yield good results, where still no pressure stabilization is used. Figure 4.5 (right) showing the relative displacement error further underlines the result. However, it is also observed that the reduced formulation up-QL for lower values of $k^F$ is almost as accurate as the more expensive uvp(2)-QL formulation.

Basically, the problem lies in the zero pressure (perfect drainage) boundary condition at the loaded top. According to the effective stress principle $(4.8)_1$, the applied load is

concurrently carried by the solid matrix and the pore fluid. Starting from an undeformed initial state, equilibrium requires the pore fluid to bear the entire load until deformation activates the resistance of the solid skeleton (consolidation process). However, at the top we have $\overline{p} = 0$ which must be compensated by an immediate pressure increase in a small layer below the boundary. In case of a coarse FE discretization, the apparent steep pressure gradient cannot be resolved, consequently yielding an inaccurate displacement solution in the strongly coupled problem. This inaccuracy is even more pronounced for mixed quadratic-linear (QL) approximations. The linear interpolation of $p$ yields wrong pressure values related to the mid-nodes of the quadratic approximation of $\mathbf{u}_S$, and thus, further falsifies the overall displacement solution. The problem is depicted in Figure 4.6, where the nodal displacement and pressure values in the first half meter below the top of the column are given for a coarse discretization with 10 elements per meter. In fact, the QQ interpolation yields an adequate approximation of the displacement and the pressure. The solution of uvp(2)-TB2-LL already shows distinct oscillations indicating that for lower permeabilities some pressure stabilization should be used. However, despite the inaccurate displacement solution at the top, the semi-explicit-implicit splitting scheme gives an accurate approximation of $\mathbf{u}_S$ in the domain and even a better pressure solution than uvp-TB2-QQ which also starts showing some very slight instability. A feasible way to principally overcome this problem is to use an anisotropic mesh with some fine layers of elements at affected permeable ($\overline{p} = 0$) and loaded ($\overline{\mathbf{t}} \neq \mathbf{0}$) boundaries. However, this is not reasonable for the semi-explicit-implicit splitting method as the CFL condition would demand too tiny global time increments.
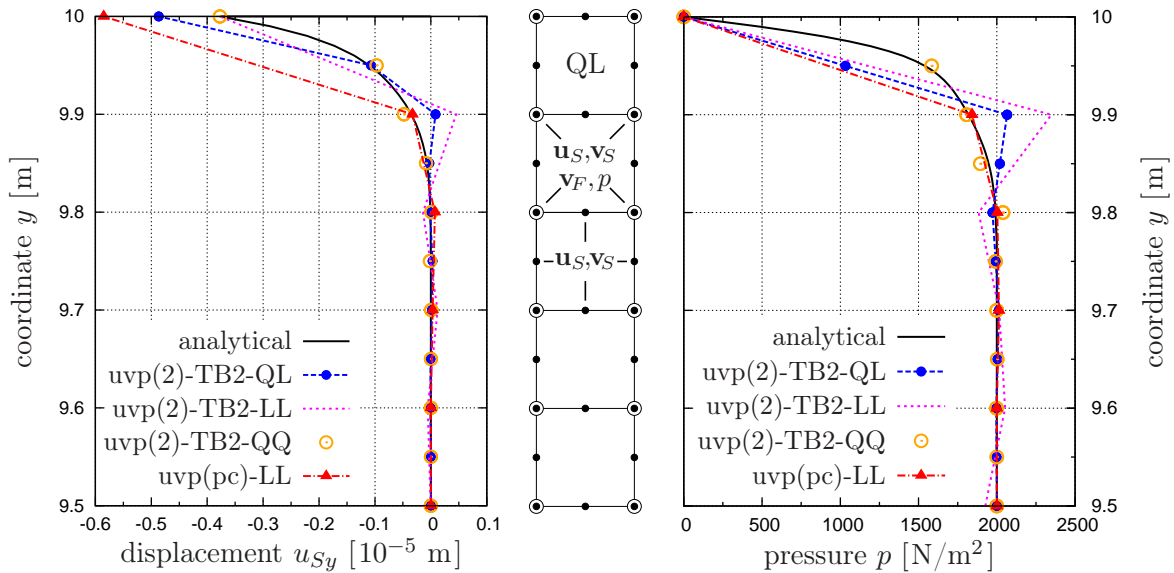


**Figure 4.6:** *Solid displacement (left) and pore pressure distribution (right) in the first half meter under the loaded top of the column for $k^F = 10^{-5}$ m/s, 10 elements/meter at $t = 0.15$ s. In the middle, exemplary mixed quadratic-linear (QL) FE discretization of the uvp(2) test case.*

In this regard, it should also be noted that although implicit methods allow large time steps associated with large Courant or CFL numbers, the size of the time increment is still
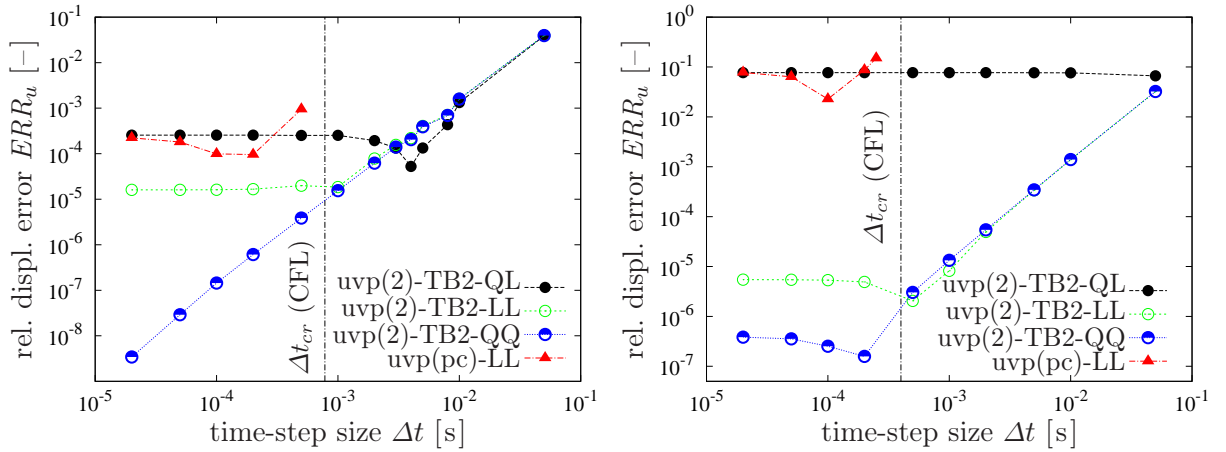
**Figure 4.7:** *Relative displacement error of a point at the top over time-step size (double logarithmic scale) at $t = 0.15$ s for $k^F = 10^{-2}$ m/s with 10 elements/meter (left) and $k^F = 10^{-5}$ m/s with 20 elements/meter (right).*

limited not only to accurately capture the phase and amplitude of the applied dynamic load[7] but also to keep the discretization error in time small enough. In Figure 4.7, we therefore compare the relative displacement error for different time increments of the implicit monolithic scheme using TR-BDF2. It is observed that there is a clear influence of $\Delta t$ on the accuracy, which in case of the mixed quadratic-linear (QL) discretization is not that much apparent due to its general poor approximation as described previously. For the linear equal-order approximation (LL) it is noticed that the somehow 'optimal' time step is close to $\Delta t_{cr}$ of the CFL condition.

Moreover, it is worth mentioning that for accuracy reasons not only the highest frequency has to be sufficiently resolved in time but also the highest wave number (reciprocal lowest wave length) must be adequately resolved in space in order to avoid the so-called pollution effect associated with the dispersion of the FEM solution, see, e.g., [23] for details. As a rule of thumb, the lowest wave length should at least be represented by 10 data points (FE nodes) which corresponds to 9 linear elements. However, in the considered uniaxial example, the incompressibility of the fluid in combination with a moderately low permeability causes an immediate damping of the propagating pressure waves, so that this example is not well suited to reveal the pollution error. Therefore, for the further reliable comparison of the test cases in Table 4.1, the column problem is deemed not meaningful and we revert instead to a real 2-d scenario giving rise to shear and surface waves. Please note that wave reflections are not discussed in this contribution. All numerical studies are computed to a time before reflections corrupt the actual solution.

---

[7] According to the Nyquist-Shannon sampling theorem, the sampling rate for perfect signal reconstruction should be at least twice the highest frequency in the original signal. Applied to the dynamic load, the maximum time step should not exceed half the minimum period, i.e., $\Delta t_{max} = 0.5\, T_{min} = 5 \cdot 10^{-2}$ s. In practice, time increments below one-tenth of the minimum period are feasible, see, e.g., [4, Sec. 9.3].

## 4.5.2    Two-Dimensional Wave Propagation

In this example, we study the 2-d dynamical wave propagation in a rectangular symmetric domain under plane-strain conditions (Figure 4.8) as presented in Breuer [15]. The ma-
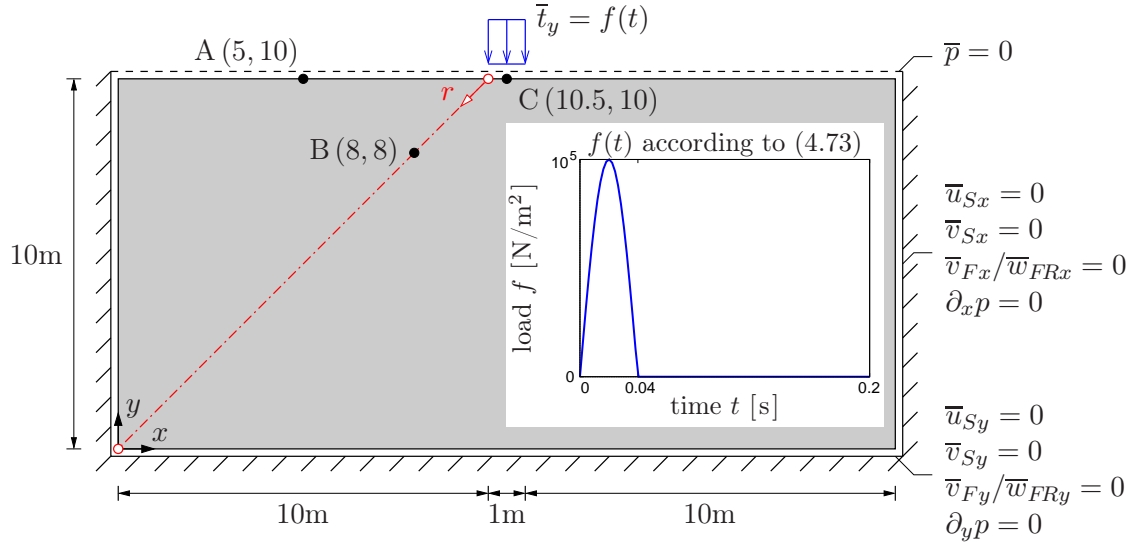


**Figure 4.8:** *Geometry, boundary conditions, and loading path of the 2-d problem.*

terial parameters are the same as before (Table 4.2) and the applied distributed impulse force is

$$f(t) = 10^5 \sin(25\,\pi\,t)\left[1 - H(t - \tau)\right] \; \text{N/m}^2 \tag{4.73}$$

with $H(t - \tau)$ as the Heaviside step function and $\tau = 0.04$ s.

**Table 4.4:** *Mesh sizes and time steps for the 2-d problem. Note that except for the coarsest mesh only half of the problem is computed by exploiting the symmetry to $x = 10.5$ m.*

| #elements (width–height) | 21–10 | 42–20 | 84–40 | 168–80 |
|---|---|---|---|---|
| $\Delta t_{cr}$ (CFL)   $[10^{-3}\,\text{s}]$ | 4.14 | 2.07 | 1.04 | 0.52 |
| $\Delta t$   (pc)    $[10^{-3}\,\text{s}]$ | 2.0 | 1.0 | 0.5 | – |
| $\Delta t$   (monol.) $[10^{-3}\,\text{s}]$ | 1.0 | 1.0 | 1.0 | 1.0 |
| $\alpha_{\min}/\alpha_0$ for uvp($\alpha$) | $2.7 \cdot 10^{-6}$ | $1.4 \cdot 10^{-6}$ | $7.0 \cdot 10^{-7}$ | $3.5 \cdot 10^{-7}$ |
| $\beta_{\min}/\beta_0$ for uvp($\beta$) | $2.7 \cdot 10^{-6}$ | $1.4 \cdot 10^{-6}$ | $7.0 \cdot 10^{-7}$ | $3.5 \cdot 10^{-7}$ |

From the problem set-up, one expects the following wave types: First, two modes of bulk waves generated inside the domain (recall footnote on page 99), i. e., the slow pressure wave (P2-wave) and the transverse shear wave (S-wave) transmitted through the elastic solid matrix. Second, at the free top surface, the Rayleigh wave (R-wave) as an elastic surface wave showing an elliptic particle movement in planes normal to the surface and parallel to the direction of propagation, commonly noticed as 'ground rolling' during earthquake events. In Figure 4.9, exemplary contour plots of the computed solid displacement field and the deformed mesh geometry make the 2-d wave propagation apparent.
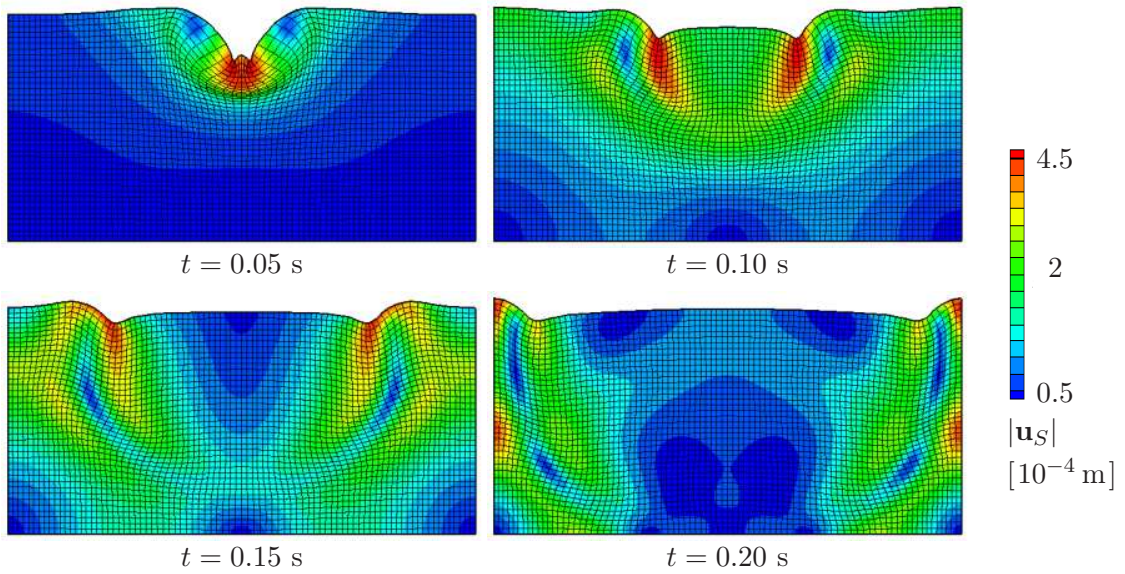
**Figure 4.9:** *Time sequence of displacement contour plots with $|\mathbf{u}_S| = \sqrt{u_{Sx}^2 + u_{Sy}^2}$ and deformed mesh (scale factor 500) using uvp(2)-TB2-QL with 84–40 elements and $k^F = 10^{-2}$ m/s.*

Again, we apply our tests and comparisons for two cases of permeabilities, where the spatial discretization is again based on fully integrated quadrilateral elements as given in Table 4.4. In particular, we focus on the displacement solution at the free surface (point A) and the pressure history in the domain (point B). In addition, we compare the displacement and pressure distribution directly under the impulse load (vertical down at point C). Finally, the pollution of the numerical solution is investigated along a diagonal cut line through the domain, cf. Figure 4.8.

Starting with the high permeability case ($k^F = 10^{-2}$ m/s), the equal-order approximation of the variables demands no stabilization of the monolithic solution as already shown in the example before. First, we examine the numerical damping and the stability of the monolithic time-stepping rules by comparing the R-wave specific motion of point A. Figure 4.10 (left) shows the strong artificial damping of the IE scheme which is reduced by choosing a smaller time step. Figure 4.10 (right) shows that TR and TR-BDF2 (TB2) exhibit no numerical damping and yield throughout a stable displacement solution for all considered formulations. Therefore, we exclude the IE scheme from the further comparisons and focus on TR and TB2 only.

Next, we study the displacement solution at point A for different mesh and time-step sizes. As can be seen in Figure 4.11 (left), uvp(2)-TB2-QL yields already a good approximation for 84–40 elements and will thus be taken as reference. From Figure 4.11 (right), it follows that the implicit monolithic time discretization is sufficiently accurate for $\Delta t = 10^{-3}$ s, which is the time step of choice.

To continue, we examine the uwp formulation for both implicit time integrators and different interpolation cases in regard to the stability of the pressure solution at point B. As depicted in Figure 4.12 (left), the combination uwp-TR-QL yields oscillations around
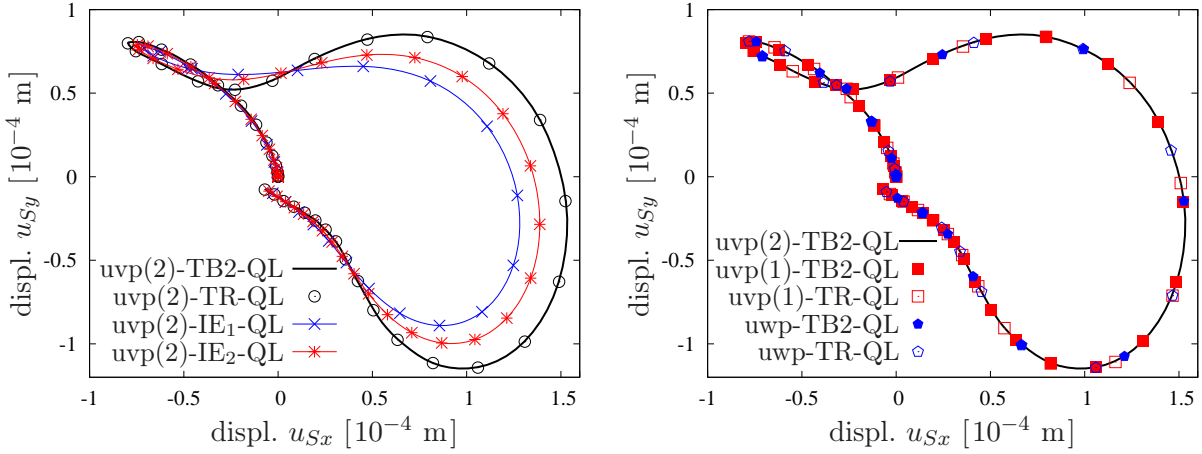
**Figure 4.10:** *Comparison of the elliptic in-plane motion of point A for $k^F = 10^{-2}$ m/s, 42–20 elements, and uniform step-size $\Delta t = 10^{-3}$ s except for $IE_2$ where $\Delta t = 5 \cdot 10^{-4}$ s.*
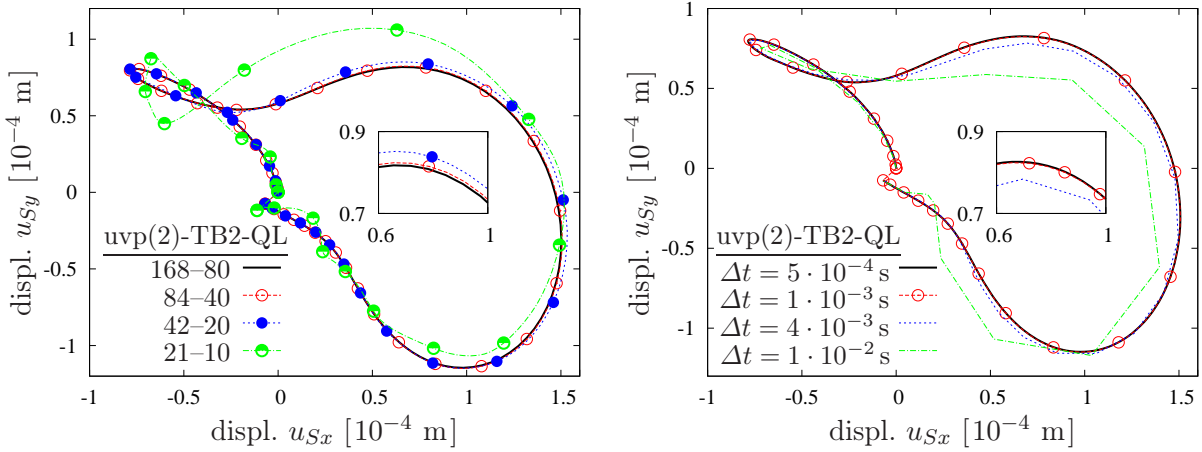


**Figure 4.11:** *Comparison of the elliptic in-plane motion of point A for $k^F = 10^{-2}$ m/s using different mesh sizes and a fixed time step $\Delta t = 10^{-3}$ s (left) and a fixed mesh with 84–40 elements but different time-step sizes (right).*

the solution due to the marginal stability of the trapezoidal rule, which, however, can be reduced by using smaller $\Delta t$ or avoided if TB2 is applied. For linear equal-order elements (LL), the uwp formulation exhibits a stable pressure solution for both TR and TB2, see Figure 4.12 (right).

In the same way, the uvp(1) and uvp(2) formulations are compared. Figure 4.13 (left) shows that unincisive oscillations occur when TR in combination with the mixed QL discretization is used independent of the formulation. As before, one obtains a stable pressure solution for both cases if TB2 instead of TR is applied or if one proceeds from LL elements which work for both time-stepping rules (Figure 4.13, right).

In this regard, we also compare the displacement and pressure solutions of different LL discretizations with the reference uvp(2)-TB2-QL using 84–40 elements and a coarse QQ elementation. Figure 4.14 shows the expected convergence of uvp(2)-TB2-LL to the reference solutions as finer meshes are considered, whereas already 42–20 QQ elements yield
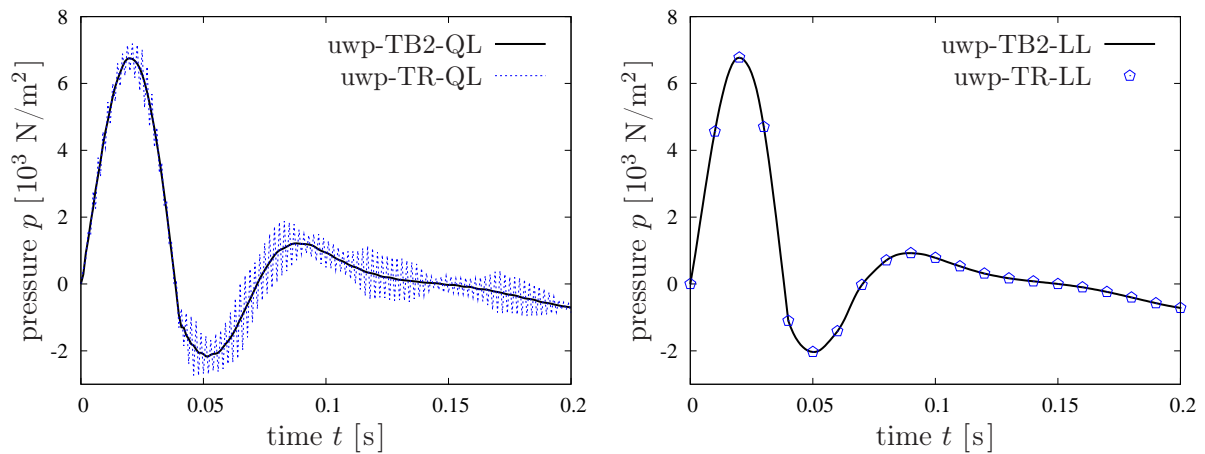
**Figure 4.12:** *Pressure history at point B for $k^F = 10^{-2}$ m/s, 42–20 elements, and $\Delta t = 10^{-3}$ s.*
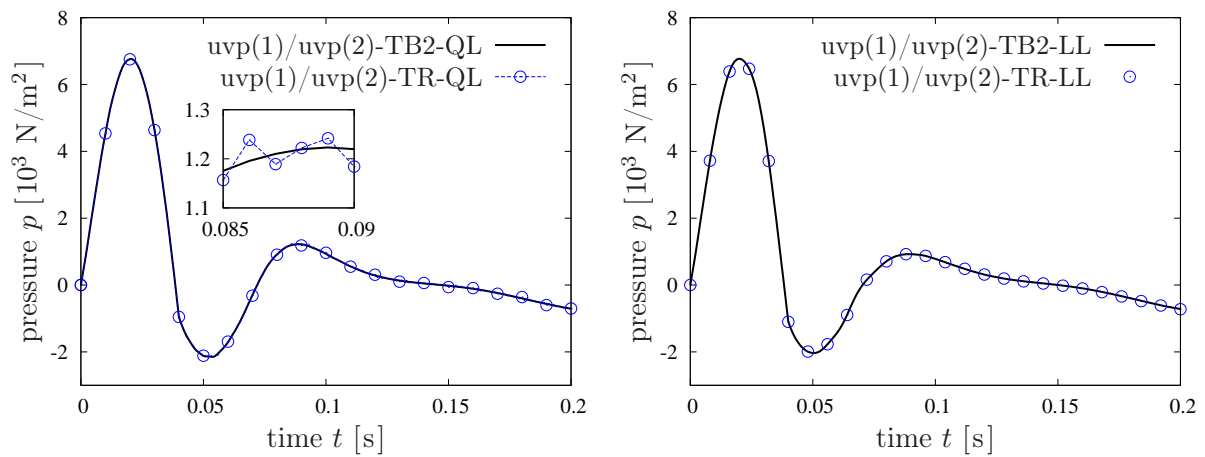


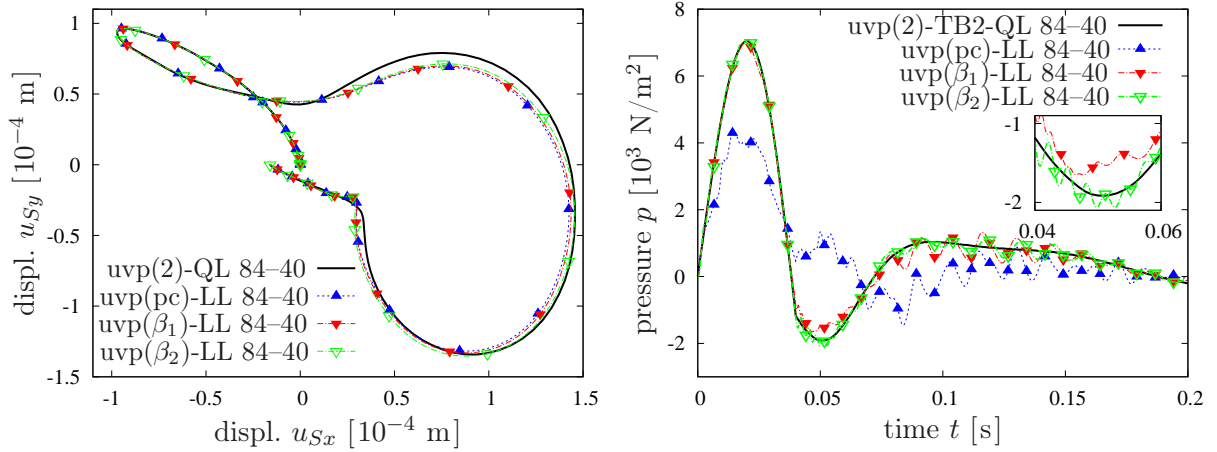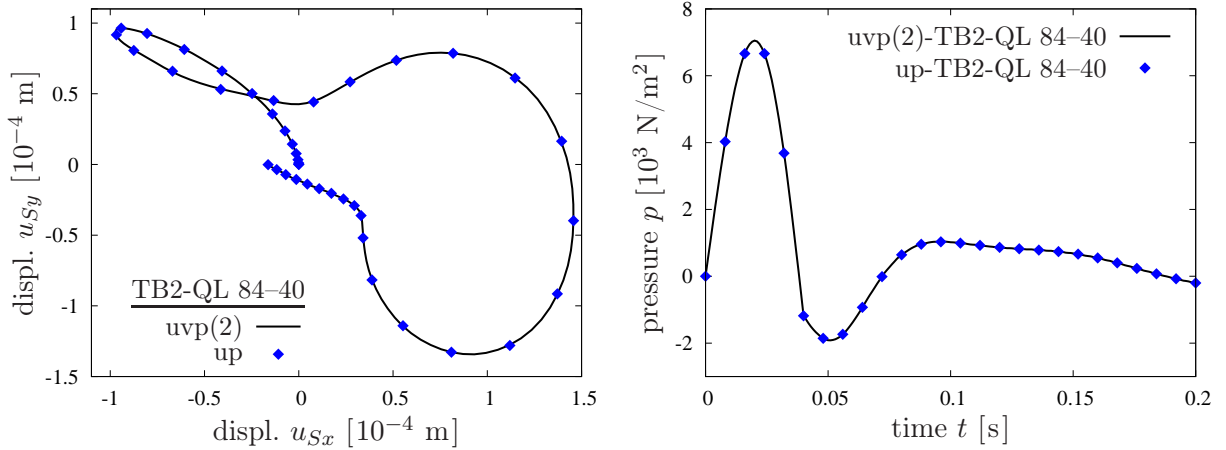**Figure 4.13:** *Pressure history at point B for $k^F = 10^{-2}$ m/s, 42–20 elements, and $\Delta t = 10^{-3}$ s.*
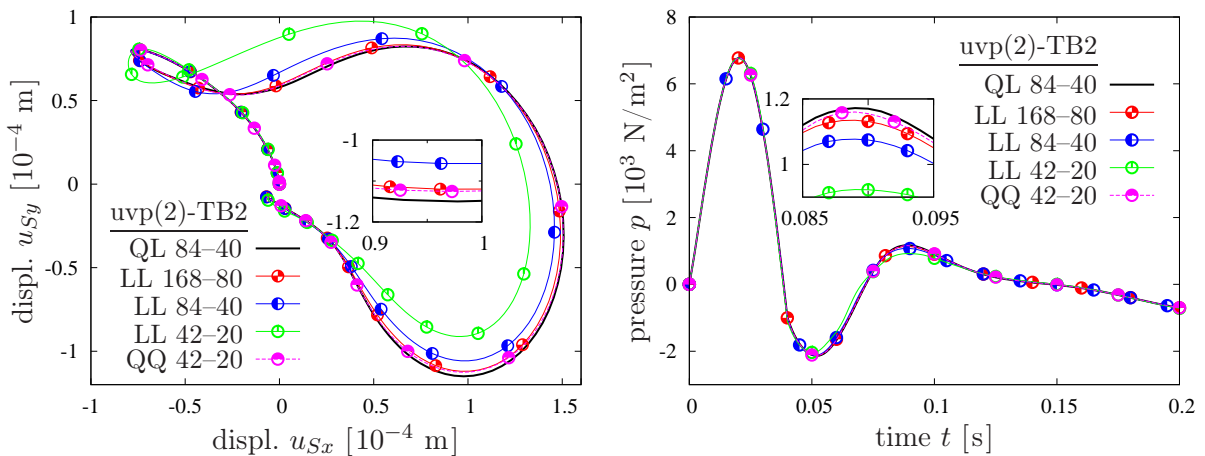


**Figure 4.14:** *In-plane motion of point A (left) and pressure history at point B (right) for $k^F = 10^{-2}$ m/s and $\Delta t = 10^{-3}$ s.*

good results. An almost identical behavior is observed for uvp(pc)-LL (Figure 4.15) not-
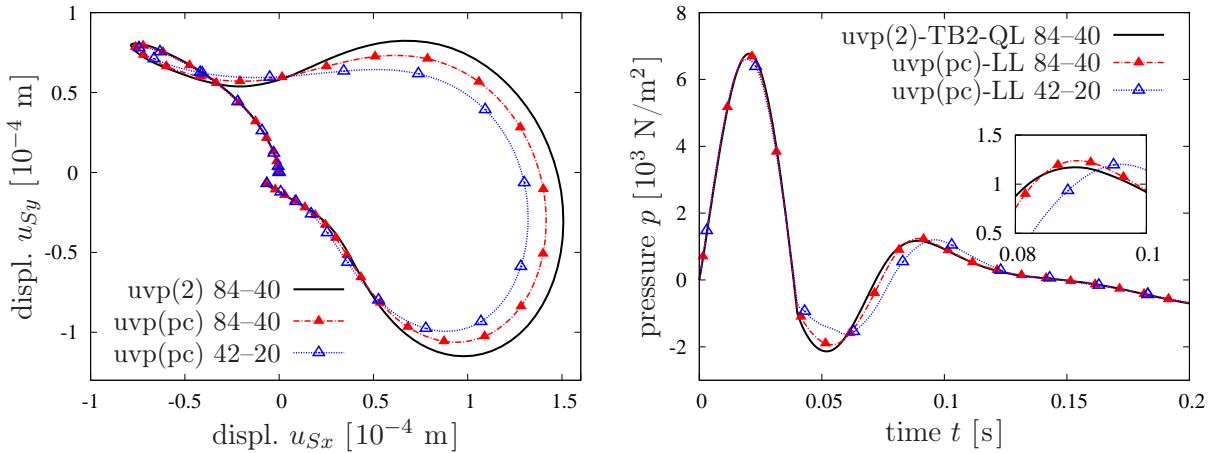
**Figure 4.15:** *In-plane motion of point A (left) and pressure history at point B (right) for* $k^F = 10^{-2}$ *m/s,* $\Delta t = 10^{-3}$ *s for uvp(2)-TB2, and* $\Delta t$ *according to Table 4.4 for uvp(pc).*
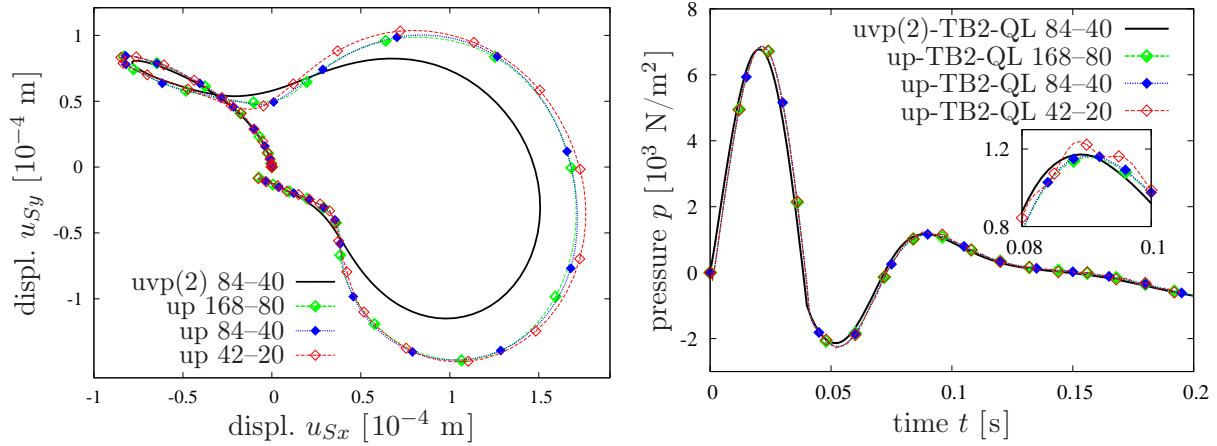


**Figure 4.16:** *In-plane motion of point A (left) and pressure history at point B (right) for* $k^F = 10^{-2}$ *m/s and* $\Delta t = 10^{-3}$ *s.*

ing that coarse meshes yield an even poorer pressure approximation than uvp(2)-TB2-LL.

The final comparison for the high permeability case reveals the deficiencies of the reduced up formulation. As depicted in Figure 4.16 (left), the simplifying assumption $(\mathbf{w}_{FR})'_S \equiv \mathbf{0}$ results in a severe overestimation of the displacement solution. However, one still obtains a good approximation of the pressure field (Figure 4.16, right).

In what follows, we switch to an extremely low permeability of $k^F = 10^{-10}$ m/s which further unveils the merits and drawbacks of the considered test cases. The monolithic solution now requires stable mixed FE formulations such as the quadratic-linear Taylor-Hood elements (QL) or some pressure stabilization as in the uvp($\alpha$) formulation if equal-order elements (LL or QQ) are used.

To begin with, we compare the monolithic solutions of the uvp(1), uvp(2), and uwp formulations. It becomes apparent from Figure 4.17 that uvp(1) yields an inaccurate displacement solution at point A and a totally wrong pore pressure history at point B.

However, for low values of $k^F$, the uwp formulation shows the same performance as uvp(2). This becomes also clear from Figure 4.18, where both exhibit the same vulnerability to pressure instabilities if the trapezoidal rule (TR) or a too coarse mesh is used.
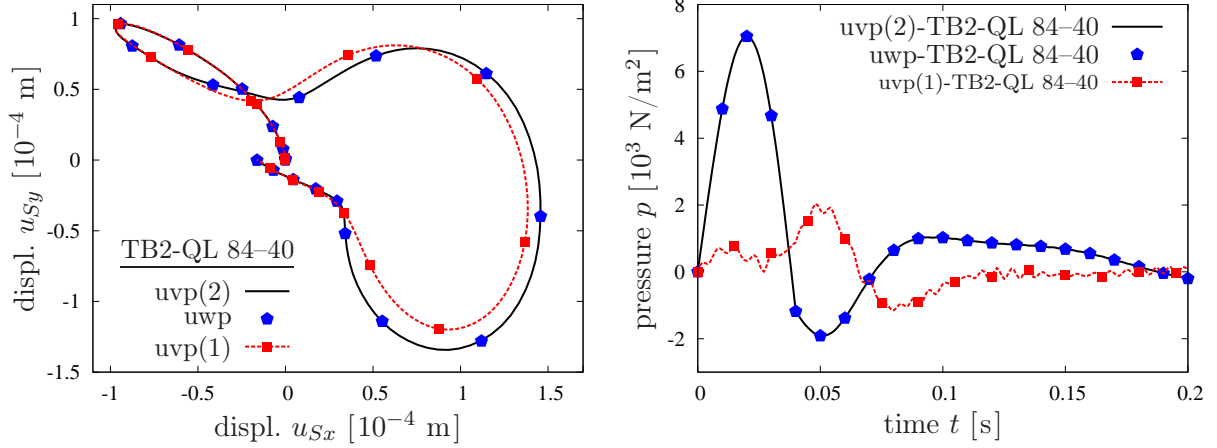


**Figure 4.17:** *In-plane motion of point A (left) and pressure history at point B (right) for $k^F = 10^{-10}$ m/s and $\Delta t = 10^{-3}$ s.*
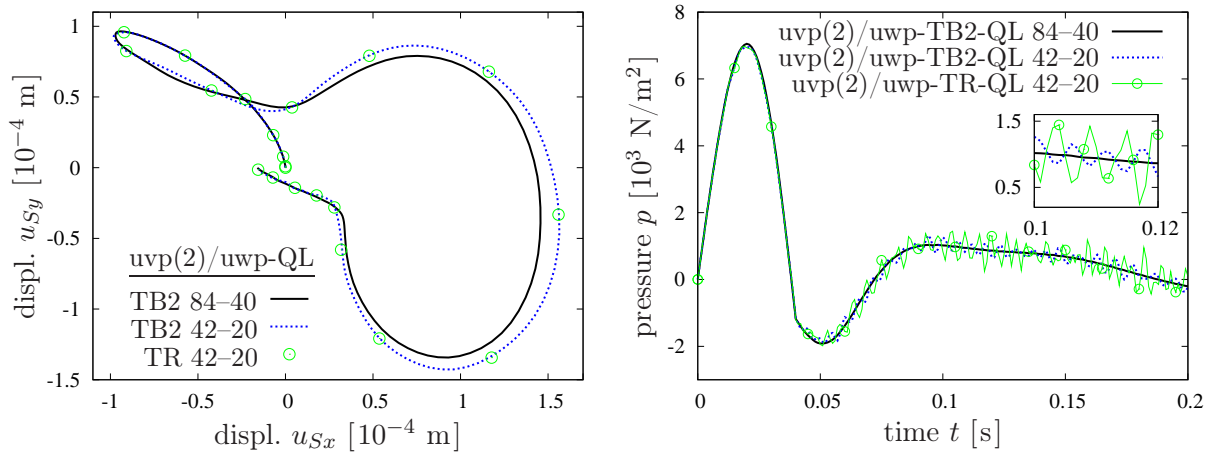


**Figure 4.18:** *In-plane motion of point A (left) and pressure history at point B (right) for $k^F = 10^{-10}$ m/s and $\Delta t = 10^{-3}$ s.*

The implicit monolithic solution by use of mixed equal-order finite elements is accomplished by use of the stabilized uvp($\alpha$) formulation. At this, the magnitude of the stabilization parameter $\alpha$ is reasonably estimated by recourse to (4.72), such that

$$\alpha_{\min} = \alpha_0 \, \Delta t_{cr} \Big( \frac{n^F}{\rho^{FR}} + \frac{n^S}{\rho^{SR}} \Big) \qquad \text{with} \qquad 0 < \alpha_0 \leq 2 \,. \qquad (4.74)$$

It follows from Figure 4.19 that the stabilizing parameter controls the accuracy of the solution. Here, $\alpha_{0(1)} = 2 \rightarrow \alpha_{min} = 1.4 \cdot 10^{-6}$ in comparison to $\alpha_{0(2)} = 0.15 \rightarrow \alpha_{min} = 1.05 \cdot 10^{-7}$ (cf. Table 4.4) yields an erroneous 'weak' response due to the added artificial compressibility.
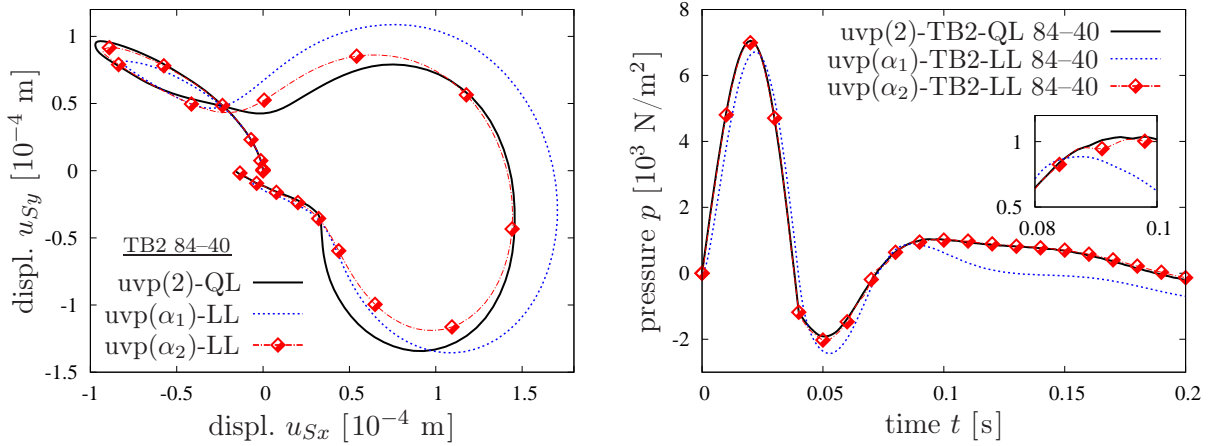
**Figure 4.19:** *In-plane motion of point A (left) and pressure history at point B (right) for* $k^F = 10^{-10}$ *m/s,* $\Delta t = 10^{-3}$ *s, and parameters* $\alpha_{0(1)} = 2$ *and* $\alpha_{0(2)} = 0.15$ *given in (4.74).*

Next, the solution behavior of the splitting scheme is investigated based on uvp(pc)-LL. Figure 4.20 shows that the formulation converges to the reference solutions, where the approximation of the pressure is better than that of the displacements.
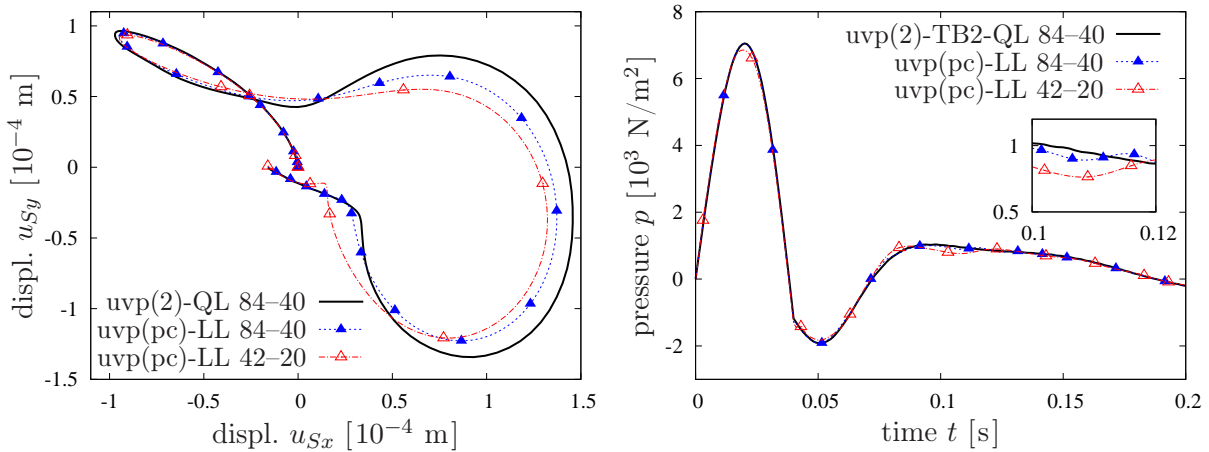


**Figure 4.20:** *In-plane motion of point A (left) and pressure history at point B (right) for* $k^F = 10^{-10}$ *m/s,* $\Delta t = 10^{-3}$ *s for uvp(2)-TB2, and* $\Delta t$ *according to Table 4.4 for uvp(pc).*

Moreover, in the context of the semi-explicit-implicit splitting scheme, we examine the case of using a time step that is much smaller than the critical one ($\Delta t = 5 \cdot 10^{-5} \approx \Delta t_{cr}/20$). Figure 4.21 shows that in this case only the stabilized uvp($\beta$) formulation yields a viable pressure solution, whereas the displacement result is not much affected. Here, two values of the stabilizing parameter $\beta$ as given in (4.72) are used, viz. $\beta_{0(1)} = 1 \rightarrow \beta_{min} = 7 \cdot 10^{-7}$ and $\beta_{0(2)} = 4 \rightarrow \beta_{min} = 2.8 \cdot 10^{-6}$ (see Table 4.4). Please note that the choice of $\beta$ is independent of the permeability.

For the considered low permeability case, the relative acceleration between the solid and the fluid constituent is negligible, i. e., $(\mathbf{w}_{FR})'_S \approx \mathbf{0}$. Consequently, the reduced up formulation yields similar results for the displacement and the pressure variable as the three-field reference uvp(2), see Figure 4.22.

**Figure 4.21:** *In-plane motion of point A (left) and pressure history at point B (right) for $k^F = 10^{-10}$ m/s with $\Delta t = 10^{-3}$ s for uvp(2)-TB2, and with $\Delta t = 5 \cdot 10^{-5}$ s for uvp(pc) and uvp($\beta$) with parameters $\beta_{0(1)} = 1$ and $\beta_{0(2)} = 4$ used in (4.72).*



**Figure 4.22:** *In-plane motion of point A (left) and pressure history at point B (right) for $k^F = 10^{-10}$ m/s and $\Delta t = 10^{-3}$ s.*

In the simple column problem, we observed an insufficient displacement solution of the mixed QL discretization at the permeable loaded boundary. As this is a systematic problem caused by the imposed boundary conditions, it should also be observable in the 2-d example. Therefore, we zoom into the domain and look what happens with the displacement and the pressure field directly under the applied load below point C. Proceeding from a moderately low permeability of $k^F = 10^{-5}$ m/s as in the 1-d problem, we consider the following spatial FE discretization: 28 elements in $x$ direction (10 for the first 10 m, 8 for the middle 1 m, and 10 for the last 10 m) and in $y$ direction 200 elements (20 elements/meter) for the QQ reference solution compared to 50 elements (5 elements/meter) for the coarse QL solution. Using uvp(2)-TB2 and the two mesh sizes 28–200 (20) and 28–50 (5), we oppose the results of the QQ 20 to the QL 5 and QL 20 elementation. Figure 4.23 shows that similarly to the column problem, a faulty approximation of $\mathbf{u}_S$ under the applied load is observed when using mixed QL elements. However, it is not that much distinctive as in the 1-d problem as the steep pressure increase
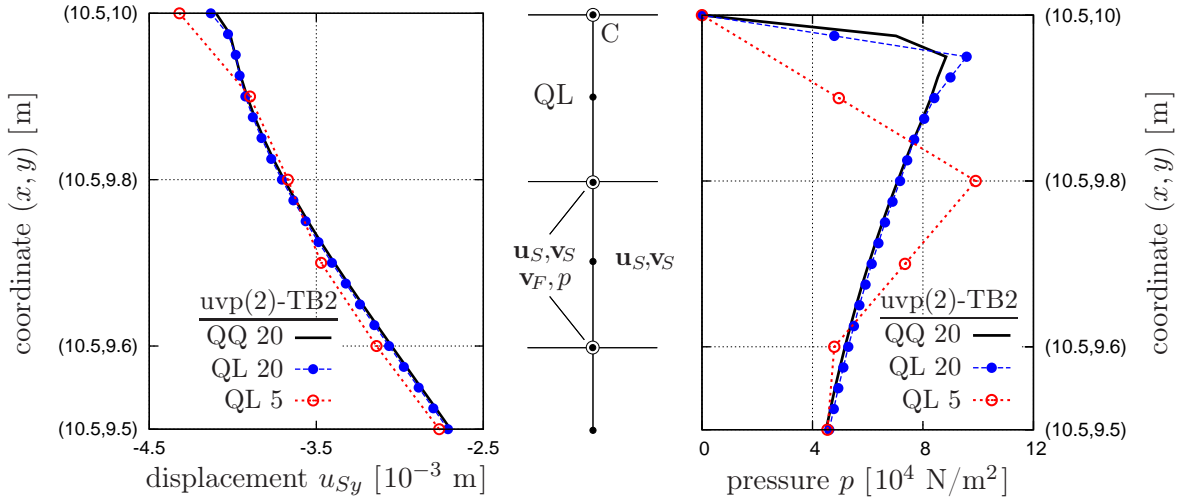
**Figure 4.23:** *Solid displacement (left) and pore pressure distribution (right) in the first half meter under the load vertical down point C for $k^F = 10^{-5}$ m/s at $t = 0.02$ s.*

is relieved also in horizontal $x$ direction. However, the principle problem is retained and might be compensated by a local mesh refinement at permeable and loaded boundaries to better resolve the pressure gradients.
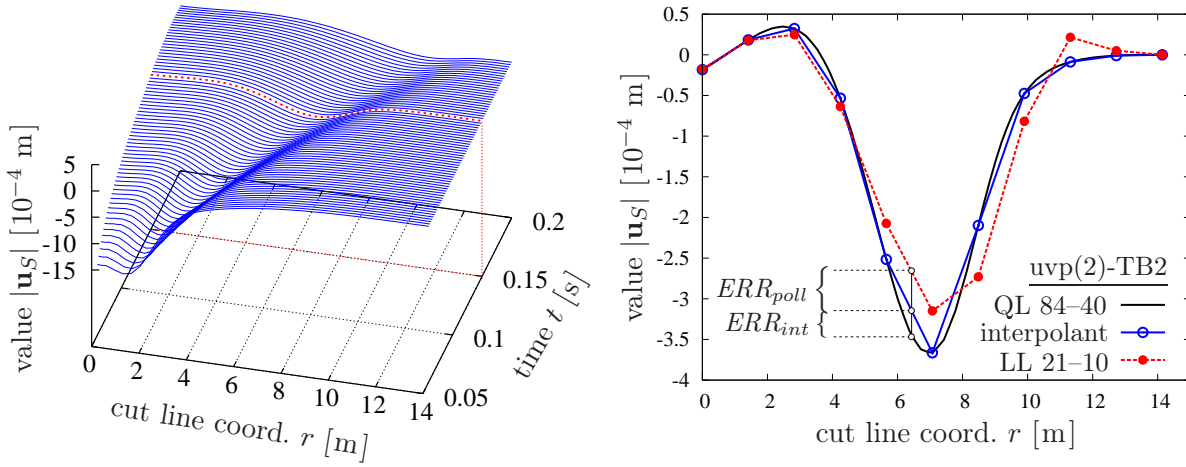
**Figure 4.24:** *Displacement value $|\mathbf{u}_S| = \sqrt{u_{Sx}^2 + u_{Sy}^2}$ along the diagonal cut line with $r = \sqrt{(x-10)^2 + (y-10)^2}$ at different times (left) and at time $t = 0.15$ s showing the interpolation and pollution errors (right).*

Finally, we reveal briefly the pollution effect which is provoked by a poor spatial resolution of the exact wave length in the dynamic problem [23] and responsible for the dispersion of the finite element solution. Therefore, proceeding from uvp(2)-TB2, the displacement value $|\mathbf{u}_S|$ is plotted along a diagonal cut line from the left corner of the applied load at (10,10) to the lower left corner of the domain at (0,0), see Figure 4.8. Figure 4.24 (left) shows the wave propagating with time along the cut line. The interpolation and pollution errors are depicted in Figure 4.24 (right) for a coarse LL elementation at time $t = 0.15$ s. Therein, the interpolant defines the curve that runs through the exact solution at

the discrete nodes, while the values in-between are approximated according to the chosen interpolation function, e. g., a linear interpolation in our example. The deviation from the interpolant to the reference solution defines the interpolation error $ERR_{int}$. The difference between the interpolation error and the total error is the pollution error $ERR_{pol}$. In fact, pollution cannot be avoided but kept small by use of finer meshes and/or higher-order elements [23].

## 4.6    Summary and Discussion of Results

For the reliable discussion of our findings, let us briefly recapitulate the preceding. We started from a dynamic TPM model with materially incompressible constituents defined by the solid and fluid momentum balances and the mixture volume balance for the determination of the primary unknowns, i. e., solid displacement, fluid velocity, and pore-fluid pressure, plus the solid velocity-displacement relation, which is just used for an order reduction in time. In fact, different formulations relying on different primal variables and governing equations are feasible, which we denoted shortly by uvp($\cdots$), uwp, and up according to Table 4.1.

The achieved sets of coupled partial differential equations (PDEs) were then cast into a variational form yielding a general three-field initial boundary-value problem. The spatial semi-discretization was carried out by the mixed Finite Element Method (FEM) resulting in a stiff system of coupled differential-algebraic equations (DAEs) of first order in time with the coupling strength mainly controlled by the permeability parameter $k^F$. For the further treatment of the time-continuous DAEs, two time-integration strategies, namely an implicit monolithic and a semi-explicit-implicit splitting scheme, were introduced, their algorithmic treatment presented, and lastly, compared on the basis of a 1-d and a 2-d wave propagation example. A summary of all investigated test cases and their solution behavior is provided in Table 4.5.

For the implicit monolithic solution, the system of equations was first discretized in space and second in time applying a diagonal implicit Runge-Kutta (DIRK) algorithm using IE, TR, and TR-BDF2 as underlying time-stepping rules. In this regard, TR-BDF2 shows the best performance for solving the dynamic TPM problem, whereas the implicit Euler (IE) scheme is unsuitable due to its strong damping behavior and the trapezoidal rule (TR) only provides marginal stability. The monolithic solution requires a stable mixed FE formulation fulfilling the LBB condition, such as the quadratic-linear (QL) Taylor-Hood elements, which is obligatory for low permeability conditions. In those cases, equal-order approximations show strange pressure instabilities unless a pressure stabilized formulation is used, which, however, is inconsistent in the sense that it implies an artificial compressibility of a de facto materially incompressible porous medium. Applying the monolithic procedure, one has to swallow the bitter pill of a generally higher computational effort due to the inversion of the Jacobian and the larger bandwidth of the system matrices coming along with quadratic interpolations if the stable QL approximation is used.

The semi-explicit-implicit splitting scheme has been implemented in form of a predictor-corrector (P-C) algorithm. In contrast to the monolithic solution, differential operator

**Table 4.5:** *Summary of the observed solution behavior for the distinct test cases. Used symbols: ✓ : successful computation, ◯ : working but not recommended, − : no convergence, computation aborted.*

| Formulation | | large $k^F$ ($10^{-2}$ m/s) | | | small $k^F$ ($10^{-10}$ m/s) | | |
|---|---|---|---|---|---|---|---|
| | | IE | TR | TB2 | IE | TR | TB2 |
| uvp(1) | LL/QQ | ◯[1] | ✓ | ✓ | − | − | − |
| | QL | ◯[1] | ✓[2] | ✓ | −[4] | −[4] | −[4] |
| uvp(2) | LL/QQ | ◯[1] | ✓ | ✓ | − | − | − |
| | QL | ◯[1] | ✓[2] | ✓ | ◯[1] | ✓[2] | ✓[5] |
| uwp | LL/QQ | ◯[1] | ✓ | ✓ | − | − | − |
| | QL | ◯[1] | ◯[3] | ✓ | ◯[1] | ✓[2] | ✓[5] |
| up | QL | ◯[1,7] | ◯[2,7] | ◯[7] | ◯[1] | ✓[2] | ✓[5] |
| uvp($\alpha$) | LL/QQ | not needed | | | ◯[1] | ✓[6] | ✓[6] |
| uvp(pc)  LL | $\Delta t \approx \Delta t_{cr}$ | | ✓ | | | ✓ | |
| | $\Delta t \ll \Delta t_{cr}$ | | − | | | − | |
| uvp($\beta$)  LL | $\Delta t \approx \Delta t_{cr}$ | not needed | | | not needed | | |
| | $\Delta t \ll \Delta t_{cr}$ | | ✓[6] | | | ✓[6] | |

[1] artificial numerical damping; reducible by using a smaller $\Delta t$
[2] pressure oscillations; reducible by using a smaller $\Delta t$ and a finer mesh
[3] strong pressure oscillations
[4] wrong pressure solution
[5] slight pressure oscillations for coarse meshes
[6] accuracy depends on stabilizing parameter
[7] inaccurate displacement solution

splitting demands first the time discretization and the split of the equations and second their spatial discretization allowing a continuous and linear equal-order FE approximation. Due to the included explicit steps, the stability of this splitting scheme is sensitive to the time-step size $\Delta t$ but independent of the permeability. In this regard, an optimal solution is obtained for $\Delta t$ being slightly smaller than the critical time step $\Delta t_{cr}$ given by the CFL condition. The use of $\Delta t \ll \Delta t_{cr}$ yields pressure oscillations and requires a stabilized formulation. The general drawback that the finest mesh patch or the highest wave speed (CFL condition) dictates the global time step might be overcome by use of multirate time-stepping strategies [52] or asynchronous variational integrators [40]. Further demerits are the observed need of finer meshes in order to obtain similar accuracy in comparison with the monolithic solution and the required special treatment of the volume efflux boundary condition.

In conclusion, based on the comprehensive investigation of the test cases and the comparison of the accuracy and stability of the implemented algorithms, we favor and recommend

the implicit monolithic solution of the uvp(2) formulation using TR-BDF2 in combination with an efficient solver that exploits the capabilities of modern hardware architectures. Moreover, such fully coupled approaches negate the need to transfer data from one solver to another, which helps to achieve good scalability on parallel systems. The procedure is also beneficial if inelastic, e.g., elastoplastic, solid properties are considered since the DIRK algorithm can as well be used for the time integration of the associated rate equations, e.g., the plastic flow rule, which are commonly evaluated at integration point level in the sense of a collocation method. Furthermore, embedded Runge-Kutta methods allow for a cheap error estimation and step-size control. In cases where the dynamic load demands a fine temporal resolution, such that pure implicit strategies cannot take advantage of their unconditionally stable step size, the application of implicit-explicit (IMEX) Runge-Kutta methods [2] might aid to further convenience. As far as it is known to the authors, IMEX schemes have not yet been discussed in the context of porous media dynamics and open an avenue for future investigations.

Concerning the choice of the mixed FE formulation, we recommend the usage of the Taylor-Hood-like quadratic-linear elements being aware of their deficiencies at permeable loaded boundaries, which can be countervailed by a locally refined mesh. The mixed equal-order elements behave well up to moderately low permeabilities. However, as in general problems the permeability is deformation-dependent and may locally change over magnitudes, one has to be aware of unphysical oscillations in the pressure variable giving rise to some pressure stabilization at the expense of accuracy. The permeability moreover governs the possibility of using the reduced and computationally cheaper $\mathbf{u}_S$-$p$ formulation, which could be shown to yield acceptable displacement solutions only for moderately small values of $k^F$ associated with negligible accelerations of the seepage flow in the low frequency range.

## 4.7   Conclusions

In this chapter, the numerical solution of wave propagation problems in porous media dynamics has been investigated. At this, the presentation proceeds from a saturated biphasic solid-fluid material with intrinsically incompressible constituents. The governing conservation laws and the constitutive equations are introduced in the framework of the established Theory of Porous Media (TPM) accounting for elastic solid matrix properties and lingering flow conditions based on a geometrically and materially linear description. As it has been shown, the choice of the primary variables and the corresponding balances plays a crucial role for the accuracy and stability of the numerical solution. In particular, two solution algorithms have been presented, viz. an implicit monolithic and a semi-explicit-implicit splitting scheme. Based on that, several test cases, differing in the multi-field formulation, the monolithic time-stepping method, and the approximation order of the primal unknowns, have been constructed and finally studied in the numerical examples. It turned out that both the monolithic and the splitting approach are basically applicable to the solution of the coupled two-phase problem. However, the implicit monolithic procedure ultimately convinced due to its more general suitability, provided

that the right multi-field formulation, stable mixed finite elements, and an appropriate time integrator are used.

## 4.8   References

[1] Arnold, D. N.: Mixed finite element methods for elliptic problems. *Computer Methods in Applied Mechanics and Engineering* **82** (1990), 281–300.

[2] Ascher, U. M.; Ruuth, S. J. & Spiteri, R. J.: Implicit-explicit Runge-Kutta methods for time-dependent partial differential equations. *Applied Numerical Mathematics* **25** (1997), 151–167.

[3] Bank, R. E.; Coughran Jr., W. M.; Fichtner, W.; Grosse, E. H.; Rose, D. J. & Smith, R. K.: Transient simulation of silicon devices and circuits. *IEEE Transactions on Electron Devices* **10** (1985), 1992–2007.

[4] Bathe, K.-J. & Wilson, E.: *Numerical Methods in Finite Element Analysis*. Prentice-Hall, New Jersey 1976.

[5] Biot, M. A.: General theory of three-dimensional consolidation. *Journal of Applied Physics* **12** (1941), 155–164.

[6] Biot, M. A.: Theory of propagation of elastic waves in a fluid-saturated porous solid, I. low frequency range. *Journal of the Acoustical Society of America* **28** (1956), 168–178.

[7] de Boer, R.: *Theory of Porous Media*. Springer-Verlag, Berlin 2000.

[8] de Boer, R. & Ehlers, W.: The development of the concept of effective stresses. *Acta Mechanica* **83** (1990), 77–92.

[9] de Boer, R.; Ehlers, W. & Liu, Z.: One-dimensional wave propagation in fluid saturated incompressible porous media. *Archive of Applied Mechanics* **63** (1993), 59–72.

[10] Boffi, D.; Brezzi, F.; Demkowicz, L. F.; Durán, R. G.; Falk, R. S. & Fortin, M.: *Mixed Finite Elements, Compatibility Conditions, and Applications: Lectures given at the C. I. M. E. Summer School held in Cetraro, Italy, June 26 - July 1, 2006.* Lecture Notes in Mathematics, Springer-Verlag 2008.

[11] Bowen, R. M.: Theory of mixtures. In Eringen, A. C. (ed.): *Continuum Physics.* Academic Press, New York 1976, vol. III, pp. 1–127.

[12] Bowen, R. M.: Incompressible porous media models by use of the theory of mixtures. *International Journal of Engineering Science* **18** (1980), 1129–1148.

[13] Bowen, R. M.: Compressible porous media models by use of the theory of mixtures. *International Journal of Engineering Science* **20** (1982), 697–735.

[14] Braess, D.: *Finite Elemente*. Springer-Verlag, Berlin 1997.

[15] Breuer, S.: Quasi-static and dynamic behavior of saturated porous media with incompressible constituents. *Transport in Porous Media* **34** (1999), 285–303.

[16] Brezzi, F. & Fortin, M.: *Mixed and Hybrid Finite Element Methods.* Springer-Verlag, New York 1991.

[17] Butcher, J. C.: *The Numerical Analysis of Ordinary Differential Equations: Runge-Kutta and General Linear Methods.* John Wiley & Sons, New York 1987.

[18] Chen, Z.; Steeb, H. & Diebels, S.: A time-discontinuous Galerkin method for the dynamical analysis of porous media. *International Journal for Numerical and Analytical Methods in Geomechanics* **30** (2006), 1113–1134.

[19] Chen, Z.; Steeb, H. & Diebels, S.: A space-time discontinuous Galerkin method applied to single-phase flow in porous media. *Computational Geosciences* **12** (2008), 525–539.

[20] Chorin, A. J.: A numerical method for solving incompressible viscous problems. *Journal of Applied Physics* **2** (1967), 12–26.

[21] Courant, R.; Friedrichs, K. & Lewy, H.: Über die partiellen Differenzengleichungen der mathematischen Physik. *Mathematische Annalen* **100** (1928), 32–74.

[22] Coussy, O.: *Mechanics of Porous Continua.* John Wiley & Sons, Chichester 1995.

[23] Deraemaeker, A.; Babuška, I. & Bouillard, P.: Dispersion and pollution of the FEM solution for the Helmholtz equation in one, two and three dimensions. *International Journal for Numerical Methods in Engineering* **46** (1999), 471–499.

[24] Diebels, S. & Ehlers, W.: Dynamic analysis of a fully saturated porous medium accounting for geometrical and material non-linearities. *International Journal for Numerical Methods in Engineering* **39** (1996), 81–97.

[25] Diebels, S.; Ellsiepen, P. & Ehlers, W.: Error-controlled Runge-Kutta time integration of a viscoplastic hybrid two-phase model. *Technische Mechanik* **19** (1999), 19–27.

[26] Drumheller, D. S.: The theoretical treatment of a porous solid using a mixture theory. *International Journal of Solids and Structures* **14** (1978), 441–456.

[27] Ehlers, W.: Foundations of multiphasic and porous materials. In Ehlers, W. & Bluhm, J. (eds.): *Porous Media: Theory, Experiments and Numerical Applications.* Springer-Verlag, Berlin 2002, pp. 3–86.

[28] Ehlers, W. & Ellsiepen, P.: Theoretical and numerical methods in environmental continuum mechanics based on the theory of porous media. In Schrefler, B. A. (ed.): *Environmental Geomechanics.* Springer-Verlag, Wien 2001, CISM Courses and Lectures No. 417, pp. 1–81.

[29] Ehlers, W. & Kubik, J.: On finite dynamic equations for fluid-saturated porous media. *Acta Mechanica* **105** (1994), 101–317.

[30] Ellsiepen, P.: *Zeit- und ortsadaptive Verfahren angewandt auf Mehrphasenprobleme poröser Medien.* Dissertation, Bericht Nr. II-3 aus dem Institut für Mechanik (Bauwesen), Universität Stuttgart 1999.

[31] Felippa, C. A.; Park, K. C. & Farhat, C.: Partitioned analysis of coupled mechanical systems. *Computer Methods in Applied Mechanics and Engineering* **190** (2001), 3247–3270.

[32] Goda, K.: A multiphase technique with implicit difference schemes for calculating two- or three- dimensional cavity flows. *Journal of Computational Physics* **30** (1979), 76–95.

[33] Gresho, P. M. & Sani, R. L.: *Incompressible Flow and the Finite Element Method*, vol. 2. John Wiley & Sons, Chichester 2000, second corrected reprint of 1998.

[34] Guermond, J.-L. & Quartapelle, L.: On stability and convergence of projection methods based on pressure Poisson equation. *International Journal for Numerical Methods in Fluids* **26** (1998), 1039–1053.

[35] Hairer, E. & Wanner, G.: *Solving Ordinary Differential Equations, Vol. 2: Stiff and Differential-Algebraic Problems.* Springer-Verlag, Berlin 1991.

[36] Hartmann, S.: Computation in finite strain viscoelasticity: Finite elements based on the interpretation as differential-algebraic equations. *Computer Methods in Applied Mechanics and Engineering* **191** (2002), 1439–1470.

[37] Hosea, M. E. & Shampine, L. F.: Analysis and implementation of TR-BDF2. *Applied Numerical Mathematics* **20** (1996), 21–37.

[38] Huang, M.; Wu, S. & Zienkiewicz, O. C.: Incompressible or nearly incompressible soil dynamic behaviour – a new staggered algorithm to circumvent restrictions of mixed formulation. *Soil Dynamics and Earthquake Engineering* **21** (2001), 169–179.

[39] Huang, M.; Yue, Z. Q.; Tham, L. G. & Zienkiewicz, O. C.: On the stable finite element procedure for dynamic problems of saturated porous media. *International Journal for Numerical Methods in Engineering* **61** (2004), 1421–1450.

[40] Lew, A.; Marsden, J.; Ortiz, M. & West, M.: Asynchronous variational integrators. *Archive for Rational Mechanics and Analysis* **167** (2003), 85–146.

[41] Lewis, R. W. & Schrefler, B. A.: *The Finite Element Method in the Static and Dynamic Deformation and Consolidation of Porous Media.* John Wiley & Sons, Chichester 1998, 2nd edn.

[42] Li, C.; Borja, R. I. & Regueiro, R. A.: Dynamics of porous media at finite strain. *Computer Methods in Applied Mechanics and Engineering* **193** (2004), 3837–3870.

[43] Li, X.; Han, X. & Pastor, M.: An iterative stabilized fractional step algorithm for finite element analysis in saturated soil dynamics. *Computer Methods in Applied Mechanics and Engineering* **85** (2003), 67–94.

[44] Markert, B.: A constitutive approach to 3-d nonlinear fluid flow through finite deformable porous continua. *Transport in Porous Media* **70** (2007), 427–450.

[45] Markert, B.: A biphasic continuum approach for viscoelastic high-porosity foams: Comprehensive theory, numerics, and application. *Archives of Computational Methods in Engineering* **15** (2008), 371–446.

[46] Matthies, H. G.; Niekamp, R. & Steindorf, J.: Algorithms for strong coupling procedures. *Computer Methods in Applied Mechanics and Engineering* **195** (2006), 2028–2049.

[47] Mow, V. C.; Kuei, S. C.; Lai, W. M. & Armstrong, C. G.: Biphasic creep and stress relaxation of articular cartilage in compression: Theory and experiments. *ASME Journal of Biomechanical Engineering* **102** (1980), 73–84.

[48] Oden, J. T. & Carey, G. F.: *Finite Elements: Mathematical Aspects*, vol. IV. Prentice-Hall, New Jersey 1983.

[49] Park, K. C.: Stabilization of partitioned solution procedures for pore-fluid interaction analysis. *International Journal for Numerical Methods in Engineering* **19** (1983), 1669–1673.

[50] Prohl, A.: *Projection and Quasi-Compressibility Methods for Solving the Incompressible Navier-Stokes Equations*. Teubner, Stuttgart 1997.

[51] Rannacher, R.: Finite element methods for the incompressible Navier-Stokes equations. In Galdi, P.; Heywood, J. & Rannacher, R. (eds.): *Fundamental Directions in Mathematical Fluid Mechanics*. Birkhäuser, Basel 2000, pp. 191–293.

[52] Savenco, V.; Hundsdorfer, W. & Verwer, J. G.: A multirate time stepping strategy for stiff ordinary differential equations. *BIT Numerical Mathematics* **47** (2007), 137–155.

[53] Schanz, M.: Transient wave propagation in a one-dimensional poroelastic column. *Acta Mechanica* **145** (2000), 1–18.

[54] Schanz, M.: Poroelastodynamics: Linear models, analytical solutions, and numerical methods. *Applied Mechanics Reviews* **62** (2009), 030803.

[55] Schanz, M. & Diebels, S.: A comparative study of Biot's theory and the linear Theory of Porous Media for wave propagation problems. *Acta Mechanica* **161** (2003), 213–235.

[56] van Kan, J.: A second-order accurate pressure-correction scheme for viscous incompressible flow. *SIAM Journal on Scientific and Statistical Computing* **7** (1986), 870–891.

[57] Wilmański, K. & Albers, B.: Acoustic waves in porous solid-fluid mixture. In Hutter, K. & Kirchner, N. (eds.): *Dynamic Response of Granular and Porous Materials under Large and Catastrophic Deformations*. Springer, Berlin 2003, pp. 285–313.

[58] Woltmann, R.: *Beyträge zur hydraulischen Architectur*, vol. 3. J. C. Dietrich, Göttingen 1794.

[59] Wood, W. L.: *Practical Time Stepping Schemes*. Clarendon Press, Oxford 1990.

[60] Zienkiewicz, O. C.; Chan, A. H. C.; Pastor, M.; Paul, D. K. & Shiomi, T.: Static and dynamic behaviour of soils: a rational approach to quantitative solutions. I. fully saturated problems. *Proceedings of the Royal Society* **429** (1990), 285–309.

[61] Zienkiewicz, O. C.; Chan, A. H. C.; Pastor, M.; Schrefler, B. A. & Shiomi, T.: *Computational geomechanics with special reference to earthquake engineering.* John Wiley & Sons, Chichester 1999.

[62] Zienkiewicz, O. C.; Huang, M.; Wu, J. & Wu, S.: A new algorithm for coupled soil-pore fluid problem. *Shock and Vibration* **1** (1993), 3–14.

[63] Zienkiewicz, O. C.; Qu, S.; Taylor, R. L. & Nakazawa, S.: The patch test for mixed formulations. *International Journal for Numerical Methods in Engineering* **23** (1986), 1873–1883.

[64] Zienkiewicz, O. C. & Shiomi, T.: Dynamic behaviour of saturated porous media: the generalized Biot formulation and its numerical solution. *International Journal for Numerical and Analytical Methods in Geomechanics* (1984), 71–96.

[65] Zienkiewicz, O. C. & Taylor, R. L.: *The Finite Element Method. Basic Formulation and Linear Problems*, vol. 1. McGraw-Hill, London 1989, 4th edn.

[66] Zienkiewicz, O. C. & Taylor, R. L.: *The Finite Element Method. The Basis*, vol. 1. Butterworth Heinemann, Oxford 2000, 5th edn.

# 5 Continuum Biomechanics of Tissues

SUMMARY

Biological tissues, no matter if soft or hard tissues are concerned, basically consist of a solid matrix saturated by an interstitial fluid, which is composed of a liquid solvent and various dissolved solutes. In case of vascular tissues, the blood system including the arteries, the capillary system and the veins has to be added. Based on the complex geometric and bio-physical nature of biological systems, a biomechanical description is based on a macroscopic, continuum-mechanical approach proceeding from homogenized microstructures rather than on a full microscopic investigation.

Consequently, the present article provides a continuum-biomechanical approach for the description of biological tissues. This includes the well-founded framework of the Theory of Porous Media (TPM), which can be seen as an extension of the classical Theory of Mixtures (TM) towards immiscible materials. Based on this approach, which easily can be extended by electro-chemical information, swelling tissues like the intervertebral disc and growth phenomena like avascular tumor growth and muscle stimulation as the basis of any motion of biological systems can be described. However, as a result of page limitations, the article excludes the incorporation of the blood system into the present modeling and simulation examples as well as the description of any muscle stimulation.

## 5.1 Introduction

General biomaterials such as soft and hard biological tissues as well as bio-like materials as, for example, hydrogel, basically fall into the category of biphasic, multi-component materials. Biomaterials consist of a cellular solid matrix, built of collagen fibers and muscle cells, as well as proteoglycans, such as aggrecan with their adhering fixed charges (negatively charged ions). Furthermore, there is an interstitial fluid composed of almost water and dissolved solutes, such as the positive and negative ions of a dissolved salt as, for example, monovalent $Na^+Cl^-$. In the frame of vascular tissues, also the blood system of its arteries, capillaries and veins has to be considered. Furthermore, if muscles are concerned, one additionally has to include the electrical stimulations leading to muscle contraction. Since biomaterials generally undergo large solid deformations, the solid behavior is described in the framework of finite elasticity or viscoelasticity, respectively.

Based on the fact that biomaterials have a very complex microstructure, one has to decide whether or not this microstructure has to be included into the mechanical description in detail or in a homogenized manner. Apart from a few articles including

bio-microstructures in an overall macroscopic framework [2, 36, 40], the majority of authors have rather proceeded from a direct macroscopic framework than from micro-to-macro transitions where the microstructure is numerically embedded into the macroscopic procedure. From the macroscopic point of view, biomaterials are often considered as a single-phasic material with complex material properties including viscosities and electro-chemical effects in a comprehensive way [6, 13, 23–28, 32, 42–44]. However, this procedure will fail to include transport and diffusion processes as they occur, for example, as nutrient transport or ion diffusion. If these effects have to be considered, which obviously is true in case of growth and swelling phenomena, one has to switch the modeling procedure from a single-phasic to a multi-phasic approach. The advantage of describing multi-phasic materials with multiple components is obvious and can be embedded in the well-founded Theory of Porous Media (TPM). A complete review of various achievements in the biomechanics of biological tissues including growth and remodeling is given, for example, by Taber [47] and Humphrey [29].

The TPM, cf. [7, 9, 10, 14–17], proceeds from the same basis as the Theory of Mixtures (TM), cf. [8], thus describing multi-component media on a homogenized basis by smearing out the individual materials over the control volume and allowing for convenient interaction terms between them. Modeling biomaterials on a macroscopic level makes use of the basic idea of the TPM describing immiscible phases, such as the solid skeleton and the interstitial fluid, by smearing out their microstructures. In addition, use is made of the TM while considering the interstitial fluid as a real mixture of the liquid solvent and the dissolved solutes. When electro-chemical interactions come into play, one has to enrich the TPM by further information describing the electrical and chemical fields, cf. [19, 22].

## 5.2 The TPM Basis

### 5.2.1 Immiscible Components and Volume Fractions

The TPM proceeds from superimposed and interacting but immiscible constituents covering the same amount of space as a result of a real or a virtual averaging process. Following this, a biological tissue $\varphi$ is understood as a multi-component continuum $\mathcal{B}$, generally consisting of $k$ components $\varphi^\alpha$, given by the solid part $\varphi^S$ of the tissue, the components of the interstitial fluid $\varphi^F$ and the components of the blood $\varphi^B$. As a result, the volume $V$ of $\mathcal{B}$ stems from the sum of the partial volumes of the components $\varphi^\alpha$ in $\mathcal{B}$:

$$V = \int_{\mathcal{B}} \mathrm{d}v = \bigcup_{\alpha=1}^{k} V^\alpha, \qquad \text{where} \qquad V^\alpha = \int_{\mathcal{B}} \mathrm{d}v^\alpha =: \int_{\mathcal{B}} n^\alpha \, \mathrm{d}v \,. \tag{5.1}$$

Therein, $n^\alpha$ is defined as the local ratio of the volume element $\mathrm{d}v^\alpha$ of a given constituent $\varphi^\alpha$ with respect to the volume element $\mathrm{d}v$ of the overall medium $\varphi$:

$$n^\alpha = \frac{\mathrm{d}v^\alpha}{\mathrm{d}v} \qquad \text{with} \qquad \sum_{\alpha=S,F,B} n^\alpha = 1 \,. \tag{5.2}$$

By use of the volume fractions $n^\alpha$, two different density functions can be introduced:

$$\rho^{\alpha R} = \frac{\mathrm{d}m^\alpha}{\mathrm{d}v^\alpha} \qquad \text{and} \qquad \rho^\alpha = \frac{\mathrm{d}m^\alpha}{\mathrm{d}v}. \tag{5.3}$$

The effective density $\rho^{\alpha R}$ is given as the local mass $\mathrm{d}m^\alpha$ over the local constituent volume $\mathrm{d}v^\alpha$, while the partial density defines the same local mass with respect to the local bulk volume $\mathrm{d}v$. As a result,

$$\rho^\alpha = n^\alpha \rho^{\alpha R}. \tag{5.4}$$

Based on the above relation, it is immediately evident that the property of material incompressibility ($\rho^{\alpha R} = \text{const.}$) is not equivalent to the property of bulk incompressibility, since the partial density functions $\rho^\alpha$ can still change through changes in the volume fractions $n^\alpha$.

## 5.2.2 Miscible Components and Molar Concentrations

If the interstitial fluid $\varphi^F$ or the blood $\varphi^B$ has to be treated as a real fluid mixture in the sense of a solution of a solute and dissolved solvents, such as nutrients or ions, it is necessary to distinguish differently between the components compared to the introduction of volume fractions. Proceeding from the fact that volume fractions cannot be measured in case of real mixtures, the mixture components $\varphi^\gamma$ are considered by their partial densities $\rho_\beta^\gamma$, which is defined with respect to the compartment of the pore space covered by $\varphi^\beta$ with $\beta = \{F, B\}$. Thus,

$$\rho^\gamma =: n^\beta \rho_\beta^\gamma, \qquad \text{where} \qquad \rho^{\beta R} = \sum_\gamma \rho_\beta^\gamma \qquad \text{and} \qquad \rho^\beta = n^\beta \rho^{\beta R}. \tag{5.5}$$

Comparable to the TM, $\rho^{\beta R}$ defines the so-called mixture density of the interstitial fluid or the blood, respectively, given through the sum of the partial densities $\rho_\beta^\gamma$ in $\varphi^\beta$. Furthermore, $\rho^\beta$ relates $\rho^{\beta R}$ to the volume of the whole aggregate, while $\rho^{\beta R}$ itself is related to the compartment of the pore space covered by $\varphi^\beta$.

Given $\rho_\beta^\gamma$, the portion of matter is defined through the molar concentration $c_m^\gamma$ and the molar mass $M_m^\gamma$ via

$$\rho_\beta^\gamma = c_m^\gamma M_m^\gamma, \qquad \text{where} \qquad c_\beta^\gamma = \frac{\mathrm{d}n_m^\gamma}{\mathrm{d}v^\beta}. \tag{5.6}$$

Therein, $\mathrm{d}n_m^\gamma$ is the local number of moles. Since $M_m^\gamma$ is a constant of the species $\varphi^\gamma$, the variation of $\rho_\beta^\gamma$ is uniquely determined by $c_m^\gamma$.

## 5.2.3 Constituent Balance Relations

Following the basic ideas and definitions of the TPM, one proceeds from the following balance relations of the components $\varphi^\alpha$ constituting the overall biological aggregate [17]:

- mass: $\qquad (\rho^\alpha)'_\alpha + \rho^\alpha \operatorname{div} \overset{'}{\mathbf{x}}_\alpha = \hat{\rho}^\alpha \,,$

- momentum: $\qquad \rho^\alpha \overset{''}{\mathbf{x}}_\alpha = \operatorname{div} \mathbf{T}^\alpha + \rho^\alpha \mathbf{b}^\alpha + \hat{\mathbf{p}}^\alpha \,,$

- m. o. m.: $\qquad \mathbf{0} = \mathbf{I} \times \mathbf{T}^\alpha + \hat{\mathbf{m}}^\alpha,$ $\qquad$ (5.7)

- energy: $\qquad \rho^\alpha (\varepsilon^\alpha)'_\alpha = \mathbf{T}^\alpha \cdot \mathbf{L}_\alpha - \operatorname{div} \mathbf{q}^\alpha + \rho^\alpha r^\alpha + \hat{\varepsilon}^\alpha,$

- entropy: $\qquad \rho^\alpha (\eta^\alpha)'_\alpha = \operatorname{div}\left(-\dfrac{1}{\theta^\alpha}\, \mathbf{q}^\alpha\right) + \dfrac{1}{\theta^\alpha}\rho^\alpha r^\alpha + s\hat{\zeta}^\alpha \,.$

Therein, $\overset{'}{\mathbf{x}}_\alpha$ and $\overset{''}{\mathbf{x}}_\alpha$ are the velocity and acceleration functions of $\varphi^\alpha$. Furthermore, $\mathbf{T}^\alpha$ stands for the partial Cauchy stress, $\mathbf{b}^\alpha$ for the body force density, $\varepsilon^\alpha$ for the mass-specific internal energy , $\mathbf{L}_\alpha$ for the spatial velocity gradient, $\mathbf{q}^\alpha$ for the heat influx vector, $r^\alpha$ for the radiation term, $\eta^\alpha$ for the mass-specific entropy and $\theta^\alpha$ for the Kelvin's temperature. Moreover, $\operatorname{div}(\,\cdot\,)$ is the divergence operator corresponding to the gradient operator $\operatorname{grad}(\,\cdot\,) = \partial(\,\cdot\,)/\partial\mathbf{x}$, while $(\,\cdot\,)'_\alpha$ characterizes the material time derivative following the individual motion of $\varphi^\alpha$. If growth phenomena are concerned, cf. Section 5.4, the concept of constituent temperatures $\theta^\alpha$ and their energetically conjugate counterparts, the entropies $\eta^\alpha$, is extended towards additional temperature-analogous "growth energies" and entropy-analogous "configurational growth entropies".

The direct production terms of mass, momentum, moment of momentum, energy and entropy, given through $\hat{\rho}^\alpha$, $\hat{\mathbf{p}}^\alpha$, $\hat{\mathbf{m}}^\alpha$, $\hat{\varepsilon}^\alpha$ and $\hat{\zeta}^\alpha$, are related to the total productions via

$$
\begin{aligned}
\hat{\mathbf{s}}^\alpha &= \hat{\mathbf{p}}^\alpha + \hat{\rho}^\alpha \overset{'}{\mathbf{x}}_\alpha \,,\\[4pt]
\hat{\mathbf{h}}^\alpha &= \hat{\mathbf{m}}^\alpha + \mathbf{x} \times (\hat{\mathbf{p}}^\alpha + \hat{\rho}^\alpha \overset{'}{\mathbf{x}}_\alpha)\,,\\[4pt]
\hat{e}^\alpha &= \hat{\varepsilon}^\alpha + \hat{\mathbf{p}}^\alpha \cdot \overset{'}{\mathbf{x}}_\alpha + \hat{\rho}^\alpha (\varepsilon^\alpha + \tfrac{1}{2}\overset{'}{\mathbf{x}}_\alpha \cdot \overset{'}{\mathbf{x}}_\alpha)\,,\\[4pt]
\hat{\eta}^\alpha &= \hat{\zeta}^\alpha + \hat{\rho}^\alpha \eta^\alpha.
\end{aligned}
\tag{5.8}
$$

By summing up the relations (5.7) over all constituents $\varphi^\alpha$, one obtains the following constraints of the production terms:

$$
\sum_\alpha \hat{\rho}^\alpha = 0\,, \qquad \sum_\alpha \hat{\mathbf{s}}^\alpha = \mathbf{0}\,, \qquad \sum_\alpha \hat{\mathbf{h}}^\alpha = \mathbf{0}\,, \qquad \sum_\alpha \hat{e}^\alpha = 0\,, \qquad \sum_\alpha \hat{\eta}^\alpha \geq 0\,. \tag{5.9}
$$

For details concerning the above setting of the balance laws of the TPM, the interested reader is again referred to [17, 35] and the quotations therein.

Given the relations (5.7)–(5.9), the entropy principle for the overall biological tissue reads

$$
\sum_{\alpha=1}^{k} \left[ \rho^\alpha (\eta^\alpha)'_\alpha + \hat{\rho}^\alpha \eta^\alpha + \operatorname{div}\left(\frac{1}{\theta^\alpha}\, \mathbf{q}^\alpha\right) - \frac{1}{\theta^\alpha}\rho^\alpha r^\alpha \right] \geq 0\,. \tag{5.10}
$$

Introducing mass-specific constituent free energy functions $\psi^\alpha$ via the Legendre transformation

$$
\psi^\alpha := \varepsilon^\alpha - \theta^\alpha \eta^\alpha \,, \tag{5.11}
$$

one obtains with the aid of the energy balance relations $(5.7)_3$ the mostly used form of the entropy principle for multi-component materials, viz.:

$$\sum_{\alpha=1}^{k} \frac{1}{\theta^\alpha} \left[ \mathbf{T}^\alpha \cdot \mathbf{L}_\alpha - \rho^\alpha \left[ (\psi^\alpha)'_\alpha + (\theta^\alpha)'_\alpha \eta^\alpha \right] - \hat{\mathbf{p}}^\alpha \cdot \overset{'}{\mathbf{x}}_\alpha - \right.$$
$$\left. - \hat{\rho}^\alpha (\psi^\alpha + \tfrac{1}{2} \overset{'}{\mathbf{x}}_\alpha \cdot \overset{'}{\mathbf{x}}_\alpha) - \frac{1}{\theta^\alpha} \mathbf{q}^\alpha \cdot \operatorname{grad} \theta^\alpha + \hat{e}^\alpha \right] \geq 0 \,. \tag{5.12}$$

## 5.3 Swelling Media as Biphasic, Four-Component Aggregates

In the mechanics of biological tissue, such as avascular cartilage or the intervertebral disc as well as in various other fields, swelling problems occur and have to be described on a computational basis. The phenomenon of swelling is triggered by the fact that negative electrical charges are fixed to the skeleton material such that the chemical equilibrium can change as a result of the composition of an external solution.

To describe swelling processes of avascular tissue and further swellable materials, one has to consider a biphasic medium of a solid skeleton $\varphi^S$ with adhering fixed charges $\varphi^{fc}$ and a pore fluid $\varphi^F$, understood as a mixture of a liquid solvent $\varphi^L$, e.g. water, and dissolved solutes, e.g. positive and negative ions $\varphi^+$ and $\varphi^-$ of a salt such as the monovalent $Na^+CL^-$. Based on the balance equations $(5.7)_{1,2}$, the biphasic, four-component material under study is governed by the following mass and momentum balances:

$$\left. \begin{aligned} (\rho^\alpha)'_\alpha + \rho^\alpha \operatorname{div} \overset{'}{\mathbf{x}}_\alpha &= 0 \,, \\ \mathbf{0} = \operatorname{div} \mathbf{T}^\alpha + \rho^\alpha \mathbf{b}^\alpha + \hat{\mathbf{p}}^\alpha \end{aligned} \right\} = \{S, \ L, \ +, \ -\} \qquad \text{and} \qquad \varphi^F = \bigcup_{\gamma=L,+,-} \varphi^\gamma . \tag{5.13}$$

To obtain (5.13), quasi-static processes $(\overset{''}{\mathbf{x}}_\alpha = \mathbf{0})$ at constant temperature $(\theta^\alpha = \theta = \text{const.})$ and a general absence of phase transitions $(\hat{\rho}^\alpha = 0)$ have been assumed. Based on the concept of material incompressibility $(\rho^{\alpha R} = \text{const.})$ of the porous solid including the fixed charges and the fluid components, liquid, cations and anions, the mass balances reduce to volume balances

$$(n^\alpha)'_\alpha + n^\alpha \operatorname{div} \overset{'}{\mathbf{x}}_\alpha = 0 \,. \tag{5.14}$$

Although the component densities $\rho^{\alpha R}$ are constant, the partial densities $\rho_F^\gamma$ of the fluid components as well as the effective pore-fluid density $\rho^{FR}$, given by (5.5) and (5.6), can vary as a result of varying molar concentrations $c_m^\gamma$ in the pore-fluid mixture:

$$\rho^{FR} = \sum_{\gamma=L,\delta} \rho_F^\gamma \qquad \text{with} \qquad \rho_F^\gamma = c_m^\gamma M_m^\gamma \qquad \text{and} \qquad \delta = \{+, -\} \,. \tag{5.15}$$

Since the molar masses $M_m^\gamma$ of the fluid components are constant, $(5.13)_1$ is rewritten to yield

$$(n^F c_m^\gamma)'_\gamma + n^F c_m^\gamma \operatorname{div} \overset{'}{\mathbf{x}}_\gamma = 0 \qquad \text{or}$$
$$n^F (c_m^\gamma)'_\gamma + c_m^\gamma \operatorname{div} (\mathbf{u}_S)'_S + n^F c_m^\gamma \operatorname{div} \mathbf{w}_\gamma + c_m^\gamma \operatorname{grad} n^F \cdot \mathbf{w}_\gamma = 0 \,, \tag{5.16}$$

respectively. Proceeding from the fact that the fixed charges adhere to the skeleton material, the fixed charges volume balance reads

$$(\rho^{fc})'_S + \rho^{fc} \operatorname{div} \overset{'}{\mathbf{x}}_S = 0 \,, \qquad \text{where} \qquad \rho^{fc} =: n^F c_m^{fc} M_m^{fc} \,. \tag{5.17}$$

Therein, $c_m^{fc}$ and $M_m^{fc}$ are the molar concentration and the molar mass of $\varphi^{fc}$.

Proceeding from an isothermal four-component formulation of a biphasic material, quasi-static computational procedures are based on a basic set of seven primary variables given by the solid displacement $\mathbf{u}_S$, the pore-fluid seepage velocity $\mathbf{w}_F$, the relative ion velocities $\mathbf{w}_+$ and $\mathbf{w}_-$, the hydraulic pore-fluid pressure $\mathcal{P}$ and the cation and anion concentrations $c_m^+$ and $c_m^-$. Under quasi-static conditions, one obtains a coupling between $\mathbf{w}_F$ and $\mathcal{P}$ as well as between $\mathbf{w}_\delta$ and $c_m^\delta$ resulting from the individual fluid momentum balances and the constitutive setting yielding Darcy-like and Nernst-Planck-like relations. Following this reduces the set of primary variables from seven to four: the solid displacement $\mathbf{u}_S$, the pore-fluid pressure $\mathcal{P}$ and the ion concentrations $c_m^\delta$. Thus, the corresponding set of governing equations is given by the overall momentum balance corresponding to $\mathbf{u}_S$, the fluid volume balance corresponding to $\mathcal{P}$ and the ion concentration balances corresponding to $c_m^\delta$. Following this, one obtains

$$\begin{aligned}
\mathbf{0} &= \operatorname{div} \mathbf{T} + \rho\,\mathbf{g} \,, \\
0 &= (n^F)'_S + n^F \operatorname{div} (\mathbf{u}_S)'_S + \operatorname{div}(n^F \mathbf{w}_F) + \frac{n^F}{\rho^{FR}}(\rho^{FR})'_F \,, \\
0 &= n^F (c_m^\delta)'_S + c_m^\delta \operatorname{div}(\mathbf{u}_S)'_S + \operatorname{div}(n^F c_m^\delta \mathbf{w}_\delta) \,.
\end{aligned} \tag{5.18}$$

Therein, $(5.18)_1$ was obtained by summing up $(5.13)_2$, where use was made of $\rho := \sum_\alpha \rho^\alpha$, $\mathbf{T} := \sum_\alpha \mathbf{T}^\alpha$ and of constant body force densities equivalent to the overall gravitation $\mathbf{g}$ through $\mathbf{b}^\alpha = \mathbf{b} =: \mathbf{g}$. Furthermore, the constraint $(5.9)_2$ was considered with the aid of $(5.8)_1$ and $\hat{\rho}^\alpha = 0$. Describing the pore-fluid mass balance $(5.18)_2$ and the ion concentration balances $(5.18)_3$ with respect to the moving solid skeleton, the relative velocities $\mathbf{w}_F = \overset{'}{\mathbf{x}}_F - (\mathbf{u}_S)'_S$ and $\mathbf{w}_\gamma = \overset{'}{\mathbf{x}}_\gamma - (\mathbf{u}_S)'_S$ come into play, where $(\mathbf{u}_S)'_S = \overset{'}{\mathbf{x}}_S$. To obtain $(5.18)_2$ and $(5.18)_3$, additional use was made of $(5.5)$ and $(5.6)$.

## 5.3.1 Restrictions Obtained from the Entropy Inequality

To close the model under consideration, constitutive equations are required for the partial Cauchy stresses $\mathbf{T}^\alpha$ and the linear momentum productions $\hat{\mathbf{p}}^\gamma$ of the fluid components. Note in passing that defining $\mathbf{T}^\alpha$ will include the constitutive equations for the chemical potentials and the osmotic pressure.

An evaluation of the overall entropy inequality

$$\mathbf{T}^S \cdot \mathbf{L}_S - \rho^S (\psi^S)'_S + \sum_\gamma \left[ \mathbf{T}^\gamma \cdot \mathbf{L}_\gamma - \rho^\gamma (\psi^\gamma)'_\gamma - \hat{\mathbf{p}}^\gamma \cdot \mathbf{w}_\gamma \right] \geq 0 \,, \tag{5.19}$$

obtained from $(5.12)$ under consideration of constant temperatures and vanishing density productions, imposes the necessary thermodynamical restrictions on the process. However, since the model includes a pore-fluid mixture instead of an immiscible combination

of pore liquids and pore gases, the free energy functions of the fluid components will be formulated per fluid volume [8] instead of per constituent mass as in (5.19). Thus,

$$\rho^\gamma \psi^\gamma = n^F(\rho_F^\gamma \psi^\gamma) =: n^F \Psi_F^\gamma, \qquad \text{where} \qquad \Psi_F^\gamma := \rho_F^\gamma \psi^\gamma. \tag{5.20}$$

In addition, the pore-fluid free energy yields

$$\Psi_F^F := \sum_\gamma \Psi_F^\gamma. \tag{5.21}$$

Inserting (5.20) and (5.21) into (5.19), the entropy inequality transforms towards

$$(\mathbf{T}^S - n^S \Psi_F^F \mathbf{I}) \cdot \mathbf{L}_S - \rho^S (\psi^S)'_S + \sum_\gamma \left[ (\mathbf{T}^\gamma - n^F \Psi_F^\gamma \mathbf{I}) \cdot \mathbf{L}_\gamma - n^F (\Psi_F^F)'_F - \right. $$
$$\left. -\operatorname{grad} \Psi_F^\gamma \cdot (n^F \mathbf{d}_{\gamma F}) - (\hat{\mathbf{p}}^\gamma + \Psi_F^\gamma \operatorname{grad} n^F) \cdot \mathbf{w}_\gamma \right] \geq 0, \tag{5.22}$$

where the diffusion velocities $\mathbf{d}_{\gamma F}$ are given through $\mathbf{d}_{\gamma F} = \mathbf{w}_\gamma - \mathbf{w}_F$. Furthermore, the process is affected by two constraints, the saturation constraint and the electroneutrality constraint. These constraints read:

$$(n^S + \sum_\gamma n^\gamma)'_S = -n^S \operatorname{div} \overset{'}{\mathbf{x}}_S - \sum_\gamma (n^\gamma \operatorname{div} \overset{'}{\mathbf{x}}_\gamma + \operatorname{grad} n^\gamma \cdot \mathbf{w}_\gamma) = 0,$$
$$(\rho_e^{fc} + \sum_\delta \rho_e^\delta)'_S = -\rho_e^{fc} \operatorname{div} \overset{'}{\mathbf{x}}_S - \sum_\delta (\rho_e^\delta \operatorname{div} \overset{'}{\mathbf{x}}_\delta + \operatorname{grad} \rho_e^\gamma \cdot \mathbf{w}_\gamma) = 0. \tag{5.23}$$

To obtain the first constraint, the solid material time derivative of the saturation condition $(5.2)_2$ has been taken, while to obtain the second one, the solid material time derivative has been applied to the electroneutrality condition

$$\rho_e = \rho_e^{fc} + \sum_\delta \rho_e^\delta = 0. \tag{5.24}$$

Therein, the densities of the volumetric electrical charges of the free moving ions $\varphi^\delta$ and of the fixed charges $\varphi^{fc}$ adhering at the skeleton are given by

$$\rho_e^\delta := n^F z^\delta c_m^\delta F \qquad \text{and} \qquad \rho_e^{fc} := n^F z^{fc} c_m^{fc} F, \tag{5.25}$$

where $z^\delta$ and $z^{fc}$ are the valances of the ions, and $F$ is the Faraday constant.

Multiplying the saturation constraint $(5.23)_1$ by the hydraulic excess pressure $\mathcal{P}$ and the electroneutrality constraint $(5.23)_2$ by the electrical potential $\varphi_e$, both acting as Lagrangean multipliers, the entropy inequality (5.22) yields after having been combined with these equations

$$(\mathbf{T}_E^S - n^S \Psi_F^F \mathbf{I}) \cdot \mathbf{L}_S - \rho^S (\psi^S)'_S + \sum_\gamma \left[ (\mathbf{T}_E^\gamma - n^F \Psi_F^\gamma \mathbf{I}) \cdot \mathbf{L}_\gamma - n^F (\Psi_F^F)'_F - \right. $$
$$\left. -\operatorname{grad} \Psi_F^\gamma \cdot (n^F \mathbf{d}_{\gamma F}) - (\hat{\mathbf{p}}_E^\gamma + \Psi_F^\gamma \operatorname{grad} n^F) \cdot \mathbf{w}_\gamma \right] \geq 0. \tag{5.26}$$

Therein, both $\mathcal{P}$ and $\varphi_e$ occur as new fields via the extra quantities indicated by $(\cdot)_E$, which are not matched by governing equations yet. In particular, in (5.26), the extra

stresses $\mathbf{T}_E^S$ and $\mathbf{T}_E^\gamma$ as well as the extra momentum productions $\hat{\mathbf{p}}_E^\gamma$ with $\gamma = \{L, \delta\}$ are defined as

$$\mathbf{T}_E^S = \mathbf{T}^S + n^S \mathcal{P}\,\mathbf{I} + \rho_e^{fc}\,\varphi_e\,\mathbf{I}\,,$$

$$\mathbf{T}_E^\delta = \mathbf{T}^\delta + n^\delta\,\mathcal{P}\,\mathbf{I} + \rho_e^\delta\,\varphi_e\,\mathbf{I}\,, \qquad \hat{\mathbf{p}}_E^\delta = \hat{\mathbf{p}}^\delta - \mathcal{P}\,\mathrm{grad}\,n^\delta - \varphi_e\,\mathrm{grad}\,\rho_e^\delta\,, \qquad (5.27)$$

$$\mathbf{T}_E^L = \mathbf{T}^L + n^L \mathcal{P}\,\mathbf{I}\,, \qquad\qquad \hat{\mathbf{p}}_E^L = \hat{\mathbf{p}}^L - \mathcal{P}\,\mathrm{grad}\,n^L\,.$$

From the above relations, one can see that the extra quantities and the total quantities are related to each other by the action of the incompressibility constraint $(5.23)_1$ multiplied by $\mathcal{P}$ and by the electroneutrality constraint $(5.23)_2$ multiplied by $\varphi_e$.

Combining (5.26) with the constitutive assumptions

$$\psi^S = \psi^S(\mathbf{F}_S) \qquad \text{and} \qquad \Psi_F^\gamma = \Psi_F^\gamma(c_m^\gamma) \qquad\qquad (5.28)$$

yields with the aid of the standard evaluation procedure:

$$\mathbf{T}_{E\,mech.}^S := \mathbf{T}_E^S + n^S \left( \sum_\gamma c_m^\gamma \frac{\partial \Psi_F^\gamma}{\partial c_m^\gamma} - \Psi_F^F \right)\mathbf{I} = \rho^S \frac{\partial \psi^S}{\mathbf{F}_S}\mathbf{F}_S^T\,,$$

$$\mathbf{T}_{E\,dis.}^\gamma := \mathbf{T}_E^\gamma + n^F \left( c_m^\gamma \frac{\partial \Psi_F^\gamma}{\partial c_m^\gamma} - \Psi_F^\gamma \right)\mathbf{I} \approx \mathbf{0}\,, \qquad\qquad (5.29)$$

$$\hat{\mathbf{p}}_{E\,dis.}^\gamma := \hat{\mathbf{p}}_E^\gamma - \left( c_m^\gamma \frac{\partial \Psi_F^\gamma}{\partial c_m^\gamma} - \Psi_F^\gamma \right)\mathrm{grad}\,n^F\,.$$

Therein, $\mathbf{T}_{E\,mech.}^S$ is the purely mechanical part of the solid extra stress, while $\mathbf{T}_{E\,dis.}^\gamma$ and $\hat{\mathbf{p}}_{E\,dis.}^\gamma$ are the frictional stresses and the drag and diffusion forces of $\varphi^\gamma$. Note in passing that it can be shown by use of a dimensional analysis that $\mathbf{T}_{E\,dis.}^\gamma$ approximately vanishes in comparison with $\hat{\mathbf{p}}_{E\,dis.}^\gamma$, cf. [21, 35]. In addition to the results obtained with (5.29), it remains the dissipation inequality

$$\mathcal{D} = -\sum_\gamma \hat{\mathbf{p}}_{E\,dis.}^\gamma \cdot \mathbf{w}_\gamma \geq 0\,. \qquad\qquad (5.30)$$

As a result, the dissipation inequality is fulfilled with

$$\hat{\mathbf{p}}_{E\,dis.}^\delta = -(\overset{'}{\mathbf{x}}_\delta - \overset{'}{\mathbf{x}}_L)\,,$$

$$\hat{\mathbf{p}}_{E\,dis.}^L = -\sum_\delta \mathbf{S}^{L\delta}(\overset{'}{\mathbf{x}}_L - \overset{'}{\mathbf{x}}_\delta) - \mathbf{S}^{LS}\,\mathbf{w}_L\,. \qquad\qquad (5.31)$$

Therein,

$$\mathbf{S}^{L\delta} = n^F \frac{n^L R\,\theta\,c_m^\delta}{D^\delta}\,\mathbf{I} \qquad \text{and} \qquad \mathbf{S}^{LS} = n^F \frac{n^L \mu^{LR}}{K^S}\,\mathbf{I} \qquad\qquad (5.32)$$

are the positive definite permeability and diffusion tensors under isotropic conditions, where $D^\delta$ is the ion diffusion coefficients of $\varphi^\delta$, $\mu^{LR}$ is the effective shear viscosity of $\varphi^L$, and $K^S$ is the intrinsic permeability of $\varphi^S$.

## 5.3.2 The Fluid Components

Based on the the assumption of vanishing frictional stresses $\mathbf{T}_{E\,dis.}^{\gamma}$, cf. $(5.29)_2$, the extra stresses of the fluid components $\varphi^{\gamma}$ read

$$\mathbf{T}_E^{\gamma} = -n^F\left(c_m^{\gamma}\frac{\partial\Psi_F^{\gamma}}{\partial c_m^{\gamma}} - \Psi_F^{\gamma}\right)\mathbf{I} \qquad \text{yielding} \qquad \mathbf{T}_E^{\gamma} - n^F\Psi_F^{\gamma}\mathbf{I} = n^F c_m^{\gamma}\frac{\partial\Psi_F^{\gamma}}{\partial c_m^{\gamma}}\mathbf{I}\,. \qquad (5.33)$$

From these relations, it is easily concluded that $(5.33)_2$ contains the molar chemical potential $\mu_m^{\gamma}$ of $\varphi^{\gamma}$, while $(5.33)_1$, as the "extra pressure" of $\varphi^{\gamma}$, is the contribution $\pi^{\gamma}$ of $\varphi^{\gamma}$ to the overall osmotic pressure $\pi$. Thus,

$$\mu_m^{\gamma} = \frac{\partial\Psi_F^{\gamma}}{\partial c_m^{\gamma}}\,, \qquad \pi^{\gamma} = c_m^{\gamma}\frac{\partial\Psi_F^{\gamma}}{\partial c_m^{\gamma}} - \Psi_F^{\gamma} = c_m^{\gamma}\mu_m^{\gamma} - \Psi_F^{\gamma} \qquad \text{and} \qquad \pi = \sum_{\gamma}\pi^{\gamma}\,. \qquad (5.34)$$

Combining $(5.27)_{(1-3)}$, (5.29) and (5.33), one obtains the constituent partial stresses as

$$\begin{aligned}
\mathbf{T}^S &= -n^S(\mathcal{P} + \pi)\,\mathbf{I} && - \rho_e^{fc}\,\varphi_e\,\mathbf{I} + \mathbf{T}_{E\,mech.}^S\,, \\
\mathbf{T}^{\delta} &= -n^{\delta}\,\mathcal{P}\,\mathbf{I} - n^F\pi^{\delta}\,\mathbf{I} - \rho_e^{\delta}\,\varphi_e\,\mathbf{I}\,, \\
\mathbf{T}^L &= -n^L\,\mathcal{P}\,\mathbf{I} - n^F\pi^L\,\mathbf{I}\,,
\end{aligned} \qquad (5.35)$$

where (5.21) has been used. Furthermore, one recovers the total momentum productions $(5.27)_{4,5}$ to yield

$$\begin{aligned}
\hat{\mathbf{p}}^{\delta} &= \mathcal{P}\,\mathrm{grad}\,n^{\delta} + \pi^{\delta}\,\mathrm{grad}\,n^F + \varphi_e\,\mathrm{grad}\,\rho_e^{\delta} + \hat{\mathbf{p}}_{E\,dis.}^{\delta}\,, \\
\hat{\mathbf{p}}^L &= \mathcal{P}\,\mathrm{grad}\,n^L + \pi^L\,\mathrm{grad}\,n^F + \hat{\mathbf{p}}_{E\,dis.}^L\,.
\end{aligned} \qquad (5.36)$$

Finally, summing over the components of the pore-fluid mixture yields the overall fluid stress and the overall fluid momentum production, viz.:

$$\begin{aligned}
\mathbf{T}^F &= -n^F(\mathcal{P} + \pi)\,\mathbf{I} - \sum_{\delta}\rho_e^{\gamma}\,\varphi_e\,\mathbf{I}\,, \\
\hat{\mathbf{p}}^F &= (\mathcal{P} + \pi)\,\mathrm{grad}\,n^F + \varphi_e\sum_{\delta}\mathrm{grad}\,\rho_e^{\delta} + \sum_{\gamma}\hat{\mathbf{p}}_{E\,dis.}^{\gamma}\,.
\end{aligned} \qquad (5.37)$$

## 5.3.3 Ion Diffusion and Fluid Flow

Proceeding from the standard assumption that the free energy of the fluid components can be given as

$$\Psi_F^{\gamma} = c_m^{\gamma}\mu_{0m}^{\gamma} + c_m^{\gamma}\,R\theta\,(\ln c_m^{\gamma} - 1)\,, \qquad (5.38)$$

where $\theta$ is the absolute Kelvin's temperature and $R$ the universal gas constant, the chemical potentials and the osmotic pressure read

$$\mu_m^{\gamma} = \mu_{0m}^{\gamma} + R\theta\ln c_m^{\gamma} \qquad \text{and} \qquad \pi = R\theta\sum_{\gamma}c_m^{\gamma}\,. \qquad (5.39)$$

Therein, $\mu_{0m}^{\gamma}$ is known as the constant standard potential.

Inserting the partial ion stress $\mathbf{T}^\delta$ from $(5.35)_2$ and the ion momentum production $\hat{\mathbf{p}}^\delta$ from $(5.36)_1$ into the ion momentum balance $(5.13)_2$ yields

$$\mathbf{0} = -n^\delta \left(\operatorname{grad} \mathcal{P} - \rho^{\delta R} \mathbf{g}\right) - n^F \operatorname{grad} \pi^\delta - \rho_e^\delta \operatorname{grad} \varphi_e + \hat{\mathbf{p}}_{E\,dis.}^\delta . \tag{5.40}$$

Since partial osmotic pressures cannot be measured, $\pi^\delta$ must be substituted by $\mu_m^\delta$ with the aid of $(5.34)_2$. Thus, with the aid of $(5.28)_2$ and $(5.34)_1$, the ion momentum balance $(5.40)$ yields

$$\mathbf{0} = -n^\delta \left(\operatorname{grad} \mathcal{P} - \rho^{\delta R} \mathbf{g}\right) - n^F c_m^\delta \operatorname{grad} \mu_m^\delta - \rho_e^\delta \operatorname{grad} \varphi_e + \hat{\mathbf{p}}_{E\,dis.}^\delta . \tag{5.41}$$

Proceeding from the assumption that the ion volume fraction $n^\delta$ is negligible compared to the liquid volume fraction $n^L$ including

$$n^\delta \ll n^L \qquad \text{and} \qquad n^L \approx n^F , \tag{5.42}$$

one obtains with the aid of $(5.5)$

$$\rho^{FR} \approx \rho_F^L \qquad \text{with} \qquad \sum_\delta \rho_F^\delta \approx 0 \qquad \text{and} \qquad \overset{\prime}{\mathbf{x}}_F \approx \overset{\prime}{\mathbf{x}}_L , \tag{5.43}$$

and $(5.41)$ transforms towards the extended Nernst-Planck equation

$$n^F \mathbf{d}_{\delta F} = -\frac{D^\delta}{R\,\theta\,c_m^\delta} \left(c_m^\delta \operatorname{grad} \mu_m^\delta + \rho_{eF}^\delta \operatorname{grad} \varphi_e\right) , \tag{5.44}$$

where $\mathbf{d}_{\delta F} = \overset{\prime}{\mathbf{x}}_\delta - \overset{\prime}{\mathbf{x}}_F \approx \overset{\prime}{\mathbf{x}}_\delta - \overset{\prime}{\mathbf{x}}_L$ has been used. Furthermore, in analogy to $(5.5)_1$, $\rho_e^\delta = n^F \rho_{eF}^\delta$. In order to obtain $(5.44)$ describing the ion diffusion process from $(5.41)$, the first term on the rhs of $(5.41)$, the drag term, has been neglected with respect to $(5.43)_1$. Expressing the chemical potentials $\mu_m^\delta$ by the concentrations $c_m^\delta$ yields the final version of the diffusion equation $(5.44)$, viz.:

$$n^F \mathbf{d}_{\delta F} = -\frac{D^\delta}{R\,\theta\,c_m^\delta} \left(R\,\theta \operatorname{grad} c_m^\delta + \rho_{eF}^\delta \operatorname{grad} \varphi_e\right) . \tag{5.45}$$

Therein, $(5.39)$ together with the assumption of isothermal processes has been used.

Inserting the fluid stress and the fluid momentum production given by $(5.37)$ into the fluid momentum balance obtained by summing $(5.13)_2$ over $\gamma = \{L, +, -\}$ yields

$$\mathbf{0} = -n^F \left[\operatorname{grad}\left(\mathcal{P} + \pi\right) - \rho^{FR} \mathbf{g} - \sum_\delta \rho_{eF}^\delta \operatorname{grad} \varphi_e\right] + \hat{\mathbf{p}}_{E\,dis.}^F . \tag{5.46}$$

Therein, $\hat{\mathbf{p}}_{E\,dis.}^F$ is obtained from $(5.31)$, $(5.32)$ and $(5.43)_1$ as

$$\hat{\mathbf{p}}_{E\,dis.}^F = \hat{\mathbf{p}}_{E\,dis.}^L + \sum_\delta \hat{\mathbf{p}}_{E\,dis.}^\delta = -(n^F)^2 \frac{\mu^{FR}}{K^S} \mathbf{w}_F . \tag{5.47}$$

Combing $(5.46)$ and $(5.47)$, one recovers the extended Darcy equation

$$n^F \mathbf{w}_F = -\frac{K^S}{\mu^{FR}} \left[\operatorname{grad}\left(\mathcal{P} + \pi\right) - \rho^{FR} \mathbf{g} - \sum_\delta \rho_{eF}^\delta \operatorname{grad} \varphi_e\right] \tag{5.48}$$

governing the fluid flow.

### 5.3.4 Electrical Potential

The electrical potential $\varphi_e$ entering the process through the entropy inequality (5.26) together with the electroneutrality constraint $(5.23)_2$ reveals that there is no matching governing equation. Thus, this additional equation must be found and added to the process. To overcome this situation, use is made of the Poisson equation of the electrical potential of electrostatics yielding

$$\operatorname{div} \operatorname{grad} \varphi_e = -\frac{1}{\epsilon^F}\,\rho_e\,, \tag{5.49}$$

where $\operatorname{div} \operatorname{grad}(\,\cdot\,) =: \Delta(\,\cdot\,)$ is the Laplace operator, $\epsilon^F$ the constant electric fluid permittivity, while the density $\rho_e$ of the electrical charges is given through (5.24) and (5.25). In contrast to the electroneutrality condition (5.24) stating $\rho_e = 0$, $\rho_e$ is usually obtained from the Gauss's law

$$\operatorname{div} \mathbf{D} = \rho_e\,, \tag{5.50}$$

where $\mathbf{D}$ is the electric displacement obtained from the electrical field $\mathbf{E}$ via

$$\mathbf{D} = \epsilon^F\,\mathbf{E} \qquad \text{with} \qquad \mathbf{E} = -\operatorname{grad}\varphi_e\,. \tag{5.51}$$

Combining (5.49) with (5.25) finally yields

$$\operatorname{div} \operatorname{grad} \varphi_e = -\frac{n^F\,F}{\epsilon^F}\Big(\sum_\delta z^\delta c_m^\gamma + z^{fc} c_m^{fc}\Big)\,. \tag{5.52}$$

This equation will be used in the numerical setting to match $\varphi_e$.

### 5.3.5 The Solid Skeleton

As was mentioned at the beginning of this section, swelling phenomena are usually combined with large solid deformations. Following this results in the fact that a non-linear elasticity law is needed to describe the elastic solid deformations. Following [20], a combination of the neo-Hookean law with a non-linear volumetric deformation yields by use of $(5.29)_1$

$$\mathbf{T}_{E\,mech.}^S = J_S^{-1}\Big[2\,\mu^S\,\mathbf{K}_S + \lambda^S\,(1 - n_{0S}^S)^2\Big(\frac{J_S}{1 - n_{0S}^S} - \frac{J_S}{J_S - n_{0S}^S}\Big)\mathbf{I}\Big]\,, \tag{5.53}$$

where $\mu^S$ and $\lambda^S$ are the Lamé constants and $J_S = \det \mathbf{F}_S$. Concerning the description of finite volumetric deformations of a materially incompressible solid skeleton, recall that the property of material incompressibility ($\rho^{SR} = \text{const.}$) does not include total incompressibility ($\rho^S = \text{const.}$), since $\rho^S$ can still change through $n^S$. As a result, the volumetric deformation included in (5.53) is only due to variations of the pore space, such as those initiated by swelling processes, and is not due to volumetric changes of the matrix material itself.

### 5.3.6   Swelling Media

**Simulation of a Swelling Experiment**

Based on the weak forms of the general swelling model, cf. [1, 18, 19], the numerical scheme governing swelling media is based on extended Taylor-Hood elements with quadratic shape functions for the solid displacement $\mathbf{u}_S$ and linear shape functions for hydraulic fluid pressure $\mathcal{P}$, the ion concentrations $c_m^+$ and $c_m^-$ and the electrical potential $\varphi_e$. The implementation is realized in the FE package PANDAS.

The following numerical example concerns a 2-d plane-strain simulation of a swelling experiment carried out by the group of Jacques Huyghe in Eindhoven (The Netherlands). In this experiment, a soot-colored hydrogel disc is taken from a given bathing solution, where it was in chemical equilibrium, and put into another solution with a lower concentration of both cations and anions. As a result, the chemical equilibrium in the disc is violated and can only be regained, when the disc absorbs a certain amount of liquid such that the internal and external solutions return to a state of chemical equilibrium. To simulate this experiment, a rectangular cross section is discretized under symmetry conditions (Figure 5.1). During the computation, the chemically uncharged hydrogel is firstly equili-
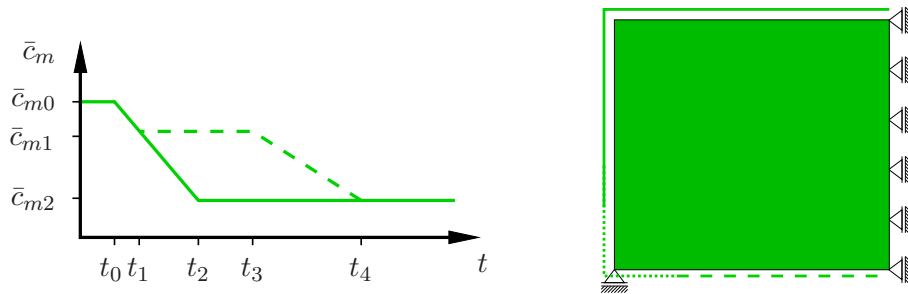


**Figure 5.1:** *Chemical loading (left) and geometry (right) of a 2-d free swelling simulation. The solid and the dashed line concentration curves on the left side belong to the respective boundaries on the right side. The dotted line at the bottom left corner of the geometry indicates the transition from the concentration value of the solid to the dashed line.*

brated in a bathing solution with the initial external concentration $\bar{c}_{m0}$. This is necessary in order to transform the hydrogel from a fictitious non-loaded reference configuration in the sense of a natural state at $t = t_0$ towards a pre-swollen initial configuration. Note in passing that there is no uncharged configuration in any real experiment, since swelling materials are always somehow in a swollen state. In the fictitious non-loaded reference configuration, there is neither a solid stress ($\mathbf{T}^S_{E\,mech.\,0S} = \mathbf{0}$) nor an osmotic pressure ($\pi_0 = 0$). To avoid numerical problems during initial loading, the initial osmotic pressure is applied slowly by increasing the referential concentration of the fixed charges from 0 to the prescribed value $c^{fc}_{m0S}$ over time. After a certain time of computation, an equilibrium state is reached defined as the "initial configuration" at which the initial osmotic pressure $\pi_0^*$, the initial concentration $c_{m0}^*$ and the initial purely mechanical solid extra stress $\mathbf{T}^{S\,*}_{E\,mech.\,0S}$ fits the volumetric deformation $(\det \mathbf{F}_S)^*_{0S}$ through the balance equations and the constitutive setting.
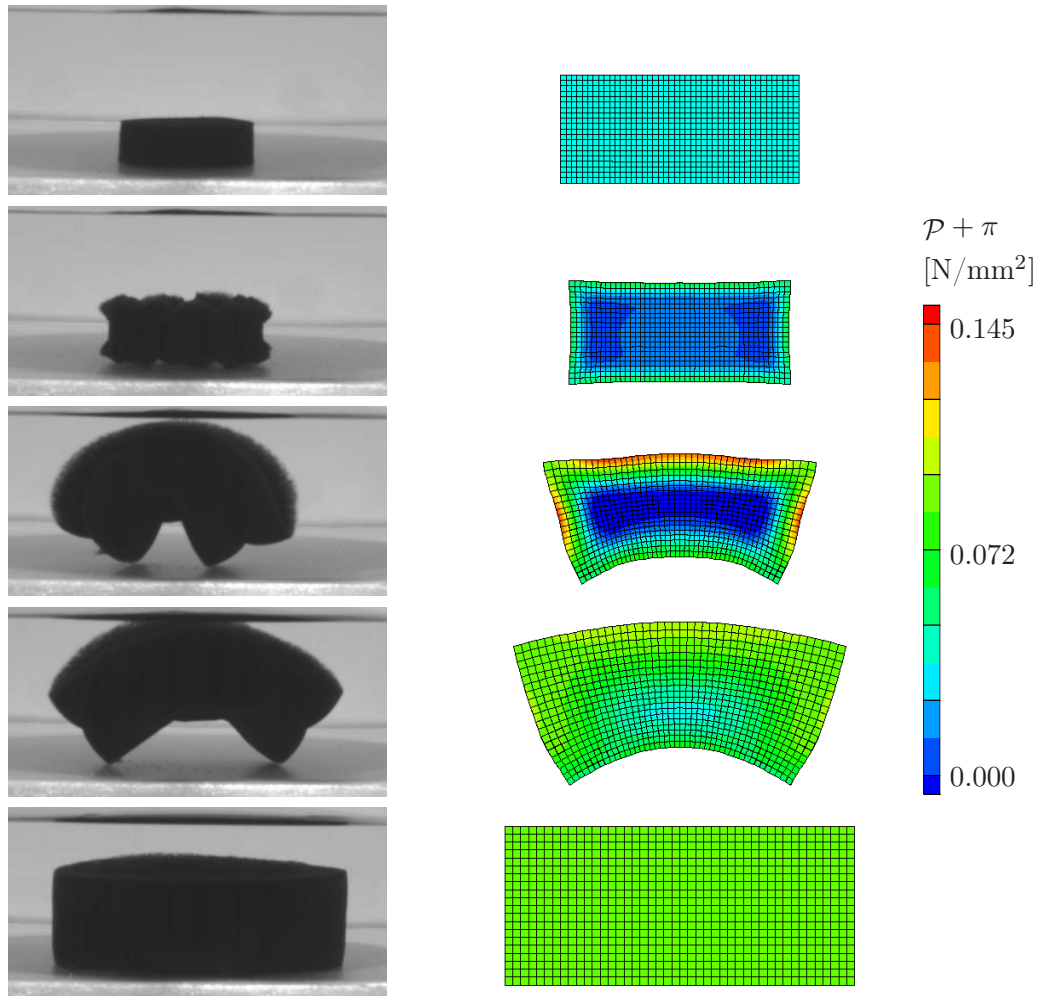
**Figure 5.2:** *Qualitative comparison between the free swelling experiment of a soot-colored hydrogel disc carried out by the group of Jacques Huyghe at the TU Eindhoven and our numerical simulation. Starting from a pre-swollen initial state (top, right), the contour plots show the deformation and the overall pressure (hydraulic and osmotic) development.*

Concerning the numerical simulation prior to the actual swelling process, the specimen is equilibrated for a period of $t_0 = 7\,000\,$s in a $\bar{c}_{m0} = 4.1$ molar sodium chloride (NaCl) solution, where $c^{fc}_{m0S}$ is increased from 0 to 0.8 meq/l within the first $4\,000\,$s. After an equilibrium state is obtained, the initial configuration is reached, and the hydrogel is placed in another NaCl solution. There, the external salt concentration is decreased at all boundaries from $\bar{c}_{m0} = 4.1\,$mol/l to $\bar{c}_{m1} = 2.7\,$mol/l until $t_1 = 7\,080\,$s. Thereafter, only the boundaries denoted by the solid line are exposed to the solution, cf. Figure 5.1. Then, the concentration is further decreased to $\bar{c}_{m2} = 0.3\,$mol/l until $t_2 = 7\,220\,$s, while the concentration at the bottom is kept constant. At $t_3 = 8\,000\,$s, the bottom of the hydrogel gets in contact with the bathing solution as well. Therefore, $\bar{c}_{m1}$ is decreased to $\bar{c}_{m2} = 0.3\,$mol/l until $t_4 = 10\,000\,$s.

Figure 5.2 compares the experiment results on the left-hand side with the simulation on the right-hand side. Besides the comparison of the deformation, the contour plots show

the development of the overall fluid pressure within the material. The first line shows the computed initial configuration ($t_0 = 7\,000\,\text{s}$) after having increased $c_{0S}^{fc}$ from 0 to its full amount and after having reached chemical equilibrium. This is a swollen state, i.e., there is an osmotic pressure and a deformation. The next line shows the phase of the negative osmosis ($t = 7\,107\,\text{s}$), during which the hydrogel shrinks initially in its inner region. Note in passing that this effect results from the state of chemical non-equilibrium at the domain boundary yielding an influx of liquid both from the bathing solution through the domain boundary and from the inner part of the specimen to the outer parts. Thereafter, the state, at which the greatest bending occurs, is shown ($t = 7\,224\,\text{s}$). The subsequent pictures present how the final equilibrium state is reached ($t = 7\,650\,\text{s}$ and $t = 11\,000\,\text{s}$). At the end of the simulation process, the cross-sectional area of the specimen is approximately 2.2 times larger than the area of the computed initial state.

### Swelling of an Intervertebral Disc

Applying the theoretical framework presented before to swelling phenomena of biological tissue such as the intervertebral disc, one is able to compute the disc-bulging observed in an in-vitro experiment by the group of Gerhard Holzapfel in Graz (Austria), cf. Figure 5.3. The computations are carried out by the additional use of Lanir's assumption [34] of an immediate chemical equilibrium not only at the domain boundary but also in the overall domain. This assumption proceeds from the fact that the ion diffusion is much faster than the solid deformation coming along with the corresponding swelling or shrinking processes. Furthermore, one proceeds from the idea that biological tissue, especially under in-vivo conditions, where it is generally in an equilibrium state, cannot be exposed suddenly to a rapid decrease or increase of the molar ion concentration of the surrounding interstitial fluid. As a result, the general model can be simplified by only using the solid
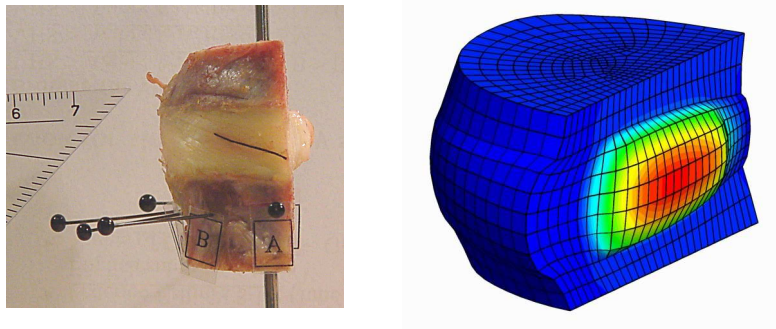


**Figure 5.3:** _Swelling of an intervertebral disc. Experiment by Gerhard Holzapfel (left) and numerical computation (right)._

deformation and the fluid pressure as primary variables solving the week forms of the overall momentum and volume balances. The chemical information is included by using the external concentration as material parameters in combination with van't Hoff's law $\Delta\pi = R\theta[(c^+ + c^-) - (\bar{c}^+ + \bar{c}^-)]$, where the concentrations $\bar{c}^\delta$ represent the boundary values of the bathing solution.

# 5.4    Avascular Growth as Energy-Controlled Phase Transition

The simulation of avascular growth in general and of tumor growth in particular poses a very difficult challenge due to the complicated biological scenario that has to be considered. With respect to the complex metabolic processes governed by nutrient, angiogenic and growth factors, it is convenient, as before, to proceed from the macroscopic modeling approach of the TPM instead of getting lost in the description of the physiochemical mechanisms at the cellular level. Thus, the hydrated organic tissue is treated as a biphasic aggregate constituted by a porous solid (tumor cells and extracellular matrix) which is permeated by an organic interstitial fluid mixture. Since the imbalances of production and degradation of the individual constituents associated with growth and necrosis of the tumor tissue are strongly influenced by several chemical factors (nutrients, enzymes etc.), the model incorporates two additional caloric state variables. These new variables are introduced as the "growth energies" compared to the thermodynamic temperatures and their energetically conjugate terms, the "configurational growth entropies" compared to the thermodynamic entropies.

In the context of biological tissue, cf. Cowin [12] for details, Preziosi & Farina [38] and Steeb & Diebels [45] formally employed the TPM to account for the separate contributions of each constituent during growth. In the same sense, Klisch & Hoger [31] additionally used the multiplicative geometric concept of Rodriguez *et al.* [39] by introducing a growth deformation gradient in combination. Humphrey & Rajagopal [30] developed a theory that considers the continual production and removal of constituents in potentially differently stressed configurations. The goal of this section is to present a consistent TPM model that enables the analysis of the early stages of solid tumor growth by considering the avascular growth of a tumor (neoplastic) cell cluster towards a tumor spheroid. As a result of not yet being supplied by blood vessels, the tumor receives nutrients from the surrounding tissue only by diffusion.

The structure of a tumor spheroid distinguishes an outer rim of proliferating tumor cells, an intermediate region where tumor cells are alive but do not proliferate (quiescent state) and a central core of nutrient-starved necrotic tumor cells. The mechanisms affecting the growth of cells are the diffusion and the consumption of nutrients and oxygen, the resistance or stress exerted by the surroundings on the cells and the frequency of mechanical loads on the cells, cf. [33, 46] The model concept and the constitutive relations presented here are inspired by and partially adopted from the already existing continuum-mechanical models for avascular tumor growth, such as the single-phasic formulation of Ambrosi & Mollica [3, 4]. This model is extended by a reaction-diffusion equation for the nutrients, whose concentration is treated like a measure of a metabolistic energy. Furthermore, it is inspired by the work of Byrne & Preziosi [11], Ambrosi & Preziosi [5], and Roose *et al.* [41], where tumor tissue is described as a multi-component material.

### 5.4.1 Biphasic Porous Media Growth Model

Following the TPM approach in Section 5.2, a solid tumor is considered as a biphasic aggregate consisting of two immiscible constituents, a solid skeleton $\varphi^S$ representing the living tumor cells embedded into the extracellular matrix and a single pore-fluid mixture consisting of interstitial liquid, necrotic debris and cell precursors, cf. Figure 5.4. Following this, the growth process is described by a distinct mass exchange between both constituents. The complex metabolic mechanisms are governed by the introduction of a non-mechanical, temperature-equivalent "growth energy" $\mathcal{C}_\theta^\alpha > 0$ ($\alpha \in \{S, F\}$) as a measure of the average amount of chemical energy available for cell metabolism, which can be regarded in full analogy to the thermodynamic temperature $\theta^\alpha$ as a measure of the average kinetic energy of atoms. To be in line with continuum thermodynamics, this further entails the introduction of an associated (conjugate) "configurational growth entropy" $\eta_c^\alpha$ as a measure for the randomness in the distribution of matter analogously to the thermal entropy $\eta^\alpha$ previously introduced.
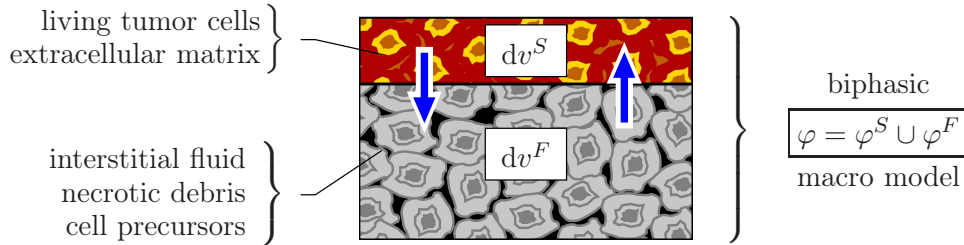


**Figure 5.4:** *Biphasic porous media model for avascular tumor growth.*

As in Section 5.3, one proceeds from quasi-static processes ($\overset{''}{\mathbf{x}}_\alpha = \mathbf{0}$) and materially incompressible constituents ($\rho^{\alpha R} = \text{const.}$). However, in contrast to Section 5.3, the density productions $\hat{\rho}^\alpha$ are not zero which, due to the incompressibility assumption, yields a volume production $\hat{n}^\alpha := \hat{\rho}^\alpha / \rho^{\alpha R}$ entering the partial volume balance

$$(n^\alpha)'_\alpha + n^\alpha \operatorname{div} \overset{'}{\mathbf{x}}_\alpha = \hat{n}^\alpha , \quad \text{where} \quad \sum_\alpha \hat{n}^\alpha = \hat{n}^S + \hat{n}^F = \hat{n}^S \Big( 1 - \frac{\rho^{SR}}{\rho^{FR}} \Big) . \tag{5.54}$$

Note that in contrast to $(5.9)_1$, $\sum_\alpha \hat{n}^\alpha \neq 0$. As a result, the corresponding volume balance of the whole aggregate obtained by summing up (5.54) over $\alpha = \{S, F\}$ yields

$$\sum_\alpha (n^\alpha)'_S = (n^S + n^F)'_S = \hat{n}^S \Big( 1 - \frac{\rho^{SR}}{\rho^{FR}} \Big) - \operatorname{div} \big[ (\mathbf{u}_S)'_S + n^F \mathbf{w}_F \big] = 0 . \tag{5.55}$$

Neglecting the gravitational body forces ($\mathbf{b}^\alpha = \mathbf{g} = \mathbf{0}$), the quasi-static partial and total momentum balances read with the aid of $(5.7)_2$, $(5.8)_1$ and $(5.9)_2$

$$\mathbf{0} = \operatorname{div} \mathbf{T}^\alpha + \hat{\mathbf{p}}^\alpha \quad \text{with} \quad \hat{\mathbf{p}}^S = -\hat{\mathbf{p}}^F + \hat{n}^S \rho^{SR} \mathbf{w}_F \quad \text{and} \quad \mathbf{0} = \operatorname{div} \mathbf{T} , \tag{5.56}$$

where, as in $(5.18)_1$, $\mathbf{T} := \mathbf{T}^S + \mathbf{T}^F$. For the determination of the growth energies, the partial energy balances are required. Proceeding from $(5.7)_4$ under the assumption of

adiabatic circumstances ($\mathbf{q}^\alpha = \mathbf{0}$, $r^\alpha = 0$) and omitting furthermore an unphysiological external supply of growth energy, one obtains

$$\rho^\alpha (\varepsilon^\alpha)'_\alpha = \mathbf{T}^\alpha \cdot \mathbf{L}_\alpha - \operatorname{div} \mathbf{j}^\alpha + \hat{\varepsilon}^\alpha \,, \tag{5.57}$$

where $\mathbf{j}^\alpha$ denotes the growth energy influx vector in analogy to the heat influx $\mathbf{q}^\alpha$.

## 5.4.2 Thermodynamical Restrictions and Constitutive Setting

In analogy to standard TPM models, one introduces the internal energies $\varepsilon^\alpha = \varepsilon^\alpha(.., \eta_c^\alpha, ..)$ as a function of the partial configurational growth entropy and further quantities. By use of the standard Legendre transformation technique, this assumption directly leads, similar to (5.12), to the formal definition of a free Helmholtz energy density:

$$\psi^\alpha := \varepsilon^\alpha - \mathcal{C}_\theta^\alpha \, \eta_c^\alpha \,. \tag{5.58}$$

Like in all other TPM models, it is a basic requirement that the saturation constraint (5.2) is fulfilled throughout the thermodynamic process. This is accomplished by adding (5.55) multiplied by a Lagrangean multiplier $\mathcal{P}$ to the general entropy inequality (5.12). Accounting for the growth energy and the associated configurational entropy, one arrives at

$$\sum_\alpha \left\{ \frac{1}{\mathcal{C}_\theta^\alpha} \left[ \mathbf{T}^\alpha \cdot \mathbf{L}_\alpha - \rho^\alpha \left[ (\psi^\alpha)'_\alpha + (\mathcal{C}_\theta^\alpha)'_\alpha \, \eta_c^\alpha \right] - \hat{\mathbf{p}}^\alpha \cdot \overset{'}{\mathbf{x}}_\alpha - \right. \right.$$
$$\left. \left. -\hat{n}^\alpha \rho^{\alpha R} \left( \psi^\alpha + \tfrac{1}{2} \overset{'}{\mathbf{x}}_\alpha \cdot \overset{'}{\mathbf{x}}_\alpha \right) - \frac{1}{\mathcal{C}_\theta^\alpha} \mathbf{j}^\alpha \cdot \operatorname{grad} \mathcal{C}_\theta^\alpha + \hat{e}^\alpha \right] - \mathcal{P} \, (n^\alpha)'_S \right\} \geq 0 \,, \tag{5.59}$$

where $\hat{e}^\alpha$ is the total energy production according to (5.8)$_3$. From Section 5.3, it is obvious that $\mathcal{P}$ represents the excess pore-fluid pressure.

Inserting the constitutive assumptions

$$\psi^S = \psi^S(\mathbf{F}_S, n^S, \mathcal{C}_\theta^S) \quad \text{and} \quad \psi^F = \psi^F(\mathcal{C}_\theta^F) \tag{5.60}$$

for the free-energy densities in (5.59) yields after some algebraic manipulations:

- solid Cauchy stress with solid growth pressure

$$\mathbf{T}^S = \underbrace{\rho^S \frac{\partial \psi^S}{\partial \mathbf{F}_S} \mathbf{F}_S^T}_{\mathbf{T}_{E\,mech.}^S} \underbrace{- n^S p_{grow.}^S \, \mathbf{I}}_{\mathbf{T}_{E\,grow.}^S} - n^S \frac{\mathcal{C}_\theta^S}{\mathcal{C}_\theta^F} \mathcal{P} \, \mathbf{I} \quad \text{with} \quad p_{grow.}^S = \rho^S \frac{\partial \psi^S}{\partial n^S} \,, \tag{5.61}$$

- fluid Cauchy stress and fluid momentum production

$$\mathbf{T}^F = \mathbf{T}_{E\,dis.}^F - n^F \mathcal{P} \, \mathbf{I} \,, \quad \hat{\mathbf{p}}^F = \hat{\mathbf{p}}_E^F + \frac{\mathcal{C}_\theta^S}{\mathcal{C}_\theta^F} \mathcal{P} \operatorname{grad} n^F \,, \tag{5.62}$$

- configurational growth entropies

$$\eta_c^S = -\frac{\partial \psi^S}{\partial \mathcal{C}_\theta^S} \, , \quad \eta_c^F = -\frac{\partial \psi^F}{\partial \mathcal{C}_\theta^F} \, . \tag{5.63}$$

The reminder of (5.59) imposes restrictions on the dissipative contributions of the process. Here, the residual inequality is sufficiently fulfilled if the following proportionalities are met:

$$\left. \begin{array}{r} \mathbf{T}_{E\,mech.}^F \propto \mathbf{L}_F \\ \hat{\mathbf{p}}_E^F \propto -\mathbf{w}_F \\ \hat{\varepsilon}^F \propto (\mathcal{C}_\theta^S - \mathcal{C}_\theta^F) \\ \mathbf{j}^\alpha \propto -\mathrm{grad}\,\mathcal{C}_\theta^\alpha \end{array} \right\} \longrightarrow \left\{ \begin{array}{ll} \mathbf{T}_{E\,mech.}^F \approx \mathbf{0} & : \text{see [21, 35]}, \\ \hat{\mathbf{p}}_E^F = -(n^F)^2\,\mathbf{S}^{FS}\,\mathbf{w}_F & : \text{cf. (5.31) and (5.32)}, \\ \hat{\varepsilon}^F = \tau_c^S\,n^S\,(\mathcal{C}_\theta^S - \mathcal{C}_\theta^F) & : \text{caloric interaction}, \\ \mathbf{j}^\alpha = -D_c^\alpha\,\mathrm{grad}\,\mathcal{C}_\theta^\alpha & : \text{energy diffusion}. \end{array} \right. \tag{5.64}$$

Herein, $\mathbf{S}^{FS}$ is the inverse permeability tensor, $\tau_c^S \geq 0$ is the growth energy absorption rate and $D_c^\alpha \geq 0$ denotes the growth energy diffusion coefficient in $\varphi^\alpha$. A more complicated restriction is found for the solid volume production:

$$\hat{n}^S \propto \left\{ \underbrace{\tfrac{1}{2}\,\rho^{SR}\,\mathbf{w}_F \cdot \mathbf{w}_F}_{\substack{\text{cell migration} \\ \text{(erosion)}}} + \underbrace{\rho^{SR}\big[\varepsilon^F - \varepsilon^S - \mathcal{C}_\theta^S\,(\eta_c^F - \eta_c^S)\big]}_{\substack{\text{metabolism} \\ \text{(growth factors)}}} \underbrace{- \frac{\mathcal{C}_\theta^S}{\mathcal{C}_\theta^F}\,\mathcal{P}\Big(1 - \frac{\rho^{SR}}{\rho^{FR}}\Big) - p_{grow.}^S}_{\substack{\text{effective pressure} \\ \text{on cell membrane}}} \right\} . \tag{5.65}$$

Although the individual terms in (5.65) can be interpreted to some extent, they are far away from being understood on a physiological basis. Therefore, we follow a reduced ansatz motivated by the work of Ambrosi & Preziosi [5] assuming $\hat{n}^S$ being controlled only by the growth energy difference $\mathcal{C}_\theta^F - \mathcal{C}_\theta^S$ and the apparent tumor cell fraction $n^S$:

$$\hat{n}^S = \left\{ \begin{array}{ll} \gamma\,\dfrac{\mathcal{C}_\theta^F - \mathcal{C}_\theta^S}{\mathcal{C}_{\theta\,bm}^S}\,n^S - \delta\,n^S & \text{if} \quad \mathcal{C}_\theta^F > \mathcal{C}_\theta^S > \mathcal{C}_{\theta\,bm}^S \, , \\[2ex] -\delta\,n^S & \text{else} \, . \end{array} \right. \tag{5.66}$$

Therein, $\gamma$ and $\delta$ are positive parameters and $\mathcal{C}_{\theta\,bm}^S$ indicates the basal metabolic energy required for keeping the tumor cells alive (quiescent state).

Moreover, for the treatment of the caloric contributions, it is convenient to accept some further simplifications. It is quite obvious that biochemical processes and growth occur on different time and space scales. Essentially, the growth energy is asymptotically at steady state on the time scale of growth such that energy diffusion and direct energy production always balance. As a consequence, proceeding from a time-scale separation and the quasi-steady-state assumption (QSSA) together with (5.64)$_{3,4}$, the partial energy balances take the simplified form

$$0 = D_c^F\,\Delta\mathcal{C}_\theta^F + \tau_c^S\,n^S\,(\mathcal{C}_\theta^S - \mathcal{C}_\theta^F) \, , \quad 0 = D_c^S\,\Delta\mathcal{C}_\theta^S + \hat{\varepsilon}^S \quad \text{with}$$
$$\hat{\varepsilon}^S = -\tau_c^S\,n^S\,(\mathcal{C}_\theta^S - \mathcal{C}_\theta^F) - \hat{\mathbf{p}}^F \cdot \mathbf{w}_F - \hat{n}^S\,\rho^{SR}\big(\varepsilon^S - \varepsilon^F - \tfrac{1}{2}\,\mathbf{w}_F \cdot \mathbf{w}_F\big) \, . \tag{5.67}$$

For the free energies (5.60), it is particularly assumed that

$$\psi^S := \psi^S_{mech.}(\mathbf{F}_S) + \psi^S_{grow.}(n^S) + \psi^S_{cal.}(\mathcal{C}^S_\theta), \quad \psi^F := \psi^F_{cal.}(\mathcal{C}^F_\theta), \tag{5.68}$$

using a convenient Ansatz for the caloric parts

$$\psi^\alpha_{cal.}(\mathcal{C}^\alpha_\theta) = -\mathcal{S}^\alpha_c\left(\mathcal{C}^\alpha_\theta \ln \mathcal{C}^\alpha_\theta - \mathcal{C}^\alpha_\theta\right), \quad \text{where} \quad \mathcal{S}^\alpha_c = -\mathcal{C}^\alpha_\theta \frac{\partial^2 \psi^\alpha_{cal.}}{\partial(\mathcal{C}^\alpha_\theta)^2}, \tag{5.69}$$

is the specific growth energy in the sense of a specific metabolic heat comparable to the specific heat in thermal problems. The mechanical part of the solid free energy $\psi^S_{mech.}$ in (5.68) is taken of neo-Hookean type yielding $\mathbf{T}^S_{E\,mech}$ as in (5.53). The solid growth part $\psi^S_{grow.}$ accounts for the cell-to-cell interaction via the solid growth pressure (5.61). Here, a formulation of Preziosi [37] is adopted, which is capable of mimicking cell attraction as well as cell repulsion:

$$p^S_{grow.} = \begin{cases} \alpha \dfrac{n^S}{n^S_{0S}} \dfrac{(n^S - n^S_{1S})^2\,(n^S - n^S_{0S})}{\sqrt{1 - n^S}} & \text{for } n^S_{1S} < n^S, \\ 0 & \text{for } 0 < n^S \le n^S_{1S}, \end{cases} \tag{5.70}$$

where $\alpha$ and $n^S_{1S}$ are positive parameters.

## 5.4.3 FE Simulation of Finite 3-D Growth of a Tumor Spheroid

For the numerical treatment, the highly nonlinear coupled five-field problem is recast in variational form using the weak formulations of the solid volume balance (5.54) with $\alpha = S$ to determine $n^S$, the overall volume balance (5.55) to get $\mathcal{P}$, the overall momentum balance $(5.56)_3$ to compute $\mathbf{u}_S$ and the QSSA solid and fluid energy balances (5.67) to obtain $\mathcal{C}^S_\theta$ and $\mathcal{C}^F_\theta$. Proceeding from an implicit monolithic solution procedure, the spatial semi-discretization is carried out with stable mixed finite elements and the time discretization is based on the implicit Euler scheme with adaptive step-size control governed by the convergence behavior of the Newton method. The implementation is realized in the FE package PANDAS.

Accounting for the symmetry properties, only one eighth of the spheroid must be computed, cf. Figure 5.5. The initial solid volume fraction is 0.6, initial and ambient pressure are set to zero and the initial distribution of the growth energies is above the basal metabolic threshold value. During the computation, the Dirichlet boundary conditions of the growth energies are kept constant at the level of the initial conditions at the outer boundary surface.

In Figure 5.5, the result of a qualitative simulation shows the finite growth behavior of the tumor spheroid. As is directly apparent from the shading representing the distribution of the tumor cell fraction, the spheroid is distinguished into the aforementioned three regions, viz. a proliferating rim (red), a transition region with quiescent cells (green) and a necrotic core (blue) of nutrient-starved fluidized tissue. Looking closer to the largest spheroid depicted in Figure 5.5, one recognizes some buckles on the tumor surface (surface instabilities) which are caused by the fact that the outer rim grows faster than the inner domain, an observation also made in in-vitro experiments.
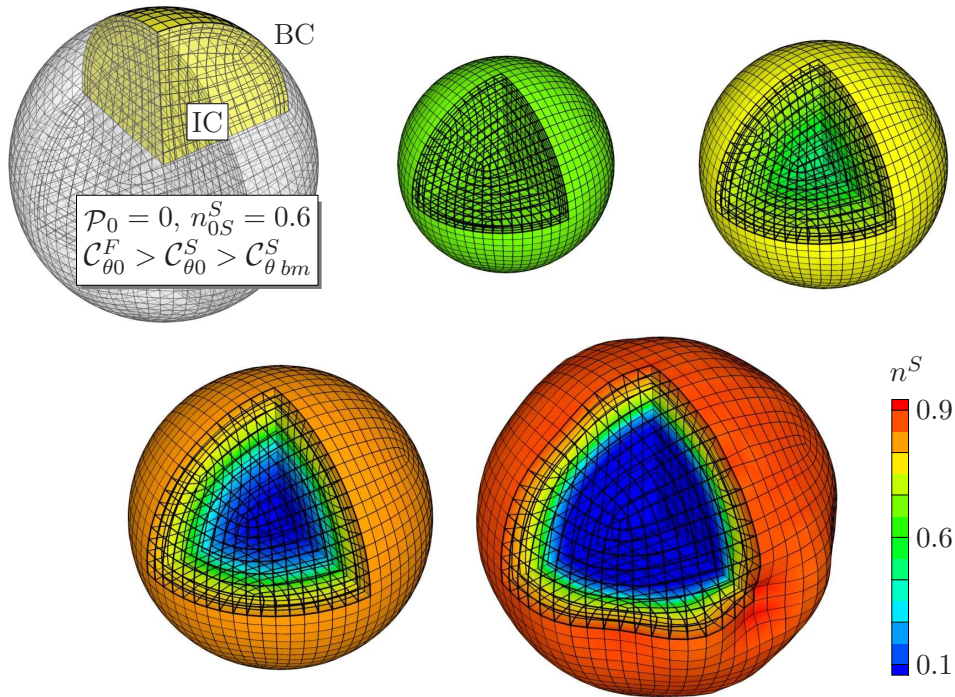
**Figure 5.5:** *3-d FE mesh with initial and boundary conditions and qualitative results of the simulated development of the solid volume fraction mimicking the early stages of avascular spheroidal tumor growth.*

## 5.5   Conclusion

In the present chapter, the complex material behavior of biological tissue was described on the basis of the TPM, thus allowing for a detailed description of solid deformation, interstitial fluid flow, ion diffusion and growth. As a result, coupled processes can be considered and computed, for example, by use of the FE package PANDAS. In addition to the examples presented in this article, further features can be described and have been omitted due to page limitations. For example, the vascular system can be added to the description such that vascular tissues can be described as well as tumor growth after blood vessels have entered the tumor region.

## 5.6   References

[1]  Acartürk, A.: *Simulation of Charged Hydrated Porous Materials.* Dissertation, Report No. II-18 of the Institute of Applied Mechanics (CE), Universität Stuttgart, Germany 2009.

[2]  Alastrué, V.; Martínez, M. A.; Doblaré, M. & Menzel, A.: Anisotropic micro-sphere-based finite elasticity applied to blood vessel modelling. *Journal of the Mechanics and Physics of Solids* **57** (2009), 178–203.

[3] Ambrosi, D. & Mollica, F.: On the mechanics of a growing tumor. *International Journal of Engineering Science* **40** (2002), 1297–1316.

[4] Ambrosi, D. & Mollica, F.: The role of stress in the growth of a multicell spheroid. *Journal of Mathematical Biology* **48** (2004), 477–499.

[5] Ambrosi, D. & Preziosi, L.: On the closure of mass balance models for tumor growth. *Mathematical Models and Methods in Applied Sciences* **12** (2002), 737–754.

[6] Balzani, D.; Neff, P.; Schröder, J. & Holzapfel, G.: A polyconvex framework for soft biological tissues. Adjustment to experimental data. *International Journal of Solids and Structures* **43** (2006), 6052–6070.

[7] de Boer, R. & Ehlers, W.: *Theorie der Mehrkomponentenkontinua mit Anwendung auf bodenmechanische Probleme.* Forschungsberichte aus dem Fachbereich Bauwesen, Heft 40, Universität-GH-Essen 1986.

[8] Bowen, R. M.: Theory of mixtures. In Eringen, A. C. (ed.): *Continuum Physics.* Academic Press, New York 1976, vol. III, pp. 1–127.

[9] Bowen, R. M.: Incompressible porous media models by use of the theory of mixtures. *International Journal of Engineering Sciences* **18** (1980), 1129–1148.

[10] Bowen, R. M.: Compressible porous media models by use of the theory of mixtures. *International Journal of Engineering Sciences* **20** (1982), 697–735.

[11] Byrne, H. & Preziosi, L.: Modelling solid tumor growth using the theory of mixtures. *IMA Journal of Mathematical Medicine and Biology* **20** (2003), 341–366.

[12] Cowin, S. C.: How is a tissue built. *ASME Journal of Biomechanical Engineering* **122** (2000), 553–569.

[13] Eberlein, R.; Holzapfel, G. A. & Fröhlich, M.: Multi-segment FEA of the human lumbar spine including the heterogeneity of the anulus fibrosus. *Computational Mechanics* **34** (2004), 147–165.

[14] Ehlers, W.: *Poröse Medien – ein kontinuumsmechanisches Modell auf der Basis der Mischungstheorie.* Habilitation, Forschungsberichte aus dem Fachbereich Bauwesen, Heft 47, Universität-GH-Essen 1989.

[15] Ehlers, W.: Constitutive equations for granular materials in geomechanical context. In Hutter, K. (ed.): *Continuum Mechanics in Environmental Sciences and Geophysics.* Springer-Verlag, Wien 1993, CISM Courses and Lectures No. 337, pp. 313–402.

[16] Ehlers, W.: Grundlegende Konzepte in der Theorie Poröser Medien. *Technische Mechanik* **16** (1996), 63–76.

[17] Ehlers, W.: Foundations of multiphasic and porous materials. In Ehlers, W. & Bluhm, J. (eds.): *Porous Media: Theory, Experiments and Numerical Applications.* Springer-Verlag, Berlin 2002, pp. 3–86.

[18] Ehlers, W.: Challenges of porous media models in geo- and biomechanical engineering including electro-chemically active polymers and gels. *International Journal of Advances in Engineering Sciences and Applied Mathematics* **1** (2009), 1–24.

[19] Ehlers, W. & Acartürk, A.: The role of weakly imposed Dirichlet boundary conditions for numerically stable computations of swelling phenomena. *Computational Mechanics* **43** (2009), 545–557.

[20] Ehlers, W. & Eipper, G.: Finite elastic deformations in liquid-saturated and empty porous solids. *Transport in Porous Media* **34** (1999), 179–191.

[21] Ehlers, W.; Ellsiepen, P.; Blome, P.; Mahnkopf, D. & Markert, B.: *Theoretische und numerische Studien zur Lösung von Rand- und Anfangswertproblemen in der Theorie Poröser Medien.* Abschlußbericht zum DFG-Forschungsvorhaben Eh 107/6-2, Bericht aus dem Institut für Mechanik (Bauwesen), Nr. 99-II-1, Universität Stuttgart 1999.

[22] Ehlers, W.; Karajan, N. & Markert, B.: An extended biphasic model for charged hydrated tissues with application to the intervertebral disc. *Biomechanics and Modeling in Mechanobiology* **8** (2009), 233–251.

[23] Elliott, D. M. & Setton, L. A.: A linear material model for fiber-induced anisotropy of the anulus fibrosus. *ASME Journal of Biomechanical Engineering* **122** (2000), 173–179.

[24] Fung, Y. C.: *Biomechanics: Mechanical Properties of Living Tissues.* Springer-Verlag, New York 1981.

[25] Holzapfel, G. A. & Gasser, T. C.: A viscoelastic model for fiber-reinforced composites at finite strains: Continuum basis, computational aspects and applications. *Computer Methods in Applied Mechanics and Engineering* **190** (2001), 4379–4403.

[26] Holzapfel, G. A.; Gasser, T. C. & Ogden, R. W.: A new constitutive framework for arterial wall mechanics and a comparative study of material models. *Journal of Elasticity* **61** (2000), 1–48.

[27] Holzapfel, G. A.; Schulze-Bauer, C. A. J.; Feigl, G. & Regitnig, P.: Mono-lamellar mechanics of the human lumbar anulus fibrosus. *Biomechanics and Modeling in Mechanobiology* **3** (2005), 125–140.

[28] Holzapfel, G. A. & Weizsäcker, H. W.: Biomechanical behavior of the arterial wall and its numerical characterization. *Computers in Biology and Medicine* **28** (1998), 377–392.

[29] Humphrey, J. D.: Continuum biomechanics of soft biological tissues. *Proceedings of the Royal Society A* **1** (2002), 1–44.

[30] Humphrey, J. D. & Rajagopal, K. R.: A constrained mixture model for growth and remodeling of soft tissues. *Mathematical Models and Methods in Applied Sciences* **12** (2002), 407–430.

[31] Klisch, S. M. & Hoger, A.: Volumetric growth of thermoelastic materials and mixtures. *Mathematics and Mechanics of Solids* **8** (2003), 377–402.

[32] Klisch, S. M. & Lotz, J. C.: Application of a fiber-reinforced continuum theory to multiple deformations of the annulus fibrosus. *Journal of Biomechanics* **32** (1999), 1027–1036.

[33] Kunz-Schughart, L. A.; Kreutz, M. & Knuechel, R.: Multicellular spheroids: a three-dimensional in vitro culture system to study tumor biology. *International Journal of Experimental Pathology* **79** (1998), 1–23.

[34] Lanir, Y.: Biorheology and fluid flux in swelling tissues. I. Biocomponent theory for small deformations, including concentration effects. *Biorheology* **24** (1987), 173–187.

[35] Markert, B.: A constitutive approach to 3-d nonlinear fluid flow through finite deformable porous continua. *Transport in Porous Media* **70** (2007), 427–450.

[36] Menzel, A.; Harrysson, M. & Ristinmaa, M.: Towards an orientation-distribution-based multi-scale approach for remodelling biological tissues. *Computer Methods in Biomechanics and Biomedical Engineering* **11** (2008), 505–524.

[37] Preziosi, L.: *Cancer Modelling and Simulation.* Chapman & Hall/CRC 2003.

[38] Preziosi, L. & Farina, A.: On Darcy's law for growing porous media. *International Journal of Non-Linear Mechanics* **37** (2002), 485–491.

[39] Rodriguez, E. K.; Hoger, A. & McCulloch, A. D.: Stress-dependent finite growth in soft elastic tissues. *Journal of Biomechanics* **27** (1994), 455–467.

[40] Röhrle, O.; Davidson, J. B. & Pullan, A. J.: Bridging scales – a three-dimensional electromechanical finite element model of skeletal muscle. *SIAM Journal on Scientific Computing* **30** (2008), 2882–2904.

[41] Roose, T.; Netti, P. A.; Munn, L. L.; Boucher, Y. & Jain, R. K.: Solid stress generated by spheroid growth estimated using a poroelasticity model. *Microvascular Research* **66** (2003), 204–212.

[42] Schmidt, H.; Heuer, F.; Simon, U.; Kettler, A.; Rohlmann, A.; Claes, L. & Wilke, H.-J.: Application of a new calibration method for a three-dimensional finite element model of a human lumbar annulus fibrosus. *Clinical Biomechanics* **21** (2006), 337–344.

[43] Shirazi-Adl, A.: Nonlinear stress analysis of the whole lumbar spine in torsion-mechanics of facet articulation. *Journal of Biomechanics* **27** (1994), 289–299.

[44] Shirazi-Adl, A.: Analysis of large compression loads on lumbar spine in flexion and torsion using a novel wrapping element. *Journal of Biomechanics* **39** (2006), 267–275.

[45] Steeb, H. & Diebels, S.: A thermodynamic-consistent model describing growth and remodeling phenomena. *Computational Materials Science* **28** (2003), 597–607.

[46] Sutherland, R. M.: Cell and environment interactions in tumor microregions: the multicell spheroid model. *Science* **240** (1988), 177–184.

[47] Taber, L. A.: Biomechanics of growth, remodeling and morphogenesis. *Applied Mechanics Review* **48** (1995), 487–545.

# 6 Fluid Penetration Effects in Porous Media Contact

SUMMARY

The contact boundary conditions at the interface between two fluid-saturated porous bodies are derived. The general derivation is performed within the well-founded framework of the Theory of Porous Media (TPM) based on the constituent balance relations of mass, momentum, and energy accounting for finite discontinuities at the contact surface. Particular attention is drawn to the effects associated with the interstitial fluid flux across the interface. The derived contact conditions include two kinetic continuity conditions for the solid velocity and the fluid seepage velocity as well as two jump conditions for the effective solid stress and the pore-fluid pressure. As an application, the common case of biphasic porous media contact proceeding from materially incompressible constituents and inviscid fluid properties is discussed in detail.

## 6.1 Introduction

The modern Theory of Porous Media (TPM) originates from the idea of combining the classical Theory of Mixtures (TM) [12] with the concept of volume fractions. It seems that Drumheller [17] was one of the first to use this idea for the description of an empty porous medium. Bowen [13, 14] extended this approach to fluid-saturated porous solids considering both incompressible and compressible constituents. The following development of the TPM has been mainly contributed by the works of de Boer & Ehlers [10], and Ehlers [19, 20].

The TPM is a multiphasic continuum theory which, proceeding from superimposed and interacting continua, allows to describe the behavior of porous materials on the macro level accounting for the microstructural composition by means of volumetric ratios, the volume fractions, which are treated as local secondary variables of the thermodynamic process. At present, the TPM is well-elaborated and established for the description of manifold multi-phase materials in all branches of engineering, such as elastoplastic soils [22], hydrated biological tissues [23], or viscoelastic polymer foams [38], to name but a few. A summary of the recent developments and new trends within the TPM can be found in the works of Ehlers [21], and de Boer [9].

Parallel to the development of the TPM, Mow and coworkers [42] suggested a model for soft biological tissues within their linear biphasic theory. Basically, the approach used by Mow and coworkers is founded on the same concepts as the TPM, viz. Bowen's TM, in principle leading to the same basic equations. The biphasic model has been intensively

exploited in numerous investigations to study the creep and stress-relaxation behavior of living tissues, in particular cartilaginous tissues [3, 37]. Extensions to linear viscoelastic solid deformations [36], large strains [43], as well as triphasic formulations accounting for electrical charges [33] have been developed. Further information on porous media theories, particularly following the ideas of Biot [7], can be found in the textbooks by Coussy [16] and Lewis & Schrefler [34].

Despite the obvious progress in the development of theoretical porous media models, there still remain some unclear problems regarding the formulation of suitable boundary conditions especially in contact situations. In fact, the problem is no less important than the task of deriving admissible constitutive equations to close the theoretical model. In order to obtain physically sound solutions, besides the relevant governing equations within a certain domain, it is necessary to pose physically adequate conditions at the boundary (cf. [44]). The problem is much more complicated if one considers the general contact of two mechanically distinct porous bodies. The conditions to be satisfied at the contact interface are by no means obvious and not intuitively clear from a mechanical point of view, such as in classical contact mechanics of single-phase materials, see, e. g., [24, 30, 46, 52] for details. The problem arises already at the stage where the boundary of a porous medium has to be defined. Beavers & Joseph [6] introduced the notion of a nominal boundary as "a smooth geometric surface assuming that the outermost perimeters of all the surface pores of the permeable material are in this surface." However, this definition as the authors say "is precise when the geometry is simple (planes, spheres, cylinders etc.) but may be not fully adequate in more complicated situations."

Among the sparse references in the related literature on the subject of deriving contact boundary conditions for porous media, the majority of the papers is devoted to the contact conditions at the saturated porous solid-to-fluid interface. One of the first contributions in this field are the papers by Beavers & Joseph [6] and Taylor [49]. The main result of these works is a semi-empirically derived boundary condition also known as Beavers and Joseph or Taylor condition. A series of subsequent theoretical investigations [15, 45, 51] confirms the validity of the contact condition under certain circumstances. For a detailed review of the different approaches for the interfacial conditions between a porous medium and a bulk fluid layer, the interested reader is referred to Alazmi & Vafai [1].

Closely related to the subject of the present chapter is the work of Hou et al. [27]. Therein, the authors use contact boundary conditions at the cartilage-synovial fluid interface which are derived from a discontinuity analysis. Their result can be extended to the case where two fluid-saturated porous solids come into contact provided the continuity of the solid displacements over the contact interface is guaranteed. However, the authors rather focus on deriving boundary conditions at the interface between a porous medium and a viscid bulk fluid than discussing the general case of porous media contact. Later, Hou et al. [28] applied the boundary conditions for the investigation of squeeze-film lubrication mechanisms in diarthrodial human joints.

Adopting the boundary conditions of Hou et al. [27], several researchers posed and solved frictionless contact problems between two biphasic porous solids [5, 18, 50, 53]. However, there are always restrictions imposed on the boundary conditions. In particular, none of the works considers the effects associated with the fluid penetration from one contacting

body into the other. Ateshian [4] suggested a theoretical formulation for boundary friction in saturated porous media taking articular cartilage as an example. He introduced the concepts of the equilibrium kinetic frictional coefficient and the effective frictional coefficient assuming that only the solid-to-solid contact areas contribute to the appearance of frictional forces. The effects due to possible fluid fluxes through the contact interface are neglected.

The objective of the present contribution is to derive convenient boundary conditions at the interface between two contacting fluid-saturated porous bodies. In this regard, the special focus lies in the effects resulting from interstitial fluid penetration from one body into the other. Due to the fluid flux across the interface, the mated bodies interact and interchange by mass, linear momentum, and energy. In the related literature, these effects are usually not considered. To begin with, in Section 2, the general derivation of the contact conditions based on the balance principles for mixtures in the framework of the TPM is presented. Section 3 is then concerned with the detailed discussion of the case where two porous bodies come into contact of which both have materially incompressible constituents and are saturated with the same inviscid liquid. Section 4 presents an analysis of the boundary conditions for some special cases: (1) quasi-static contact, (2) the contact of identical porous bodies, and (3) the contact of a porous body and a bulk medium. Finally, the conclusions and discussions are given in Section 5 at the end of the chapter.

# 6.2 Saturated Porous Body with Discontinuity Surface

## 6.2.1 Preliminaries

For the purpose of this work but without loss of generality, we study the contact interaction of two biphasic porous bodies each consisting of a solid skeleton saturated by a single interstitial fluid (pore fluid). The theoretical framework is provided by the macroscopic Theory of Porous Media (TPM), where a biphasic porous body is treated as a de facto immiscible mixture $\varphi$ of superimposed and interacting solid and fluid constituents $\varphi^\alpha$ ($\alpha = S$ : solid skeleton; $\alpha = F$ : pore fluid). In the macroscopic model, $\varphi = \varphi^S \cup \varphi^F$, the incorporated physical quantities are then understood as the local averages of their microscopic representatives and the microstructural composition of the mixture is captured by local volumetric ratios. In particular, the volume fractions $n^\alpha := \mathrm{d}v^\alpha/\mathrm{d}v$ of $\varphi^\alpha$ are defined as the local ratios of the partial volume elements $\mathrm{d}v^\alpha$ with respect to the bulk volume element $\mathrm{d}v$ of $\varphi$. Apparently, assuming fully saturated conditions implies the saturation constraint to hold:

$$\sum_\alpha n^\alpha = n^S + n^F = 1 \quad \text{with} \quad \left\{ \begin{array}{ll} n^S & :\text{solidity}\,, \\ n^F & :\text{porosity}\,. \end{array} \right. \tag{6.1}$$

The introduction of the $n^\alpha$ is furthermore associated with two density functions, namely a material (realistic or effective) density $\rho^{\alpha R}$ and a partial density $\rho^\alpha$ relating the local mass of $\varphi^\alpha$ to the partial or the bulk volume element, respectively. It is easily concluded

that $\rho^\alpha = n^\alpha \rho^{\alpha R}$, which underlines the general compressibility of porous solids through possible changes of the volume fractions.

Next, concerning the kinematics of mixtures, the idea of superimposed and interacting continua implies that, starting from different reference positions $\mathbf{X}_\alpha$ at time $t_0$, each constituent is supposed to follow its unique individual Lagrangean (material) motion function $\boldsymbol{\chi}_\alpha$ and has its own velocity and acceleration fields, viz.:

$$\mathbf{x} = \boldsymbol{\chi}_\alpha(\mathbf{X}_\alpha, t) \;\; \Leftrightarrow \;\; \mathbf{X}_\alpha = \boldsymbol{\chi}_\alpha^{-1}(\mathbf{x}, t)\,,$$

$$\mathbf{v}_\alpha := \overset{\prime}{\mathbf{x}}_\alpha = \frac{\mathrm{d}_\alpha \mathbf{x}}{\mathrm{d}t}\,, \quad \overset{\prime\prime}{\mathbf{x}}_\alpha = \frac{\mathrm{d}_\alpha^2 \mathbf{x}}{\mathrm{d}t^2}\,. \tag{6.2}$$

Therein, supposing that $\boldsymbol{\chi}_\alpha$ is a local diffeomorphism, $\boldsymbol{\chi}_\alpha^{-1}$ represents the inverse (Eulerian or spatial) motion function and

$$(\,\cdot\,)'_\alpha := \frac{\mathrm{d}_\alpha(\,\cdot\,)}{\mathrm{d}t} = \frac{\partial(\,\cdot\,)}{\partial t} + \mathrm{grad}(\,\cdot\,) \cdot \overset{\prime}{\mathbf{x}}_\alpha \tag{6.3}$$

indicates the material time derivative following the motion of $\varphi^\alpha$. According to Equation $(6.2)_1$, each spatial point $\mathbf{x}$ of the current configuration at time $t$ is simultaneously occupied by material points of both constituents reflecting the overlay of the partial continua.

In porous media theories, it is moreover convenient to proceed from a Lagrangean description of the solid matrix via the solid displacement $\mathbf{u}_S$ and velocity $\mathbf{v}_S$ as the primary kinematical variables. In contrast, according to Gibson *et al.* [25], the pore-fluid flow is better expressed in a modified Eulerian setting via the seepage velocity vector $\mathbf{w}_{FR}$ describing the fluid motion relative to the deforming skeleton. Moreover, relating $\mathbf{w}_{FR}$ only to the fluid part of the mixture, the so-called filter or superficial velocity $\mathbf{w}_F$ can be introduced. In detail,

$$\mathbf{u}_S = \mathbf{x} - \mathbf{X}_S\,, \quad \mathbf{v}_S = (\mathbf{u}_S)'_S = \overset{\prime}{\mathbf{x}}_S\,, \quad \mathbf{w}_{FR} = \mathbf{v}_F - \mathbf{v}_S\,, \quad \mathbf{w}_F = n^F \mathbf{w}_{FR}\,. \tag{6.4}$$

## 6.2.2   Introduction of a Singular Surface

In preparation for a convenient treatment of porous media contact, consider a porous mixture body $\mathcal{B} = \bigcup_\alpha \mathcal{B}^\alpha$ with boundary surface $\mathcal{S} = \bigcup_\alpha \mathcal{S}^\alpha$ that is separated by a persistent, immaterial smooth surface $\Gamma$ into two parts indicated by $+$ and $-$, such that $\mathcal{B} = \mathcal{B}^+ \cup \mathcal{B}^-$ and $\mathcal{S} = \mathcal{S}^+ \cup \mathcal{S}^-$ with outward oriented unit surface normal vectors $\mathbf{n}$ and $\mathbf{n}^+$, $\mathbf{n}^-$, respectively (see Figure 6.1). Obviously, $\mathcal{S}^\pm \cup \Gamma$ builds the entire surface of the partitions $\mathcal{B}^\pm$ not to be confused with the partial bodies $\mathcal{B}^\alpha$ of $\varphi^\alpha$. The inner surface $\Gamma$ with unit normal vector $\mathbf{n}_\Gamma$ pointing from $\mathcal{B}^-$ to $\mathcal{B}^+$ is allowed to propagate through $\mathcal{B}$, and we introduce its velocity as well as the relative velocity of a constituent $\varphi^\alpha$ with respect to the moving interface $\Gamma$ as

$$\mathbf{v}_\Gamma := \overset{\prime}{\mathbf{x}}_\Gamma\,, \quad \mathbf{w}_{\alpha\Gamma} = \mathbf{v}_\alpha - \mathbf{v}_\Gamma\,, \tag{6.5}$$

where $(\,\cdot\,)'_\Gamma = \mathrm{d}_\Gamma(\,\cdot\,)/\mathrm{d}t$ is in analogy to (6.3). Note that here only one singular surface is introduced for the description of the contact surface. In general, discontinuity surfaces can be introduced for each individual constituent $\varphi^\alpha$ of the mixture.
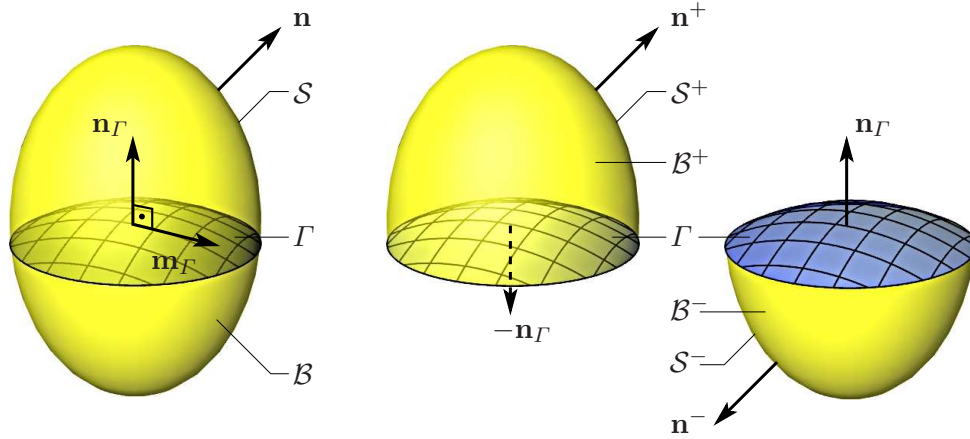
**Figure 6.1:** *Mixture body $\mathcal{B} = \mathcal{B}^+ \cup \mathcal{B}^-$ separated by a singular surface $\Gamma$.*

Now, consider a scalar-valued function $\Psi(\mathbf{x}, t)$ which is continuous in $\mathcal{B}^+$ and $\mathcal{B}^-$ and has the following limits on $\Gamma$ with $\mathbf{x}_\Gamma \in \Gamma$:

$$\Psi^+ = \lim_{\epsilon \to 0} \Psi(\mathbf{x}_\Gamma + \epsilon\,\mathbf{n}_\Gamma, t)\,, \quad \Psi^- = \lim_{\epsilon \to 0} \Psi(\mathbf{x}_\Gamma - \epsilon\,\mathbf{n}_\Gamma, t)\,. \tag{6.6}$$

The jump of $\Psi$ at $\Gamma$ is then defined as the difference of the limits, viz.

$$[\![\Psi]\!] := \Psi^+ - \Psi^-\,. \tag{6.7}$$

If the jump exists with $[\![\Psi]\!] \neq 0$, the surface $\Gamma$ is said to be singular with respect to $\Psi$, where the order $n = m + 1$ of the singular surface is defined by the maximum order $m$ of jump-free position derivatives of $\Psi$, see [26, 32, 35] for details. From the above, it is moreover apparent that the normal vector on $\Gamma$ and the interface velocity are jump-free, i.e.,

$$[\![\mathbf{n}_\Gamma]\!] = \mathbf{0}\,, \quad [\![\mathbf{v}_\Gamma]\!] = \mathbf{0}\,. \tag{6.8}$$

In connection with the jump expression (6.7) recall the product rule

$$[\![\Psi\,\Phi]\!] = [\![\Psi]\!]\,\langle\Phi\rangle + \langle\Psi\rangle\,[\![\Phi]\!] \quad \text{with} \quad \langle\Psi\rangle = \tfrac{1}{2}\left(\Psi^+ + \Psi^-\right)\,. \tag{6.9}$$

### 6.2.3  Modified Reynolds' Transport Theorem

First, recall Reynolds' transport theorem for a volume-specific density of a physical quantity $\Psi^\alpha$ of a constituent $\varphi^\alpha$ in the mixture body $\mathcal{B}$:

$$\frac{\mathrm{d}_\alpha}{\mathrm{d}t} \int_\mathcal{B} \Psi^\alpha \,\mathrm{d}v = \int_\mathcal{B} \frac{\partial \Psi^\alpha}{\partial t} \,\mathrm{d}v + \int_\mathcal{S} \Psi^\alpha\,\mathbf{v}_\alpha \cdot \mathbf{n} \,\mathrm{d}a\,. \tag{6.10}$$

Then, expressing the rate of change of $\Psi^\alpha$ relative to the surface $\Gamma$ moving with velocity $\mathbf{v}_\Gamma$ through $\mathcal{B}$, one obtains with $(6.5)_2$

$$\frac{\mathrm{d}_\alpha}{\mathrm{d}t} \int_\mathcal{B} \Psi^\alpha \,\mathrm{d}v = \frac{\mathrm{d}_\Gamma}{\mathrm{d}t} \int_\mathcal{B} \Psi^\alpha \,\mathrm{d}v + \int_\mathcal{S} \Psi^\alpha\,\mathbf{w}_{\alpha\Gamma} \cdot \mathbf{n} \,\mathrm{d}a\,. \tag{6.11}$$

Next, supposing all field functions to be continuous in $\mathcal{B}^+$ and $\mathcal{B}^-$ as well as on $\Gamma$, we allow for finite discontinuities and jumps at the interface. Evaluating (6.11) separately for both partitions of $\mathcal{B}$ accounting for the discontinuity $\Gamma$ in the sense of a singular surface yields

$$\frac{\mathrm{d}_\alpha}{\mathrm{d}t} \int_{\mathcal{B}^+} \Psi^\alpha \, \mathrm{d}v = \frac{\mathrm{d}_\Gamma}{\mathrm{d}t} \int_{\mathcal{B}^+} \Psi^\alpha \, \mathrm{d}v + \int_{\mathcal{S}^+} \Psi^\alpha \, \mathbf{w}_{\alpha\Gamma} \cdot \mathbf{n}^+ \, \mathrm{d}a + \int_\Gamma (\Psi^\alpha)^+ \, \mathbf{w}_{\alpha\Gamma}^+ \cdot \mathbf{n}_\Gamma^+ \, \mathrm{d}a, \qquad (6.12)$$

$$\frac{\mathrm{d}_\alpha}{\mathrm{d}t} \int_{\mathcal{B}^-} \Psi^\alpha \, \mathrm{d}v = \frac{\mathrm{d}_\Gamma}{\mathrm{d}t} \int_{\mathcal{B}^-} \Psi^\alpha \, \mathrm{d}v + \int_{\mathcal{S}^-} \Psi^\alpha \, \mathbf{w}_{\alpha\Gamma} \cdot \mathbf{n}^- \, \mathrm{d} + \int_\Gamma (\Psi^\alpha)^- \, \mathbf{w}_{\alpha\Gamma}^- \cdot \mathbf{n}_\Gamma^- \, \mathrm{d}a. \qquad (6.13)$$

Finally, summation of (6.12) and (6.13) together with the transport theorem (6.10), the jump operator (6.7), and the normal vectors on $\Gamma$ associated with $\mathcal{B}^+$ and $\mathcal{B}^-$ (Figure 6.1),

$$\mathbf{n}_\Gamma^+ = -\mathbf{n}_\Gamma^- =: -\mathbf{n}_\Gamma, \qquad (6.14)$$

yields a modified form of Reynolds' transport theorem:

$$\frac{\mathrm{d}_\alpha}{\mathrm{d}t} \int_{\mathcal{B}} \Psi^\alpha \, \mathrm{d}v = \int_{\mathcal{B}\backslash\Gamma} \frac{\partial \Psi^\alpha}{\partial t} \, \mathrm{d}v + \int_{\mathcal{S}} \Psi^\alpha \, \mathbf{v}_\alpha \cdot \mathbf{n} \, \mathrm{d}a - \int_\Gamma [\![ \Psi^\alpha \, \mathbf{w}_{\alpha\Gamma} ]\!] \cdot \mathbf{n}_\Gamma \, \mathrm{d}a. \qquad (6.15)$$

Analogous considerations for a vector-valued quantity $\boldsymbol{\Psi}^\alpha$ lead to

$$\frac{\mathrm{d}_\alpha}{\mathrm{d}t} \int_{\mathcal{B}} \boldsymbol{\Psi}^\alpha \, \mathrm{d}v = \int_{\mathcal{B}\backslash\Gamma} \frac{\partial \boldsymbol{\Psi}^\alpha}{\partial t} \, \mathrm{d}v + \int_{\mathcal{S}} (\boldsymbol{\Psi}^\alpha \otimes \mathbf{v}_\alpha) \, \mathbf{n} \, \mathrm{d}a - \int_\Gamma [\![ \boldsymbol{\Psi}^\alpha \otimes \mathbf{w}_{\alpha\Gamma} ]\!] \, \mathbf{n}_\Gamma \, \mathrm{d}a. \qquad (6.16)$$

In (6.15) and (6.16), the left-hand sides describe the material temporal change of $\Psi^\alpha, \boldsymbol{\Psi}^\alpha$ with respect to a material volume element that varies with time. The right-hand sides describe the local temporal change and the convective flux of the physical quantity with respect to spatially fixed (temporally constant) volume and area elements of the control space. The integrals over the jump expression in (6.15) and (6.16) represent for $\mathbf{w}_{\alpha\Gamma} \neq 0$ the internal flux of $\Psi^\alpha, \boldsymbol{\Psi}^\alpha$ across the interface $\Gamma$.

### 6.2.4   Modified Constituent Master Balances

Following the same arguments, by considering the flux through an inner discontinuity surface and additionally a fictitious influx at $\Gamma$ implying an intrinsic surface production, one straightforwardly arrives at global master balance relations for the constituent $\varphi^\alpha$:

$$\frac{\mathrm{d}_\alpha}{\mathrm{d}t} \int_{\mathcal{B}} \Psi^\alpha \, \mathrm{d}v = \int_{\mathcal{B}\backslash\Gamma} \sigma^\alpha \, \mathrm{d}v + \int_{\mathcal{B}\backslash\Gamma} \widehat{\Psi}^\alpha \, \mathrm{d}v + \int_{\mathcal{S}} (\boldsymbol{\phi}^\alpha \cdot \mathbf{n}) \, \mathrm{d}a - \int_\Gamma \widehat{\Psi}_\Gamma^\alpha \, \mathrm{d}a - \int_\Gamma [\![ \boldsymbol{\phi}^\alpha ]\!] \cdot \mathbf{n}_\Gamma \, \mathrm{d}a, \quad (6.17)$$

$$\frac{\mathrm{d}_\alpha}{\mathrm{d}t} \int_{\mathcal{B}} \boldsymbol{\Psi}^\alpha \, \mathrm{d}v = \int_{\mathcal{B}\backslash\Gamma} \boldsymbol{\sigma}^\alpha \, \mathrm{d}v + \int_{\mathcal{B}\backslash\Gamma} \widehat{\boldsymbol{\Psi}}^\alpha \, \mathrm{d}v + \int_{\mathcal{S}} (\boldsymbol{\Phi}^\alpha \, \mathbf{n}) \, \mathrm{d}a - \int_\Gamma \widehat{\boldsymbol{\Psi}}_\Gamma^\alpha \, \mathrm{d}a - \int_\Gamma [\![ \boldsymbol{\Phi}^\alpha ]\!] \, \mathbf{n}_\Gamma \, \mathrm{d}a. \quad (6.18)$$

Therein, $\Psi^\alpha, \boldsymbol{\Psi}^\alpha$ are the volume-specific densities of the physical quantity to be balanced, $\sigma^\alpha, \boldsymbol{\sigma}^\alpha$ are the volume densities describing the supply (external source), and $\widehat{\Psi}^\alpha, \widehat{\boldsymbol{\Psi}}^\alpha$ represent the total production (intrinsic supply) of the physical quantity due to mutual

couplings and interactions of the $\varphi^\alpha$. Moreover, $(\boldsymbol{\phi}^\alpha \cdot \mathbf{n}), (\boldsymbol{\Phi}^\alpha \mathbf{n})$ are the surface densities representing the efflux of the physical quantity at the outer surface $\mathcal{S}$ of $\mathcal{B}$. In the same way, $[\![\boldsymbol{\phi}^\alpha]\!] \cdot \mathbf{n}_\Gamma, [\![\boldsymbol{\Phi}^\alpha]\!] \mathbf{n}_\Gamma$ and $\widehat{\Psi}_\Gamma^\alpha = (\phi_\Gamma^\alpha \cdot \mathbf{n}_\Gamma), \widehat{\boldsymbol{\Psi}}_\Gamma^\alpha = (\boldsymbol{\Phi}_\Gamma^\alpha \mathbf{n}_\Gamma)$ consider the changes of $\Psi^\alpha, \boldsymbol{\Psi}^\alpha$ due to the flux across and the total production at the interface $\Gamma$, respectively.

Following the mixture approach, the local partial continua can be regarded as open systems staying in thermodynamical exchange with each other through the intrinsic supply and production terms. However, the way of introducing these terms is of somehow constitutive nature as their link to the other field variables eventually depends on the physical problem at hand. Here, the fictitious surface influxes $\phi_\Gamma^\alpha, \boldsymbol{\Phi}_\Gamma^\alpha$ are introduced to render the hardly distinguishable surface and body contributions to the interaction transfers at $\Gamma$, thus accounting for the inherent physical nature of the singular surface in the sense of a thin, immaterial transition layer within a reacting mixture continuum [2, 29, 48]. Further possible motivations and interpretations of the intrinsic surface supplies are discussed by Kelly [31], Morland & Gray [40], and Morland & Sellers [41] among others.

To continue, we insert (6.15) and (6.16) into (6.17) and (6.18), respectively, and apply the Gaussian theorem to the integrals over the outer surface $\mathcal{S}$. As intermediate results, one obtains

$$
\int_{\mathcal{B} \setminus \Gamma} \left( \frac{\partial \Psi^\alpha}{\partial t} + \operatorname{div}(\Psi^\alpha \mathbf{v}_\alpha) - \operatorname{div} \boldsymbol{\phi}^\alpha - \sigma^\alpha - \widehat{\Psi}^\alpha \right) \mathrm{d}v =
$$
$$
= \int_\Gamma \left( [\![ \Psi^\alpha \mathbf{w}_{\alpha\Gamma} - \boldsymbol{\phi}^\alpha ]\!] \cdot \mathbf{n}_\Gamma - \widehat{\Psi}_\Gamma^\alpha \right) \mathrm{d}a \,,
\tag{6.19}
$$

$$
\int_{\mathcal{B} \setminus \Gamma} \left( \frac{\partial \boldsymbol{\Psi}^\alpha}{\partial t} + \operatorname{div}(\boldsymbol{\Psi}^\alpha \otimes \mathbf{v}_\alpha) - \operatorname{div} \boldsymbol{\Phi}^\alpha - \boldsymbol{\sigma}^\alpha - \widehat{\boldsymbol{\Psi}}^\alpha \right) \mathrm{d}v =
$$
$$
= \int_\Gamma \left( [\![ \boldsymbol{\Psi}^\alpha \otimes \mathbf{w}_{\alpha\Gamma} - \boldsymbol{\Phi}^\alpha ]\!] \mathbf{n}_\Gamma - \widehat{\boldsymbol{\Psi}}_\Gamma^\alpha \right) \mathrm{d}a \,.
\tag{6.20}
$$

Proceeding from adequate continuity properties for all occurring fields in $\mathcal{B}$ outside the discontinuity surface $\Gamma$, the equivalent local (differential) forms of the left-hand sides of (6.19) and (6.20) read

$$
\left. \begin{aligned}
(\Psi^\alpha)'_\alpha + \Psi^\alpha \operatorname{div} \mathbf{v}_\alpha &= \operatorname{div} \boldsymbol{\phi}^\alpha + \sigma^\alpha + \widehat{\Psi}^\alpha \,, \\
(\boldsymbol{\Psi}^\alpha)'_\alpha + \boldsymbol{\Psi}^\alpha \operatorname{div} \mathbf{v}_\alpha &= \operatorname{div} \boldsymbol{\Phi}^\alpha + \boldsymbol{\sigma}^\alpha + \widehat{\boldsymbol{\Psi}}^\alpha
\end{aligned} \right\} \quad \forall\, \mathbf{x} \in \mathcal{B} \setminus \Gamma \,.
\tag{6.21}
$$

In the same way, one obtains the local relations for the interface $\Gamma$ as

$$
\left. \begin{aligned}
[\![ \Psi^\alpha \mathbf{w}_{\alpha\Gamma} - \boldsymbol{\phi}^\alpha ]\!] \cdot \mathbf{n}_\Gamma &= \widehat{\Psi}_\Gamma^\alpha \,, \\
[\![ \boldsymbol{\Psi}^\alpha \otimes \mathbf{w}_{\alpha\Gamma} - \boldsymbol{\Phi}^\alpha ]\!] \mathbf{n}_\Gamma &= \widehat{\boldsymbol{\Psi}}_\Gamma^\alpha
\end{aligned} \right\} \quad \forall\, \mathbf{x} = \mathbf{x}_\Gamma \in \Gamma \,.
\tag{6.22}
$$

Analogous results can be obtained for the averaged physical fields of the whole multiphasic continuum $\varphi$ accounting for additional summation conditions in regard to the overall conservation of the mixture quantities (cf. [21]).

# 6.3 Contact Boundary Conditions for Saturated Porous Media

## 6.3.1 Solid-Skeleton Contact

Following the preceding, consider the situation depicted in Figure 6.1 as a contact problem of two deformable porous bodies. Then, $\Gamma$ represents a contact surface defined as the nominal surface of mutual solid-skeleton contact. Accordingly, $\Gamma$ is material, i. e., at rest, with respect to the normal motion of $\varphi^S$, which for the mated bodies implies the following condition at the interface:

$$\mathbf{v}_\Gamma \cdot \mathbf{n}_\Gamma = \mathbf{v}_S \cdot \mathbf{n}_\Gamma \quad \Leftrightarrow \quad \mathbf{w}_{S\Gamma} \cdot \mathbf{n}_\Gamma = 0 \,. \tag{6.23}$$

The condition states that the solid matrices of the porous bodies are in normal contact but their mutual sliding is not forbidden. However, (6.23) does not provide any information about the movement of the fluid constituent $\varphi^F$. From a physical perspective, it is apparent that the contact of fluid-saturated porous bodies generally provokes the existence of a pore-fluid flux across the contact surface depending on the apparent pore pressure and the local hydraulic properties. At this point, we merely assume that the seepage flow through the interface remains subsonic, which applies to common TPM problems.

It is now our goal to derive the contact boundary conditions at the interface based on the modified constituent balance relations, namely of mass, momentum, and energy.

## 6.3.2 Distinct Balances and Jump Conditions

Proceeding from the modified constituent master balances (6.17), (6.18) and (6.21), (6.22), respectively, one identifies the physical quantities according to Table 1. In detail, $\widehat{\rho}^\alpha$

**Table 6.1:** *Identified physical quantities of the modified constituent master balances.*

| Balance | $\Psi^\alpha, \mathbf{\Psi}^\alpha$ | $\boldsymbol{\phi}^\alpha, \mathbf{\Phi}^\alpha$ | $\sigma^\alpha, \boldsymbol{\sigma}^\alpha$ | $\widehat{\Psi}^\alpha, \widehat{\mathbf{\Psi}}^\alpha$ | $\widehat{\Psi}^\alpha_\Gamma, \widehat{\boldsymbol{\Psi}}^\alpha_\Gamma$ |
|---------|------|------|------|------|------|
| mass | $\rho^\alpha$ | $\mathbf{0}$ | $0$ | $\widehat{\rho}^\alpha$ | $\widehat{\varrho}^\alpha_\Gamma$ |
| momentum | $\rho^\alpha \mathbf{v}_\alpha$ | $\mathbf{T}^\alpha$ | $\rho^\alpha \mathbf{b}^\alpha$ | $\widehat{\mathbf{s}}^\alpha$ | $\widehat{\boldsymbol{s}}^\alpha_\Gamma$ |
| energy | $\rho^\alpha(\varepsilon^\alpha + \frac{1}{2}\mathbf{v}_\alpha \cdot \mathbf{v}_\alpha)$ | $(\mathbf{T}^\alpha)^T \mathbf{v}_\alpha - \mathbf{q}^\alpha$ | $\rho^\alpha(\mathbf{v}_\alpha \cdot \mathbf{b}^\alpha + r^\alpha)$ | $\widehat{\mathrm{e}}^\alpha$ | $\widehat{e}^\alpha_\Gamma$ |

and $\widehat{\varrho}^\alpha_\Gamma$ are the density productions describing the mass exchanges and phase transitions between the $\varphi^\alpha$ in $\mathcal{B}$ and at $\Gamma$, $\mathbf{T}^\alpha$ denotes the partial Cauchy stress tensor, $\mathbf{b}^\alpha$ is the external mass-specific body force, and $\widehat{\mathbf{s}}^\alpha$ and $\widehat{\boldsymbol{s}}^\alpha_\Gamma$ are the total momentum productions of $\varphi^\alpha$ in $\mathcal{B}$ and at $\Gamma$. Moreover, $\varepsilon^\alpha$ is the mass-specific internal energy of $\varphi^\alpha$, $\mathbf{q}^\alpha$ is the heat influx vector, $r^\alpha$ is the external heat supply, and $\widehat{\mathrm{e}}^\alpha$ and $\widehat{e}^\alpha_\Gamma$ are the total constituent energy productions in $\mathcal{B}$ and at $\Gamma$.

In mixture theories, it is moreover convenient to split the total production terms into direct parts and parts including productions of the preceding (lower) balances [21]. In

particular, we have

$$\left.\begin{aligned}
\widehat{\mathbf{s}}^\alpha &= \widehat{\mathbf{p}}^\alpha + \widehat{\rho}^\alpha\, \mathbf{v}_\alpha\,, \\
\widehat{e}^\alpha &= \widehat{\varepsilon}^\alpha + \widehat{\mathbf{p}}^\alpha \cdot \mathbf{v}_\alpha + \widehat{\rho}^\alpha\left(\varepsilon^\alpha + \tfrac{1}{2}\,\mathbf{v}_\alpha \cdot \mathbf{v}_\alpha\right)
\end{aligned}\right\} \quad \forall\, \mathbf{x} \in \mathcal{B} \setminus \varGamma\,, \tag{6.24}$$

where $\widehat{\mathbf{p}}^\alpha$ denotes the direct momentum production which can be interpreted as the volume-specific local interaction force between $\varphi^\alpha$ and the other constituents of $\varphi$ and $\widehat{\varepsilon}^\alpha$ is the direct part of the energy production. Moreover, proceeding from a closed mixture system, the following restrictions hold:

$$\sum_\alpha \widehat{\rho}^\alpha = 0\,, \quad \sum_\alpha \widehat{\mathbf{s}}^\alpha = \mathbf{0}\,, \quad \sum_\alpha \widehat{e}^\alpha = 0\,. \tag{6.25}$$

Applying the same procedure to the intrinsic surface supplies yields

$$\left.\begin{aligned}
\widehat{\boldsymbol{s}}^\alpha_\varGamma &= \widehat{\boldsymbol{\pi}}^\alpha_\varGamma + \widehat{\varrho}^\alpha_\varGamma\, \mathbf{v}_\alpha\,, \\
\widehat{e}^\alpha_\varGamma &= \widehat{\epsilon}^\alpha_\varGamma + \widehat{\boldsymbol{\pi}}^\alpha_\varGamma \cdot \mathbf{v}_\alpha + \widehat{\varrho}^\alpha_\varGamma\left(\varepsilon^\alpha + \tfrac{1}{2}\,\mathbf{v}_\alpha \cdot \mathbf{v}_\alpha\right)
\end{aligned}\right\} \quad \forall\, \mathbf{x} = \mathbf{x}_\varGamma \in \varGamma\,. \tag{6.26}$$

where, in analogy to (6.25), we claim

$$\sum_\alpha \widehat{\varrho}^\alpha_\varGamma = 0\,, \quad \sum_\alpha \widehat{\boldsymbol{s}}^\alpha_\varGamma = \mathbf{0}\,, \quad \sum_\alpha \widehat{e}^\alpha_\varGamma = 0\,. \tag{6.27}$$

In (6.26), $\widehat{\boldsymbol{\pi}}^\alpha_\varGamma$ and $\widehat{\epsilon}^\alpha_\varGamma$ represent the direct parts of the intrinsic surface productions of momentum and energy at the interface $\varGamma$.

In summary, by substituting the partial physical quantities of Table 1 into (6.21) and (6.22) under consideration of (6.23), one obtains the well-known local balances plus additional jump conditions at the nominal solid-skeleton contact surface:

- mass:

$$\begin{aligned}
(\rho^\alpha)'_\alpha + \rho^\alpha\, \mathrm{div}\, \mathbf{v}_\alpha &= \widehat{\rho}^\alpha \quad \forall\, \mathbf{x} \in \mathcal{B} \setminus \varGamma\,, \ \alpha = \{S, F\}\,, \\
[\![\rho^F\, \mathbf{w}_{F\varGamma}]\!] \cdot \mathbf{n}_\varGamma &= \widehat{\varrho}^F \qquad \forall\, \mathbf{x} = \mathbf{x}_\varGamma \in \varGamma\,,
\end{aligned} \tag{6.28}$$

- momentum:

$$\left.\begin{aligned}
\rho^\alpha\,(\mathbf{v}_\alpha)'_\alpha &= \mathrm{div}\, \mathbf{T}^\alpha + \rho^\alpha\, \mathbf{b} + \widehat{\mathbf{p}}^\alpha \quad \forall\, \mathbf{x} \in \mathcal{B} \setminus \varGamma\,, \ \alpha = \{S, F\}\,, \\
[\![-\mathbf{T}^S]\!]\, \mathbf{n}_\varGamma &= \widehat{\boldsymbol{s}}^S_\varGamma \\
[\![\rho^F\, \mathbf{v}_F \otimes \mathbf{w}_{F\varGamma} - \mathbf{T}^F]\!]\, \mathbf{n}_\varGamma &= \widehat{\boldsymbol{s}}^F_\varGamma
\end{aligned}\right\} \quad \forall\, \mathbf{x} = \mathbf{x}_\varGamma \in \varGamma\,, \tag{6.29}$$

- energy:

$$\left.\begin{aligned}
\rho^\alpha\,(\varepsilon^\alpha)'_\alpha &= \mathbf{T}^\alpha \cdot \mathrm{grad}\, \mathbf{v}_\alpha - \mathrm{div}\, \mathbf{q}^\alpha + \rho^\alpha\, r^\alpha + \widehat{\varepsilon}^\alpha \quad \forall\, \mathbf{x} \in \mathcal{B} \setminus \varGamma\,, \ \alpha = \{S, F\}\,, \\
[\![-(\mathbf{T}^S)^T\, \mathbf{v}_S + \mathbf{q}^S]\!] \cdot \mathbf{n}_\varGamma &= \widehat{e}^S_\varGamma \\
[\![\rho^F\,(\varepsilon^F + \tfrac{1}{2}\,\mathbf{v}_F \cdot \mathbf{v}_F)\, \mathbf{w}_{F\varGamma} - (\mathbf{T}^F)^T\, \mathbf{v}_F + \mathbf{q}^F]\!] \cdot \mathbf{n}_\varGamma &= \widehat{e}^F_\varGamma
\end{aligned}\right\} \quad \forall\, \mathbf{x} = \mathbf{x}_\varGamma \in \varGamma\,. \tag{6.30}$$

### 6.3.3   Simplifying Assumptions

With regard to a concise derivation of the relevant boundary conditions at $\Gamma$, we restrict the presentation to a special but most common case of biphasic porous media contact accepting some simplifying assumptions. In particular, we proceed from:

- inert constituents with $\widehat{\rho}^{\alpha} \equiv 0$ and $\widehat{\varrho}_{\Gamma}^{\alpha} \equiv 0$,

- negligible body forces, i.e., $\mathbf{b}^{\alpha} = \mathbf{0}$,

- non-polar Boltzmann continua such that $\mathbf{T}^{\alpha} = (\mathbf{T}^{\alpha})^{T}$,

- isothermal and adiabatic processes with $\mathbf{q}^{\alpha} \equiv \mathbf{0}$ and $r^{\alpha} \equiv 0$.

Moreover, the contacting biphasic solid-fluid mixture bodies $\mathcal{B}^{\pm}$ are assumed to be composed of materially incompressible constituents, i.e.,

$$\rho^{\alpha R} = \text{const.} \quad \forall \, \alpha = \{S, F\}, \tag{6.31}$$

and the pore fluid is supposed to be the same on both sides, such that

$$(\rho^{FR})^{+} = (\rho^{FR})^{-} \quad \Leftrightarrow \quad [\![\rho^{FR}]\!] = 0. \tag{6.32}$$

Then, by virtue of (6.31), the constituent mass balances $(6.28)_1$ reduce to volume balances reading

$$(n^{\alpha})'_{\alpha} + n^{\alpha} \, \text{div} \, \mathbf{v}_{\alpha} = 0 \quad \forall \, \mathbf{x} \in \mathcal{B} \setminus \Gamma, \; \alpha = \{S, F\}. \tag{6.33}$$

Moreover, proceeding from isothermal conditions and $\rho^{FR} = \text{const.}$ entails that the internal energy of the fluid constituent is constant in the domain, and thus, jump-free across $\Gamma$:

$$\varepsilon^{F} = \text{const.} \quad \longrightarrow \quad [\![\varepsilon^{F}]\!] = 0. \tag{6.34}$$

Hence, the general jump conditions $(6.28)_2$, $(6.29)_{2,3}$, and $(6.30)_{2,3}$ at the contact surface between $\mathcal{B}^{+}$ and $\mathcal{B}^{-}$ reduce to

$$[\![n^{F} \, \mathbf{w}_{F\Gamma}]\!] \cdot \mathbf{n}_{\Gamma} = 0 \quad \Leftrightarrow \quad [\![n^{S} \, \mathbf{v}_{S} + n^{F} \, \mathbf{v}_{F}]\!] \cdot \mathbf{n}_{\Gamma} = 0, \tag{6.35}$$

$$[\![\mathbf{T}^{S} + \mathbf{T}^{F}]\!] \, \mathbf{n}_{\Gamma} = \rho^{FR} [\![n^{F} \, \mathbf{v}_{F} \otimes \mathbf{w}_{F\Gamma}]\!] \, \mathbf{n}_{\Gamma}, \tag{6.36}$$

$$[\![\mathbf{T}^{S} \, \mathbf{v}_{S} + \mathbf{T}^{F} \, \mathbf{v}_{F}]\!] \cdot \mathbf{n}_{\Gamma} = \rho^{FR} [\![n^{F} \, \tfrac{1}{2} \, (\mathbf{v}_{F} \cdot \mathbf{v}_{F}) \, \mathbf{w}_{F\Gamma}]\!] \cdot \mathbf{n}_{\Gamma}. \tag{6.37}$$

Herein, the alternative representation of the jump condition on the right-hand side of (6.35) can be obtained with the saturation constraint (6.1) and the continuity of the normal components of the solid velocity vector according to (6.8) and (6.23). The contact conditions (6.36) and (6.37) represent the sums of the original partial relations under consideration of (6.27). It is worth mentioning that this procedure is very convenient due to the fact that no separation into actions on the different phases is needed as it is well-established for the treatment of traction boundary conditions when solving TPM problems based on some variational formulation associated with the Finite Element Method (FEM).

### 6.3.4 Derivation of the Contact Conditions

To continue, we exploit the effective stress principle [8, 11, 47]

$$\mathbf{T}^\alpha = -n^\alpha\, p\, \mathbf{I} + \mathbf{T}_E^\alpha \quad \forall\, \alpha = \{S, F\}\,, \tag{6.38}$$

where $p$ is the excess pore-fluid pressure, $\mathbf{I}$ is the second-order identity tensor, and $\mathbf{T}_E^\alpha$ denotes the extra or effective stresses to be determined from constitutive equations. Admittedly, on the basis of a dimensional analysis, the fluid extra (friction) stress $\mathbf{T}_E^F$ can be a priori neglected implying that the fluid behaves more or less inviscid in the flow and the fluid viscosity is not considered explicitly but only implicitly via the viscous drag (interphase friction) included in the fluid momentum production governed by a constitutive filter law [39]. In this regard, note that (6.38) is not of constitutive nature as it can be deduced from thermodynamical considerations with $p$ entering the mixture entropy principle as a Lagrangean multiplier to preserve the saturation constraint (6.1) in the sense of a penalty per violation of a continuity-like condition [38].

Then, inserting (6.38) into (6.36) and (6.37) accounting for $\mathbf{T}_E^F \approx \mathbf{0}$ and (6.35)$_2$, the jump conditions are rewritten as

$$-[\![p]\!]\, \mathbf{n}_\Gamma + [\![\mathbf{T}_E^S]\!]\, \mathbf{n}_\Gamma = \rho^{FR} [\![n^F\, \mathbf{v}_F \otimes \mathbf{w}_{F\Gamma}]\!]\, \mathbf{n}_\Gamma\,, \tag{6.39}$$

$$-[\![p]\!]\, (n^S\, \mathbf{v}_S + n^F\, \mathbf{v}_F) \cdot \mathbf{n}_\Gamma + [\![\mathbf{T}_E^S\, \mathbf{v}_S]\!] \cdot \mathbf{n}_\Gamma = \rho^{FR} [\![n^F\, \tfrac{1}{2}\, (\mathbf{v}_F \cdot \mathbf{v}_F)\, \mathbf{w}_{F\Gamma}]\!] \cdot \mathbf{n}_\Gamma\,. \tag{6.40}$$

Although we proceed from isothermal conditions and inviscid fluid properties ($\mathbf{T}_E^F \approx \mathbf{0}$), the jump relation related to the energy balance (6.40) is still required to derive separated contact conditions for the pore pressure and the effective solid stress. In this context, for simplicity, we assume frictionless contact, which requires the absence of frictional forces associated with the solid skeleton at $\Gamma$. This is ensured if

$$(\mathbf{T}_E^S\, \mathbf{n}_\Gamma)^+ \cdot \mathbf{m}_\Gamma = (\mathbf{T}_E^S\, \mathbf{n}_\Gamma)^- \cdot \mathbf{m}_\Gamma = 0 \tag{6.41}$$

with $\mathbf{m}_\Gamma$ denoting any unit tangential vector to $\Gamma$ (cf. Figure 6.1), where $[\![\mathbf{m}_\Gamma]\!] = \mathbf{0}$ and $\mathbf{n}_\Gamma \cdot \mathbf{m}_\Gamma = 0$. Then, taking the scalar product of Equation (6.39) and $\mathbf{m}_\Gamma$ together with (6.9), (6.35)$_1$, and (6.41) yields the continuity of the tangential component of the fluid velocity along the contact surface:

$$[\![\mathbf{v}_F]\!] \cdot \mathbf{m}_\Gamma = 0\,. \tag{6.42}$$

Moreover, with (6.23), (6.41), and the symmetry of the stress tensors, the solid stress expression in (6.40) can be rewritten as

$$\begin{aligned}
[\![\mathbf{T}_E^S\, \mathbf{v}_S]\!] \cdot \mathbf{n}_\Gamma &= [\![\mathbf{T}_E^S\, \mathbf{n}_\Gamma \cdot \mathbf{v}_S]\!] \\
&= [\![\mathbf{T}_E^S\, \mathbf{n}_\Gamma \cdot \{(\mathbf{v}_S \cdot \mathbf{n}_\Gamma)\, \mathbf{n}_\Gamma + (\mathbf{v}_S \cdot \mathbf{m}_\Gamma)\, \mathbf{m}_\Gamma\}]\!] \\
&= [\![\mathbf{T}_E^S\, \mathbf{n}_\Gamma \cdot \mathbf{n}_\Gamma]\!]\, (\mathbf{v}_\Gamma \cdot \mathbf{n}_\Gamma)\,.
\end{aligned} \tag{6.43}$$

Next, taking the scalar product between (6.39) and $(\mathbf{v}_\Gamma \cdot \mathbf{n}_\Gamma)\, \mathbf{n}_\Gamma$ and subtracting the result from (6.40) including (6.43), after straightforward manipulation, we obtain

$$[\![p]\!] = -\rho^{FR} [\![\tfrac{1}{2}\, (\mathbf{v}_F \cdot \mathbf{n}_\Gamma)^2 - (\mathbf{v}_F \cdot \mathbf{n}_\Gamma)\, (\mathbf{v}_S \cdot \mathbf{n}_\Gamma)]\!]\,. \tag{6.44}$$

By insertion of the resulting jump condition for the pore pressure into (6.39), we determine the corresponding condition for the normal component of the effective solid-skeleton traction. Omitting the details, the final result reads

$$\llbracket \mathbf{T}_E^S \, \mathbf{n}_\Gamma \rrbracket \cdot \mathbf{n}_\Gamma = -\rho^{FR} \llbracket \tfrac{1}{2} \left( \mathbf{v}_F \cdot \mathbf{n}_\Gamma \right)^2 - \left( \mathbf{v}_F \cdot \mathbf{n}_\Gamma \right) \left( n^F \, \mathbf{v}_F + n^S \, \mathbf{v}_S \right) \cdot \mathbf{n}_\Gamma \rrbracket . \tag{6.45}$$

Hence, we have obtained the boundary conditions (6.35), (6.44), and (6.45) at the interface between two contacting fluid-saturated porous bodies provided they share the same pore fluid. This set of boundary conditions must be completed by relation (6.23) accounting for normal solid-skeleton contact at the interface.

However, in order to emphasize more the effects caused by the fluid percolation, we bring the above conditions in a more transparent shape. Therefore, it is expedient to introduce the volumetric average velocity of the biphasic mixture as

$$\mathbf{v} := n^F \mathbf{v}_F + n^S \mathbf{v}_S \,, \quad \text{where} \quad \llbracket \mathbf{v} \rrbracket \cdot \mathbf{n}_\Gamma = 0 \tag{6.46}$$

is apparent from $(6.35)_2$. Using (6.46), the fluid velocity $\mathbf{v}^F$ can be eliminated from (6.44) and (6.45), so that by means of the relations

$$\llbracket \mathbf{v}_F \cdot \mathbf{n}_\Gamma \rrbracket = \left( \mathbf{v}_F^+ - \mathbf{v}_F^- \right) \cdot \mathbf{n}_\Gamma = \left\llbracket \frac{1}{n^F} \right\rrbracket \left( \mathbf{v} - \mathbf{v}_S \right) \cdot \mathbf{n}_\Gamma \,,$$

$$\tfrac{1}{2} \left( \mathbf{v}_F^+ + \mathbf{v}_F^- \right) \cdot \mathbf{n}_\Gamma = \left\langle \frac{1}{n^F} \right\rangle \left( \mathbf{v} - \mathbf{v}_S \right) \cdot \mathbf{n}_\Gamma \,, \tag{6.47}$$

after some algebraic transformations, we obtain

$$\llbracket p \rrbracket = -\rho^{FR} \left\llbracket \frac{1}{n^F} \right\rrbracket \left( \mathbf{v} - \mathbf{v}_S \right) \cdot \mathbf{n}_\Gamma \left( \left\langle \frac{1}{n^F} \right\rangle \left( \mathbf{v} - \mathbf{v}_S \right) \cdot \mathbf{n}_\Gamma - \mathbf{v}_S \cdot \mathbf{n}_\Gamma \right) , \tag{6.48}$$

$$\llbracket \mathbf{T}_E^S \, \mathbf{n}_\Gamma \rrbracket \cdot \mathbf{n}_\Gamma = -\rho^{FR} \left\llbracket \frac{1}{n^F} \right\rrbracket \left( \mathbf{v} - \mathbf{v}_S \right) \cdot \mathbf{n}_\Gamma \left( \left\langle \frac{1}{n^F} \right\rangle \left( \mathbf{v} - \mathbf{v}_S \right) \cdot \mathbf{n}_\Gamma - \mathbf{v} \cdot \mathbf{n}_\Gamma \right) . \tag{6.49}$$

The influence of the pore-fluid flow in the above conditions becomes obvious by means of the identity (recall (6.4))

$$\mathbf{v} - \mathbf{v}_S = n^F \, \mathbf{w}_{FR} = \mathbf{w}_F \,. \tag{6.50}$$

Eventually, by combining (6.48) and (6.49), we arrive at a jump condition for the traction force normal to $\Gamma$ acting on the whole mixture $\varphi$:

$$\llbracket \left( -p \, \mathbf{I} + \mathbf{T}_E^S \right) \mathbf{n}_\Gamma \rrbracket \cdot \mathbf{n}_\Gamma = \rho^{FR} \left\llbracket \frac{1}{n^F} \right\rrbracket \left( \mathbf{w}_F \cdot \mathbf{n}_\Gamma \right)^2 . \tag{6.51}$$

It is worth noting that this relation could also be deduced from (6.36) exploiting $(6.35)_1$ in combination with (6.23), the effective stress principle (6.38), and the relation $(6.47)_1$.

## 6.4 Application to Specific Contact Situations

### 6.4.1 Quasi-Static Contact

In the dynamic case, the biphasic TPM model under consideration incorporates four independent fields, namely the solid displacement and velocity $\mathbf{u}_S$ and $\mathbf{v}_S$, the seepage velocity

$\mathbf{w}_{FR}$, as well as the effective pore-fluid pressure $p$. Proceeding from quasi-static conditions associated with $(\mathbf{v}_\alpha)'_\alpha = \mathbf{0}$, $\mathbf{v}_S = (\mathbf{u}_S)'_S$ does no more belong to the set of unknowns and, based on an admissible constitutive ansatz for the fluid momentum production, the seepage velocity can be explicitly computed from the fluid momentum balance and substituted into the other equations. Consequently, also $\mathbf{w}_{FR}$ looses the nature of an independent field variable, so that the number of degrees of freedom (DOFs) of the process as well as the number of associated conditional equations is reduced. More precisely, in porous media theories, the fluid percolation through the solid skeleton is generally governed by some constitutive filter law. For instance, neglecting the external body forces during contact, a convenient 3-d form of such a filter law is given by

$$\mathbf{w}_F = -\mathbf{K}^F \operatorname{grad} p \tag{6.52}$$

with $\mathbf{K}^F$ representing a specific permeability tensor (unit: $\mathrm{m^4/N\,s}$) which may depend on the deformable pore structure, the fluid properties, and also on the filter velocity to render the most relevant nonlinearities of a general non-Darcy filtration process (cf. [39]). In this context, it is moreover obvious from $(6.35)_1$ that

$$[\![-\mathbf{K}^F \operatorname{grad} p]\!] \cdot \mathbf{n}_\Gamma = 0 \,. \tag{6.53}$$

Inserting (6.52) in the traction jump relation (6.51) of the mixture, together with the continuity conditions (6.23) and (6.53), one ends up with the boundary conditions for quasi-static porous media contact in displacement-pressure formulation. It should be noted that the $\mathbf{u}_S$-$p$ formulation allows for an efficient numerical treatment within the mixed Finite Element Method (FEM).

## 6.4.2 Contact of Identical Porous Bodies

From (6.48) and (6.49) or (6.51), respectively, it is easy to note that for the case of contact of two identical porous bodies, the jump conditions simplify to continuity conditions for the pore-fluid pressure and the normal component of the solid stress vector or of the overall traction vector, respectively, because $[\![1/n^F]\!] = 0$, and consequently, the right-hand sides of (6.48), (6.49), and (6.51) vanish:

$$[\![p]\!] = 0 \,, \quad [\![\mathbf{T}_E^S \mathbf{n}_\Gamma]\!] \cdot \mathbf{n}_\Gamma = 0 \,, \quad [\![(-p\,\mathbf{I} + \mathbf{T}_E^S)\,\mathbf{n}_\Gamma]\!] \cdot \mathbf{n}_\Gamma = 0 \,. \tag{6.54}$$

The above continuity conditions for the pore pressure and the normal component of the solid stress vector can also be obtained by a priori neglecting the products of the constituent velocities in (6.44) and (6.45). Doing so, one recovers the results of Hou *et al.* [27].

## 6.4.3 Contact of a Porous Body with a Bulk Medium

The derived boundary conditions at the interface between two fluid-saturated porous solids given by (6.23), $(6.46)_2$, (6.48), and (6.49) remain also valid at the interface between a biphasic porous medium and a bulk fluid. It is only required that both the pore fluid and

the bulk fluid are the same substance. In this case one simply has to set $(n^F)^- = 1$ (pure fluid) in the respective relations with the superscript $-$ indicating the side of the bulk fluid.

However, if we consider the contact between a porous medium and a bulk solid body, the associated boundary conditions cannot be obtained directly as some of the quantities appearing in the jump relations have no physical meaning for a dense solid material. For the separate treatment of this contact problem let $-$ now indicate the solid bulk body, so that $+$ as before denotes the porous counterpart of the contacting couple. In order to derive the relevant boundary conditions, we return to relations $(6.35)_1$, $(6.36)$, and $(6.37)$. By setting $(n^F)^- = 0$, which implies $(n^S)^- = 1$ (pure solid), in $(6.35)_1$, we arrive at

$$(n^F)^+ \, \mathbf{w}_{F\Gamma}^+ \cdot \mathbf{n}_\Gamma = \mathbf{w}_F^+ \cdot \mathbf{n}_\Gamma = 0 \,. \tag{6.55}$$

The physical meaning of $(6.55)$ is merely the absence of fluid flux through the contact interface. This sounds reasonable as dense, non-porous solids are impenetrable for fluids making $(6.52)$ needless. Note that by virtue of $(6.42)$, it is moreover apparent that $\mathbf{v}_F^+ \cdot \mathbf{m}_\Gamma = 0$. Next, inserting $(6.55)$ into $(6.36)$ or $(6.37)$ finally yields

$$-p^+ \mathbf{n}_\Gamma + (\mathbf{T}_E^S)^+ \mathbf{n}_\Gamma = \mathbf{T}^- \mathbf{n}_\Gamma \tag{6.56}$$

with $\mathbf{T}^-$ denoting the Cauchy stress tensor of the bulk solid.

## 6.5   Conclusions and Discussion

In this chapter, we derived the contact conditions at the interface between two fluid-saturated porous bodies on the basis of a discontinuity analysis. The theoretical treatment has been carried out within the framework of the Theory of Porous Media (TPM), a well-established continuum model for the description of porous solid behavior. However, following this macroscopic approach, the microtopography of the contact surface is not distinguished. More precisely, the surface microstructure of the contacting porous boundaries is only taken into account by limit boundary values of the volume fractions in the sense of an average macrocharacteristic of the real surface topography. In this regard, it is perspective to investigate more accurate descriptions of the surface topography in porous media contact and to find significant surface characteristics both on the micro and the macro level.

Two of the four derived contact conditions are simple continuity conditions, namely for the solid-phase velocity and the seepage velocity normal to the contact interface, while the two others represent jump conditions, namely for the pore-fluid pressure and the effective normal stress of the solid skeleton. Alternatively, the latter can be combined in a single jump relation for the normal traction on the entire mixture. The discontinuities are caused by the penetration of the pore fluid from one porous body into the other, which is associated with an exchange of momentum and energy due to the mutual fluid mass interchange. The order of the jumps is thereby defined by products of the constituent velocities. By neglecting these terms, one recovers the boundary conditions usually used

in the related literature. However, for the derivation of the boundary conditions some restrictions have been imposed. In detail, the contacting porous bodies were assumed to be saturated by the same pore fluid, which is actually not a rigorous simplification as it holds for the majority of conceivable porous media contact problems. Besides that dissipative effects at the contact interface have been neglected, thus remaining some area of unexplored space for further investigations.

## 6.6　References

[1] Alazmi, B. & Vafai, K.: Analysis of fluid flow and heat transfer interfacial conditions between a porous medium and a fluid layer. *International Journal of Heat and Mass Transfer* **44** (2001), 1735–1749.

[2] Alts, T. & Hutter, K.: Continuum description of the dynamics and thermodynamics of phase boundaries between ice and water. Parts I and II. *Journal of Non-Equilibrium Thermodynamics* **13** (1988), 221–280.

[3] Armstrong, C. G.; Lai, W. M. & Mow, V. C.: An analysis of the unconfined compression of articular cartilage. *ASME Journal of Biomechanical Engineering* **106** (1984), 165–173.

[4] Ateshian, G. A.: A theoretical formulation for boundary friction in articular cartilage. *ASME Journal of Biomechanical Engineering* **119** (1997), 81–86.

[5] Ateshian, G. A.; Lai, W. M.; Zhu, W. B. & Mow, V. C.: An asymptotic solution for two contacting biphasic cartilage layers. *Journal of Biomechanics* **27** (1994), 1347–1360.

[6] Beavers, G. S. & Joseph, D. D.: Boundary conditions at a naturally permeable wall. *Journal of Fluid Mechanics* **30** (1967), 197–207.

[7] Biot, M. A.: General theory of three-dimensional consolidation. *Journal of Applied Physics* **12** (1941), 155–164.

[8] Bishop, A. W.: The effective stress principle. *Teknisk Ukeblad* **39** (1959), 859–863.

[9] de Boer, R.: *Trends in Continuum Mechanics of Porous Media.* Springer, Dordrecht 2005.

[10] de Boer, R. & Ehlers, W.: *Theorie der Mehrkomponentenkontinua mit Anwendung auf bodenmechanische Probleme.* Forschungsberichte aus dem Fachbereich Bauwesen, Heft 40, Universität-GH-Essen 1986.

[11] de Boer, R. & Ehlers, W.: The development of the concept of effective stresses. *Acta Mechanica* **83** (1990), 77–92.

[12] Bowen, R. M.: Theory of mixtures. In Eringen, A. C. (ed.): *Continuum Physics.* Academic Press, New York 1976, vol. III, pp. 1–127.

[13] Bowen, R. M.: Incompressible porous media models by use of the theory of mixtures. *International Journal of Engineering Science* **18** (1980), 1129–1148.

[14] Bowen, R. M.: Compressible porous media models by use of the theory of mixtures. *International Journal of Engineering Science* **20** (1982), 697–735.

[15] Cieszko, M. & Kubik, J.: Derivation of matching conditions at the contact surface between fluid-saturated porous solid and bulk fluid. *Transport in Porous Media* **34** (1999), 319–336.

[16] Coussy, O.: *Mechanics of Porous Continua.* John Wiley & Sons, Chichester 1995, 2nd edn.

[17] Drumheller, D. S.: The theoretical treatment of a porous solid using a mixture theory. *International Journal of Solids and Structures* **14** (1978), 441–456.

[18] Dunbar Jr., W. L.; Ün, K.; Donzelli, P. S. & Spilker, R. L.: An evaluation of three-dimensional diarthrodial joint contact using penetration data and the finite element method. *ASME Journal of Biomechanical Engineering* **123** (2001), 333–340.

[19] Ehlers, W.: *Poröse Medien – ein kontinuumsmechanisches Modell auf der Basis der Mischungstheorie.* Habilitation, Forschungsberichte aus dem Fachbereich Bauwesen, Heft 47, Universität-GH-Essen 1989.

[20] Ehlers, W.: Grundlegende Konzepte in der Theorie Poröser Medien. *Technische Mechanik* **16** (1996), 63–76.

[21] Ehlers, W.: Foundations of multiphasic and porous materials. In Ehlers, W. & Bluhm, J. (eds.): *Porous Media: Theory, Experiments and Numerical Applications.* Springer-Verlag, Berlin 2002, pp. 3–86.

[22] Ehlers, W.; Graf, T. & Ammann, M.: Deformation and localization analysis of partially saturated soil. *Computer Methods in Applied Mechanics and Engineering* **193** (2004), 2885–2910.

[23] Ehlers, W. & Markert, B.: A linear viscoelastic biphasic model for soft tissues based on the Theory of Porous Media. *ASME Journal of Biomechanical Engineering* **123** (2001), 418–424.

[24] Fisher-Cripps, A. C.: *Introduction to Contact Mechanics.* Mechanical Engineering Series, Springer-Verlag, New York 2000.

[25] Gibson, R. E.; England, G. L. & Hussey, M. J. L.: The theory of one-dimensional consolidation of saturated clays. *Géotechnique* **17** (1967), 261–273.

[26] Hadamard, J.: *Leçons sur la propagation des ondes et les equations de l'hydrodynamique.* Chelsea, New York 1949, reprint of Herman, Paris 1903.

[27] Hou, J. S.; Holmes, M. H.; Lai, W. M. & Mow, V. C.: Boundary conditions at the cartilage-synovial fluid interface for joint lubrication and theoretical verifications. *ASME Journal of Biomechanical Engineering* **111** (1989), 78–87.

[28] Hou, J. S.; Mow, V. C.; Lai, W. M. & Holmes, M. H.: An analysis of the squeeze-film lubrication mechanism for articular cartilage. *Journal of Biomechanics* **25** (1992), 247–259.

[29] Irschik, H.: On the necessity of surface growth terms for the consistency of jump relations at a singular surface. *Acta Mechanica* **162** (2003), 195–211.

[30] Johnson, K. L.: *Contact Mechanics.* Cambridge University Press 1985.

[31] Kelly, P. D.: A reacting continuum. *International Journal of Engineering Science* **2** (1964), 129–153.

[32] Kosinski, W.: *Field singularities and wave analysis in continuum mechanics.* Ellis Horwood, Chichester 1986.

[33] Lai, W. M.; Hou, J. S. & Mow, V. C.: A triphasic theory for the swelling and deformation behaviors of articular cartilage. *ASME Journal of Biomechanical Engineering* **113** (1991), 245–258.

[34] Lewis, R. W. & Schrefler, B. A.: *The Finite Element Method in the Static and Dynamic Deformation and Consolidation of Porous Media.* John Wiley & Sons, Chichester 1998, 2nd edn.

[35] Mahnkopf, D.: *Lokalisierung fluidgesättigter poröser Festkörper bei finiten elastoplastischen Deformationen.* Dissertation, Bericht Nr. II-5 aus dem Institut für Mechanik (Bauwesen), Universität Stuttgart, Germany 2000.

[36] Mak, A. F.: Unconfined compression of hydrated soft viscoelastic tissues: a biphasic poroviscoelastic analysis. *Biorheology* **23** (1986), 371–383.

[37] Mak, A. F.; Lai, W. M. & Mow, V. C.: Biphasic indentation of articular cartilage – Part 1: Theoretical analysis. *Journal of Biomechanics* **20** (1987), 703–714.

[38] Markert, B.: *Porous Media Viscoelasticity with Application to Polymeric Foams.* Dissertation, Report No. II-12 of the Institute of Applied Mechanics (CE), Universität Stuttgart, Germany 2005.

[39] Markert, B.: A constitutive approach to 3-d nonlinear fluid flow through finite deformable porous continua. *Transport in Porous Media* **70** (2007), 427–450.

[40] Morland, L. W. & Gray, J. M. N. T.: Phase change interactions and singular fronts. *Continuum Mechanics and Thermodynamics* **7** (1995), 387–414.

[41] Morland, L. W. & Sellers, S.: Multiphase mixtures and singular surfaces. *International Journal of Non-Linear Mechanics* **36** (2001), 131–146.

[42] Mow, V. C.; Kuei, S. C.; Lai, W. M. & Armstrong, C. G.: Biphasic creep and stress relaxation of articular cartilage: theory and experiments. *ASME Journal of Biomechanical Engineering* **102** (1980), 73–84.

[43] Mow, V. C.; Kwan, M. K.; Lai, W. M. & Holmes, M. H.: A finite deformation theory of linearly permeable soft hydrated tissues. In Schmid-Schönbein, G. W.; Woo, S. L.-Y. & Zweifach, B. W. (eds.): *Frontiers in Biomechanics.* Springer-Verlag, New York 1986, pp. 73–84.

[44] Rajagopal, K. R.; Wineman, A. S. & Gandhi, M.: On boundary conditions for a certain class of problems in mixture theory. *International Journal of Engineering Science* **24** (1986), 1453–1463.

[45] Richardson, S.: A model of the boundary condition of a porous material. Part 2. *Journal of Fluid Mechanics* **49** (1971), 327–336.

[46] Shillor, M.; Sofonea, M. & Telega, J. J.: *Models and Analysis of Quasistatic Contact: Variational Methods.* Lecture Notes in Physics, Springer, Berlin 2004.

[47] Skempton, A. W.: Significance of Terzaghi's concept of effective stress (Terzaghi's discovery of effective stress). In Bjerrum, L.; Casagrande, A.; Peck, R. B. & Skempton, A. W. (eds.): *From Theory to Practice in Soil Mechanics.* John Wiley & Sons, New York 1960, pp. 42–53.

[48] Slattery, J. C.: *Interfacial transport phenomena.* Springer-Verlag, New York 1990.

[49] Taylor, G. I.: A model of the boundary condition of a porous material. part 1. *Journal of Fluid Mechanics* **49** (1971), 319–326.

[50] Ün, K. & Spilker, R. L.: A penetration-based finite element method for hyperelastic tissues in contact: Part1 – Derivation of contact boundary conditions. *ASME Journal of Biomechanical Engineering* **128** (2006), 124–130.

[51] Williams, W. O.: Constitutive equations for flow of an incompressible viscous fluid through a porous medium. *Quarterly of Applied Mathematics* **128** (1978), 255–267.

[52] Wriggers, P.: *Computational Contact Mechanics.* John Wiley & Sons, Chichester 2002.

[53] Wu, J. Z.; Herzog, W. & Epstein, M.: An improved solution for the contact of two biphasic cartilage layers. *Journal of Biomechanics* **30** (1997), 371–375.

# 7 An Extended Biphasic Model for Charged Hydrated Tissues

## SUMMARY

Finite element models for hydrated soft biological tissue are numerous but often exhibit certain essential deficiencies concerning the reproduction of relevant mechanical and electro-chemical responses. As a matter of fact, singlephasic models can never predict the interstitial fluid flow or related effects like osmosis. Quite a few models have more than one constituent, but are often restricted to the small-strain domain, are not capable of capturing the intrinsic viscoelasticity of the solid skeleton, or do not account for a collagen fiber reinforcement.

It is the goal of this contribution to overcome these drawbacks and to present a thermodynamically consistent model, which is formulated in a very general way in order to reproduce the behavior of almost any charged hydrated tissue. Herein, the Theory of Porous Media (TPM) is applied in combination with polyconvex Ogden-type material laws describing the anisotropic and intrinsically viscoelastic behavior of the solid matrix on the basis of a generalized Maxwell model. Moreover, other features like the deformation-dependent permeability, the possibility to include inhomogeneities like varying fiber alignment and behavior, or osmotic effects based on the simplifying assumption of Lanir are also included.

Finally, the human intervertebral disc is chosen as a representative for complex soft biological tissue behavior. In this regard, two numerical examples will be presented with focus on the viscoelastic and osmotic capacity of the model.

## 7.1 Introduction and Overview

Finite element models of hydrated soft biological tissues can remarkably aid the design of new implants, thereby serving as a diagnostic tool or numerical laboratory. In the context of spine mechanics, the intervertebral disc (IVD) plays a key role, as it is a representative for complex soft biological tissue behavior dominating the overall mechanical performance of the spine. Hence, the IVD is chosen for the development of a general model describing several relevant effects.

Note in passing that in industrialized western countries, almost everybody has been suffering from low back pain (LBP) at least once in his lifetime, e. g., in a representative survey carried out in the early nineties and another one conducted ten years later, about 85 % of the German population had already experienced this widespread disease Raspe *et al.* [74], Schmidt *et al.* [80]. Moreover, LBP is the number one cause of work related

health problems in many European countries. The fourth European survey on working conditions in 2007 reported an overall average of 25 % of the working people in Europe suffering from LBP, cf. Parent-Thirion *et al.* [73]. This clearly reveals the need for research in the field of IVD mechanics, in order to better understand the complex, coupled behavior of the IVD and its influence on the overall performance.

Before discussing the features of an appropriate finite element model, a short overview of the necessary tissue properties is given. For a more detailed description, the reader is referred to Urban & Roberts [96], Ayad & Weiss [3], Mow & Hayes [69], Marchand & Ahmed [63], Ehlers *et al.* [31] and references therein. As the name implies, the IVD is embedded in between two vertebrae, where the cartilaginous endplates build the transition between the disc and the bony vertebrae but will not be addressed separately in this contribution. Two main regions can be distinguished in an axial cut through the IVD, a gelatinous core, the nucleus pulposus (NP) enclosed by a fibrous, lamellar structure, the anulus fibrosus (AF). Both regions are composed of a porous multi-component microstructure consisting of a charged, hydrated extracellular matrix (ECM) as well as an ionized interstitial fluid yielding a swelling-active material. The ECM, also referred to as solid skeleton, consists of proteoglycans (PGs), glycosaminoglycans (GAGs), and collagen fibers of type I and II saturated by a liquid containing dissolved anions and cations as solutes. In this regard, the collagen of type I forms large parallel fiber bundles representing the structural collagen in the AF, whereas the collagen of type II is distributed statistically equal, thereby forming a loose network of fibrils contributing to the isotropic behavior of the NP. The relatively large PGs and GAGs carry negative fixed charges, but cannot move freely as they are trapped in the fine collagen network. Thus, the fixed negative charges underly the same movement as the whole solid matrix. Apart from that, the fixed charge density (FCD) is highest in the NP and lowest at the perimeter of the AF, cf. Iatridis *et al.* [47], Urban & Holm [95] or Urban & Roberts [96]. Moreover, the structural collagen is inhomogeneously distributed throughout the AF concerning its alignment as well as its occurrence yielding varying mechanical properties of the lamellae, cf. Holzapfel *et al.* [44], Eberlein *et al.* [18], Ebara *et al.* [17] or Skaggs *et al.* [87]. Finally, the IVD is characterized by a coupled dissipative behavior resulting from the viscous fluid flow, the intrinsic viscoelasticity of the ECM protein meshwork and the resulting swelling phenomena, see, e.g., Ehlers & Markert [28], Ehlers *et al.* [29] or Iatridis *et al.* [48, 50] and references therein. Thus, all the properties characterizing soft biological tissues in general are unified within the IVD.

Currently, there are several models and modules available, which are used to describe soft biological tissues in general. However, most of them do not cover all the requirements needed for the continuum mechanical modeling of the IVD. For example, the models used for state-of-the-art simulations of the spine are often restricted to singlephasic materials, thereby *a priori* excluding effects resulting from interstitial fluid flow and osmosis. The first spine simulations with an advanced IVD model were carried out by Shirazi-Adl [83, 84] or Shirazi-Adl *et al.* [85, 86] using a deformation-dependent Hooke-type material tangent and non-linear spring elements to capture the collagen fibers in the AF. In order to overcome the resulting grid dependency of the alignment of the spring elements, the anisotropic continuum theory based on Spencer [89, 90] and Boehler [9] was adopted and applied to the unique behavior of the collagen fibers by, e.g., Klisch & Lotz [53], Elliott

& Setton [33] or Holzapfel & Gasser [42], whereas Schröder & Neff [81], Balzani *et al.*
[6] or Markert *et al.* [66] further developed the theory towards a polyconvex framework.
This knowledge was then incorporated in the lumbar spine simulations of Eberlein *et al.*
[18, 19].

Since these models are singlephasic, they do not account for the fluid flow in the disc
which is important for nutritional purposes and maintaining the biological composition,
see, e.g., Holm & Nachemson [41] or Urban & Holm [95]. Hence, at least a second phase,
the interstitial fluid, has to be introduced to overcome this deficiency. In this context,
several biphasic models, based on the works of Biot [7], Bowen [11] and Mow *et al.* [70],
are applied to describe soft biological tissues in general or with application to the IVD,
see, e.g., Argoubi & Shirazi-Adl [1], Iatridis *et al.* [49], Klisch & Lotz [54], Ayotte *et al.*
[4], Li *et al.* [60, 61] or Riches *et al.* [76]. However, as the occurring osmotic effects
influence the fluid flow in the tissue, it also has to be considered. In order to include
these electro-chemomechanically driven swelling phenomena, the biphasic models need to
be extended which can be accomplished in two different approaches. On the one hand,
there is the independent description of the freely movable ions of the pore fluid yielding a
complex and strongly coupled system of partial differential equations (PDEs) leading to
a difficult numerical treatment, cf. Frijns *et al.* [36, 37], Ehlers *et al.* [29], Huyghe *et al.*
[46], Kaasschieter *et al.* [51], Lai *et al.* [55], van Loon *et al.* [97] or Sun *et al.* [92]. On
the other hand, a much simpler algorithm capable of describing osmosis is based on the
assumption of an instantaneous chemical equilibrium throughout the domain of the IVD,
cf. Lanir [57]. Following this, only the solid skeleton is extended by the almost volume-
free, fixed negative charges and a constitutively computed osmotic pressure is added to
the hydrostatic pressure. This procedure is adopted in the context of a two-phase model
by Laible *et al.* [56], Iatridis *et al.* [47], Hsieh *et al.* [45] or Ehlers *et al.* [31]. A comparison
of the two approaches yields a good approximation of the exact solution for the simplified
model, even when simulating sudden concentration changes in the external solution, cf.
Wilson *et al.* [101]. However, as sudden changes in the surrounding concentration are
usually not applicable for living organisms, Lanir's assumption is perfectly suitable for
the numerical simulation of the IVD for instance.

Most of the models in the above cited works suffer from the limitation to the small strain
domain with often purely elastic material behavior. In contrast, the solid skeleton of soft
biological tissues or cartilage emerges intrinsic viscoelastic properties, see, e.g., Hayes &
Bodine [40] and Ehlers & Markert [28] among others. In this regard, it is still not clear,
to what extent intrinsic viscoelastic effects stem from the proteoglycans, the loose (type
II) collagen network, or the structural (type I) collagen. In this contribution, only the
isotropic part of the solid matrix including the randomly distributed type II collagen is
modeled to be viscoelastic, while the structural collagen fibers of type I remain hyper-
elastic. The reason for this assumption becomes clear when the findings of Holzapfel *et al.*
[44] are observed, stating that there was little to no rate dependency when a lamella of
the AF is pulled in fiber direction. Hence, the dissipative effects must stem from the
isotropic part of the matrix.

Moreover, the efficient numerical treatment of the governing equations is often not imple-
mented, and therefore, the presented numerical exames are restricted to rather simple 1-d

and 2-d boundary-value problems (BVP), respectively. Thus, the goal of this contribution is to present a thermodynamically consistent model based on the well-founded Theory of Porous Media (TPM), cf. Bowen [12], Mow *et al.* [68], de Boer [10] and Ehlers [23], which is suitable for the simulation of any electro-chemically active soft biological tissues in general and the IVD in particular. In addition, the respective constitutive equations needed to include the anisotropic and viscoelastic material behavior as well as the osmotic pressure are presented in a modular manner allowing for a convenient handling. Finally, the efficiency of the model is shown by two fully coupled 3-d simulations. Firstly, a torsional shear experiment is used to fit the viscoelastic parameters to the experimental findings of Iatridis *et al.* [48], which are then taken for a swelling experiment of the nucleus pulposus in an *ex vivo* sagittally cut IVD.

## 7.2   Theory of Porous Media (TPM)

The TPM, originally designed for geotechnical problems, is a well-founded macroscopic continuum theory, which is based on the theory of mixtures extended by the concept of volume fractions, cf. Bowen [12], Mow *et al.* [68], de Boer [10] and Ehlers [23]. In the case of a liquid-saturated linear elastic and quasi-static material behavior in the small strain domain, the TPM results in the same set of equations as the theory of Biot [7], cf. Schanz & Diebels [79]. However, when extended to finite deformations with varying porosity in combination with arbitrary, non-linear dissipative material laws, the TPM offers a transparent theoretical access regarding the separation of the balance and constitutive equations. In contrast to Biot's constitutively derived theory, the TPM approach allows for a clear identification of materially independent equations (i. e. balance equations) and so-called constitutive equations characterizing the material behavior (i. e. viscoelasticity, anisotropy or osmosis), thereby ensuring a convenient modular character of the overall theoretical framework.

Proceeding from a binary aggregate composed of solid and fluid constituents $\varphi^\alpha$ denoted by $\alpha = \{S, F\}$, the solid phase (i. e. the ECM consisting of PGs, GAGs and collagen) is extended by incorporating the almost volume-free fixed negative charges $\varphi^{fc}$ (cf. Figure 7.1). Furthermore, the interstitial fluid $\varphi^F$ as an ionic solution is composed of water as a liquid solvent $\varphi^L$ and mobile electrolytes ($Na^+Cl^-$) as solutes $\varphi^+$ and $\varphi^-$. In this context, it is assumed that all constituents $\varphi^\alpha$ are statistically equal distributed throughout a representative elementary volume (REV). Hence, a real or a virtual averaging process over the REV is possible finally leading to a model of superimposed and interacting continua, i. e., the homogenized or 'smeared' model.

Following this leads to a quadriphasic model describing each of the solutes $\varphi^+$ and $\varphi^-$ independently, cf. Frijns *et al.* [36]. Exploiting the electroneutrality condition allows for a reduction to a triphasic model yielding a decrease of the primary variables from four to three (i. e. the solid displacement, the hydraulic pressure and the cation concentration) as is described in, e. g., Ehlers *et al.* [29, 30]. However, the first benchmark computations on simple geometries using the triphasic displacement-pressure-concentration formulation were accompanied by oscillations and a general numerical instability, cf. Ehlers &
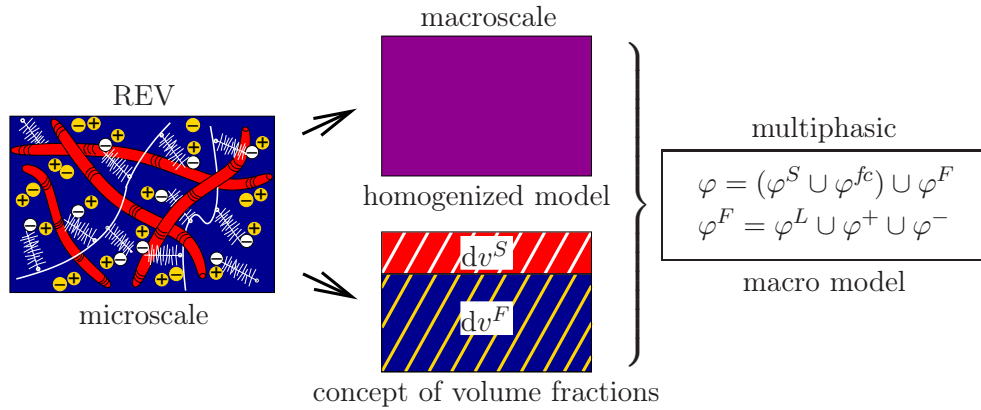
**Figure 7.1:** *Multicomponent TPM model of charged hydrated biological tissues.*

Acartürk [24]. The cause of the oscillations can be traced back to the dependence of the concentration boundary condition (BC) on the solution of the solid displacement field inside the domain. A numerical stabilization is only possible if the BC is weakly fulfilled and included in the iteration process, cf. Ehlers *et al.* [30]. Hence, an alternative modeling ansatz must be applied, bearing in mind that future simulations of the intensely inhomogeneous, anisotropic IVD (including the much stiffer, adjacent vertebrae) already evolve several other numerical difficulties. Note in passing, that other triphasic theories which exhibit four primary degrees of freedom, i.e., solid displacement and 3 modified chemical potentials for water, cations and anions, do not suffer from these oscillations, cf. Lai *et al.* [55], Sun *et al.* [92].

As already mentioned in the introduction, it is possible to further reduce this model by applying the assumption of Lanir [57] stating that the tiny mobile ions are assumed to diffuse rapidly through the liquid and by themselves, do not give rise to concentration gradients. In the context of living soft biological tissues, such as the IVD, this simplification makes sense because sudden concentration changes of the surrounding fluid yielding large perturbations of the chemical equilibrium do not occur. Hence, the soft biological tissue is always immediately in electro-chemical equilibrium, which allows the application of the Donnan [16] equilibrium not only at the domain boundary but also in the inside. The arising osmotic properties can therefore be sufficiently described without considering the ion concentrations (or electro-chemical potentials) as additional unknowns of the process. The resulting osmotic pressure is simply computed via a constitutive equation depending on the fixed charge density inside the domain and added to the hydraulic pore pressure. The result is an extended biphasic formulation consisting of a fully saturated solid skeleton carrying volume-free fixed negative charges and an incompressible pore fluid.

In this context, the volume fractions $n^\alpha = \mathrm{d}v^\alpha/\mathrm{d}v$ (partial volume $\mathrm{d}v^\alpha$ per bulk volume $\mathrm{d}v$) serve as describing physical quantities consistent with the saturation constraint

$$\sum_\alpha n^\alpha = n^S + n^F = 1\,, \qquad \text{where} \qquad n^{fc} \approx 0\,. \tag{7.1}$$

Exploiting the definition of the volume fractions $n^\alpha$, a partial density $\rho^\alpha = \mathrm{d}m^\alpha/\mathrm{d}v$ (constituent mass $m^\alpha$) and a material or realistic density $\rho^{\alpha R} = \mathrm{d}m^\alpha/\mathrm{d}v^\alpha$ can be defined

for each constituent $\varphi^\alpha$, which are related to each other via

$$\rho^\alpha = n^\alpha \rho^{\alpha R}. \tag{7.2}$$

The kinematics for such an ansatz is based on the framework of superimposed continua, where each spatial point $\mathbf{x}$ of the current configuration is at any time $t$ simultaneously occupied by material points $P^\alpha$ of all constituents. Following this, all particles proceed from different reference positions $\mathbf{X}_\alpha$, which leads to individual motion and velocity fields for each constituent reading

$$\mathbf{x} = \boldsymbol{\chi}_\alpha(\mathbf{X}_\alpha, t) \qquad \text{and} \qquad \overset{\prime}{\mathbf{x}}_\alpha = \frac{\mathrm{d}\boldsymbol{\chi}_\alpha(\mathbf{X}_\alpha, t)}{\mathrm{d}t}, \tag{7.3}$$

respectively. Therein, $(\,\cdot\,)'_\alpha$ denotes the material time derivative following the motion of $\varphi^\alpha$. Describing multiphasic materials, it is convenient to express the solid in a Lagrangean setting via the displacement vector $\mathbf{u}_S = \mathbf{x} - \mathbf{X}_S$ and the overall fluid in a modified Eulerian setting relative to the deforming solid skeleton through the seepage velocity $\mathbf{w}_F = \overset{\prime}{\mathbf{x}}_F - \overset{\prime}{\mathbf{x}}_S$. Furthermore, the fixed charges are assumed to move with the deforming solid skeleton described by the solid deformation gradient given by $\mathbf{F}_S = \partial \mathbf{x}/\partial \mathbf{X}_S$.

## 7.3   Balance Relations

Materially independent balance equations are needed to solve for the previously introduced unknown field quantities, i. e., the solid displacement $\mathbf{u}_S$ and the seepage velocity $\mathbf{w}_F$ as well as to restrict the necessary constitutive equations needed to close the set of equations. In this context, the mass and the momentum balances for each of the constituents are usually applied as well as the entropy inequality. Moreover, the model under consideration is assumed to be composed of materially incompressible constituents (defined by $\rho^{\alpha R} =$ const.), which is always valid for the case of soft biological tissues under physiological levels of pressure, cf. Bachrach *et al.* [5], yielding a reduction of the mass balance to a volume balance. Note in passing that the property of material incompressibility does not lead to a macroscopic incompressibility as the partial density $\rho^\alpha$ can still change through changes in the volume fraction $n^\alpha$, cf. equation (7.2). Furthermore, all thermal effects as well as internal mass productions are neglected in this contribution, thereby excluding any biochemical reactions and growth processes. Proceeding from quasi-static and isothermal conditions in accordance to Ehlers [23], the respective volume and momentum balances as well as the entropy inequality in the Clausius-Planck form for the solid and fluid constituents (denoted by $\alpha$) read

$$(n^\alpha)'_\alpha + n^\alpha \operatorname{div} \overset{\prime}{\mathbf{x}}_\alpha = 0\,,$$

$$\operatorname{div} \mathbf{T}^\alpha + \rho^\alpha \mathbf{b} + \hat{\mathbf{p}}^\alpha = \mathbf{0}\,, \tag{7.4}$$

$$\sum_\alpha \left( \mathbf{T}^\alpha \cdot \mathbf{L}_\alpha - \rho^\alpha (\psi^\alpha)'_\alpha - \hat{\mathbf{p}}^\alpha \cdot \overset{\prime}{\mathbf{x}}_\alpha \right) \geq 0\,.$$

Herein, $\mathbf{T}^\alpha$ is the partial Cauchy stress tensor and $\rho^\alpha \mathbf{b}$ is the body force. Furthermore, a measure for the produced interaction force of the fluid while it percolates through the pore

space is represented by the direct momentum production term $\hat{\mathbf{p}}^\alpha$ satisfying the conservation constraint $\hat{\mathbf{p}}^S + \hat{\mathbf{p}}^F = \mathbf{0}$. The spatial velocity gradient is denoted by $\mathbf{L}_\alpha = \operatorname{grad}\overset{\prime}{\mathbf{x}}_\alpha$, while $\psi^\alpha$ stands for the Helmholtz free energy. As usual for multi-component models, equations (7.4) are combined for the solid and the fluid phase yielding the respective set of governing equations for the overall aggregate in local form

$$\operatorname{div}\left[(\mathbf{u}_S)'_S + n^F \mathbf{w}_F\right] = 0\,,$$

$$\operatorname{div}\left(\mathbf{T}^S + \mathbf{T}^F\right) + \left(n^S \rho^{SR} + n^F \rho^{FR}\right)\mathbf{b} = \mathbf{0}\,, \tag{7.5}$$

$$\mathbf{T}^S\!\cdot\mathbf{L}_S - \rho^S\,(\psi^S)'_S + \mathbf{T}^F\!\cdot\mathbf{L}_F - \rho^F\,(\psi^F)'_F - \hat{\mathbf{p}}^F\!\cdot\mathbf{w}_F \geq 0\,,$$

where $\mathbf{T} := \mathbf{T}^S + \mathbf{T}^F$ defines the overall stress of the model, when lingering flow conditions are assumed inside the tissue.

In order to include the electro-chemical effects while the tissue is deforming, it is necessary to derive an equation describing the extensive change of the number of the fixed negative charges via an intensive concentration measure. As the fixed charges almost behave like dissolved ions when they are surrounded by a pore fluid, the molar concentration $c_m^{fc}$ of the fixed charges is introduced, relating the molar number of charges to the surrounding fluid volume. In this regard, we do not distinguish between the intra- and extrafibrillar fluid compartments and relate the fixed charges $\varphi^{fc}$ to the total local fluid volume knowing well that this may lead to an overestimate in the AF with its high collagen content, cf. Schröder *et al.* [82]. Following this, two different densities can be introduced for the fixed charges, one relating to the fluid volume, $\rho_F^{fc}$, and the other one relating to the overall volume of the aggregate, $\rho^{fc}$. Making use of the constant molar mass of a single fixed negative charge, i.e., the molar mass of an electron $M_m^{fc} \approx 5.486 \cdot 10^{-7}\,\mathrm{kg/mol}$, the following relations become obvious

$$\rho^{fc} =: n^F \rho_F^{fc} = n^F c_m^{fc} M_m^{fc}\,. \tag{7.6}$$

Bearing in mind that the fixed charges are attached to the solid skeleton and thus, undergo the same movement, the mass balance of the fixed charge density $\rho^{fc}$ is applied with respect to the deforming solid yielding

$$(\rho^{fc})'_S + \rho^{fc}\operatorname{div}\overset{\prime}{\mathbf{x}}_S \;= 0\,, \tag{7.7}$$

or after insertion of (7.6) and dividing by the constant molar mass $M_m^{fc}$

$$(n^F c_m^{fc})'_S + n^F c_m^{fc}\operatorname{div}\overset{\prime}{\mathbf{x}}_S \;= 0\,. \tag{7.8}$$

Following this, the volume balance $(7.4)_1$ of the solid skeleton for $\alpha = S$ as well as the mass balance (7.8) can be analytically integrated

$$\begin{aligned} n^S &= n_{0S}^S\,\det\mathbf{F}_S^{-1}\,,\\ c_m^{fc} &= c_{0S}^{fc}\,n_{0S}^F\,(\det\mathbf{F}_S - n_{0S}^S)^{-1} \end{aligned} \tag{7.9}$$

from an initial solidity $n_{0S}^S$, porosity $n_{0S}^F$, and molar concentration $c_{0S}^{fc}$, respectively. Herein, the latter relation can be understood as an evolution equation for the concentration of the fixed charges needed for the postulation of a constitutive equation used to compute the osmotic pressure contribution.

## 7.4  Constitutive Assumptions

In order to close the set of governing equations, certain constitutive assumptions for the Helmholtz free energies $\psi^\alpha$, the partial Cauchy stress tensors $\mathbf{T}^\alpha$ as well as the interaction term $\hat{\mathbf{p}}^F = -\hat{\mathbf{p}}^S$ need to be defined. In this regard, the chosen constitutive equations must reflect the material behavior in a best possible manner, thereby embracing anisotropic and viscoelastic effects, the viscous fluid flow as well as the electro-chemical couplings yielding the osmotic pressure contribution.

### 7.4.1  Saturation Constraint and Entropy Inequality

Proceeding from general thermodynamical considerations, cf. Ehlers [22], a Lagrangean multiplier $\mathcal{P}$ is introduced in the sense of an incompressibility constraint. This becomes clear, when the material time derivative of the saturation constraint (7.1) is taken with respect to the deforming solid. Utilization of $(7.4)_1$ yields a continuity-like condition

$$-\mathcal{P}\left[(n^S)'_S + (n^F)'_S\right] = \mathcal{P}\left[n^S \operatorname{div} \overset{'}{\mathbf{x}}_S + n^F \operatorname{div} \overset{'}{\mathbf{x}}_F + \operatorname{grad} n^F \cdot \mathbf{w}_F\right] = 0\,, \qquad (7.10)$$

which is then added to the Clausius-Planck inequality $(7.5)_3$ yielding

$$\begin{aligned}
(\mathbf{T}^S + n^S\,\mathcal{P}\,\mathbf{I}) \cdot \mathbf{L}_S - \rho^S\,(\psi^S)'_S + (\mathbf{T}^F + n^F\,\mathcal{P}\,\mathbf{I}) \cdot \mathbf{L}_F - \\
-\rho^F\,(\psi^F)'_F - (\hat{\mathbf{p}}^F - \mathcal{P}\operatorname{grad} n^F) \cdot \mathbf{w}_F \geq 0\,.
\end{aligned} \qquad (7.11)$$

Herein, use was made of the relation $\operatorname{div} \overset{'}{\mathbf{x}}_\alpha = \mathbf{L}_\alpha \cdot \mathbf{I}$, where $\mathbf{I}$ denotes the identity tensor. Hence, the partial quantities $\mathbf{T}^\alpha$ and $\hat{\mathbf{p}}^F$ are split into an undetermined part resulting from $\mathcal{P}$ and a so-called extra term $(\,\cdot\,)_E$ to be determined via appropriate constitutive equations, viz.:

$$\mathbf{T}^\alpha = -n^\alpha \mathcal{P}\,\mathbf{I} + \mathbf{T}^\alpha_E \qquad \text{and} \qquad \hat{\mathbf{p}}^F = \mathcal{P}\operatorname{grad} n^F + \hat{\mathbf{p}}^F_E\,. \qquad (7.12)$$

The overall Cauchy stress of the model is simply obtained by a summation of the partial stresses under utilization of (7.1) such that

$$\mathbf{T} = -\mathcal{P}\,\mathbf{I} + \mathbf{T}_E \qquad \text{with} \qquad \mathbf{T}_E = \mathbf{T}^S_E + \mathbf{T}^F_E\,, \qquad (7.13)$$

where according to Bishop [8] or Skempton [88], $\mathbf{T}_E$ is known as the effective or extra stress. Hence, $\mathcal{P}$ is easily identified as the unspecified hydraulic pore pressure, whereas the extra stress is purely governed by an electro-chemical contribution, the deformation state as well as the fluid viscosity and velocity.

### 7.4.2  Effective Stress of the Fluid and Solid Constituent

As a usual assumption in hydraulics, the fluid extra stress is neglected (i.e. $\mathbf{T}^F_E \approx \mathbf{0}$) in comparison with the extra momentum production term $\hat{\mathbf{p}}^F_E$, which is responsible for the

drag force resulting from the percolating fluid. This fact can be deduced from an order-of-magnitude analysis, see, e. g., Hassanizadeh & Gray [39], Ehlers *et al.* [25] or Markert [65] and quotations therein. Moreover, concerning the incompressible fluid constituent, it can be shown that the set of constitutive variables for the free energy function is empty, i. e., its free energy $\psi^F = \psi^F(\cdot)$ is constant, cf. Ehlers [23].

The remaining undetermined solid extra stress is then further split into an osmotic and a mechanical contribution. The reason for this split becomes clear, when the physical effect of the attached negative fixed charges of the ECM on the behavior of the overall tissue is analyzed. Herein, a phenomenon called osmosis is activated, which results in a spontaneous fluid movement across the tissue boundary. In this context, the fluid will flow from places with lower solute concentration to regions with higher concentrations, thereby dilating the tissue. As the incompressible fluid constituent is assumed to be non-sensitive to changes in porosity $n^F$, the volume dilatation is solely carried via tension in the solid matrix. This is due to the fact that an externally applied hydrostatic pore pressure is constant in an incompressible fluid, no matter how much space (i. e. $n^F$) is available for the pore-fluid. The osmosis-driven inflow of fluid takes place until it is balanced with the outflow of fluid resulting from the "squeezing force" of the dilated solid matrix. Finally, the tension in the ECM at osmotic equilibrium is then defined as the osmotic pressure difference $\Delta\pi$ contributing to the hydrostatic stress state. Thus, the solid extra stress is further split, viz.:

$$\mathbf{T}_E^S = \mathbf{T}_{E,\,\mathrm{OSM}}^S + \mathbf{T}_{E,\,\mathrm{MECH}}^S\,, \qquad \text{where} \qquad \mathbf{T}_{E,\,\mathrm{OSM}}^S = -\Delta\pi\,\mathbf{I}\,. \qquad (7.14)$$

Moreover, concerning the purely mechanical behavior of the anisotropic and viscoelastic ECM, another additive concept is assumed yielding

$$\mathbf{T}_{E,\,\mathrm{MECH}}^S = \mathbf{T}_{\mathrm{ISO}}^S + \mathbf{T}_{\mathrm{ANISO}}^S \qquad \text{with} \qquad \mathbf{T}_{\mathrm{ISO}}^S = \mathbf{T}_{\mathrm{EQ}}^S + \mathbf{T}_{\mathrm{NEQ}}^S\,, \qquad (7.15)$$

where the respective mechanical Cauchy stress is split into an isotropic (PGs, GAGs etc.) and an anisotropic (oriented collagen of type I) contribution. In this regard, the isotropic part is further split into equilibrium and non-equilibrium parts accounting for the intrinsic viscoelastic behavior of the isotopic fraction of the ECM.

## 7.4.3 Inelastic Solid Kinematics

In order to describe finite viscoelasticity, it is convenient to proceed from a generalized Maxwell model as depicted in Figure 7.2 and described in Ehlers *et al.* [29], Markert [64] or Reese & Govindjee [75], which accounts for the purely elastic equilibrium (EQ) stress via its elastic spring as well as for the non-equilibrium (NEQ) overstresses via the respective $n = 1, ..., N$ Maxwell branches. As usual in finite inelasticity, the model is constitutively based on a multiplicative split of the solid deformation gradient $\mathbf{F}_S = (\mathbf{F}_{Se})_n\,(\mathbf{F}_{Si})_n$ into inelastic deformations $(\mathbf{F}_{Si})_n$ operating between the reference and the stress-free intermediate configurations of the $n^{\mathrm{th}}$ Maxwell element as well as elastic deformations $(\mathbf{F}_{Se})_n$ connecting the respective $n^{\mathrm{th}}$ intermediate configuration with the actual frame. In this context, an additive decomposition of the resulting finite strain measures into elastic and
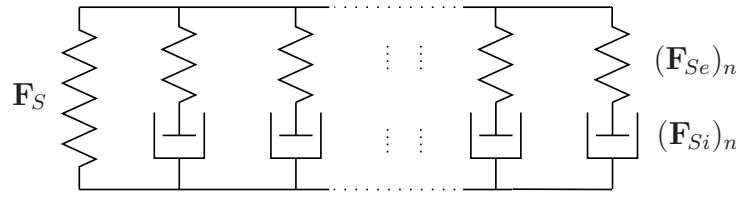
**Figure 7.2:** *Generalized Maxwell model composed of a spring-element and n Maxwell elements.*

inelastic parts is achieved, cf. Lee [59], Kleiber [52] or Ehlers [20, 21, 22]

$$\mathbf{E}_S = \tfrac{1}{2}\left(\mathbf{C}_S - \mathbf{I}\right), \quad (\mathbf{E}_{Si})_n = \tfrac{1}{2}\left[(\mathbf{C}_{Si})_n - \mathbf{I}\right],$$
$$(\mathbf{E}_{Se})_n = \mathbf{E}_S - (\mathbf{E}_{Si})_n = \tfrac{1}{2}\left[\mathbf{C}_S - (\mathbf{C}_{Si})_n\right], \tag{7.16}$$

directly reflecting the structure of the underlying rheological model given in Figure 7.2. Herein, $\mathbf{E}_S$, $(\mathbf{E}_{Si})_n$, and $(\mathbf{E}_{Se})_n$ are the respective total, inelastic and elastic Green-Lagrangean strains, which are defined in the reference configuration. Note in passing that

$$(\widehat{\boldsymbol{\Gamma}}_{Se})_n = (\mathbf{F}_{Si}^{T-1})_n\,(\mathbf{E}_{Se})_n\,(\mathbf{F}_{Si}^{-1})_n = \tfrac{1}{2}\left[(\widehat{\mathbf{C}}_{Se})_n - \mathbf{I}\right] \tag{7.17}$$

are the associate elastic strain measures defined on the intermediate configurations of the respective Maxwell branches, subsequently denoted by $(\widehat{\cdot})$, and can be computed via an inelastic push-forward of $(\mathbf{E}_{Se})_n$, cf. Ehlers [20, 21, 22]. In this regard, the intermediate configurations can be understood as the reference configurations of the springs in the Maxwell branches. Moreover, the respective right Cauchy-Green deformation tensors are defined as

$$\mathbf{C}_S = \mathbf{F}_S^T\,\mathbf{F}_S, \qquad (\widehat{\mathbf{C}}_{Se})_n = (\mathbf{F}_{Se}^T)_n\,(\mathbf{F}_{Se})_n, \qquad (\mathbf{C}_{Si})_n = (\mathbf{F}_{Si}^T)_n\,(\mathbf{F}_{Si})_n. \tag{7.18}$$

## 7.4.4 Entropy Principle for Viscoelastic Solid Skeleton

As a next step, the modified Clausius-Planck inequality (7.11) has to be evaluated in order to achieve rules for the computation of the solid extra stress as well as restrictions for the evolution equations of the internal variables. Proceeding from an incompressible fluid at thermodynamical equilibrium, i.e., $[\psi^F(\,\cdot\,)]'_F = 0$ and $\mathbf{T}_E^F \equiv \mathbf{0}$, respectively, the inequality (7.11) is evaluated using the conjugate pair of the solid stress power in the referential frame,

$$\mathbf{S}_E^S \cdot (\mathbf{E}_S)'_S - \rho_{0S}^S\,(\psi^S)'_S - \hat{\mathbf{p}}_E^F \cdot \mathbf{w}_F \geq 0, \tag{7.19}$$

where $\mathbf{S}_E^S$ is the 2nd Piola-Kirchhoff solid extra stress. Due to the fundamental principles of constitutive modeling, cf. Noll [71] and Truesdell [94], namely determinism, local action and equipresence, the solid Helmholtz free energy $\psi^S$ may depend on the solid deformation gradient $\mathbf{F}_S$ as well as on some 2nd-order structural tensors $\boldsymbol{\mathcal{M}}^S$ characterizing the kind of anisotropy. In view of the fact that the free energy can only be stored as an elastic potential in the spring elements, the non-equilibrium parts of the Maxwell elements have to depend on $(\mathbf{F}_{Se})_n$. Thus, the suggested split of $\psi^S$ yields osmotic $(\psi_{\text{OSM}}^S)$, equilibrium $(\psi_{\text{EQ}}^S)$,

and anisotropic $(\psi^S_{\text{ANISO}})$ contributions, each associated with the total deformation $\mathbf{F}_S$, as well as a non-equilibrium part $(\psi^S_{\text{NEQ}})$ explicitly depending on the elastic deformations $(\mathbf{F}_{Se})_n$ of the Maxwell branches, thereby including an implicit dependence on the internal variables $(\mathbf{F}_{Si})_n$, as the respective time-dependent dashpot deformations influence the elastic deformation gradient.

Recalling the arguments stemming from the concept of material frame indifference (objectivity), the respective deformation gradients are not admissible as process variables and have to be replaced by the set of deformation tensors (7.18), or according to (7.16) by the corresponding strain measures. Proceeding from the definition of a strain-energy function $W^S = \rho^S_{0S}\,\psi^S$ representing the stored elastic energy defined per unit reference volume, the stress power in the referential frame evolves as

$$(W^S)'_S = \Big[\frac{\partial W^S_{\text{OSM}}}{\partial \mathbf{E}_S} + \frac{\partial W^S_{\text{EQ}}}{\partial \mathbf{E}_S} + \frac{\partial W^S_{\text{ANISO}}}{\partial \mathbf{E}_S}\Big] \cdot (\mathbf{E}_S)'_S + \sum_{n=1}^{N} \frac{\partial W^S_{\text{NEQ}}}{\partial (\mathbf{E}_{Se})_n} \cdot [(\mathbf{E}_{Se})_n]'_S . \quad (7.20)$$

The implicit dependence of $W^S_{\text{NEQ}}$ on the inelastic deformations $(\mathbf{F}_{Si})_n$ is identified, when the derivative of the non-equilibrium part is rewritten with the aid of the inelastic push-forward used in equation (7.17) yielding

$$\frac{\partial W^S_{\text{NEQ}}}{\partial \mathbf{E}_{Se}} = \Big(\frac{\partial \widehat{\boldsymbol{\Gamma}}_{Se}}{\partial \mathbf{E}_{Se}}\Big)^T \frac{\partial W^S_{\text{NEQ}}}{\partial \widehat{\boldsymbol{\Gamma}}_{Se}} = \Big[\frac{\partial (\mathbf{F}^{T-1}_{Si}\,\mathbf{E}_{Se}\,\mathbf{F}^{-1}_{Si})}{\partial \mathbf{E}_{Se}}\Big]^T \frac{\partial W^S_{\text{NEQ}}}{\partial \widehat{\boldsymbol{\Gamma}}_{Se}} = \mathbf{F}^{-1}_{Si}\,\frac{\partial W^S_{\text{NEQ}}}{\partial \widehat{\boldsymbol{\Gamma}}_{Se}}\,\mathbf{F}^{T-1}_{Si} ,$$
$$(7.21)$$

carried out in an exemplary way using $N = 1$. The latter part of (7.21) clearly reveals that the non-equilibrium strain energy depends explicitly on the elastic strain, while the inelastic push-forward $\mathbf{F}^{-1}_{Si}(\,\cdot\,)\mathbf{F}^{T-1}_{Si}$ is associated with the movement of the time-dependent position of the inelastic intermediate configuration. Thus, in regard of an iterative numerical implementation, the need for evolution equations of the internal variables $(\mathbf{F}_{Si})_n$ or $(\mathbf{C}_{Si})_n$ becomes clear.

Inserting equations (7.20) and (7.21) into the inequality (7.19) as well as utilizing the material time derivative $[(\mathbf{E}_{Se})_n]'_S = (\mathbf{E}_S)'_S - [(\mathbf{E}_{Si})_n]'_S$ stemming from equation $(7.16)_3$, finally yields an expression for the determination of the solid extra stress $\mathbf{S}^S_E$,

$$\Big[\mathbf{S}^S_E - \underbrace{\frac{\partial W^S_{\text{OSM}}}{\partial \mathbf{E}_S}}_{\mathbf{S}^S_{\text{OSM}}} - \underbrace{\frac{\partial W^S_{\text{EQ}}}{\partial \mathbf{E}_S}}_{\mathbf{S}^S_{\text{EQ}}} - \underbrace{\sum_{n=1}^{N} \overbrace{(\mathbf{F}^{-1}_{Si})_n \frac{\partial W^S_{\text{NEQ}}}{\partial (\widehat{\boldsymbol{\Gamma}}_{Se})_n}(\mathbf{F}^{T-1}_{Si})_n}^{\mathbf{S}^S_n}}_{\mathbf{S}^S_{\text{NEQ}}} - \underbrace{\frac{\partial W^S_{\text{ANISO}}}{\partial \mathbf{E}_S}}_{\mathbf{S}^S_{\text{ANISO}}}\Big] \cdot (\mathbf{E}_S)'_S = 0 \;\; \forall\,(\mathbf{E}_S)'_S ,$$
$$(7.22)$$

where $\mathbf{S}^S_n$ is the non-equilibrium stress of a single Maxwell element and $\mathbf{S}^S_{\text{NEQ}}$ is the sum of the generalized model. The remainder of (7.19) is known as dissipation inequality

$$\sum_{n=1}^{N} (\mathbf{F}^{-1}_{Si})_n \frac{\partial W^S_{\text{NEQ}}}{\partial (\widehat{\boldsymbol{\Gamma}}_{Se})_n} (\mathbf{F}^{T-1}_{Si})_n \cdot [(\mathbf{E}_{Si})_n]'_S - \hat{\mathbf{p}}^F_E \cdot \mathbf{w}_F \geq 0 \qquad \forall\,\big\{[(\mathbf{E}_{Si})_n]'_S , \mathbf{w}_F\big\} , \quad (7.23)$$

which is needed to derive the evolution equations for the internal variables $(\mathbf{F}_{Si})_n$ or $(\mathbf{C}_{Si})_n$ as well as the constitutive assumption for the fluid momentum production $\hat{\mathbf{p}}^F_E$. Finally,

the Cauchy extra stress $\mathbf{T}_E^S$ and the Kirchoff extra stress $\boldsymbol{\tau}_E^S$ can be computed applying a push-forward operation to the 2nd Piola-Kirchhoff stress such that

$$\boldsymbol{\tau}_E^S = \mathbf{F}_S \, \mathbf{S}_E^S \, \mathbf{F}_S^T \qquad \text{and} \qquad \mathbf{T}_E^S = \det \mathbf{F}_S^{-1} \, \boldsymbol{\tau}_E^S \,. \tag{7.24}$$

## 7.4.5   Dissipation of the Viscous Solid Skeleton

In order to derive the evolution equation for the chosen internal variables $(\mathbf{C}_{Si})_n$, the solid part of the dissipation inequality (7.23) is expressed in terms of the respective intermediate configuration as the current configuration of the inelastic process. This is done, because one describes the dissipation process of the solid material using real quantities on its actual (i. e. intermediate) configuration rather than using the image of these quantities in the reference configuration. Having in mind the push-forward $(7.24)_1$, it is easily concluded that a similar transport with the inelastic part of the deformation gradient yields the intermediate-state overstress tensor of a Maxwell branch

$$\widehat{\boldsymbol{\tau}}_n^S = (\mathbf{F}_{Si})_n \, (\mathbf{S}_n^S) \, (\mathbf{F}_{Si}^T)_n \,. \tag{7.25}$$

Note that the computation of an entire intermediate-state overstress tensor $\widehat{\boldsymbol{\tau}}_{\text{NEQ}}^S$ is only possible in the case of $N = 1$, as the individual intermediate overstresses of more than one Maxwell element may operate on different intermediate configurations. For $N \geq 1$, a summation has to be carried out on the referential or the actual configuration using $\mathbf{S}_n^S$ or $\boldsymbol{\tau}_n^S$, respectively. Hence, the first part of the dissipation inequality (7.23) has to be evaluated in a mathematically sufficient sense for every Maxwell element and can be rewritten as

$$\widehat{\boldsymbol{\tau}}_n^S \cdot (\mathbf{F}_{Si}^{T-1})_n \, [(\mathbf{E}_{Si})_n]_S' \, (\mathbf{F}_{Si}^{-1})_n = \widehat{\boldsymbol{\tau}}_n^S \cdot (\widehat{\mathbf{D}}_{Si})_n \geq 0 \,, \tag{7.26}$$

where $(\widehat{\mathbf{D}}_{Si})_n$ are the respective symmetric deformation velocity tensors of the intermediate configurations. This inequality is sufficiently satisfied with the simple ansatz

$$(\widehat{\mathbf{D}}_{Si})_n \propto \widehat{\boldsymbol{\tau}}_n^S \qquad \longrightarrow \qquad (\widehat{\mathbf{D}}_{Si})_n = \frac{1}{2\,\eta_n^S} \, \widehat{\boldsymbol{\tau}}_n^S - \frac{\zeta_n^S}{2\,\eta_n^S\,(2\,\eta_n^S + 3\,\zeta_n^S)} \, (\widehat{\boldsymbol{\tau}}_n^S \cdot \mathbf{I}) \, \mathbf{I} \,, \tag{7.27}$$

where $\eta_n^S$ and $\zeta_n^S$ are the macroscopic shear and bulk viscosities of the dashpot in a Maxwell element, respectively. In this context, relation $(7.27)_2$ is the inverse from the well-known stress-strain rate relation for a dashpot yielding a linear relation between $\widehat{\boldsymbol{\tau}}_n^S$ and $(\widehat{\mathbf{D}}_{Si})_n$, see, e. g., Markert [64]. Since inequality (7.26) has to be satisfied, it is easily concluded, that the restrictions on the viscosities $\eta_n^S > 0$ and $2\,\eta_n^S + 3\,\zeta_n^S > 0$ must hold. However, with regard to the numerical evaluation of the evolution equation, it is most convenient, when the spatio-temporal discretization of $(7.27)_2$ is carried out on the constant reference configuration. Applying the known transport mechanisms for $\widehat{\mathbf{D}}_{Si}$ described in (7.26) as well as for $\widehat{\boldsymbol{\tau}}_n^S$ in (7.25) yields the final form of the evolution equation

$$[(\mathbf{C}_{Si})_n]_S' - \frac{1}{\eta_n^S} \, (\mathbf{C}_{Si})_n \, \mathbf{S}_n^S \, (\mathbf{C}_{Si})_n + \frac{\zeta_n^S}{\eta_n^S\,(2\,\eta_n^S + 3\,\zeta_n^S)} \, [\mathbf{S}_n^S \cdot (\mathbf{C}_{Si})_n] \, (\mathbf{C}_{Si})_n = \mathbf{0} \,, \tag{7.28}$$

where the chosen internal variables $(\mathbf{C}_{Si})_n$ appear in an explicit manner, when integrated using a backward Euler scheme.

### 7.4.6 Dissipation of the Viscous Interstitial Fluid

Finally, the remaining unspecified extra quantity $\hat{\mathbf{p}}_E^F$ needs to be defined by an appropriate constitutive law reflecting the properties of a viscous interstitial fluid. Inserting the constitutive assumption $\hat{\mathbf{p}}_E^F = -(n^F)^2 (\mathbf{K}^F)^{-1} \mathbf{w}_F$ into equation (7.12) and then into the fluid momentum balance $(7.4)_2$ leads to the well known Darcy filter law

$$n^F \mathbf{w}_F = -\mathbf{K}^F (\operatorname{grad} \mathcal{P} - \rho^{FR} \mathbf{b}) \quad \text{with} \quad \mathbf{K}^F = \frac{K^S}{\mu^{FR}} \mathbf{I} \tag{7.29}$$

relating the hydraulic pressure gradient to the filter velocity $n^F \mathbf{w}_F$ via the Darcy permeability tensor $\mathbf{K}^F$. In this context, $K^S$ is the intrinsic permeability, which is solely a measure of the pore geometry, and $\mu^{FR} > 0$ is the effective fluid viscosity. A deformation dependence can be introduced for the intrinsic permeability which, according to Markert [65], can be computed using

$$K^S = K_{0S}^S \left( \frac{J_S - n_{0S}^S}{n_{0S}^F} \right)^\kappa. \tag{7.30}$$

Herein, $K_{0S}^S$ is the initial permeability of the undeformed tissue and $\kappa \geq 0$ is a parameter governing the non-linearity of the deformation dependency. Note that $\kappa = 0$ turns off the deformation dependency. Moreover, due to the positive definiteness of $\mathbf{K}^F$, the remaining fluid part of the entropy inequality (7.19) is satisfied for $K_{0S}^S > 0$.

### 7.4.7 General Structure of the Solid Strain Energy

Regarding the definition of constitutive equations describing the respective parts of $W^S$, it is advantageous to *a priori* define a general structure to be used. Starting with the osmotic part, the beginning of the section states that osmosis triggers a variation of the volume which is occupied by the incompressible pore-fluid. In this regard, a purely volumetric deformation can be initiated in the case of purely isotropic material behavior, which is accompanied by shape changes in the case of an anisotropic behavior resulting from the presence of collagen fibers. Following this, the most suitable process variable would be $\det \mathbf{F}_S = (\det \mathbf{C}_S)^{\frac{1}{2}}$ which describes the local dilatation of the ECM. The change in shape may then be caused by the anisotropic stress response of the material. Moreover, the solid strain energy functions are often formulated in a very general way using the principal stretches of the deformation. In this regard and in order to adopt the results of the classical mechanics of single phase materials, the process variables of choice are $\mathbf{C}_S$ and $(\widehat{\mathbf{C}}_{Se})_n$. This allows for the conclusive form

$$W^S = W_{\text{OSM}}^S(\det \mathbf{C}_S) + W_{\text{EQ}}^S(\mathbf{C}_S) + \sum_{n=1}^{N} W_{\text{NEQ}}^S[(\widehat{\mathbf{C}}_{Se})_n] + W_{\text{ANISO}}^S(\mathbf{C}_S, \boldsymbol{\mathcal{M}}^S). \tag{7.31}$$

Applying the chain rule to equations $(7.16)_1$ and (7.17), the stress computation concluded from equation (7.22) can be rewritten in terms of the actual configuration yielding the

Kirchhoff stress

$$
\boldsymbol{\tau}_E^S = \underbrace{2\,\mathbf{F}_S\frac{\partial W_{\mathrm{OSM}}^S}{\partial \mathbf{C}_S}\mathbf{F}_S^T}_{\boldsymbol{\tau}_{\mathrm{OSM}}^S} + \underbrace{2\,\mathbf{F}_S\frac{\partial W_{\mathrm{EQ}}^S}{\partial \mathbf{C}_S}\mathbf{F}_S^T}_{\boldsymbol{\tau}_{\mathrm{EQ}}^S} + \underbrace{2\sum_{n=1}^{N}(\mathbf{F}_{Se})_n\overbrace{\frac{\partial W_{\mathrm{NEQ}}^S}{\partial (\widehat{\mathbf{C}}_{Se})_n}}^{\boldsymbol{\tau}_{n}^S}(\mathbf{F}_{Se}^T)_n}_{\boldsymbol{\tau}_{\mathrm{NEQ}}^S} + \underbrace{2\,\mathbf{F}_S\frac{\partial W_{\mathrm{ANISO}}^S}{\partial \mathbf{C}_S}\mathbf{F}_S^T}_{\boldsymbol{\tau}_{\mathrm{ANISO}}^S}\,.
$$

$$(7.32)$$

## 7.4.8  Specific Solid Strain Energies

As a final step, the respective solid strain energies need to be defined, which is achieved by the concept of scalar-valued isotropic tensor functions. Starting with the osmotic contribution, a volumetric strain energy is postulated by use of $(7.9)_2$ together with the relation $\det \mathbf{F}_S = (\det \mathbf{C}_S)^{\frac{1}{2}}$ yielding

$$
W_{\mathrm{OSM}}^S[c_m^{fc}(\det \mathbf{C}_S)] = R\,\Theta\,c_{0S}^{fc}\,n_{0S}^F\left[\frac{2\,\bar{c}_m}{c_m^{fc}} - \frac{\sqrt{4\,\bar{c}_m^2 + (c_m^{fc})^2}}{c_m^{fc}} + \operatorname{arsinh}\left(\frac{c_m^{fc}}{2\,\bar{c}_m}\right)\right],
$$

$$(7.33)$$

$$
\text{where}\qquad c_m^{fc} = c_{0S}^{fc}\,n_{0S}^F\left[(\det \mathbf{C}_S)^{\frac{1}{2}} - n_{0S}^S\right]^{-1}.
$$

Herein, $R$ denotes the universal gas constant, $\Theta$ is the absolute temperature, whereas $\bar{c}_m$ is the molar concentration of the external monovalent solution surrounding the tissue, which can be treated as a material parameter. In this regard, $(7.33)_1$ yields the scalar-valued function relating the osmotic pressure difference $\Delta\pi$ to the concentration differences between the pore fluid and the external solution. Hence, (7.33) in combination with $(7.24)_2$ and (7.32) is equivalent to the classical way, where one proceeds from the simple example of a reservoir filled with two solutions of different concentrations being separated by a semi-permeable membrane. Following this approach, van't Hoff's osmotic law can be applied yielding the osmotic pressure difference of the two chemically active solutions at the semi-permeable membrane:

$$
\mathbf{T}_{E,\,\mathrm{OSM}}^S = \det \mathbf{F}_S^{-1}\,\boldsymbol{\tau}_{E,\,\mathrm{OSM}}^S = -\Delta\pi\,\mathbf{I}\quad\text{with}\quad \Delta\pi = R\Theta\big[(c_m^+ + c_m^-) - (\bar{c}_m^+ + \bar{c}_m^-)\big].\quad(7.34)
$$

Herein, $c_m^\gamma$ and $\bar{c}_m^\gamma$ for $\gamma = +,-$ are the molar solute concentrations (i.e. anions and cations) of the internal and external solutions, respectively. Following this, the concentrations of one solution can be prescribed in the sense of a boundary condition, while the concentrations of the other solution may be determined using the Donnan [16] equation,

$$
c_m^+\,c_m^- = \bar{c}_m^+\,\bar{c}_m^-\,,
$$

$$(7.35)$$

which provides the chemical equilibrium at the semi-permeable membrane. Applying this concept to the IVD means firstly that the two solutions will be referred to as internal and external (surrounding) solutions while the semi-permeable membrane must be understood as the boundary surface of the IVD. Note in passing that exploiting the Lanir [57]

assumption allows to extend the applicability of equation (7.35) from the domain boundary to the whole IVD. Secondly, it is crucial to incorporate the fixed negative charges as they contribute to the ion-concentration of the internal solution yielding the osmotic effect. Hence, the electro-neutrality condition needs to be applied, thereby always ensuring enough cations being left to balance out the fixed negative charges. In this context, the following relations hold for the external and internal solutions, respectively:

$$
\begin{aligned}
z^+ \bar{c}_m^+ + z^- \bar{c}_m^- = 0 & \quad \longrightarrow \quad \bar{c}_m^- = \bar{c}_m^+ =: \bar{c}_m & : \text{external solution}, \\
z^+ c_m^+ + z^- c_m^- + z^{fc} c_m^{fc} = 0 & \quad \longrightarrow \quad c_m^- = c_m^+ - c_m^{fc} & : \text{internal solution}.
\end{aligned}
\tag{7.36}
$$

Therein, use was made of the corresponding valences for a monovalent salt solution (i.e. $\mathrm{Na^+Cl^-}$) reading $z^+ = 1$ and $z^- = z^{fc} = -1$. Inserting the results of equations (7.36) into the Donnan equation (7.35) yields the two relations

$$
c_m^+ = \sqrt{\bar{c}_m^2 + \left(\frac{c_m^{fc}}{2}\right)^2} + \frac{c_m^{fc}}{2} \qquad \text{and} \qquad c_m^- = \sqrt{\bar{c}_m^2 + \left(\frac{c_m^{fc}}{2}\right)^2} - \frac{c_m^{fc}}{2}
\tag{7.37}
$$

also known as the Donnan equilibrium. Finally, the constitutive equation for the osmotic pressure (i.e. osmotic pressure caused by large molecules, such as PGs and GAGs) can be postulated by inserting equations (7.37) and (7.36)$_1$ into (7.34) and (7.14)$_2$ yielding

$$
\mathbf{T}_{E,\,\mathrm{OSM}}^S = -\Delta\pi\,\mathbf{I} = -2R\,\Theta\,[\,\sqrt{\bar{c}_m^2 + (c_m^{fc}/2)^2} - \bar{c}_m\,]\,\mathbf{I},
\tag{7.38}
$$

where $c_m^{fc}$ is deformation dependent as seen in equation (7.9)$_2$.

In order to keep the model as general as possible, an Ogden ansatz is chosen for the mechanical equilibrium and non-equilibrium strain-energies, thereby allowing for the simulation of any complexity level ranging from very simple to highly non-linear material behavior

$$
W_{\mathrm{EQ}}^S = \mu_0^S \sum_{m=1}^{M_0} \left[ \sum_{k=1}^{3} \frac{\mu_{0(m)}^*}{\alpha_{0(m)}} \left( \lambda_{S(k)}^{\alpha_{0(m)}/2} - 1 \right) - \mu_{0(m)}^* \ln\left(J_S\right) \right] + U_{\mathrm{EQ}}^S(J_S),
$$

$$
W_{\mathrm{NEQ}}^S = \sum_{n=1}^{N} \mu_n^S \sum_{m=1}^{M_n} \left[ \sum_{k=1}^{3} \frac{\mu_{n(m)}^*}{\alpha_{n(m)}} \left( (\lambda_{Se(k)}^{\alpha_{n(m)}/2})_n - 1 \right) - \mu_{n(m)}^* \ln\left((J_{Se})_n\right) \right] + U_{\mathrm{NEQ}}^S[(J_{Se})_n].
\tag{7.39}
$$

Herein, $\lambda_{S(k)}$ and $\lambda_{Se(k)}$ for $k = 1, 2, 3$ denote the eigenvalues of the right $\mathbf{C}_S$ and $\mathbf{C}_{Se}$ or the left $\mathbf{B}_S$ and $\mathbf{B}_{Se}$ deformation tensors, respectively. The Jacobians are defined as $J_S = \det \mathbf{F}_S$ and $(J_{Se})_n = \det (\mathbf{F}_{Se})_n$, and the indices $m$ and $k$ denote the number of Ogden terms to be taken and the dimension in space, respectively. Moreover, $\mu_0^S > 0$ and $\mu_n^S > 0$ are the first Lamé constants, i.e., the classical ground-state shear moduli, whereas $\mu_{0(m)}^*$, $\mu_{n(m)}^*$, $\alpha_{0(m)}$, and $\alpha_{n(m)}$ represent dimensionless, real-valued material parameters. By making specific choices of the parameters $M$, $\mu_m^*$ and $\alpha_m$ it turns out that the Ogden law (7.39)$_1$ comprises other well-known finite elasticity models, such as the Varga, neo-Hooke, or Mooney-Rivlin model, see, e.g., Mooney [67], Rivlin [77], Varga [98], and Treloar [93] (see Table 7.1). Since the strain energies (7.39) describe a porous material, a volumetric response function needs to be defined in order to ensure the compaction point, which is

**Table 7.1:** *Elasticity models included in the general Ogden law* $(7.39)_1$.

| Model | $M$ | $\mu_m^*$ | $\alpha_m$ |
|---|---|---|---|
| Varga | 1 | $\mu_1^* = 2$ | $\alpha_1 = 1$ |
| neo-Hooke | 1 | $\mu_1^* = 1$ | $\alpha_1 = 2$ |
| Mooney–Rivlin | 2 | $\mu_1^* - \mu_2^* = 1$ | $\alpha_1 = 2,\ \alpha_2 = -2$ |

reached when there is no pore space left. However, due to the very small permeability of soft biological tissues in general, the volumetric response function mainly serves to limit the dilatation of the ECM, as the compaction point is rarely reached. Thus, the volumetric extension can be taken in accordance to Eipper [32], viz.:

$$
U_{\mathrm{EQ}}^S = \frac{\Lambda_0^S}{\gamma_0^S\big(\gamma_0^S - 1 + \frac{1}{(1-n_{0S}^S)^2}\big)} \Big( J_S^{\gamma_0^S} - 1 - \gamma_0^S \ln \frac{J_S - n_{0S}^S}{1 - n_{0S}^S} + \gamma_0^S\, n_{0S}^S\, \frac{J_S - 1}{1 - n_{0S}^S} \Big),
$$

$$
U_{\mathrm{NEQ}}^S = \sum_{n=1}^{N} \frac{\Lambda_n^S}{\gamma_n^S\big(\gamma_n^S - 1 + \frac{1}{[1-(n_{Si}^S)_n]^2}\big)} \tag{7.40}
$$
$$
\Big( (J_{Se}^{\gamma_n^S})_n - 1 - \gamma_n^S \ln \frac{(J_{Se})_n - (n_{Si}^S)_n}{1 - (n_{Si}^S)_n} + \gamma_n^S\, (n_{Si}^S)_n\, \frac{(J_{Se})_n - 1}{1 - (n_{Si}^S)_n} \Big).
$$

Herein, $\Lambda_0^S > 0$ and $\Lambda_n^S > 0$ are the second Lamé constants, whereas $\gamma_0^S > 1$ and $\gamma_n^S > 1$ are dimensionless material parameters governing the non-linearity of the volumetric extension terms. Moreover, the inelastic solidities $(n_{Si}^S)_n := n_{0S}^S (J_{Si}^{-1})_n$ are introduced with the aid of the inelastic Jacobian determinants $(J_{Si}^{-1})_n = \det (\mathbf{F}_{Si})_n$.

The anisotropic contribution of the strain-energy function describing the locally orthotropic fiber reinforcements (cf. Markert *et al.* [66]) can be postulated following a similar polynomial concept as is used in the Ogden ansatz yielding

$$
W_{\mathrm{ANISO}}^S = \sum_{q=1}^{M_f} \Big[ \frac{\tilde{\mu}_q^S}{\tilde{\gamma}_q^S} (\mathrm{I}_4^{\tilde{\gamma}_q^S/2} + \mathrm{I}_6^{\tilde{\gamma}_q^S/2} - 2) - \tilde{\mu}_q^S \ln (\mathrm{I}_4\, \mathrm{I}_6)^{1/2} \Big] \qquad \forall\, \mathrm{I}_4, \mathrm{I}_6 \geq 1\,. \tag{7.41}
$$

Therein, $M_f$ denotes the number of polynomials to be used, $\tilde{\mu}_q$ and $\gamma_q$ are material parameters, and

$$
\mathrm{I}_4 = \boldsymbol{\mathcal{M}}_a^S \cdot \mathbf{C}_S = (\mathbf{a}_0 \otimes \mathbf{a}_0) \cdot \mathbf{C}_S = \mathbf{a}_0 \cdot \mathbf{C}_S\, \mathbf{a}_0\,,
$$
$$
\mathrm{I}_6 = \boldsymbol{\mathcal{M}}_b^S \cdot \mathbf{C}_S = (\mathbf{b}_0 \otimes \mathbf{b}_0) \cdot \mathbf{C}_S = \mathbf{b}_0 \cdot \mathbf{C}_S\, \mathbf{b}_0 \tag{7.42}
$$

are the mixed invariants describing the squared stretches in the respective fiber directions, thereby having a clear physical interpretation, cf. Spencer [91]. In this context, the unit fiber vectors $\mathbf{a}_0$ and $\mathbf{b}_0$ are defined in the undeformed state. Like in the theory of ropes, the collagen fibers are assumed to carry loads only under tension. Therefore, the restriction $\{\mathrm{I}_4, \mathrm{I}_6\} \geq 1$ must hold, which simultaneously satisfies restrictions stemming from polyconvexity considerations, cf. Holzapfel *et al.* [43] and Schröder & Neff [81]. Note in passing that the equilibrium and non-equilibrium parts also fulfill the polyconvexity requirement, thereby ensuring the existence of minimizers in variational problems appearing in the framework of the finite element method (FEM).

## 7.5 Numerical Modeling

The FEM has been proven to provide a suitable algorithm to approximate the resulting set of coupled partial differential equations stemming from the extended biphasic solid-fluid model. In this context, the local forms of the governing multi-field equations $(7.5)_{1,2}$ must be brought into a form suitable for the numerical approximation process. After inserting equation (7.29) into equation $(7.5)_1$, the quasi-static model under consideration incorporates two main fields, namely the solid displacement $\mathbf{u}_S$ and the hydraulic pore-fluid pressure $\mathcal{P}$. As the osmotic pressure difference $\Delta\pi$ of the solid extra stress $\mathbf{T}_{E,\,\mathrm{OSM}}^S$ can be added on the hydraulic pressure $\mathcal{P}$, the entire pressure $p = \Delta\pi + \mathcal{P}$ of the model is introduced.

In regard of the FEM as the chosen variational approximation method, the corresponding local forms of the field equations are transferred into a so-called weak formulation claiming to be fulfilled in an integral sense instead of seeking for a closed-form solution for the strong formulation. Thus, the strong forms $(7.5)_{1,2}$ are integrated over the spatial domain $\Omega$ occupied by the porous tissue at time $t$. Subsequently, the variational formulation is obtained, when the respective terms are weighted by independent test functions $\delta\mathbf{u}_S$ and $\delta\mathcal{P}$. However, in order to allow the application of boundary conditions, some of the volume integrals have to be transformed into surface integrals. As there are two coupled differential equations, the overall surface $\Gamma = \partial\Omega$ of the domain $\Omega$ is mathematically split into

$$\begin{aligned}
\Gamma = \Gamma_{\mathbf{u}} \cup \Gamma_{\mathbf{t}} \qquad &\text{with} \quad \Gamma_{\mathbf{u}} \cap \Gamma_{\mathbf{t}} = \emptyset\,, \\
\Gamma = \Gamma_{\mathcal{P}} \cup \Gamma_q \qquad &\text{with} \quad \Gamma_{\mathcal{P}} \cap \Gamma_q = \emptyset\,,
\end{aligned} \tag{7.43}$$

where $\Gamma_{\mathbf{u}}$ and $\Gamma_{\mathcal{P}}$ are the Dirichlet boundaries for the unknown quantities $\mathbf{u}_S$ and $\mathcal{P}$, while $\Gamma_{\mathbf{t}}$ and $\Gamma_q$ represent the respective Neumann parts. After applying the product rule and the Gaußian integral theorem, the weak formulations for the corresponding balances evolve

$$\int_\Omega \mathrm{div}\,(\mathbf{u}_S)_S' \,\delta\mathcal{P}\,\mathrm{d}v + \int_\Omega \Big[\, \frac{K^S}{\mu^{FR}} \left(\mathrm{grad}\,\mathcal{P} - \rho^{FR}\mathbf{b}\right) \Big] \cdot \mathrm{grad}\,\delta\mathcal{P}\,\mathrm{d}v + \int_{\Gamma_q} \overline{q}\,\delta\mathcal{P}\,\mathrm{d}a = 0\,,$$

$$\int_\Omega (\mathbf{T}_{E,\,\mathrm{MECH}}^S - p\,\mathbf{I}) \cdot \mathrm{grad}\,\delta\mathbf{u}_S\,\mathrm{d}v - \int_\Omega (n^S\rho^{SR} + n^F\rho^{FR})\,\mathbf{b}\cdot\delta\mathbf{u}_S\,\mathrm{d}v - \int_{\Gamma_{\mathbf{t}}} \overline{\mathbf{t}}\cdot\delta\mathbf{u}_S\,\mathrm{d}a = 0\,.$$

$$(7.44)$$

Herein, $\overline{q} = n^F\mathbf{w}_F \cdot \mathbf{n}$ is the volume efflux of $\varphi^F$ over the boundary $\Gamma_q$ with the outward oriented unit surface normal $\mathbf{n}$ and $\overline{\mathbf{t}} = (\mathbf{T}_{E,\,\mathrm{MECH}}^S - p\,\mathbf{I})\,\mathbf{n}$ denotes the external load vector acting on the boundary $\Gamma_{\mathbf{t}}$. Note that the respective Neumann boundaries include the surface fractions of all constituents, i. e., solid and fluid, thereby ensuring physically meaningful boundary conditions. However, it is still possible to set conditions for $\bar{q}$ and $\overline{\mathbf{t}}$ at the same surface, while a simultaneous application of a Dirichlet and a Neumann condition is forbidden according to (7.43). Following the standard Bubnov-Galerkin method, the basis functions for the trial functions of $\mathbf{u}_S$ and $\mathcal{P}$ as well as the corresponding test functions of $\delta\mathbf{u}_S$ and $\delta\mathcal{P}$ are identical. As a result, the respective test functions correspond with the trial functions, which causes $\delta\mathbf{u}_S$ and $\delta\mathcal{P}$ to vanish at Dirichlet boundaries $\Gamma_{\mathbf{u}}$ and $\Gamma_{\mathcal{P}}$, where discrete values are prescribed.

As a next step, the weak forms (7.44) have to be discretized in space, i. e., an appropriate approximation for the unknowns $\mathbf{u}_S$ and $\mathcal{P}$ has to be defined. Concerning the spatial discretization, i. e., the semi-discretization with respect to the space variable $\mathbf{x}$, special care must be taken, as the governing equations represent a strongly coupled solid-fluid model, i. e., the unknown field quantities $\mathbf{u}_S$ and $\mathcal{P}$ appear in both equations of (7.44), cf., e. g., Zienkiewicz & Taylor [103]. Hence, the unknowns have to be approximated simultaneously yielding a so-called mixed finite element formulation. Regarding the volume balance $(7.44)_1$ of the overall aggregate, the gradient of the hydraulic pressure field needs to be computed, leading to at least a linear discretization of $\mathcal{P}$. Moreover, as the solid Cauchy extra stress tensor $\mathbf{T}^S_{E,\,\mathrm{MECH}}$ implicitly depends on the gradient of the discretized displacement field $\mathbf{u}_S$, its approximation needs to be one order higher compared with the approximation used for the hydraulic pressure field $\mathcal{P}$. Then, an equal order approximation of the first term in equation $(7.44)_2$ is achieved. Thus, according to Sandhu & Wilson [78] the natural choice yields the usage of so-called Taylor-Hood elements having quadratic basis functions for the displacement $\mathbf{u}_S$ and linear basis functions for the hydraulic pressure $\mathcal{P}$.

However, regarding numerical accuracy, stability and numerical costs, the suitable choice of mixed finite element formulations is by no means phenomenological, but rather strictly mathematical. In this regard, the inf-sup condition, often referred to as Ladyzhenskaya-Babuška-Brezzi (LBB) condition, needs to be fulfilled, cf., e. g., Brezzi & Fortin [14], Braess [13] or Wieners [99]. Following this, the Taylor-Hood elements fulfill the LBB condition and are the best possible choice from a stability and accuracy point of view. In regard of the complex geometries frequently involved in computational biomechanics, the quadratic discretization also leads to a good geometry approximation, even with a small number of elements. However, concerning the general 3-d case, the enormous number of mid nodes in finer meshes causes quite large systems of equations, which often have to be solved in parallel, cf. Wieners *et al.* [100] or Ehlers *et al.* [27]. One possibility to overcome this problem is to use the so-called MINI element of Arnold *et al.* [2] which has an enriched linear ansatz for $\mathbf{u}_S$ using a bubble node. This leads to stable results but the obtained solution is not as accurate anymore. Note that a linear-linear approximation of $\mathbf{u}_S$ and $\mathcal{P}$ leads to strange instabilities causing mesh dependent solutions due to the so-called spurious pressure modes, cf. Brezzi & Fortin [14].

Finally, the weak forms (7.44) have to be discretized in time using a suitable numerical time integration method. In this regard, finite differences are applied using the implicit Euler scheme. More detailed information on how the biphasic model is solved using general Runge-Kutta methods can be found in Ellsiepen [34], Diebels *et al.* [15] or in the special case of viscoelastic solid deformations in Markert [64].

As a next step, a brief introduction into the structure of the resulting system of equations is given. Following the abstract illustration of Ellsiepen [34], the space-discrete variables at $N_u$ nodes are unified in $\boldsymbol{u}$ and the internal variables at $N_q$ quadrature points can be combined to $\boldsymbol{q}$ yielding

$$
\left.
\begin{aligned}
\boldsymbol{u} &= \big[\, (\mathbf{u}_S^1, \mathcal{P}^1), \ldots., (\mathbf{u}_S^{N_u}, \mathcal{P}^{N_u}) \,\big]^T, \\
\boldsymbol{q} &= \big[\, C_{Si(kl)}^1, \ldots., C_{Si(kl)}^{N_q} \,\big]^T
\end{aligned}
\right\}
\quad
\boldsymbol{y} = (\boldsymbol{u}^T, \boldsymbol{q}^T)^T,
\qquad (7.45)
$$

where $C_{Si(kl)}$ are the six scalar history variables of the symmetric inelastic deformation tensor $\mathbf{C}_{Si}$. If more than one Maxwell element is used, the number of inelastic history deformation tensors is increased proportionally. The vector $\boldsymbol{u}$ includes all the nodal degrees of freedom while $\boldsymbol{q}$ contains all the history variables. Note that for the sake of clarity, the different ansatz functions for the solid displacement (quadratic) and the hydraulic pressure (linear) are not regarded in (7.45). Using the abbreviation $(\,\cdot\,)' := (\,\cdot\,)'_S$, the entire semi-discrete initial-value problem of first order in time can be condensed to

$$\boldsymbol{F}(t, \boldsymbol{y}, \boldsymbol{y}') = \left[ \begin{array}{c} \boldsymbol{g}(t, \boldsymbol{u}, \boldsymbol{u}', \boldsymbol{q}) \\ \boldsymbol{l}(t, \boldsymbol{q}, \boldsymbol{q}', \boldsymbol{u}) \end{array} \right] = \left[ \begin{array}{c} \boldsymbol{M}\,\boldsymbol{u}' + \boldsymbol{k}(\boldsymbol{u}, \boldsymbol{q}) - \boldsymbol{f} \\ \boldsymbol{A}\,\boldsymbol{q}' \ - \boldsymbol{r}(\boldsymbol{q}, \boldsymbol{u}) \end{array} \right] \stackrel{!}{=} \boldsymbol{0}\,. \qquad (7.46)$$

Herein, initial conditions can be prescribed by applying $\boldsymbol{y}(t_0) = \boldsymbol{y}_0$ at an initial time $t_0 < t$. Moreover, $\boldsymbol{k}$ represents the generalized stiffness vector containing the non-linear dependencies on $(\boldsymbol{u}, \boldsymbol{q})$, while $\boldsymbol{f}$ denotes the vector of the external forces including the Neumann load functionals. The property of material incompressibility leads then to a non-regular generalized mass matrix $\boldsymbol{M}$, which turns the global system $\boldsymbol{g}(t, \boldsymbol{u}, \boldsymbol{u}', \boldsymbol{q})$ into a system of differential algebraic equations (DAEs). A possible time integration scheme solving this system is the implicit or backward Euler scheme which is also used for the computations in the next section. For more information on the systematic comparison of the available time-integration schemes towards their performance, the reader is referred to Diebels *et al.* [15] and Ellsiepen [34]. As the material behaves partly inelastic, the non-linear system $\boldsymbol{g}$ cannot be solved straight forward using Newton's method. Instead, the local system $\boldsymbol{l}(t, \boldsymbol{q}, \boldsymbol{q}', \boldsymbol{u})$ containing the space-discrete evolution equation (7.28) has to be solved in each step of the global Newton iteration. Comparing the structure of (7.28) with the general structure of $\boldsymbol{l}$ allows for the identification of the regular matrix $\boldsymbol{A}$ with $\boldsymbol{r}$ denoting the rest of the evolution equation. This local system of ordinary differential equations (ODE) is also best suitably solved using the backward Euler scheme in combination with a local Newton iteration on element level. For more detailed information on this so-called multilevel-Newton method, the reader is referred to the comprehensive work of Ellsiepen & Hartmann [35] and references therein. In this regard, the convergence of Newton's method strongly depends on the consistent linearization of the non-linear DAEs, which will not be given here due to its rather lengthy form. However, apart from the osmotic and anisotropic contributions to the material tangent, a comprehensive description of the missing linearization of the remaining major parts can be found in Markert [64].

During every iteration step of the global Newton iteration, a finite element code requires an algorithm computing the solid Cauchy extra stress tensor $\mathbf{T}^S_{E,\,\mathrm{MECH}}$ at every integration point of the numerical quadrature. According to the known procedure from elastoplasticity, every time the stress needs to be computed in the global iteration, the local ODE have to be solved on element level in order to accumulate the viscoelastic overstress with the isotropic and anisotropic equilibrium parts. The only difference is that no yield criterion has to be checked in the case of viscoelastic material behavior. As a first step, the actual left solid deformation tensor $(\mathbf{B}_S)^{\mathrm{act}}$ as well as its eigenvalues and eigentensors, needed to compute the purely elastic Kirchhoff stress $\boldsymbol{\tau}^S_{\mathrm{EQ}}$, is obtained from the actual solid deformation gradient $(\mathbf{F}_S)^{\mathrm{act}}$. Thereafter, the local Newton iteration starts and an

independent elastic trial state

$$(\mathbf{B}_{Se})_n^{\text{trial}} = (\mathbf{F}_S)^{\text{act}} (\mathbf{C}_{Si}^{-1})_n^{\text{last}} (\mathbf{F}_S^T)^{\text{act}} \tag{7.47}$$

is computed via a transport of the last deformation tensor $(\mathbf{C}_{Si}^{-1})_n^{\text{last}}$ taken from the last time step, but using the actual deformation gradient $(\mathbf{F}_S)^{\text{act}}$ as transporting quantity. Once more, the elastic eigenvalues and tensors are calculated, but now in order to obtain the trial overstress $(\boldsymbol{\tau}_{\text{NEQ}}^S)^{\text{trial}}$ from the elastic part of the trial deformation tensor $(\mathbf{B}_{Se})_n^{\text{trial}}$. As the right-hand side of the viscoelastic evolution equation contains the non-equilibrium trial stress expressed in the referential frame, the non-equilibrium trial stress is pulled back using the transport $(\mathbf{S}_{\text{NEQ}}^S)^{\text{trial}} = (\mathbf{F}_S^{-1})^{\text{act}} (\boldsymbol{\tau}_{\text{NEQ}}^S)^{\text{trial}} (\mathbf{F}_S^{T-1})^{\text{act}}$. If the evolution equation is fulfilled on a satisfactory level, the local iteration is stopped and the isotropic Kirchhoff stress is finally obtained with the last trial stress satisfying (7.28). The anisotropic contribution is computed thereafter using equations (7.32) and (7.41). Together with equation $(7.24)_2$, the sum of the isotropic and anisotropic parts finally yields the purely mechanical solid Cauchy extra stress tensor $\mathbf{T}_{E,\text{MECH}}^S$.

Due to the choice of $\mathcal{P}$ as primary variable, the model does not a priori exhibit a stress-free reference configuration. This becomes clear when the overall stress (7.14) of the model is computed, thereby using values of the natural state, i.e., $\mathbf{u}_S = \mathbf{0}$ and $\mathcal{P} = 0$. Due to (7.34), there is always an initial osmotic pressure

$$\Delta \pi_{0S} = R\Theta \left[ \sqrt{4\,\bar{c}_m^2 + (c_{0S}^{fc})^2} - 2\,\bar{c}_m \right]. \tag{7.48}$$

Hence, the constant part $\Delta\pi_{0S}\,\mathbf{I}$ is added onto the mechanical extra stress (7.15) to enforce a stress-free reference configuration in the sense of classical continuum mechanics. Note that without this modification, the model would describe an initial swelling of the tissue until equilibrium between (7.48) and the tension in the mechanical extra stress (7.15) is reached. For the sake of this contribution, the described simpler approach is followed and all computations start from a stress free reference configuration having the initial osmotic pressure (7.48) added onto the mechanical solid extra stress.

## 7.6    Numerical Examples

### 7.6.1    Torsion Experiment on a Cylindrical NP Specimen

The first example addresses the intrinsic viscoelastic material behavior of the nucleus pulposus in shear. In this context, a numerical torsion experiment is computed, following the real experiments on non-degenerated cylindrical NP specimens performed by Iatridis *et al.* [48]. Herein, the specimens were harvested from shock frozen IVDs (region L2–L5) and directly placed in a humidity chamber of a testing apparatus. Note that according to the preliminary swelling tests performed by Iatridis *et al.* [48], the humidity chamber provides the most stable hydration environment yielding a relatively constant water content of the discs over the three hours of testing time, i.e., no swelling occurs due to the extraction of the specimen from its natural environment. The specimen was then imposed to an axial

compression of 10 % of the original height of the disc in order to ensure a sufficient grip between the specimen and the two fully planar and impermeable testing plates, when the angular displacement $\varphi$ is applied, thereafter. The relaxation of the recorded torque $M_T$ of the top platen was then measured over time, whereas the respective average maximum shear stress $\tau$ was computed using the Saint-Venant theory for a circular cross section, i.e.,

$$\tau = 2 M_T / \pi r^3, \tag{7.49}$$

where $r$ is the radius of the cylinder. For the numerical parameter fit of the presented model to the experiments performed in Iatridis *et al.* [48], the disc was discretized using 20-noded mixed Taylor-Hood elements, as it is seen in Figure 7.3. The upper and lower
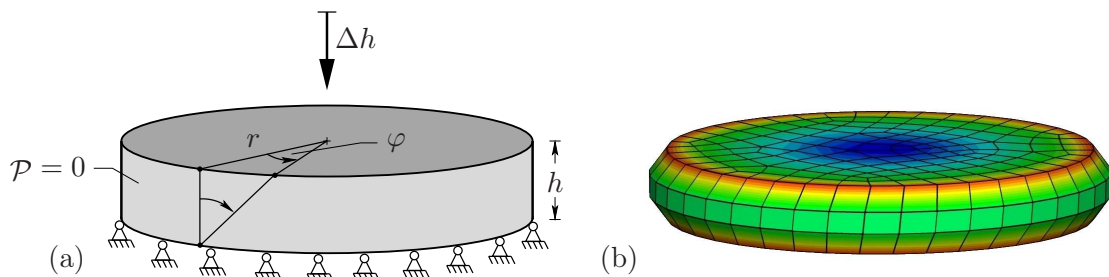


**Figure 7.3:** *(a) Average dimensions (radius $r = 4$ mm, height $h = 1.44$ mm) of the cylindrical NP specimen, boundary conditions (vertical displacement $\Delta h = 0.144$ mm, rotation angle $\varphi$) and (b) spatial discretization (441 elements) for the torsion experiment. The coloring indicates the qualitative distribution of the shear stress $\tau$ after the vertical displacement $\Delta h$ and the rotation angle $\varphi$ was applied. Note that the angular outer shape of the deformed specimen in (b) is due to the incapability of the post-processing to resolve quadratic elements.*

surface of the disc have movements prevented in the horizontal direction, whereas the upper surface is displacement-driven in axial direction for 0.144 mm and a duration of 2.0 s. This vertical displacement is then held constant over the rest of the computation as well as the hydrostatic pressure $\mathcal{P} = 0$ MPa at the hoop surface and the concentration $\bar{c}_m = 0$ mol/l of the external solution. Six hundred seconds after the vertical displacement was applied, a rotation angle $\varphi$ is induced within 0.025 s on the top surface and is again held constant for another 600 s, while the relaxation of the torsional shear stress is computed. For a better comparability of the experiments in Iatridis *et al.* [48] and in order to overcome the problem of local solution deficiencies, the torque $M_T$ is computed, i.e., the corresponding shear stresses are integrated over the top surface, and afterwards inserted into (7.49).

In a first approach, the isotropic NP specimen was modeled using one of the simpler material laws included in (7.39), i.e., the neo-Hooke model. In contrast, a total number of two Maxwell elements was needed, in order to reproduce the rapid relaxation of the shear stress depicted in Figure 7.4. Herein, the lines indicate the computed curves using the model described above, whereas the circles display the measured values from Iatridis *et al.* [48]. In this context, the parameters were fit manually to the curve corresponding to an angular displacement of $\varphi = 0.036$. The other two curves, i.e., $\varphi = 0.018$ and
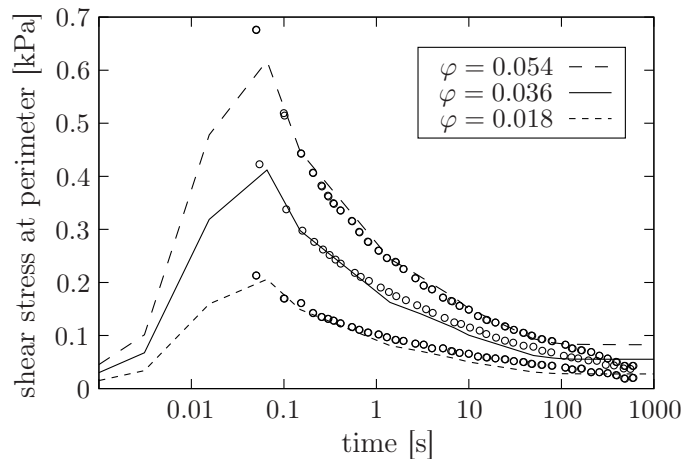
**Figure 7.4:** *Results of the parameter fit for the torsion experiment in Iatridis et al. [48]. The lines (dashed, solid, dotted) show the shear-stress relaxation of the numerical simulation, while the dots are the measured points at three different rotation angles, respectively. The parameter fit was carried out for $\varphi = 0.036$ and held constant for $\varphi = 0.018$ and $\varphi = 0.054$.*

$\varphi = 0.054$, were then computed with the identified parameters yielding a good agreement with the measured points.

Some of the respective material parameters for the NP (i.e. $\mu_j^S$, $\Lambda_j^S$, $\eta_j^S$, and $\zeta_j^S$ for j=0,1,2) have been fitted using the shear stress-relaxation experiment and are listed in Table 7.2. As the parameters occurring in (7.40) have an influence on the volumetric deformations solely, they can hence not be determined clearly. In this context, the assumption of a constant Poisson ratio was made and the relation stemming from the linear theory $\Lambda_j^S = 2\,\mu_j^S\,\nu/(1-2\,\nu)$ with $\nu = 0.2$ has been used, even though it is in the strict sense only valid around the natural state. Moreover, it was assumed that the volumetric viscosities have the same values as the solid shear viscosities, i.e., $\zeta_j^S = \eta_j^S$. The parameters $\gamma_j^S$ were chosen to limit the disc bulge in the swelling experiment of the IVD, as seen in Figure 7.5, whereas remaining isotropic parameters (also for the AF as well as for the vertebrae) were taken in accordance to the average values given in Argoubi & Shirazi-Adl [1], Eberlein *et al.* [19], Iatridis *et al.* [48, 50], Lee *et al.* [58], Lim & Hong [62], Ochia & Ching [72], Shirazi-Adl *et al.* [86], Wu & Chen [102] and references therein. The parameters for the anisotropic stress contribution (7.41) were fitted to the regional curves given in Holzapfel *et al.* [44]. Note in passing that according to Gu *et al.* [38] the young AF has an anisotropic permeability which becomes isotropic with age or degeneration. Due to the almost impermeable character of the AF and the fact that the directional variation of the permeability is 'only' of factor two while the values given in literature span over decades, the anisotropic permeability of the AF is neglected in this contribution.

## 7.6.2   Swelling Experiment of a Sagittally Cut NP

The second example concerns with the swelling capability of the presented model. In this context, a swelling phenomenon is computed, which occurred while Holzapfel *et al.* [44]

**Table 7.2:** *Material parameters of the biphasic model for the vertebrae, nucleus pulposus and anulus fibrosus, respectively. Isotropic contributions are always using the neo-Hookean model and inhomogeneities as is described in Ehlers et al. [26].*

| | | | |
|---|---|---|---|
| **Vertebrae: treated with no distinction between cortical shell and spongiosa** | | | |
| $K_{0S}^S = 2.7 \cdot 10^{-5}$ [mm$^2$] $\quad$ $n_{0S}^S = 0.2$ [-] $\quad$ $\mu_0^S = 192.0$ [MPa] $\quad$ $\kappa = 0.0$ [-] | | | |
| $\mu^{FR} = 3.8 \cdot 10^{-8}$ [MPa·s] $\quad$ $c_{0S}^{fc} = 0.0$ [mol/l] $\quad$ $\Lambda_0^S = 88.7$ [MPa] $\quad$ $\gamma_0^S = 1.0$ [-] | | | |

| | | | |
|---|---|---|---|
| **Nucleus pulposus: treated as isotropic, viscoelastic and charged material** | | | |
| $K_{0S}^S = 3.5 \cdot 10^{-12}$ [mm$^2$] $\quad$ $n_{0S}^S = 0.2$ [-] $\quad$ $\mu_0^S = 0.5$ [kPa] $\quad$ $\kappa = 0.0$ [-] | | | |
| $\mu^{FR} = 6.9 \cdot 10^{-10}$ [MPa·s] $\quad$ $c_{0S}^{fc} = 0.3$ [mol/l] $\quad$ $\Lambda_0^S = 0.3$ [kPa] $\quad$ $\gamma_0^S = 50.0$ [-] | | | |
| 1st Maxwell element: $\quad$ $\zeta_1^S = 0.37$ [kPa·s] $\quad$ $\mu_1^S = 2.8$ [kPa] $\quad$ [-] | | | |
| $\eta_1^S = 0.37$ [kPa·s] $\quad$ $\Lambda_1^S = 1.9$ [kPa] $\quad$ $\gamma_1^S = 12.0$ [-] | | | |
| 2nd Maxwell element: $\quad$ $\zeta_2^S = 10.0$ [kPa·s] $\quad$ $\mu_2^S = 0.85$ [kPa] $\quad$ [-] | | | |
| $\eta_2^S = 10.0$ [kPa·s] $\quad$ $\Lambda_2^S = 0.57$ [kPa] $\quad$ $\gamma_2^S = 12.0$ [-] | | | |

| | | | |
|---|---|---|---|
| **Anulus fibrosus: treated as inhomogeneous anisotropic charged material** | | | |
| $K_{0S}^S = 6.2 \cdot 10^{-12}$ [mm$^2$] $\quad$ $n_{0S}^S = 0.3$ [-] $\quad$ $\mu_0^S = 0.95$ [MPa] $\quad$ $\kappa = 0.0$ [-] | | | |
| $\mu^{FR} = 6.9 \cdot 10^{-10}$ [MPa·s] $\quad$ $c_{0S}^{fc} = 0.1$ [mol/l] $\quad$ $\Lambda_0^S = 2.2$ [MPa] $\quad$ $\gamma_0^S = 1.0$ [-] | | | |

| | Ventro-lat. int. | Ventro-lat. ext. | Dorsal ent. | Dorsal ext. |
|---|---|---|---|---|
| $\tilde{\mu}_1^S$ [kPa] | 34.3 | 146.3 | 5.9 | 50.8 |
| $\tilde{\gamma}_1^S$ [-] | 44.1 | 97.1 | 30.5 | 54.2 |

performed an experiment on a sagittally cut motion segment. Right after the specimen was cut in half and placed on the laboratory table, the NP started to swell out of the IVD and reached a maximum bulge of 4.9 mm, cf. Figure 4 in Holzapfel *et al.* [44].

This behavior is clearly a result of the tissue being removed from its physiological setting, i. e., the state where the net movement of fluid over the tissue boundary is balanced out between the osmotically driven influx of fluid and the mechanically driven efflux due to the pre-stressed solid skeleton. Whenever this equilibrium is disturbed, the tissue tends to gain chemical equilibrium again. For example, the excess of ions inside the tissue attracts the surrounding fluid with a lower ion concentration to get sucked inside, until equilibrium is reached with the resulting excess of tension in the solid skeleton. The cylindrical NP specimens could not swell as they were not surrounded by any fluid. Even though the sagittally cut motion segment is also not surrounded by a fluid, the IVD is still connected with the adjacent vertebrae, and hence, to the bone marrow. The results of the computation in Figure 7.5 (b) shows clearly that the influx of fluid, which is responsible for the bulge, stems from the vertebrae.

The simulations are carried out on a sagittally cut geometry of an L4-L5 motion segment, which is discretized using 1898 20-noded Taylor-Hood elements, cf. Figure 7.5 (a), where the vertebrae, the NP, and the AF are highlighted in blue, red and yellow, respectively. The corresponding material parameters are listed in Table 7.2, whereas the

inhomogeneities are modeled as is described in Ehlers *et al.* [26]. Following the swelling experiment, only essential boundary conditions are applied, which do not lead to a mechanical loading of the tissue. In this regard, the top and bottom surfaces of the vertebrae are fixed in space and a drainage ($\mathcal{P} = 0\,\mathrm{MPa}$) is ensured on all free surfaces. Furthermore, the concentration of the external solution is lowered from $\bar{c}_m = 0.15$ to $0.0\,\mathrm{mol/l}$ within 50 s and is then held constantly at zero for another 5000 s.
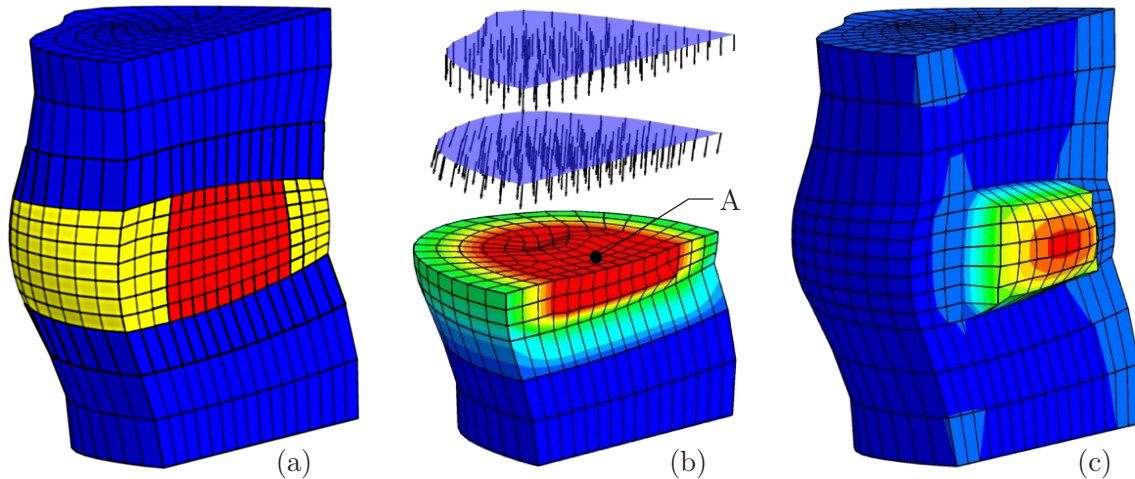


**Figure 7.5:** *(a) Discretization of the L4-L5 motion segment using 1898 Taylor-Hood elements, where the vertebrae are displayed in blue, the NP in red and the AF in yellow. (b) Visualization at $t = 50\,s$, where the arrows indicate the seepage velocity of the fluid inside the vertebra and the colors display the osmotic pressure contribution (red $\widehat{=} 0.78\,MPa$ and blue $\widehat{=} 0.0\,MPa$). (c) The coloring indicates the bulge of the NP with a peak value of 5.7 mm.*

Figure 7.5 (b) shows the tendency of the fluid movement when $\bar{c}_m$ reaches zero, i. e., at $t = 50\,\mathrm{s}$. The seepage velocity of the bone marrow is directed towards the IVD with its maximum osmotic pressure difference $\Delta\pi = 0.78\,\mathrm{MPa}$ indicated in red. The reason for the fluid being attracted by an excess of pressure becomes clear when Figure 7.6 (a) is observed, which shows the evolution of $p$, $\Delta\pi$, and $\mathcal{P}$ measured at point $A$ depicted in Figure 7.5 (b). In the beginning of the computation, i. e., at $t_0 = 0\,\mathrm{s}$, there is an initial osmotic pressure of $\Delta\pi_0 = 0.31\,\mathrm{MPa}$, which is solely carried via an 'ingrown' pre-stress in the solid skeleton. Hence, the hydraulic pressure vanishes at $t_0 = 0\,\mathrm{s}$. As the concentration $\bar{c}_m$ of the surrounding fluid is lowered, the osmotic pressure difference $\Delta\pi$ rises gradually inside the NP and the fluid starts to flow into the IVD to equal out the excess of ions, thereby causing a volume dilatation. However, due to the almost impermeable characteristics of the IVD, the inflow is constrained, and hence, the volume dilatation inside the IVD happens really slowly. Thus, the excess osmotic pressure difference is firstly carried via a suction power of the hydraulic pressure $\mathcal{P}$ (part I in Figure 7.6 (a)) and is then gradually released into tension carried by the dilated solid skeleton (part II). The duration of this process is strongly dependent upon the filter velocity of the fluid that gets sucked inside, which is finally a function of the gradient of the negative hydraulic pressure and the resistance (i. e. permeability) of the tissue. In principle, this behavior is just like a reverse consolidation problem from geomechanics, where a load on the top surface is firstly carried by the pore fluid alone and later via the extra stress of the solid skeleton.

Note that if the medium was permeable without any resistance, the consolidation or the swelling process would be finished just after applying the load or concentration drop.
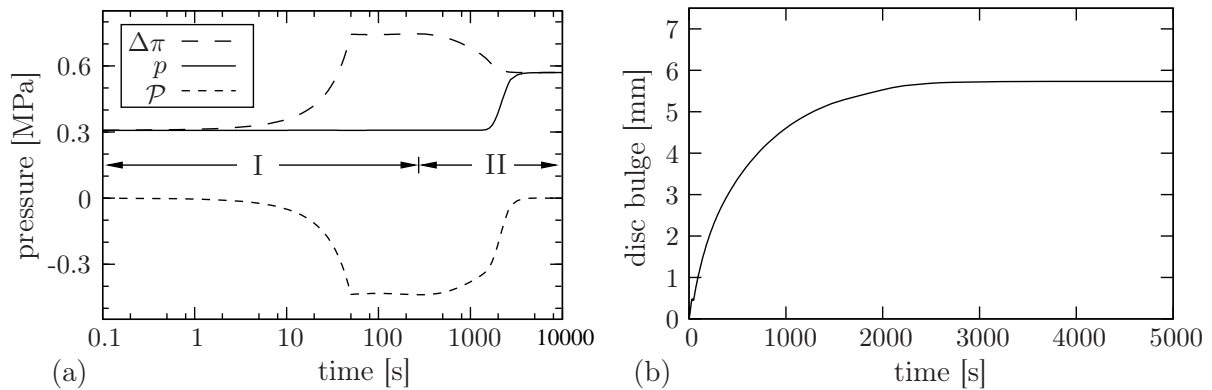


**Figure 7.6:** *(a) Evolution of the osmotic pressure difference $\Delta\pi$, the hydraulic pressure $\mathcal{P}$ and the overall pressure $p$ measured at point A, cf. Figure 7.5 (b), inside the NP and (b) development of the NP bulge for the viscoelastic computation of the swelling experiment.*

The endpoint of the swelling process is reached, when the negative hydraulic pressure inside the tissue is discharged. According to Figure 7.6, this is the case at about $t \approx 3000\,\text{s}$. The resulting bulge of the NP can be seen in Figure 7.5 (c) with the maximum bulge of $5.7\,\text{mm}$, whereas the development of the bulge is depicted in Figure 7.6 (b).

## 7.7 Conclusions

Even though the presented numerical examples included only the simpler possibilities of the constitutive equations (7.39) and (7.41), the results clearly reveal the high capacity of the model. In this regard, it was the idea to develop a model which includes several levels of complexity, thereby having the advantage of relatively easy identified material parameters on the one hand and the possibility to describe arbitrary material behavior on the other.

In particular, it is a huge benefit to have a model, which is capable to describe finite deformations with finite material behavior in the framework of a thermodynamically consistent biphasic theory. In this context, the constitutive equations involved fully satisfy the premise of polyconvexity and therefore, solutions of the numerical approximation are guaranteed. Moreover, it is possible to numerically reproduce all the key functions that occur in charged tissues. On that account any complexity level concerning the mechanical behavior of the solid skeleton, i.e., viscoelasticity, elasticity and anisotropy, is possible. Regarding the electro-chemical couplings, it is unfortunately not practicable to simultaneously have a tri- or quadriphasic model in combination with the presented extended biphasic model, as the resulting set of governing equations cannot be treated in a nice modular manner. Keeping in mind that the model is to be used on complex geometries in combination with other materials in the framework of real applications, the choice was

made in favor of the simpler approach to only capture the basic osmotic effects. This is adequate for most of the applications, thereby ensuring a reasonable computation time on today's personal computers.

As a matter of fact, the application range of the model is rather vast. For instance, it is possible to model any soft biological tissue, i. e., cartilage, IVD or brain tissue, as well as hard tissues like bones. Even man-made materials like charged hydro-gel or super-absorbent polymers (SAP), which are able to absorb as much as a thousandfold of their own dry weight, are easily modeled.

The next step in the enhancement of this model is to include degeneration effects like the loss of the fixed charge density which, as a consequence, is often accompanied by calcification, fracture or other mechanical damage. As already seen in the numerical examples, the concentration of the fixed negative charges attracts a certain amount of water, thereby causing a certain extra pressure in the tissue. If this mechanism is disturbed, the basic load-bearing behavior is modified, and in the case of the IVD, the collagen fibers might be loaded with pressure instead of tension. This again might trigger a cell metamorphosis leading to substantial structural and, therefore, mechanical changes in the tissue. In this context, it is necessary to derive appropriate evolution equations, which trigger the respective damage due to certain mechanical or chemical influences. With focus on the IVD, it is then possible to identify possible mechanisms leading to herniation or calcification of the disc.

# 7.8 References

[1] Argoubi, M. & Shirazi-Adl, A.: Poroelastic creep response analysis of a lumbar motion segment in compression. *Journal of Biomechanics* **29** (1996), 1331–1339.

[2] Arnold, D. N.; Brezzi, F. & Fortin, M.: A stable finite element for the Stokes equations. *Calcolo* **21** (1984), 337–344.

[3] Ayad, S. & Weiss, J. B.: Biochemistry of the intervertebral disc. In Jayson, M. I. V. (ed.): *The Lumbar Spine and Back Pain.* Churchill Livingstone, New York 1987, 3rd edn., pp. 100–137.

[4] Ayotte, D. C.; Ito, K.; Perren, S. M. & Tepic, S.: Direction-dependent constriction flow in a poroelastic solid: The intervertebral disc valve. *ASME Journal of Biomechanical Engineering* **122** (2000), 587–593.

[5] Bachrach, N. M.; Mow, V. C. & Guilak, F.: Incompressibility of the solid matrix of articular cartilage under high hydrostatic pressures. *Journal of Biomechanics* **31** (1998), 445–451.

[6] Balzani, D.; Neff, P.; Schröder, J. & Holzapfel, G.: A polyconvex framework for soft biological tissues. Adjustment to experimental data. *International Journal of Solids and Structures* **43** (2005), 6052–6070.

[7] Biot, M. A.: General theory of three dimensional consolidation. *Journal of Applied Physics* **12** (1941), 155–164.

[8] Bishop, A. W.: The effective stress principle. *Teknisk Ukeblad* **39** (1959), 859–863.

[9] Boehler, J. P.: Introduction of the invariant formulation of anisotropic constitutive equations. In Boehler, J. P. (ed.): *Applications of Tensor Functions in Solid Mechanics*. Springer-Verlag, Wien 1987, CISM Courses and Lectures No. 292, pp. 13–30.

[10] de Boer, R.: *Theory of Porous Media*. Springer-Verlag, Berlin 2000.

[11] Bowen, R. M.: Theory of mixtures. In Eringen, A. C. (ed.): *Continuum Physics*. Academic Press, New York 1976, vol. III, pp. 1–127.

[12] Bowen, R. M.: Incompressible porous media models by use of the theory of mixtures. *International Journal of Engineering Science* **18** (1980), 1129–1148.

[13] Braess, D.: *Finite Elemente*. Springer-Verlag, Berlin 1997.

[14] Brezzi, F. & Fortin, M.: *Mixed and Hybrid Finite Element Methods*. Springer-Verlag, New York 1991.

[15] Diebels, S.; Ellsiepen, P. & Ehlers, W.: Error-controlled Runge-Kutta time integration of a viscoplastic hybrid two-phase model. *Technische Mechanik* **19** (1999), 19–27.

[16] Donnan, F. G.: Theorie der Membrangleichgewichte und Membranpotentiale bei Vorhandensein von nicht dialysierenden Elektrolyten.Ein Beitrag zur physikalisch-chemischen Physiologie. *Zeitschrift für Elektrochemie und angewandte physikalische Chemie* **17** (1911), 572–581.

[17] Ebara, S.; Iatridis, J. C.; Setton, L. A.; Foster, R. J.; Mow, V. C. & Weidenbaum, M.: Tensile properties of nondegenerate human lumbar anulus fibrosus. *Spine* **21** (1996), 452–461.

[18] Eberlein, R.; Holzapfel, G. A. & Fröhlich, M.: Multi-segment FEA of the human lumbar spine including the heterogeneity of the anulus fibrosus. *Computational Mechanics* **34** (2004), 147–165.

[19] Eberlein, R.; Holzapfel, G. A. & Schulze-Bauer, C. A. J.: An anisotropic model for annulus tissue and enhanced finite element analysis of intact lumbar disc bodies. *Computer Methods in Biomechanical and Biomedical Engineering* **4** (2001), 209–229.

[20] Ehlers, W.: *Poröse Medien – ein kontinuumsmechanisches Modell auf der Basis der Mischungstheorie*. Habilitation, Forschungsberichte aus dem Fachbereich Bauwesen, Heft 47, Universität-GH-Essen 1989.

[21] Ehlers, W.: Toward finite theories of liquid-saturated elasto-plastic Porous Media. *International Journal of Plasticity* **7** (1991), 433–475.

[22] Ehlers, W.: Constitutive equations for granular materials in geomechanical context. In Hutter, K. (ed.): *Continuum Mechanics in Environmental Sciences and Geophysics.* Springer-Verlag, Wien 1993, CISM Courses and Lectures No. 337, pp. 313–402.

[23] Ehlers, W.: Foundations of multiphasic and porous materials. In Ehlers, W. & Bluhm, J. (eds.): *Porous Media: Theory, Experiments and Numerical Applications.* Springer-Verlag, Berlin 2002, pp. 3–86.

[24] Ehlers, W. & Acartürk, A.: The role of implicit dirichlet boundary conditions for numerically stable computations of swelling phenomena. *Computational Mechanics* **43** (2009), 545–557.

[25] Ehlers, W.; Ellsiepen, P.; Blome, P.; Mahnkopf, D. & Markert, B.: *Theoretische und numerische Studien zur Lösung von Rand- und Anfangswertproblemen in der Theorie Poröser Medien, Abschlußbericht zum DFG-Forschungsvorhaben Eh 107/6-2.* Tech. Rep. Bericht Nr. 99-II-1 aus dem Institut für Mechanik (Bauwesen), Universität Stuttgart 1999.

[26] Ehlers, W.; Karajan, N. & Markert, B.: A porous media model describing the inhomogeneous behaviour of the human intervertebral disc. *Materials Science and Engineering Technology* **37** (2006), 546–551.

[27] Ehlers, W.; Karajan, N. & Wieners, C.: Parallel 3-d simulation of a biphasic porous media model in spine mechanics. In Ehlers, W. & Karajan, N. (eds.): *Proceedings of the 2nd GAMM Seminar on Continuum Biomechanics*, 2007, vol. Report No. II-16 of the Institute of Applied Mechanics (CE), Universität Stuttgart, Germany, pp. 11–20.

[28] Ehlers, W. & Markert, B.: A linear viscoelastic biphasic model for soft tissues based on the Theory of Porous Media. *ASME Journal of Biomechanical Engineering* **123** (2001), 418–424.

[29] Ehlers, W.; Markert, B. & Acartürk, A.: Large strain viscoelastic swelling of charged hydrated porous media. In Auriault, J.-L.; Geindreau, C.; Royer, P.; Bloch, J. F.; Boutin, C. & Lewandowska, J. (eds.): *Poromechanics II, Proceedings of the 2nd Biot Conference on Poromechanics.* Swets & Zeitlinger, Lisse 2002, pp. 185–191.

[30] Ehlers, W.; Markert, B. & Acartürk, A.: Swelling phenomena of hydrated porous materials. In Abousleiman, Y. N.; Cheng, A. H.-D. & Ulm, F. J. (eds.): *Poromechanics III, Proceedings of the 3rd Biot Conference on Poromechanics.* Balkema Publishers 2005, pp. 781–786.

[31] Ehlers, W.; Markert, B. & Karajan, N.: A coupled FE analysis of the intervertebral disc based on a multiphasic TPM formulation. In Holzapfel, G. A. & Ogden, R. W. (eds.): *Mechanics of Biological Tissue.* Springer-Verlag, Berlin 2006, pp. 373–386.

[32] Eipper, G.: *Theorie und Numerik finiter elastischer Deformationen in fluidgesättig-ten Porösen Medien.* Dissertation, Bericht Nr. II-1 aus dem Institut für Mechanik (Bauwesen), Universität Stuttgart 1998.

[33] Elliott, D. A. & Setton, L. A.: A linear material model for fiber-induced anisotropy of the anulus fibrosus. *ASME Journal of Biomechanical Engineering* **122** (2000), 173–179.

[34] Ellsiepen, P.: *Zeit- und ortsadaptive Verfahren angewandt auf Mehrphasenprobleme pröser Medien.* Dissertation, Bericht Nr. II-3 aus dem Institut für Mechanik (Bauwesen), Universität Stuttgart 1999.

[35] Ellsiepen, P. & Hartmann, S.: Remarks on the interpretation of current non-linear finite element analyses as differential-algebraic equations. *International Journal for Numerical Methods in Engineering* **51** (2001), 679–707.

[36] Frijns, A. J. H.; Huyghe, J. M. & Janssen, J. D.: A validation of the quadriphasic mixture theory for intervertebral disc tissue. *International Journal of Engineering Science* **35** (1997), 1419–1429.

[37] Frijns, A. J. H.; Huyghe, J. M.; Kaasschieter, E. F. & Wijlaars, M. W.: Numerical simulation of deformations and electrical potentials in a cartilage substitute. *Biorheology* **40** (2003), 123–131.

[38] Gu, W. Y.; Mao, X. G.; Foster, R. J.; Weidenbaum, M.; Mow, V. C. & Rawlins, B.: The anisotropic hydraulic permeability of human lumbar anulus fibrosus. *Spine* **24** (1999), 2449–2455.

[39] Hassanizadeh, S. M. & Gray, W. G.: High velocity flow in porous media. *Transport in Porous Media* **2** (1987), 521–531.

[40] Hayes, W. C. & Bodine, A. J.: Flow-independent viscoelastic properties of articular cartilage matrix. *Journal of Biomechanics* **11** (1978), 407–419.

[41] Holm, S. & Nachemson, A.: Variations in the nutrition of the canine intervertebral disc induced by motion. *Spine* **8** (1983), 866–974.

[42] Holzapfel, G. A. & Gasser, T. C.: A viscoelastic model for fiber-reinforced composites at finite strains: Continuum basis, computational aspects and applications. *Computer Methods in Applied Mechanics and Engineering* **190** (2001), 4379–4403.

[43] Holzapfel, G. A.; Gasser, T. C. & Ogden, R. W.: Comparison of a multi-layer structural model for arterial walls with a Fung-type model, and issues of material stability. *ASME Journal of Biomechanical Engineering* **126** (2004), 264–275.

[44] Holzapfel, G. A.; Schulze-Bauer, C. A. J.; Feigl, G. & Regitnig, P.: Mono-lamellar mechanics of the human lumbar anulus fibrosus. *Biomechanics and Modeling in Mechanobiology* **3** (2005), 125–140.

[45] Hsieh, A. H.; Wagner, D. R.; Cheng, L. Y. & Lotz, J. C.: Dependence of mechanical behavior of the murine tail disc on regional material properties: A parametric finite element study. *ASME Journal of Biomechanical Engineering* **127** (2005), 1158–1167.

[46] Huyghe, J. M.; Houben, G. B. & Drost, M. R.: An ionised/non-ionised dual porosity model of intervertebral disc tissue. *Biomechanics and Modeling in Mechanobiology* **2** (2003), 3–19.

[47] Iatridis, J. C.; Laible, J. P. & Krag, M. H.: Influence of fixed charge density magnitude and distribution on the intervertebral disc: Applications of a Poroelastic and Chemical Electric (PEACE) model. *Transactions of the ASME* **125** (2003), 12–24.

[48] Iatridis, J. C.; a. Setton, L.; Weidenbaum, M. & Mow, V. C.: The viscoelastic behavior of the non-degenerate human lumbar nucleus pulposus in shear. *Journal of Biomechanics* **30** (1997), 1005–1013.

[49] Iatridis, J. C.; Setton, L. A.; Foster, R. J.; Rawlins, B. A.; Weidenbaum, M. & Mow, V. C.: Degeneration affects the anisotropic and nonlinear behaviors of human anulus fibrosus in compression. *Journal of Biomechanics* **31** (1998), 535–544.

[50] Iatridis, J. C.; Weidenbaum, M.; Setton, L. A. & Mow, V. C.: Is the nucleus pulposus a solid or a fluid? Mechanical behaviors of the human intervertebral disc. *Spine* **21** (1996), 1174–1184.

[51] Kaasschieter, E. F.; Frijns, A. J. H. & Huyghe, J. M.: Mixed finite element modelling of cartilaginous tissues. *Mathematics and Computers in Simulation* **61** (2003), 549–560.

[52] Kleiber, M.: Kinematics of deformation processes in materials subjected to finite elastic-plastic strains. *International Journal of Engineering Science* **13** (1975), 513–525.

[53] Klisch, S. M. & Lotz, J. C.: Application of a fiber-reinforced continuum theory to multiple deformations of the annulus fibrosus. *Journal of Biomechanics* **32** (1999), 1027–1036.

[54] Klisch, S. M. & Lotz, J. C.: A special theory of biphasic mixtures and experimental results for human annulus fibrosus tested in confined compression. *ASME Journal of Biomechanical Engineering* **122** (2000), 180–188.

[55] Lai, W. M.; Hou, J. S. & Mow, V. C.: A triphasic theory for the swelling and deformation behaviours of articular cartilage. *ASME Journal of Biomechanical Engineering* **113** (1991), 245–258.

[56] Laible, J. P.; Pflaster, D. S.; Krag, M. H.; Simon, B. R. & Haugh, L. D.: A poroelastic-swelling finite element model with application to the intervertebral disc. *Spine* **18** (1993), 659–670.

[57] Lanir, Y.: Biorheology and fluid flux in swelling tissues. I. Bicomponent theory for small deformations, including concentration effects. *Biorheology* **24** (1987), 173–187.

[58] Lee, C.-K.; Kim, Y. E.; Lee, C.-S.; Hong, Y.-M.; Jung, J.-M. & Goel, V. K.: Impact response of the intervertebral disc in a Finite-Element Model. *Spine* **25** (2000), 2431–2439.

[59] Lee, E. H.: Elastic-plastic deformation at finite strains. *Journal of Applied Mechanics* **36** (1969), 1–6.

[60] Li, L. P.; Shirazi-Adl, A. & Buschmann, M. D.: Investigation of mechanical behavior of articular cartilage by fibril reinforced poroelastic models. *Biorheology* **40** (2003), 227–233.

[61] Li, L. P.; Soulhat, J.; Buschmann, M. D. & Shirazi-Adl, A.: Nonlinear analysis of cartilage in unconfined ramp compression using a fibril reinforced poroelastic model. *Clinical Biomechanics* **14** (1999), 673–682.

[62] Lim, T.-H. & Hong, J. H.: Poroelastic properties of bovine vertebral trabecular bone. *Journal of Orthopaedic Research* **18** (2000), 671–677.

[63] Marchand, F. & Ahmed, A. M.: Investigation of the laminate structure of the lumbar disc anulus. *Spine* **15** (1990), 402–410.

[64] Markert, B.: *Porous media viscoelasticity with application to polymeric foams.* Dissertation, Bericht Nr. II-12 aus dem Institut für Mechanik (Bauwesen), Universität Stuttgart, Germany 2005.

[65] Markert, B.: A constitutive approach to 3-d nonlinear fluid flow through finite deformable porous continua with application to a high-porosity polyurethane foam. *Transport in Porous Media* **70** (2007), 427–450.

[66] Markert, B.; Ehlers, W. & Karajan, N.: A general polyconvex strain-energy function for fiber-reinforced materials. *Proceedings in Applied Mathematics and Mechanics* **5** (2005), 245–246.

[67] Mooney, M.: A theory of large elastic deformation. *Journal of Applied Physics* **11** (1940), 582–592.

[68] Mow, V. C.; Gibbs, M. C.; Lai, W. M.; Zhu, W. B. & Athanasiou, K. A.: Biphasic indentation of articular cartilage-II. A numerical algorithm and an experimental study. *Journal of Biomechanics* **22** (1989), 853–861.

[69] Mow, V. C. & Hayes, W. C.: *Basic Orthopaedic Biomechanics.* Lippincott-Raven, New York 1997, 2nd edn.

[70] Mow, V. C.; Kuei, S. C.; Lai, W. M. & Armstrong, C. G.: Biphasic creep and stress relaxation of articular cartilage in compression: Theory and experiments. *ASME Journal of Biomechanical Engineering* **102** (1980), 73–84.

[71] Noll, W.: A mathematical theory of the mechanical behavior of continuous media. *Archive for Rational Mechanics and Analysis* **2** (1958), 197–226.

[72] Ochia, R. S. & Ching, R. P.: Hydraulic resistance and permeability in human lumbar vertebral bodies. *ASME Journal of Biomechanical Engineering* **124** (2002), 533–537.

[73] Parent-Thirion, A.; Fernández Macías, E.; Hurley, J. & Vermeylen, G.: *Fourth European Working Conditions Survey*. Tech. rep., European Foundation for the Improvement of Living and Working Conditions, Dublin 2007, URL `http://www.eurofound.europa.eu/publications/htmlfiles/ef0698.htm`.

[74] Raspe, H.; Hueppe, A. & Neuhauser, H.: Back pain, a communicable disease? *International Journal of Epidemiology* **37** (2008), 69–74.

[75] Reese, S. & Govindjee, S.: A theory of finite viscoelasticity and numerical aspects. *International Journal of Solids and Structures* **35** (1998), 3455–3482.

[76] Riches, P. E.; Dhillon, N.; Lotz, J.; Woods, A. W. & McNally, D. S.: The internal mechanics of the intervertebral disc under cyclic loading. *Journal of Biomechanics* **35** (2002), 1263–1271.

[77] Rivlin, R. S.: Large elastic deformations of isotropic materials. *Proceedings of the Royal Society of London Series A* **241** (1948), 379–397.

[78] Sandhu, R. S. & Wilson, E. L.: Finite-element analysis of seepage in elastic media. *ASCE Journal of the Engineering Mechanics Division* **95** (1969), 641–652.

[79] Schanz, M. & Diebels, S.: A comparative study of Biot's theory and the linear Theory of Porous Media for wave propagation problems. *Acta Mechanica* **161** (2003), 213–235.

[80] Schmidt, C. O.; Raspe, H.; Pfingsten, M.; Hasenbring, M.; Basler, H. D.; Eich, W. & Kohlmann, T.: Back pain in the german adult population. Prevalence, severity, and sociodemographic correlations in a multiregional survey. *Spine* **32** (2007), 2005–2011.

[81] Schröder, J. & Neff, P.: Invariant formulation of hyperelastic transverse isotropy based on polyconvex free energy functions. *International Journal of Solids and Structures* **40** (2003), 401–445.

[82] Schröder, Y.; Sivan, S.; Wilson, W.; Merkher, Y.; Huyghe, J. M.; Maroudas, A. & Baaijens, F. P. T.: Are disc pressure, stress and osmolarity affected by intra- and extrafibrillar fluid exchange? *Journal of Orthopaedic Research* **25** (2007), 1317–1324.

[83] Shirazi-Adl, A.: Nonlinear stress analysis of the whole lumbar spine in torsion-mechanics of facet articulation. *Journal of Biomechanics* **27** (1994), 289–299.

[84] Shirazi-Adl, A.: Analysis of large compression loads on lumbar spine in flexion and torsion using a novel wrapping element. *Journal of Biomechanics* **39** (2006), 267–275.

[85] Shirazi-Adl, A.; Ahmed, A. M. & Shrivastava, S. C.: A finite element study of a lumbar motion segment subjected to pure sagittal plane moments. *Journal of Biomechanics* **19** (1986), 331–350.

[86] Shirazi-Adl, A.; Ahmed, A. M. & Shrivastava, S. C.: Mechanical response of a lumbar motion segment in axial torque alone and combined with compression. *Spine* **11** (1986), 914–927.

[87] Skaggs, D. L.; Weidenbaum, M.; Iatridis, J. C.; Ratcliffe, A. & Mow, V. C.: Regional variation in tensile properties and biochemical composition of the human lumbar anulus fibrosus. *Spine* **19** (1994), 1310–1319.

[88] Skempton, A. W.: Significance of Terzaghi's concept of effective stress (Terzaghi's discovery of effective stress). In Bjerrum, L.; Casagrande, A.; Peck, R. B. & Skempton, A. W. (eds.): *From Theory to Practice in Soil Mechanics*. Wiley, New York 1960, pp. 42–53.

[89] Spencer, A. J. M.: *Deformations of Fiber-Reinforced Materials*. Oxford University Press 1972.

[90] Spencer, A. J. M.: The formulation of constitutive equations for anisotropic solids. In Boehler, J. P. (ed.): *Mechanical Behavior of Anisotropic Solids*. Martinus Nijhoff Publishers, The Haque 1982, Proceedings of the Euromech Colloquium 115, pp. 2–26.

[91] Spencer, A. J. M.: Constitutive theory for strongly anisotropic solids. In Spencer, A. J. M. (ed.): *Continuum Theory of the Mechanics of Fibre Reinforced Composites*. Springer-Verlag, Wien 1984, CISM Courses and Lectures No. 282, pp. 1–32.

[92] Sun, D. N.; Gu, W. Y.; Guo, X. E.; Lai, W. M. & Mow, V. C.: A mixed finite element formulation of triphasic mechano-electrochemical theory for charged, hydrated biological soft tissues. *International Journal for Numerical Methods in Engineering* **45** (1999), 1375–1402.

[93] Treloar, L. R. G.: *The Physics of Rubber Elasticity*. Clarendon Press, Oxford 1975, 3rd edn.

[94] Truesdell, C.: *A new Definition of a Fluid, II. The Maxwellian fluid*. Tech. Rep. P-3553, §19, US Naval Research Laboratory 1949.

[95] Urban, J. P. G. & Holm, S.: Intervertebral disc nutrition as related to spinal movements and fusion. In Hargens, A. R. (ed.): *Tissue Nutrition and Viability*. Springer-Verlag, Berlin 1986, pp. 101–119.

[96]  Urban, J. P. G. & Roberts, S.: Intervertebral disc. In Comper, W. D. (ed.): *Extracellular Matrix, Volume 1, Tissue Function.* Harwood Academic Publishers GmbH 1996, pp. 203–233.

[97]  van Loon, R.; Huyghe, F. M.; Wijlaars, M. W. & Baaijens, F. P. T.: 3D FE implementation of an incompressible quadriphasic mixture model. *International Journal for Numerical Methods in Engineering* **57** (2003), 1243–1258.

[98]  Varga, O. H.: *Stress-Strain Behavior of Elastic Materials.* Interscience, New York 1966.

[99]  Wieners, C.: Taylor-hood elements in 3d. In Wendland, W. L. & Efendiev, M. (eds.): *Analysis and Simulation of Multifield Problems.* Springer-Verlag, Berlin 2003, pp. 189–196.

[100]  Wieners, C.; Ehlers, W.; Ammann, M.; Karajan, N. & Markert, B.: Parallel solution methods for porous media models in biomechanics. *Proceedings in Applied Mathematics and Mechanics* **5** (2005), 35–38.

[101]  Wilson, W.; van Donkelar, C. C. & Huyghe, J. M.: A comparison between mechano-electrochemical and biphasic swelling theories for soft hydrated tissues. *ASME Journal of Biomechanical Engineering* **127** (2005), 158–165.

[102]  Wu, J. S. S. & Chen, J. H.: Clarification of the mechanical behavior of spinal motion segments through a three-dimensional poroelastic mixed finite element model. *Medical Engineering and Physics* **18** (1996), 215–224.

[103]  Zienkiewicz, O. C. & Taylor, R. L.: *The Finite Element Method. The Basis, Vol. 1.* Butterworth Heinemann, Oxford 2000, 5th edn. edn.

# Nomenclature

As far as possible, the nomenclature in this monograph follows the conventions and symbols that are commonly used in modern tensor calculus, such as in the books by de Boer [1], Ehlers [4], Papastavridis [6], or Holzapfel [5, Ch. 1].Concerning porous media theories, the work adheres to the established notations given by de Boer [2] and Ehlers [3].

## Conventions

*Index and suffix conventions*

| | |
|---|---|
| $i, j, k, l, \ldots$ | indices as sub- or superscripts range from $1$ to $N$; usually $N = 3$ in the 3-d physical space of our experience |
| $( \cdot )_k ( \cdot )^k = \sum_k ( \cdot )_k ( \cdot )^k$ | *Einstein*'s summation convention, i. e., summation over indices that appear twice unless stated otherwise, e. g., $\sum k$ |
| $( \cdot )_S$, $( \cdot )_F$ | capital subscripts indicate the belonging of kinematical quantities to a constituent within mixture theories |
| $( \cdot )^S$, $( \cdot )^F$ | capital superscripts indicate the belonging of non-kinematical quantities to a constituent within mixture theories |

*Kernel conventions*

| | |
|---|---|
| $( \cdot )$ | place holder for kernel quantity |
| $s, t, \ldots$ or $\sigma, \tau, \ldots$ | scalars (0th-order tensors) |
| $\mathbf{s}, \mathbf{t}, \ldots$ or $\boldsymbol{\sigma}, \boldsymbol{\tau}, \ldots$ | vectors (1st-order tensors) |
| $\mathbf{S}, \mathbf{T}, \ldots$ or $\boldsymbol{\sigma}, \boldsymbol{\tau}, \ldots$ | 2nd-order tensors |
| $\overset{n}{\mathbf{S}}, \overset{n}{\mathbf{T}}, \ldots$ or $\overset{n}{\boldsymbol{\sigma}}, \overset{n}{\boldsymbol{\tau}}, \ldots$ | $n$th- or higher-order tensors, e. g., $\overset{4}{\mathbf{D}}, \overset{3}{\mathbf{E}}, \overset{2}{\mathbf{F}} = \mathbf{F}, \overset{1}{\mathbf{G}} = \mathbf{g}$ |
| $\boldsymbol{s}, \boldsymbol{t}, \ldots$ and $\boldsymbol{S}, \boldsymbol{T}, \ldots$ | general column vectors ($n \times 1$) and general matrices ($n \times m$) |

*Selected tensor operations*[1]

| | |
|---|---|
| $( \cdot )^T$ | transpose of vectors, tensors or matrices |
| $( \cdot )^{\overset{kl}{T}}$ | special transposition of higher-order tensors by an exchange of the $k$th and the $l$th basis system of the tensorial basis |
| $\overset{n}{\mathbf{S}} \, \overset{s}{\mathbf{T}} = \overset{n-s}{\mathbf{R}}$ with $n \geq s$ | contracting (inner) tensor product (linear mapping) |
| $\overset{n}{\mathbf{S}} \cdot \overset{n}{\mathbf{T}} = r$ | scalar (dot) product (special contracting tensor product) |
| $\overset{n}{\mathbf{S}} \otimes \overset{s}{\mathbf{T}} = \overset{n+s}{\mathbf{R}}$ | dyadic (vector space) tensor product |
| $\mathbf{s} \times \mathbf{t} = \mathbf{r}$ or $\mathbf{S} \times \mathbf{T} = \mathbf{r}$ | outer vector (cross) product of vectors or tensors |
| $\mathbf{s} \times \mathbf{T} = \mathbf{R}$ | outer (cross) tensor product of vector and tensor |
| $\mathbf{S} \barwedge \mathbf{T} = \mathbf{R}$ | outer (double cross) tensor product of tensors |

---

[1] Further specific formulae and rules of tensor algebra and analysis are directly provided in the text.

# Acronyms

| Acronym | Definition |
| --- | --- |
| ADI | alternating direction implicit |
| ADR | advection diffusion reaction |
| AF | anulus fibrosus |
| BC | boundary condition |
| BDD | balancing domain decomposition |
| BDF | backward differentiation formula |
| BDF2 | 2nd-order backward differentiation formula |
| BEM | Boundary Element Method |
| BT | Biot's Theory |
| BVP | boundary-value problem |
| CFD | computational fluid dynamics |
| CFL | Courant-Friedrichs-Lewy |
| CSS | conventional serial staggered |
| DAE | differential-algebraic equation |
| DD | domain decomposition |
| DE | differential equation |
| DEM | Discrete Element Method |
| DIRK | diagonal-implicit Runge-Kutta |
| DOF | degree of freedom |
| EAP | electroactive polymer |
| ECM | extracellular matrix |
| EQ | equilibrium |
| FCD | fixed charge density |
| FDM | Finite Difference Method |
| FE | finite element |
| FEM | Finite Element Method |
| FETI | finite element tearing and interconnect |
| FVM | Finite Volume Method |
| FSI | fluid-structure interaction |
| GAG | glycosaminoglycan |
| IBVP | initial boundary-value problem |
| IE | implicit (backward) Euler |
| IMEX | implicit-explicit |
| IRK | implicit Runge-Kutta |
| IVD | intervertebral disc |

| IVP | initial-value problem |
| LBB | Ladyzhenskaya-Babuška-Brezzi |
| LBP | low back pain |
| MKS | meter-kilogram-second |
| NEQ | non-equilibrium |
| NP | nucleus pulposus |
| ODE | ordinary differential equation |
| PDE | partial differential equation |
| PG | proteoglycans |
| QSSA | quasi-steady-state assumption |
| REV | representative elementary volume |
| RK | Runge-Kutta |
| RKN | Runge-Kutta-Nyström |
| SAP | super-absorbent polymer |
| SDIRK | singly diagonal-implicit Runge-Kutta |
| TG | Taylor-Galerkin |
| TM | Theory of Mixtures |
| TPM | Theory of Porous Media |
| TR | trapezoidal rule |

**Remark:** Acronyms are viewed as ordinary words such that plural forms are generated by simply adding "s"; apostrophes are only used for possessives. ∎

# References

[1] de Boer, R.: *Vektor- und Tensorrechnung für Ingenieure.* Springer-Verlag, Berlin 1982.

[2] de Boer, R.: *Theory of Porous Media.* Springer-Verlag, Berlin 2000.

[3] Ehlers, W.: Foundations of multiphasic and porous materials. In Ehlers, W. & Bluhm, J. (eds.): *Porous Media: Theory, Experiments and Numerical Applications.* Springer-Verlag, Berlin 2002, pp. 3–86.

[4] Ehlers, W.: *Vector and Tensor Calculus: An Introduction.* Lecture notes, Institute of Applied Mechanics (Chair of Continuum Mechanics), Universität Stuttgart, Germany 1995–2010, URL http://www.mechbau.de.

[5] Holzapfel, G. A.: *Nonlinear Solid Mechanics: A Continuum Approach for Engineering.* John Wiley & Sons, Chichester 2000.

[6] Papastavridis, J. G.: *Tensor calculus and analytical dynamics.* CRC Press LLC, Boca Raton 1999.

# List of Figures

# List of Tables

# Released Report Series

II-1 Gernot Eipper: *Theorie und Numerik finiter elastischer Deformationen in fluidgesättigten porösen Festkörpern*, June 1998.

II-2 Wolfram Volk: *Untersuchung des Lokalisierungsverhaltens mikropolarer poröser Medien mit Hilfe der Cosserat-Theorie*, May 1999.

II-3 Peter Ellsiepen: *Zeit- und ortsadaptive Verfahren angewandt auf Mehrphasenprobleme poröser Medien*, July 1999.

II-4 Stefan Diebels: *Mikropolare Zweiphasenmodelle: Formulierung auf der Basis der Theorie Poröser Medien*, March 2000.

II-5 Dirk Mahnkopf: *Lokalisierung fluidgesättigter poröser Festkörper bei finiten elastoplastischen Deformationen*, March 2000.

II-6 Heiner Müllerschön: *Spannungs-Verformungsverhalten granularer Materialien am Beispiel von Berliner Sand*, August 2000.

II-7 Stefan Diebels (Ed.): *Zur Beschreibung komplexen Materialverhaltens: Beiträge anläßlich des 50. Geburtstages von Herrn Prof. Dr.-Ing. Wolfgang Ehlers*, August 2001.

II-8 Jack Widjajakusuma: *Quantitative Prediction of Effective Material Parameters of Heterogeneous Materials*, June 2002.

II-9 Alexander Droste: *Beschreibung und Anwendung eines elastisch-plastischen Materialmodells mit Schädigung für hochporöse Metallschäume*, October 2002.

II-10 Peter Blome: *Ein Mehrphasen-Stoffmodell für Böden mit Übergang auf Interface-Gesetze*, October 2003.

II-11 Martin Ammann: *Parallel Finite Element Simulations of Localization Phenomena in Porous Media*, April 2005.

II-12 Bernd Markert: *Porous Media Viscoelasticity with Application to Polymeric Foams*, July 2005.

II-13 Saeed Reza Ghadiani: *A Multiphasic Continuum Mechanical Model for Design Investigations of an Effusion-Cooled Rocket Thrust Chamber*, September 2005.

II-14 Wolfgang Ehlers & Bernd Markert (Eds.): *Proceedings of the 1st GAMM Seminar on Continuum Biomechanics*, September 2005.

II-15 Bernd Scholz: *Application of a Micropolar Model to the Localization Phenomena in Granular Materials: General Model, Sensitivity Analysis and Parameter Optimization*, November 2007.

II-16 Wolfgang Ehlers & Nils Karajan (Eds.): *Proceedings of the 2nd GAMM Seminar on Continuum Biomechanics*, December 2007.

II-17 Tobias Graf: *Multiphasic Flow Processes in Deformable Porous Media under Consideration of Fluid Phase Transitions*, June 2008.

II-18 Ayhan Acartürk: *Simulation of Charged Hydrated Porous Materials*, March 2009.

II-19 Nils Karajan: *An Extended Biphasic Description of the Inhomogeneous and Anisotropic Intervertebral Disc*, March 2009.

II-20 Bernd Markert: *Weak or Strong – On Coupled Problems in Continuum Mechanics*, June 2010.